Radiation Dosimetry: Electron Beams with Energies Between 1 and 50 MeV

Library of Congress Cataloging in Publication Data

International Commission on Radiation Units and Measurements.
Radiation dosimetry.

(ICRU report ; 35)
"Issued 15 September 1984."
Supersedes: Radiation dosimetry. 1972. (ICRU report ; 21)
Bibliography: p.
Includes index.
1. Radiation dosimetry—Congresses. 2. Electron beams—Congresses. I. Title. II. Series. [DNLM: 1. Radiation Dosage. 2. Radiometry—standards. WN 650 I605r]

RA1231.R2155 no. 35 612'.01448 s [612'.01448] 84-12763 [QC795.32.R3]
ISBN 0-913394-29-7

ICRU REPORT 35

Radiation Dosimetry: Electron Beams with Energies Between 1 and 50 MeV

Issued 15 September 1984

INTERNATIONAL COMMISSION ON RADIATION
UNITS AND MEASUREMENTS.
7910 WOODMONT AVENUE
BETHESDA, MARYLAND 20814
U.S.A.

THE INTERNATIONAL COMMISSION ON RADIATION UNITS AND MEASUREMENTS

INDIVIDUALS PARTICIPATING IN THE PREPARATION OF THIS REPORT

Commission Membership During Preparation of This Report

H. O. WYCKOFF, *Chairman*
A. ALLISY, *Vice Chairman*
R. S. CASWELL, *Secretary*
G. E. D. ADAMS
G. COWPER
P. EDHOLM
J. R. GREENING
D. HARDER
A. M. KELLERER
H. H ROSSI
W. K. SINCLAIR
J. VAN DER SCHOOT
A. WAMBERSIE
L. S. TAYLOR, *Honorary Member and Member Emeritus*

Current Commission Membership

H. O. WYCKOFF, *Chairman*
A. ALLISY, *Vice Chairman*
R. S. CASWELL, *Secretary*
G. E. D. ADAMS
G. COWPER
L. FEINENDEGEN
I. ISHERWOOD
A. M. KELLERER
H. H. ROSSI
W. K. SINCLAIR
J. VAN DER SCHOOT
A. WAMBERSIE
L. S. TAYLOR, *Honorary Chairman and Member Emeritus*

Executive Secretary

W. R. NEY

Commission Sponsors

D. HARDER (until 1981)
Institut für Medizinische Physik und Biophysik
Göttingen, Germany
A. WAMBERSIE
Universite Catholique de Louvain
Bruxelles, Belgium

Senior Advisor

D. HARDER (from 1981)

Report Committee

H. SVENSSON, *Chairman*
University of Umeå
Umeå, Sweden
P. ALMOND
M. D. Anderson Hospital and Tumor Institute
Houston, Texas, U.S.A.
A. BRAHME
Karolinska Institute
Stockholm, Sweden
A. DUTREIX
Institute Gustave Roussy
Villejuif, France
H. K. LEETZ
Institut für Biophysik
Homburg, Germany

Consultants to the Report Committee

M. BERGER
National Bureau of Standards
Washington, D.C., U.S.A.
B. MARKUS
Abteilung für Strahlenphysik und Strahlenbiologie
Göttingen, Germany
A. NAHUM
University of Umea
Umea, Sweden

The Commission wishes to express its appreciation to the individuals involved in the preparation of this report for the time and effort they devoted to this task and to express its appreciation to the organizations with which they are affiliated.

(For detailed information on the availability of this and other ICRU Reports, see page 152)

Preface

Scope of ICRU Activities

The International Commission on Radiation Units and Measurements (ICRU), since its inception in 1925, has had as its principal objective the development of internationally acceptable recommendations regarding:

(1) Quantities and units of radiation and radioactivity,

(2) Procedures suitable for the measurement and application of these quantities in clinical radiology and radiobiology,

(3) Physical data needed in the application of these procedures, the use of which tends to assure uniformity in reporting.

The Commission also considers and makes similar types of recommendations for the radiation protection field. In this connection, its work is carried out in close cooperation with the International Commission on Radiological Protection (ICRP).

Policy

The ICRU endeavors to collect and evaluate the latest data and information pertinent to the problems of radiation measurement and dosimetry and to recommend the most acceptable values and techniques for current use.

The Commission's recommendations are kept under continual review in order to keep abreast of the rapidly expanding uses of radiation.

The ICRU feels it is the responsibility of national organizations to introduce their own detailed technical procedures for the development and maintenance of standards. However, it urges that all countries adhere as closely as possible to the internationally recommended basic concepts of radiation quantities and units.

The Commission feels that its responsibility lies in developing a system of quantities and units having the widest possible range of applicability. Situations may arise from time to time when an expedient solution of a current problem may seem advisable. Generally speaking, however, the Commission feels that action based on expediency is inadvisable from a long-term viewpoint; it endeavors to base its decisions on the long-range advantages to be expected.

The ICRU invites and welcomes constructive comments and suggestions regarding its recommendations and reports. These may be transmitted to the Chairman.

Current Program

The Commission has divided its field of interest into twelve technical areas and has assigned one or more members of the Commission the responsibility for identification of potential topics for new ICRU activities in each area. A body of consultants has been constituted for each technical area to advise the Commission on the need for ICRU recommendations relating to the technical area and on the means for meeting an identified need. Each area is reviewed periodically by its sponsors and consultants. Recommendations of such groups for new reports are then reviewed by the Commission and a priority assigned.

The technical areas are:

Radiation Therapy
Diagnostic Radiology
Nuclear Medicine
Radiobiology
Radioactivity
Radiation Physics—X Rays, Gamma Rays and Electrons
Radiation Physics—Neutrons and Heavy Particles
Radiation Protection
Radiation Chemistry
Critical Data
Theoretical Aspects
Quantities and Units

The actual preparation of ICRU reports is carried out by ICRU report committees. One or more Commission members serve as sponsors to each committee and provide close liaison with the Commission. The currently active report committees are:

Absolute and Relative Dosimetry at High Doses
Characterization of Irradiation for Materials-Effect Studies
Chemical Dosimetry
Clinical Dosimetry for Neutrons
Computer Uses in Radiotherapy
Definitions and Terminology for Computed Tomography
Definitions of Physical Parameters to Specify Performance of Imaging Instruments
Determination of Absorbed Dose Distribution Around a Source Used for Interstitial Therapy
Dose Specification for Reporting Intracavitary and Interstitial Therapy
Measurement of Dose Equivalent
Modulation Transfer Function for Screen-Film Systems
Practical Determination of Dose Equivalent Index
Quality Assurance in External Beam Therapy
Stopping Power
Tissue Equivalent Materials

ICRU Reports

In 1962 the ICRU, in recognition of the fact that its triennial reports were becoming too extensive and in

some cases too specialized to justify single-volume publication, initiated the publication of a series of reports, each dealing with a limited range of topics. This series was initiated with the publication of six reports:

ICRU Report 10a, *Radiation Quantities and Units*
ICRU Report 10b, *Physical Aspects of Irradiation*
ICRU Report 10c, *Radioactivity*
ICRU Report 10d, *Clinical Dosimetry*
ICRU Report 10e, *Radiobiological Dosimetry*
ICRU Report 10f, *Methods of Evaluating Radiological Equipment and Materials*

These reports were published, as had been many of the previous reports of the Commission, by the United States Government Printing Office as Handbooks of the National Bureau of Standards.

In 1967, the Commission determined that in the future the recommendations formulated by the ICRU would be published by the Commission itself. This report is published by the ICRU pursuant to this policy. With the exception of ICRU Reports 10a, 10d, and 10e, the other reports of the "10" series have continuing validity and, since no subsequent reports were designed specifically to supersede them, they will remain available until the material is essentially obsolete. All future reports of the Commission, however, will be published under the ICRU's own auspices. Information about the availability of ICRU Reports is given on page 152.

ICRU's Relationships With Other Organizations

In addition to its close relationship with the International Commission on Radiological Protection, the ICRU has developed relationships with other organizations interested in the problems of radiation quantities, units and measurements. Since 1955, the ICRU has had an official relationship with the World Health Organization (WHO) whereby the ICRU is looked to for primary guidance in matters of radiation units and measurements and, in turn, the WHO assists in the world-wide dissemination of the Commission's recommendations. In 1960, the ICRU entered into consultative status with the International Atomic Energy Agency. The Commission has a formal relationship with the United Nations Scientific Committee on the Effects of Atomic Radiation (UNSCEAR), whereby ICRU observers are invited to attend UNSCEAR meetings. The Commission and the International Organization for Standardization (ISO) informally exchange notifications of meetings and the ICRU is formally designated for liaison with two of the ISO Technical Committees. The ICRU also corresponds and exchanges final reports with the following organizations:

Bureau International de Metrologie Legale
Bureau International des Poids et Mesures
Commission of the European Communities
Council for International Organizations of Medical Sciences
Food and Agriculture Organization
International Council of Scientific Unions
International Electrotechnical Commission
International Labor Office
International Radiation Protection Association
International Union of Pure and Applied Physics
United Nations Educational, Scientific and Cultural Organization

The Commission has found its relationship with all of these organizations fruitful and of substantial benefit to the ICRU program. Relations with these other international bodies do not affect the basic affiliation of the ICRU with the International Society of Radiology.

Operating Funds

In the early days of its existence, the ICRU operated essentially on a voluntary basis, with the travel and operating costs being borne by the parent organizations of the participants. (Only token assistance was originally available from the International Society of Radiology.) Recognizing the impracticability of continuing this mode of operation on an indefinite basis, operating funds were sought from various sources.

Financial support has been received from the following organizations:

Agfa-Gevaert, N.V.
Atomic Energy Control Board
B.A.T. Cigaretten Fabriken GMBH
Central Electricity Generating Board
CGR Medical Corporation
Commission of the European Communities
Council for International Organizations of Medical Sciences
Danish Scientific Fund
Dutch Society for Radiodiagnostics
Eastman Kodak Company
E. I. duPont de Nemours and Company
Ford Foundation
Fuji Photo Company
General Electric Company
Gilbert X-ray Company
Hitachi Medic
International Atomic Energy Agency
International Radiation Protection Association
International Society of Radiology
Italian Radiological Association
Japan Industries Association of Radiation Apparatus
John och Augusta Perssons stiftelse
Konishi-Roku Photo Company
National Cancer Institute of the U.S. Department of Health and Human Services
N.V. Philips Gloeilampenfabrieken
Philips Medical Systems, Incorporated
Picker Corporation
Pyne Corporation
Radiological Society of North America
Rockefeller Foundation
Shimadzu Corporation
Siemens Aktiengesellschaft

Society of Nuclear Medicine
Statens laegevidenskabelige Forskiningsrad
Toshiba Corporation
United Nations
U.S. Bureau of Radiological Health of the Food and Drug Administration
World Health Organization
Xerox Corporation

In addition to the direct monetary support provided by these organizations, many organizations provide indirect support for the Commission's program. This support is provided in many forms, including, among others, subsidies for (1) the time of individuals participating in ICRU activities, (2) travel costs involved in ICRU meetings, and (3) meeting facilities and services.

In recognition of the fact that its work is made possible by the generous support provided by all of the organizations supporting its program, the Commission expresses its deep appreciation.

HAROLD O. WYCKOFF
Chairman, ICRU

Bethesda, Maryland, U.S.A.
15 February 1984

Contents

Preface iii
List of Symbols ix
1. Introduction 1
2. Fundamentals of the Interaction of Electron Beams with Matter 3
2.1 Rationale 3
2.2 Basic Electron Interaction Data 3
2.2.1 Total Mass Stopping Power 3
2.2.2 Mass Collision Stopping Power 3
2.2.3 Restricted Mass Collision Stopping Power 9
2.2.4 Mass Radiative Stopping Power 11
2.2.5 The Continuous-Slowing-Down Range 14
2.2.6 Mass Scattering Power 18
2.3 Differential Electron Fluence 22
2.4 Energy Spectra 23
2.4.1 General 23
2.4.2 Spectrum of Electrons Traversing a Plane-Parallel Slab 24
2.4.3 Energy Distribution of the Electron Fluence Inside an Absorber 26
2.4.4 Slowing-Down Spectra Independent of the Space Coordinates 27
2.5 Angular Distribution 28
2.5.1 General 28
2.5.2 Angular Distribution of the Electrons Crossing a Plane Surface 28
2.6 Lateral Distribution 29
2.6.1 General 29
2.6.2 Incident Narrow Gaussian Beams 30
2.6.3 Rectangular and Circular Incident Beams 31
2.7 Depth Distribution 31
2.7.1 General 31
2.7.2 Fluence and Planar Fluence 31
2.7.3 Particle and Charge Transport 32
2.8 Absorbed-Dose Distribution 34
2.8.1 General 34
2.8.2 Point Monodirectional Beam 35
2.8.3 Plane-Parallel Beam 36
2.8.4 Point Isotropic Source 37
2.8.5 Plane Isotropic Source 38
2.8.6 Reciprocity 39
2.9 Secondary Particle Production 39
2.9.1 General 39
2.9.2 Bremsstrahlung 39
2.9.3 Positrons 40
2.9.4 Photonuclear Reactions 40
2.9.5 Electronuclear Reactions 41
3. Characteristics of Clinical Electron Beams 43
3.1 General 43
3.2 Irradiation Geometry 43
3.2.1 Emittance and Beam Optics 43
3.2.2 Beam Flattening 45
3.2.3 Beam Collimation 46
3.2.4 Irradiation Geometry Parameters 48
3.3 Energy 55

3.3.1 Energy Parameters 55
3.3.2 Determination of Electron Energy 57
3.4 Time Structure 63
4. Determination of Absorbed Dose 65
4.1 Relationship Between Absorbed Dose in the Detector and in the Medium 65
4.1.1 General 65
4.1.2 Small Detector 65
4.1.3 Large Detector 65
4.2 Location of Effective Point of Measurement and Values of Perturbation Correction Factor 66
4.2.1 Gas-Filled Detectors 66
4.2.2 Solid and Liquid Detectors 68
4.3 Stopping Power ratio 70
4.3.1 Fundamentals 70
4.3.2 Transition Material Between Wall and Radiation Sensitive Material of a Detector 71
4.3.3 Wall-Less Detectors 72
4.3.4 Comparison of Calculated and Experimental Values ... 74
4.3.5 Recommended Stopping Power Ratios 76
5. Absorbed Dose Measurement Techniques 77
5.1 General 77
5.2 Calorimetry 77
5.2.1 Introduction 77
5.2.2 Experimental Work with Calorimeters 77
5.2.3 Uncertainty in the Determination of Absorbed Dose in a Reference Material 78
5.2.4 Transfer of Absorbed Dose Calibration to Different Dosimetric Systems and to a Point in Water 79
5.3 Chemical Methods 80
5.3.1 Introduction 80
5.3.2 Ferrous Sulphate Dosimeter 80
5.4 Gas Ionization Chambers 83
5.4.1 Gas-Ionization Chamber for Absolute Determinations .. 84
5.4.2 Field Instruments 86
5.4.3 Calibration of Field Instrument Against a Chamber of Known Sensitivity 87
5.4.4 Calibration of a Thimble Chamber as a Field Instrument in a Cobalt-60 Gamma-Ray or 2 MV X-Ray Beam ... 87
5.5 Liquid Ionization Chambers 90
5.6 Solid State Dosimetry 90
5.6.1 Introduction 90
5.6.2 Thermoluminescent Phosphors 91
5.6.3 Optical Absorption in Clear Polymethyl Methacrylate (PMMA) 92
5.6.4 Silicon Diode Detectors 92
5.7 Film Dosimeters 92
6. Absorbed Dose in a Phantom Irradiated with an Electron Beam 96
6.1 General 96
6.2 Phantoms 96
6.2.1 Standard Phantom 96
6.2.2 Material Equivalence 96
6.2.3 Reference Plane and Reference Point 97
6.3 Absorbed Dose at the Reference Point 99
6.3.1 General 99

6.3.2 Determination of Absorbed Dose 99
6.4 Absorbed Dose on the Reference Axis 101
6.4.1 General 101
6.4.2 Absorbed Dose Determination 101
6.4.3 Characteristics of the Depth-Dose Curve 103
6.5 Absorbed Dose in Planes Perpendicular to or Parallel to the Beam Axis 109
6.5.1 General 109
6.5.2 Measurements 109
6.5.3 Uniformity 110
6.5.4 Penumbra 111
6.5.5 Leakage Radiation 111
7. Determination of Absorbed Dose Distribution in a Patient .. 112
7.1 General 112
7.2 Conversion of Phantom Data to Tissue Data 112
7.3 Correction for Oblique Incidence 112
7.4 Corrections for Inhomogeneities 113
7.5 Decelerators, Bolus and Wedges 115
7.5.1 Decelerators 115
7.5.2 Bolus 116
7.5.3 Wedges 116
7.6 Electron Beam Treatment Planning 116
7.6.1 General 116
7.6.2 Multiple Beams 117
7.6.3 Moving Beams 117
7.7 Computerized Treatment Planning 119
7.7.1 Empirical Methods 119
7.7.2 Analytical Methods 120
7.7.3 Monte Carlo Methods 121
7.7.4 Conclusions 121
8. Electron Beam Monitors 122
8.1 Introduction 122
8.2 Transmission Ionization Chambers 122
8.3 Choice of Monitor Systems—Practical Implications and Safety Considerations 123
9. Tests of Constancy of Performance Parameters and Schedules for Such Testing 125
9.1 Introduction 125
9.2 What Should be Checked and When 125
9.2.1 Light Beam, Radiation Beam Alignment, Distance Indicators and Mechanical Alignments 125
9.2.2 Monitor Check 125
9.2.3 Absorbed Dose Checks 125
9.2.4 Energy Check 126
9.2.5 Radiation Beam Uniformity Checks 126
9.2.6 Contamination and Leakage Measurements 126
9.2.7 Summary 127
9.3 Dosimetric Measurements on the Patient 127
10. Radiobiological Aspects 128
10.1 Introduction 128
10.2 Survey of the Radiobiological Data 128
10.3 Theoretical Considerations 130
10.4 Conclusions: Implications in Radiotherapy 132
References 133
ICRU Reports 152
Index 155

List of Symbols

a	area
A	nucleon number
ΔA	increase in absorbance
c	velocity of light in vacuum
C_{ET}	coefficient of equivalent thickness
D	absorbed dose
D_i	absorbed dose in detector material, i
D_m	absorbed dose in material, m
D_w	absorbed dose in water
E	kinetic energy of electrons
$\overline{E}$	mean energy
E_a	intrinsic accelerator energy
E_i	initial energy
E_{max}	maximum energy
E_0	energy at absorber surface
E_p	most probable energy
E_{th}	threshold energy
E_z or $E(z)$	energy at a depth z in a phantom
G	radiation chemical yield
G	normalized dose gradient
I	mean excitation energy
J_g	electric charge (of one sign) per unit mass of a gas, g
l	length, distance
m_e	rest mass of electron
M	meter reading
M_A	molar mass of substance A
n	refractive index
$N(\vec{\omega})$	number of particles crossing a plane in the direction $\vec{\omega}$
N_A	Avogadro constant
N_D	absorbed dose to air calibration factor
N_K	air-kerma calibration factor
N_x	exposure calibration factor
p	pressure
$p_{m,i}$	perturbation correction factor for a detector of material, i, in a medium, m
P	point of interest
P′	center of a detector
P_{eff}	effective point of measurement
$P_{80/20}$	physical penumbra
Q	electric charge
$\vec{r}$	field position vector
r_e	electron radius
r_{eff}	radius of the effective electron source
r_0	continuous-slowing-down range
r_{rms}	root mean square radial displacement
R_{ex}	extrapolated range
R_{max}	maximum range
R_p	practical range
R_t	therapeutic range
$R_{t'}$	the near-surface extension of the therapeutic interval
R_{50}	half-value depth
R_{100}	depth of dose maximum
s_{eff}	effective source surface distance
s_{vir}	virtual point source surface distance
$s_{m,i}$	mass collision stopping power ratio of material m to material i at a specified energy
$s_{m,i}^{BG}$	mass collison stopping power ratio under the csda approximation (Bragg-Gray)
$s_{m,i}^{H}$	mass collision stopping power ratio using a treatment suggested by Harder
$s_{m,i}^{SA}$	mass collision stopping power ratio using a treatment suggested by Spencer and Attix
S_Δ	restricted collision stopping power
S/ρ	total mass stopping power
$(S/\rho)_{col}$	mass collision stopping power
$(S/\rho)_{rad}$	mass radiative stopping power
T/ρ	mass scattering power
$U_{90/50}$	uniformity index
v	velocity
V	volume
W	mean energy expended by electrons per ion pair formed
X_0	radiation length
$\overline{y}_D$	dose mean lineal energy
Y_E	distribution of the track length differential in energy
$\overline{y}_F$	frequency mean of lineal energy
z	depth in absorber in beam direction
z	specific energy
Z	atomic number
α	fine structure constant
β	velocity of the electron relative to the velocity of light in vacuum
Γ	energy spread
δ	density effect correction
Δ	cut-off energy
ϵ	emittance of an electron beam
$\bar{\epsilon}$	the mean energy imparted
ϵ_m	molar extinction coefficient
η_A	fractional absorption coefficient
η_B	fractional backscattering coefficient
η_T	fractional transmission coefficient
θ	angle of deflection of an electron
θ_m	cut off angle for large deflections
θ_μ	screening angle for small deflections
κ	ratio between the most probable energy loss, ΔE_p, and the energy spread, Γ
ρ	density
τ	ratio of kinetic energy of the electron to the rest energy
Φ	particle fluence
$\vec{\Phi}(\vec{r})$	vectorial electron fluence density at a

	field position $\vec{r}$
$\Phi_{E,\vec{\Omega}}(\vec{r})$	differential distribution of fluence in energy and angle at a field position $\vec{r}$
Φ^{p}	planar particle fluence
Ψ	energy fluence
$\vec{\Psi}(\vec{r})$	vectorial energy fluence at a field position $\vec{r}$
$\vec{\omega}$	vector normal to the reference surface
Ω	solid angle
$\vec{\Omega}$	particle direction

Radiation Dosimetry: Electron Beams with Energies Between 1 and 50 MeV

1. Introduction

ICRU Report 21 (ICRU, 1972) treated the basic aspects of electron-beam dosimetry with special attention to the use of electron beams in radiation therapy. Since that report was completed, the use of high-energy electrons in radiation therapy has expanded and linear accelerators and microtrons have come into more frequent use beside the previously dominating betatrons. The properties of the clinical electron beams in present use are, therefore, greatly diversified and new characterizations are needed to describe the beam qualities for dosimetric and therapeutic use. Furthermore, the accuracy of the determination of many important quantities in electron dosimetry has been improved. This is the case, for example, with stopping- and scattering-power values, stopping-power ratios and perturbation corrections, where the old data have been revised. The knowledge in the field of clinical electron dosimetry has also expanded in areas such as inhomogeneity corrections and computerized dose-planning. The present report covers all aspects of electron beam dosimetry, making reference to ICRU Report 21 (ICRU, 1972) unnecessary, except for bibliographic purposes.

ICRU Report 33 (ICRU, 1980) gives a set of concepts and definitions of quantities related to ionizing radiations which are internally consistent and of sufficient generality to cover the needs of this report. Most of the dosimetric quantities such as fluence, absorbed dose and mass stopping power used in this report are those defined in ICRU Report 33. Other needed quantities, such as planar fluence, mass scattering power and perturbation correction factor, are defined in this report.

This report explains how these quantities, particularly absorbed dose, can be determined for electrons with initial energies between 1 and 50 MeV, a range chosen to include beams which are produced by linear and circular accelerators used in medicine, radiation chemistry and radiation biology.

This report is primarily concerned with quantities and methods which are sufficiently well established to be useful in standardization. However, in some important areas in clinical electron-beam dosimetry such methods do not exist. An attempt has been made to analyze these situations and suggest some quantities and methods which may fill the gaps. This is the case, particularly, with the characteristics of a clinical electron beam (see Section 3) and also with the parameters of the absorbed dose distributions (see Section 6).

The dosimetric accuracy obtainable with high-energy electron beams is highly dependent upon the knowledge of physical properties of the particular electron beam in use. Therefore, Section 2 has been devoted to the interaction of electron beams with matter, with special attention devoted to the relationships between concepts like fluence, planar fluence, and absorbed dose, and also the energy and angular distribution in electron beams. A full knowledge of Section 2 and parts of Sections 3 and 4 is not essential in practice, but they have been included because no general text covering these topics is available, and because a good theoretical background is necessary for an adequate understanding of the many complicated problems encountered in the dosimetry of high-energy electron beams. Knowledge of Sections 5, 6 and 7 is needed for the practical determination of absorbed dose in radiation therapy with electron beams. Appropriate monitors and checking routines are essential for accurate dosimetry in routine therapy and these are discussed in Sections 8 and 9. The relationship between absorbed dose and biological response is compared and discussed for different radiation modalities in Section 10.

Due to the sensitive dependence of the absorbed-dose distributions on the detailed design of a particular treatment unit, it is impossible to give general dose distributions for clinical applications. Instead, the

spread in the values of dose distribution parameters from different treatment units is illustrated.

Radiation protection of patients or staff is not dealt with in this report. Information on this subject can be found in ICRP Publications 3 (ICRP, 1960), 4 (ICRP, 1964), 15 (ICRP, 1970), 21 (ICRP, 1972) and NCRP Reports No. 31 (NCRP, 1964), No. 38 (NCRP, 1971), No. 51 (NCRP, 1977) and the German standard on this subject (DIN, 1972).

2. Fundamentals of the Interaction of Electron Beams with Matter

2.1 Rationale

The basic interaction processes of high-energy electron beams with matter are of fundamental importance for the determination of the absorbed dose in a medium irradiated by a high-energy electron beam. In most absorbed-dose measurements, the accuracy of a result is directly related to an understanding of the basic physical processes. The basic interactions of high-energy electron beams with matter are, therefore, briefly reviewed in Section 2.2, with special reference to the situations encountered in radiation therapy and radiation biology.

2.2 Basic Electron Interaction Data

The most important quantitative data on electron slowing down and scattering are presented in five tables set out in this section. A short explanation of the calculation of the tabulated values and the limits of their applicability is given to enable the reader to check the numbers provided and to derive corresponding data for other cases which could not be included here.

2.2.1 Total Mass Stopping Power

For electrons, the total mass stopping power, $(S/\rho)_{tot}$, as defined by the ICRU (ICRU, 1980), includes the total energy loss, dE, by collision and radiation for a pathlength, dl, in matter of density ρ. For energies at which nuclear interactions may be neglected, the total mass stopping power can be separated into two components:

$$\frac{1}{\rho}\left(\frac{dE}{dl}\right)_{tot} = (S/\rho)_{tot} = (S/\rho)_{col} + (S/\rho)_{rad} \quad (2.1)$$

The first component, $(S/\rho)_{col}$, includes all energy losses in particle collisions which directly produce secondary electrons and atomic excitations. It also includes energy losses due to the production of Cerenkov radiation. The second component, $(S/\rho)_{rad}$, includes all energy losses of the primary electron which lead to bremsstrahlung production.

2.2.2 Mass Collision Stopping Power

Following the theoretical derivation of Bethe (1933) and Rohrlich and Carlsson (1954), the mass collision stopping power can be calculated from (Berger and Seltzer, 1964):

$$(S/\rho)_{col} = \frac{2\pi r_e^2 m_e c^2 N_A Z}{\beta^2 M_A} \cdot \left\{\ln\left[\frac{\tau^2(\tau+2)}{2(I/m_e c^2)^2}\right] + F(\tau) - \delta\right\} \quad (2.2)$$

where δ is the density effect correction (Sternheimer, 1952, 1953, 1956; Sternheimer and Peierls, 1971; Inokuti and Smith, 1982; Ashley, 1982), and

$F(\tau) = 1 - \beta^2 + [\tau^2/8 - (2\tau+1)\ln 2]/(\tau+1)^2$
$m_e c^2$ = rest energy of the electron
$\tau = E/m_e c^2$ = ratio of kinetic energy, E, of the electrons to the rest energy
$\beta = v/c$
v = velocity of the electrons
c = velocity of light in vacuum
N_A = Avogadro constant ($= 6.02252 \cdot 10^{23} mol^{-1}$)
r_e = electron radius $= e^2/m_e c^2$ ($= 2.818 \cdot 10^{-15} m$)
Z = atomic number
M_A = molar mass of substance A
I = mean excitation energy

It can be seen from this formulation that the density effect correction (δ) and the mean excitation energy (I) are needed to determine the mass collision stopping power. An ICRU committee presently reviewing the current information on stopping power in order to provide recommended values has addressed the matter of δ and I. Unfortunately, their work (to be ICRU Report 37) is not yet published. However, the mean excitation energies (see Tables 2.1a and b) and density effect corrections being used by that committee are used here except for the analysis of electron dosimetry data (see below). Thus, the density effect correction employed is based on the method by Sternheimer (1952) using atomic binding energies from Carlson (1975). The resulting values are given in Table 2.2a.

Density-effect correction values have recently been evaluated by Inokuti and Smith (1982) for aluminum and by Ashley (1982) for water. The percentage differences in collision stopping-power values obtained using these, as compared to those obtained using corresponding Sternheimer-Carlson correction values, are smaller than 0.2% and 0.5%, respectively. This very satisfactory agreement, as well as evidence from high-energy charged-particle penetration data, gives confidence in these results. It is, therefore, expected that the overall uncertainty of the mass collision stopping power values, based on the I-values in Tables 2.1a and b and the Sternheimer (1952)–Carlson (1975) density correction values for energies above 100 keV, is between 1 and 2%.

Many determinations of absorbed dose depend upon the product of the stopping power ratio and the average energy required to produce an ion pair, W, in a gas.

Some of the determinations of W used to obtain mean values as given, for example, in Table 5.5, also required values of stopping power ratios. The values of stopping power used for this purpose are somewhat different ratios than those in Table 2.2a. Thus, to provide stopping power values that are consistent with those used in the W determinations, Table 2.2b is provided for the materials of interest in reviewing published data. These values were evaluated by using the Sternheimer-Peierls, 1971, density-effect treatment.

It may be noted that stopping power values in Tables 2.2a and 2.2b differ for some energies by up to about 1.5%. It must be recognized that, although the density-effect treatment in the forthcoming ICRU Report 37 represents state-of-the-art physics, the use of the Sternheimer-Peierls density effect correction, in conjunction with the Spencer-Attix cavity ionization theory and the W-value for air given in ICRU Report 31, and Table 5.5, gives better agreement with state-of-the-art experimental dosimetry data, by about 1% (see Section 4.3.4). Therefore, for the purpose of the analysis of already published electron dosimetry data, the Sternheimer-Peierls density effect will be used (see Tables 5.3, 5.7, and 6.3).

The density effect theory is designed for homogeneous media. This condition is, however, not met for graphite. The crystallite density is 2.265 g cm^{-3}, whereas the bulk density of polycrystalline graphite may range from 1.5 to 1.9 g cm^{-3}, depending on the manufacturing method. The porosity structure is complicated and, according to Berger and Seltzer 1982, it is not clear what density should be used in a simple theory which neglects these complications. Collision stopping-power values given, therefore, are for densities of 1.7 and 2.265 (or 2.25, see Table 2.1a) g cm^{-3}. The use of the higher density will change the carbon stopping power values by up to 1% at high energies, i.e., above 30 MeV (see Table 2.2).

TABLE 2.1a—*Properties of elements*

Name and Symbol	Mean[a] Excitation Energy, I/eV	Density, ρ/g cm^{-3}
Hydrogen ($_1$H)	19.2	$8.375 \cdot 10^{-5}$ [b]
Helium ($_2$He)	41.8	$1.663 \cdot 10^{-4}$ [b]
Beryllium ($_4$Be)	63.7	1.85
Carbon ($_6$C)	78.0	2.265[c], 2.25[c], 1.7[c]
Nitrogen ($_7$N)	82.0	$1.165 \cdot 10^{-3}$ [b]
Oxygen ($_8$O)	95.0	$1.332 \cdot 10^{-3}$ [b]
Aluminum ($_{13}$Al)	166	2.70
Silicon ($_{14}$Si)	173	2.33
Titanium ($_{22}$Ti)	233	4.54
Iron ($_{26}$Fe)	286	7.87
Copper ($_{29}$Cu)	322	8.96
Molybdenum ($_{42}$Mo)	424	10.22
Tin ($_{50}$Sn)	488	7.31
Tungsten ($_{74}$W)	727	19.30
Lead ($_{82}$Pb)	823	11.35
Uranium ($_{92}$U)	890	18.95

[a] See forthcoming ICRU Report 37 or Berger and Seltzer (1982) for discussion of values for mean excitation energy.

[b] At 20°C and 1.013×10^5 Pa.

[c] Tabular data on stopping powers are supplied below for the crystallite density, 2.265 g cm^{-3} and for a bulk density of 1.7 g cm^{-3} (the bulk density may range from 1.5 to 1.9 g cm^{-3} depending upon the method of manufacture) as well as for a density of 2.25 g cm^{-3}. Data for the first two densities are from the forthcoming ICRU Report 37 and Berger and Seltzer, 1982; data for a density of 2.25 g cm^{-3} are from Berger, 1980.

TABLE 2.1b—*Properties and composition of compounds and mixtures*

Material	Mean Excitation energy[a] I/eV	Density ρ/g cm^{-3}	Elemental Composition/Weight Fractions H	C	N	O	Others	Reference
Tissues								
Adipose Tissue	63.2	0.92	0.120	0.637	0.008	0.232	0.001 Na, 0.001 S, 0.001 Cl	ICRP (1975)
Bone (cortical)	106.7	1.85	0.047	0.144	0.042	0.444	0.002 Mg, 0.104 P, 0.003 S, 0.005 Cl, 0.209 Ca	ICRP (1975)
Muscle (skeletal)	75.3	1.04	0.101	0.108	0.028	0.754	0.001 Na, 0.002 P, 0.003 S, 0.003 K	ICRP (1975)
Muscle (striated)	74.6	1.04	0.102	0.123	0.035	0.729	0.001 Na, 0.002 P, 0.005 S, 0.003 K	ICRU (1964)
Liquids								
Water (H_2O)	75.0	1.00	0.112	—	—	0.888		
Ferrous Sulphate Solution	76.4	1.024	0.108	—	0.00003	0.878	0.013 S, 0.0001(Na + Cl + Fe)	Green *et al.* (1973)
Muscle Equivalent without Sucrose	74.2	1.07	0.102	0.120	0.036	0.742		Goodman (1969)
Gases								
Air (dry)	85.7	$1.205 \cdot 10^{-3}$ [b]	—	—	0.755	0.232	0.013 Ar	ICRU (1964)
Carbon Dioxide (CO_2)	85.0	$1.842 \cdot 10^{-3}$ [b]	—	0.273	—	0.727		
Tissue Equivalent with Methane	61.2	$1.064 \cdot 10^{-3}$ [b]	0.102	0.456	0.035	0.407		Rossi & Failla (1956)
Solids								
A 150 (tissue equivalent plastic)	65.1	1.127	0.101	0.776	0.035	0.052	0.017 F, 0.018 Ca	ICRU (1977)
C 552 (air equivalent plastic)	86.8	1.76	0.025	0.502	—	0.004	0.465 F, 0.004 Si	ICRU (1977)
Glass (Pyrex)	134.0	2.23	—	—	—	0.540	0.040 B, 0.028 Na, 0.011 Al, 0.337 Si	Hubbell (1969)
M 3	67.9	1.05	0.114	0.656	—	0.092	0.135 Mg, 0.003 Ca	Markus (1956)
MS 20	75.1	1.00	0.081	0.584	0.018	0.186	0.130 Mg, 0.001 Cl	White *et al.* (1977)
Polyamide (Nylon 6) ($C_6H_{11}ON$)	63.9	1.14	0.098	0.637	0.124	0.141		
Polyethylene (C_2H_4)	57.4	0.94	0.144	0.856	—	—		
Polyethylene Terephthalate (Mylar) ($C_{10}H_8O_4$)	78.7	1.40	0.042	0.625	—	0.333		ICRU (1977)
Polymethylmethacrylate (PMMA) ($C_5H_8O_2$)	74.0	1.19	0.080	0.600	—	0.320		
Polystyrene (C_8H_8)	68.7	1.06	0.077	0.923	—	—		
Polytetrafluoroethylene (Teflon) (C_2F_4)	99.1	2.20	—	0.240	—	—	0.760 F	
Polyvinylchloride (C_2H_3Cl)	108.2	1.30	0.048	0.384	—	—	0.567 Cl	
Lithium Flouride (LiF)	94.0	2.635	—	—	—	—	0.268 Li, 0.732 F	
Film Emulsion	331.0	3.815	0.014	0.072	0.019	0.066	0.002 S, 0.349 B, 0.474 Ag, 0.003 I	Barkas *et al.* (1958)

[a] See forthcoming ICRU Report 37 or Berger and Seltzer (1982) for discussion of values for mean excitation energy.
[b] At 20°C and 1.013×10^5 Pa.

TABLE 2.2a—*Mass collision stopping power*[a,b] $(S/\rho)_{col}$, *in* MeV cm^2 g^{-1}.
[The density effect correction is applied according to Sternheimer (1952)—Carlson (1975)]

		Elements										Elements								
E/MeV	Exp[c]	$_1$H	$_2$He	$_4$Be	$_6$C[d]	$_6$C[e]	$_7$N	$_8$O	$_{13}$Al	$_{14}$Si	Exp[c]	Exp[c]	$_{22}$Ti	$_{26}$Fe	$_{29}$Cu	$_{42}$Mo	$_{50}$Sn	$_{74}$W	$_{82}$Pb	$_{92}$U	Exp[c]
0.010	+1	5.125	2.267	1.862	2.014	2.014	1.995	1.937	1.649	1.689	+1	+1	1.446	1.388	1.318	1.167	1.075	8.974	8.428	7.984	0
0.015		3.682	1.642	1.356	1.471	1.471	1.458	1.419	1.220	1.25[illegible]			1.078	1.040	9.904	8.843	8.186	6.945	6.561	6.24[illegible]	
0.02		2.9[illegible]7	1.307	1.083	1.177	1.177	1.168	1.138	9.844	1.010		0	8.737	8.456	8.066	7.238	6.719	5.753	5.453	5.198	
0.03		2.1[illegible]0	9.521	7.923	8.626	8.624	8.564	8.359	7.287	7.480	0		6.503	6.316	6.040	5.452	5.078	4.394	4.182	3.995	
0.04		1.687	7.642	6.375	6.950	6.948	6.904	6.746	5.909	6.067			5.290	5.149	4.931	4.467	4.169	3.631	3.463	3.313	
0.05		1.424	6.471	5.407	5.901	5.899	5.865	5.735	5.039	5.175			4.522	4.408	4.226	3.838	3.587	3.137	2.997	2.870	
0.06		1.245	5.669	4.743	5.179	5.177	5.150	5.039	4.439	4.559			3.990	3.893	3.736	3.400	3.181	2.791	2.670	2.557	
0.08		1.0[illegible]5	4.638	3.887	4.249	4.247	4.229	4.142	3.661	3.761			3.298	3.223	3.098	2.826	2.649	2.335	2.237	2.144	
0.10	0	8.737	4.003	3.358	3.674	3.671	3.660	3.586	3.177	3.265			2.867	2.804	2.698	2.467	2.315	2.047	1.964	1.883	
0.15		6.8[illegible]9	3.137	2.634	2.886	2.883	2.881	2.826	2.513	2.583			2.274	2.226	2.146	1.970	1.852	1.646	1.583	1.518	
0.20		5.851	2.700	2.266	2.485	2.482	2.486	2.441	2.174	2.236			1.971	1.930	1.861	1.715	1.615	1.439	1.387	1.330	
0.30		4.898	2.269	1.901	2.087	2.083	2.097	2.061	1.839	1.892			1.670	1.636	1.579	1.463	1.380	1.234	1.193	1.144	
0.40		4.445	2.064	1.726	1.896	1.891	1.914	1.882	1.680	1.729			1.528	1.497	1.444	1.344	1.269	1.138	1.102	1.057	
0.50		4.193	1.952	1.627	1.788	1.782	1.813	1.784	1.592	1.638			1.449	1.420	1.370	1.279	1.209	1.085	1.053	1.011	
0.60		4.042	1.884	1.566	1.722	1.716	1.753	1.725	1.540	1.585			1.402	1.374	1.326	1.240	1.174	1.055	1.026	9.842	−1
0.80		3.883	1.815	1.501	1.650	1.643	1.693	1.667	1.486	1.529			1.355	1.327	1.281	1.203	1.140	1.025	1.000	9.604	
1.00		3.816	1.787	1.471	1.617	1.609	1.670	1.646	1.465	1.507			1.335	1.308	1.263	1.190	1.128	1.016	9.939	9.544	
1.50		3.788	1.780	1.450	1.593	1.584	1.670	1.647	1.460	1.502			1.330	1.304	1.259	1.192	1.132	1.021	1.004	9.649	
2.00		3.823	1.801	1.455	1.597	1.587	1.693	1.671	1.475	1.518			1.343	1.317	1.273	1.209	1.149	1.037	1.024	9.844	
3.00		3.924	1.854	1.477	1.621	1.611	1.749	1.727	1.510	1.553			1.376	1.349	1.305	1.246	1.186	1.072	1.063	1.022	0
4.00		4.020	1.903	1.499	1.647	1.636	1.799	1.777	1.540	1.591			1.405	1.378	1.334	1.277	1.218	1.101	1.095	1.054	
5.00		4.103	1.946	1.517	1.669	1.658	1.842	1.820	1.564	1.618			1.430	1.403	1.358	1.302	1.244	1.126	1.120	1.079	
6.00		4.175	1.983	1.532	1.689	1.676	1.879	1.857	1.583	1.639			1.451	1.424	1.378	1.322	1.266	1.146	1.142	1.100	
8.00		4.295	2.043	1.555	1.720	1.707	1.940	1.918	1.613	1.672			1.485	1.457	1.411	1.355	1.301	1.178	1.175	1.132	
10.00		4.391	2.092	1.572	1.745	1.730	1.988	1.967	1.636	1.697			1.510	1.483	1.436	1.379	1.328	1.203	1.201	1.157	
15.00		4.559	2.182	1.602	1.787	1.770	2.079	2.057	1.676	1.740			1.555	1.529	1.482	1.421	1.374	1.247	1.246	1.199	
20.00		4.698	2.247	1.623	1.816	1.797	2.144	2.122	1.704	1.769			1.584	1.560	1.513	1.450	1.404	1.277	1.277	1.223	
30.00		4.881	2.339	1.652	1.852	1.832	2.235	2.214	1.743	1.809			1.622	1.600	1.555	1.488	1.444	1.316	1.318	1.266	
40.00		5.010	2.405	1.672	1.877	1.856	2.290	2.272	1.769	1.837			1.648	1.627	1.582	1.514	1.471	1.343	1.345	1.292	
50.00		5.091	2.456	1.687	1.895	1.874	2.327	2.310	1.789	1.853			1.667	1.647	1.603	1.533	1.491	1.362	1.365	1.311	
60.00		5.114	2.498	1.700	1.910	1.888	2.355	2.338	1.805	1.874			1.683	1.663	1.619	1.549	1.506	1.378	1.381	1.323	
80.00		5.213	2.564	1.720	1.932	1.911	2.395	2.379	1.829	1.900			1.707	1.687	1.643	1.572	1.530	1.401	1.406	1.349	
100.00		5.259	2.609	1.735	1.950	1.928	2.424	2.409	1.847	1.913			1.724	1.705	1.661	1.589	1.548	1.419	1.423	1.365	

		Tissues[f]				Liquids[f]				Gases[f]			
E/MeV	Exp[c]	Adipose Tissue	Bone (cortical)	Muscle (skeletal)	Muscle (striated)	Water (H_2O)	Ferrous Sulphate Solution	Muscle Equiv. without Sucrose	Exp[c]	Exp[c]	Air	CO_2	Tissue Equiv with Methane
0.010	+1	2.347	1.971	2.231	2.237	2.256	2.241	2.241	+1	+1	1.975	1.981	2.325
0.015		1.709	1.447	1.628	1.633	1.647	1.636	1.635			1.445	1.449	1.692
0.02		1.365	1.161	1.303	1.306	1.317	1.309	1.308			1.157	1.160	1.352
0.03	0	9.384	8.546	9.547	9.571	9.653	9.594	9.584	0	0	8.492	8.515	9.882
0.04		8.034	6.903	7.892	7.711	7.777	7.730	7.721			6.848	6.866	7.950
0.05		6.316	5.872	6.531	6.547	6.603	6.564	6.555			5.819	5.834	6.743
0.06		5.379	5.163	5.733	5.747	5.797	5.763	5.754			5.111	5.124	5.915
0.08		4.303	4.246	4.706	4.717	4.757	4.730	4.722			4.198	4.208	4.849
0.10		4.238	3.678	4.071	4.080	4.115	4.092	4.085			3.633	3.642	4.191
0.15		3.330	2.901	3.203	3.210	3.238	3.220	3.213			2.861	2.868	3.293
0.20		2.871	2.507	2.763	2.769	2.793	2.778	2.772			2.470	2.476	2.838
[illegible]		2.418	2.119	2.329	2.335	2.355	2.342	2.337			2.084	2.089	2.390
[illegible]		2.204	1.931	2.125	2.129	2.148	2.136	2.131			1.902	1.906	2.178
[illegible]		2.081	1.825	2.012	2.016	2.034	2.023	2.018			1.802	1.806	2.061
[illegible]		2.005	1.760	1.941	1.945	1.963	1.953	1.946			1.743	1.747	1.992
[illegible]		1.921	1.690	1.863	1.866	1.886	1.876	1.867			1.683	1.687	1.921
1.[illegible]		1.880	1.658	1.827	1.830	1.849	1.839	1.830			1.661	1.665	1.894
1.50		1.849	1.637	1.799	1.802	1.823	1.812	1.802			1.661	1.664	1.890

2.00		1.850	1.643	1.801	1.804	1.824	1.815	1.804		1.684	1.688	1.915						
3.00		1.872	1.670	1.824	1.826	1.846	1.837	1.826		1.740	1.744	1.975						
4.00		1.897	1.697	1.848	1.851	1.870	1.861	1.850		1.790	1.794	2.030						
5.00		1.920	1.720	1.870	1.873	1.892	1.883	1.872		1.833	1.837	2.077						
6.00		1.939	1.740	1.889	1.892	1.911	1.903	1.891		1.870	1.874	2.117						
8.00		1.972	1.773	1.921	1.924	1.943	1.934	1.923		1.931	1.935	2.184						
10.00		1.997	1.799	1.946	1.949	1.968	1.959	1.948		1.979	1.983	2.237						
15.00		2.042	1.844	1.992	1.995	2.014	2.005	1.993		2.069	2.074	2.337						
20.00		2.073	1.874	2.023	2.026	2.046	2.037	2.025		2.134	2.139	2.408						
30.00		2.113	1.915	2.066	2.068	2.089	2.080	2.067		2.226	2.222	2.501						
40.00		2.141	1.942	2.094	2.097	2.118	2.109	2.095		2.282	2.271	2.554						
50.00		2.161	1.962	2.115	2.118	2.139	2.130	2.116		2.319	2.305	2.590						
60.00		2.178	1.978	2.132	2.134	2.156	2.147	2.133		2.347	2.331	2.618						
80.00		2.203	2.003	2.158	2.160	2.182	2.173	2.158		2.387	2.369	2.658						
100.00		2.223	2.022	2.177	2.180	2.202	2.193	2.178		2.417	2.398	2.688						

		Solids[f]							Solids[f]									
E/MeV	Exp[c]	A 150	C 552	Glass (Pyrex)	M3	MS 20	Exp[c]	Exp[c]	Polyamide (Nylon 6) ($C_6H_{11}ON$)	Polyethylene (C_2H_4)	Mylar ($C_{10}H_8O_4$)	PMMA ($C_5H_8O_2$)	Polystyrene (C_8H_8)	Teflon (C_2F_4)	Polyvinyl chloride (C_2H_3Cl)	Lithium Fluorride (LiF)	Film Emulsion	Exp[c]
0.010	+1	2.294	1.972	1.787	2.301	2.189	+1	+1	2.298	2.441	2.095	2.198	2.223	1.843	1.930	1.796	1.302	+1
0.015		1.671	1.442	1.317	1.577	1.598			1.673	1.775	1.530	1.604	1.621	1.351	1.416	1.315	9.798	0
0.02		1.335	1.156	1.060	1.340	1.279			1.337	1.417	1.225	1.283	1.296	1.084	1.137	1.055	7.984	
0.03	0	9.769	8.482	7.822	9.310	9.368	0	0	9.778	1.035	8.978	9.400	9.485	7.965	8.370	7.743	5.983	
0.04		7.863	6.841	6.331	7.398	7.547			7.869	8.325	7.236	7.573	7.637	6.430	6.762	6.252	4.887	
0.05		6.671	5.813	5.393	6.703	6.408			6.676	7.060	6.145	6.429	6.481	5.468	5.753	5.315	4.190	
0.06		5.853	5.106	4.746	5.382	5.626			5.857	6.191	5.396	5.644	5.688	4.806	5.058	4.670	3.706	
0.08		4.800	4.194	3.909	4.325	4.617			4.803	5.074	4.430	4.631	4.666	3.951	4.160	3.838	3.075	
0.10		4.150	3.630	3.390	4.172	3.994			4.152	4.384	3.832	4.006	4.034	3.421	3.604	3.323	2.680	
0.15		3.262	2.859	2.679	3.280	3.142			3.263	3.443	3.013	3.152	3.172	2.697	2.843	2.619	2.136	
0.20		2.812	2.468	2.318	2.828	2.711			2.813	2.967	2.603	2.719	2.735	2.330	2.457	2.261	1.858	
0.30		2.369	2.083	1.962	2.383	2.285			2.369	2.497	2.195	2.292	2.305	1.968	2.077	1.907	1.585	
0.40		2.156	1.899	1.793	2.171	2.085			2.156	2.272	2.001	2.090	2.101	1.797	2.896	1.737	1.453	
0.50		2.033	1.794	1.698	2.049	1.972			2.032	2.142	1.889	1.978	1.984	1.699	1.793	1.642	1.381	
0.60		1.957	1.729	1.640	1.974	1.901			1.956	2.061	1.821	1.903	1.911	1.639	1.730	1.583	1.338	
0.80		1.874	1.659	1.579	1.892	1.825			1.872	1.972	1.745	1.828	1.832	1.573	1.663	1.521	1.295	
1.00		1.834	1.626	1.552	1.853	1.789			1.832	1.930	1.710	1.788	1.794	1.543	1.633	1.491	1.278	
1.50		1.803	1.602	1.538	1.823	1.764			1.801	1.895	1.684	1.760	1.766	1.522	1.615	1.471	1.278	
2.00		1.804	1.605	1.547	1.826	1.767			1.802	1.895	1.685	1.762	1.768	1.525	1.623	1.474	1.294	
3.00		1.827	1.627	1.576	1.849	1.792			1.823	1.917	1.709	1.784	1.791	1.546	1.653	1.493	1.331	
4.00		1.852	1.650	1.604	1.875	1.818			1.848	1.942	1.734	1.809	1.816	1.569	1.683	1.513	1.363	
5.00		1.874	1.671	1.627	1.898	1.841			1.870	1.965	1.755	1.832	1.839	1.589	1.708	1.531	1.390	
6.00		1.894	1.690	1.647	1.917	1.860			1.889	1.984	1.775	1.851	1.859	1.606	1.730	1.547	1.412	
8.00		1.926	1.719	1.678	1.949	1.892			1.921	2.017	1.808	1.883	1.891	1.635	1.765	1.572	1.448	
10.00		1.951	1.742	1.703	1.974	1.917			1.946	2.042	1.831	1.908	1.916	1.657	1.791	1.592	1.475	
15.00		1.995	1.783	1.746	2.019	1.962			1.990	2.087	1.874	1.952	1.960	1.697	1.837	1.629	1.523	
20.00		2.024	1.811	1.775	2.049	1.992			2.019	2.117	1.903	1.982	1.989	1.724	1.866	1.654	1.555	
30.00		2.063	1.848	1.814	2.089	2.033			2.058	2.157	1.941	2.022	2.027	1.761	1.906	1.688	1.598	
40.00		2.089	1.873	1.840	2.116	2.060			2.085	2.184	1.967	2.049	2.053	1.785	1.933	1.711	1.626	
50.00		2.109	1.892	1.860	2.137	2.080			2.104	2.204	1.986	2.069	2.073	1.803	1.953	1.728	1.648	
60.00		2.125	1.907	1.876	2.153	2.096			2.121	2.221	2.001	2.085	2.089	1.818	1.969	1.742	1.665	
80.00		2.151	1.930	1.900	2.179	2.121			2.145	2.247	2.025	2.109	2.113	1.840	1.995	1.764	1.690	
100.00		2.170	1.948	1.918	2.199	2.140			2.165	2.267	2.043	2.128	2.132	1.857	2.014	1.780	1.709	

[a] To convert the mass collision stopping power values in MeV cm^2 g^{-1} to coherent SI units (J m^2 kg^{-1}), multiply the values in the table by $1.602 \cdot 10^{14}$.

[b] See forthcoming ICRU Report 37 (1984) or Berger and Seltzer, 1982, for discussion of calculations.

[c] The lines enclose figures with the same value of the exponent. Thus, for hydrogen at 0.01 MeV, the exponent is +1 and the mass collision stopping power is $5.125 \cdot 10^{+1}$ MeV cm^2 g^{-1}.

[d] The density $\rho = 1.70$ g cm^{-3} was used in order to calculate the density effect correction.

[e] The density $\rho = 2.265$ g cm^{-3} was used in order to calculate the density effect correction.

[f] The composition of the different compounds and mixtures is given in Table 2.1b.

TABLE 2.2b—*Mass collision stopping power*[a], $(S/\rho)_{col}$, *in* MeV cm^2 g^{-1}.

[The density effect correction is applied according to the method by Sternheimer and Peierls (1971). The density of graphite ($_6$C) used was the crystallite value, ρ = 2.25 g cm^{-3}, used by Berger (1980) (for the relative difference in $(S/\rho)_{col}$-values between bulk and crystallite density, consult Table 2.2a). The computations were made by Berger (1980)]

E/MeV	Exp[b]	$_6$C	Water (H_2O)	Ferrous Sulphate Solution	Exp[b]
0.010	+1	2.015	2.256	2.241	+1
0.015		1.471	1.647	1.636	
0.020		1.178	1.317	1.309	
0.030	0	8.631	9.653	9.593	0
0.04		6.956	7.777	7.730	
0.05		5.907	6.603	6.564	
0.06		5.186	5.797	5.763	
0.08		4.257	4.757	4.730	
0.10		3.683	4.115	4.092	
0.15		2.899	3.238	3.220	
0.20		2.501	2.793	2.778	
0.30		2.109	2.355	2.342	
0.40		1.924	2.148	2.136	
0.50		1.818	2.033	2.022	
0.60		1.750	1.962	1.952	
0.80		1.675	1.886	1.877	
1.0		1.641	1.852	1.843	
1.5		1.615	1.831	1.823	
2.0		1.618	1.839	1.830	
3.0		1.639	1.868	1.860	
4.0		1.661	1.896	1.888	
5.0		1.680	1.920	1.911	
6.0		1.697	1.939	1.931	
8.0		1.723	1.970	1.962	
10.0		1.743	1.994	1.986	
15.0		1.778	2.035	2.027	
20.0		1.803	2.063	2.054	
30.0		1.835	2.099	2.091	
40.0		1.858	2.125	2.116	
50.0		1.875	2.144	2.135	
60.0		1.889	2.160	2.151	
80.0		1.912	2.184	2.176	
100.0		2.929	2.204	2.195	

[a] To convert the mass collision stopping power values in MeV cm^2 g^{-1} to coherent SI units (J m^2 kg^{-1}), multiply the values in the Table by $1.602 \cdot 10^{-14}$.

[b] The line under the third line of tabular values separates values to be multipled by 10 (exponent 1) from those to be multiplied by 1 (exponent 0).

2.2.3 Restricted Mass Collision Stopping Power

In the description of the electron-electron collision, the outgoing electron with the larger kinetic energy is defined by convention as the primary electron and the other electron is defined as the secondary electron. Therefore, the energy of the secondary electron is always smaller than half the energy of the incident electron. In many situations (see Section 4) only those energy losses which lead to secondary electrons with energy below a cut-off energy, Δ, are of interest. The restricted mass collision stopping power, L_Δ/ρ, includes only such energy losses and is, therefore, smaller than the unrestricted mass collision stopping power (Section 2.2.2). The restricted mass collision stopping power can be obtained from Eq. 2.2 if $F(\tau)$ is changed to $F(\tau, \Delta)$ (Berger and Seltzer, 1964):

$$F(\tau, \Delta) = -1 - \beta^2 + \ln\{4\Delta(\tau - \Delta)\tau^{-2}\} + \tau/(\tau - \Delta) + \{\Delta^2/2 + (2\tau + 1)\ln(1 - \Delta/\tau)\} \cdot (\tau + 1)^{-2} \quad (2.3)$$

where Δ, like τ in Eq. 2.2, is expressed as a fraction of the rest energy of the electron (Rohrlich and Carlsson, 1954; Berger and Seltzer, 1964).

In Table 2.3, the ratio of the restricted to the unrestricted collision stopping power for water, air, carbon, aluminum, copper, and lead is given for cut-off energies, Δ, of 10^3, 10^4, and 10^5 eV, which correspond to electron ranges of about $5 \cdot 10^{-6}$, $2.5 \cdot 10^{-4}$, and $1.5 \cdot 10^{-2}$ g cm^{-2}, respectively, in low atomic number materials (Berger, 1980). The ratio of restricted to unrestricted stopping power varies slowly with atomic number for non-gaseous elements, a fact which may be used for interpolation to other atomic numbers. Furthermore, for a given electron energy, the ratio is close to a linear function of the logarithm of the cut-off energy (Berger and Seltzer, 1964). This linear relationship can be used for extrapolation to other cut-off energies.

TABLE 2.3—*Ratio of restricted to unrestricted collision stopping power (Berger, 1980)*

Δ/eV / E/MeV	Water			Air			Graphite		
	10^3	10^4	10^5	10^3	10^4	10^5	10^3	10^4	10^5
0.010	0.8685	1.0000	1.0000	0.8648	1.0000	1.0000	0.8675	1.0000	1.0000
0.015	0.8439	1.0000	1.0000	0.8398	1.0000	1.0000	0.8428	1.0000	1.0000
0.02	0.8278	1.0000	1.0000	0.8236	1.0000	1.0000	0.8266	1.0000	1.0000
0.03	0.8070	0.9729	1.0000	0.8025	0.9723	1.0000	0.8057	0.9727	1.0000
0.04	0.7933	0.9568	1.0000	0.7888	0.9559	1.0000	0.7921	0.9565	1.0000
0.05	0.7833	0.9446	1.0000	0.7787	0.9434	1.0000	0.7820	0.9443	1.0000
0.06	0.7755	0.9347	1.0000	0.7708	0.9334	1.0000	0.7742	0.9344	1.0000
0.08	0.7637	0.9193	1.0000	0.7589	0.9177	1.0000	0.7623	0.9189	1.0000
0.10	0.7549	0.9075	1.0000	0.7501	0.9058	1.0000	0.7535	0.9070	1.0000
0.15	0.7396	0.8866	1.0000	0.7349	0.8845	1.0000	0.7383	0.8860	1.0000
0.20	0.7293	0.8721	1.0000	0.7246	0.8698	1.0000	0.7280	0.8714	1.0000
0.30	0.7156	0.8522	0.9773	0.7108	0.8497	0.9769	0.7142	0.8515	0.9771
0.40	0.7064	0.8386	0.9627	0.7016	0.8360	0.9620	0.7050	0.8379	0.9625
0.50	0.6995	0.8284	0.9512	0.6949	0.8258	0.9504	0.6976	0.8273	0.9509
0.60	0.6938	0.8201	0.9417	0.6898	0.8178	0.9409	0.6910	0.8185	0.9412
0.80	0.6851	0.8074	0.9267	0.6825	0.8058	0.9261	0.6810	0.8049	0.9257
1.0	0.6785	0.7979	0.9152	0.6774	0.7972	0.9149	0.6734	0.7947	0.9138
1.5	0.6672	0.7816	0.8950	0.6698	0.7834	0.8958	0.6605	0.7772	0.8929
2.0	0.6596	0.7708	0.8814	0.6657	0.7749	0.8836	0.6518	0.7656	0.8787
3.0	0.6493	0.7566	0.8635	0.6613	0.7649	0.8682	0.6403	0.7503	0.8601
4.0	0.6422	0.7470	0.8517	0.6591	0.7589	0.8587	0.6325	0.7402	0.8476
5.0	0.6367	0.7398	0.8428	0.6578	0.7549	0.8519	0.6266	0.7326	0.8384
6.0	0.6323	0.7341	0.8359	0.6570	0.7519	0.8469	0.6218	0.7265	0.8312
8.0	0.6254	0.7253	0.8252	0.6560	0.7478	0.8395	0.6144	0.7173	0.8201
10.0	0.6199	0.7186	0.8172	0.6555	0.7449	0.8343	0.6087	0.7103	0.8118
15.0	0.6100	0.7066	0.8031	0.6550	0.7404	0.8258	0.5984	0.6978	0.7972
20.0	0.6030	0.6982	0.7934	0.6549	0.7376	0.8204	0.5912	0.6892	0.7873
30.0	0.5931	0.6866	0.7801	0.6549	0.7342	0.8135	0.5811	0.6774	0.7736
40.0	0.5862	0.6786	0.7709	0.6534	0.7307	0.8081	0.5741	0.6692	0.7643
50.0	0.5809	0.6724	0.7640	0.6514	0.7276	0.8037	0.5688	0.6630	0.7572
60.0	0.5767	0.6675	0.7584	0.6497	0.7249	0.8001	0.5645	0.6580	0.7515
80.0	0.5701	0.6599	0.7498	0.6467	0.7206	0.7944	0.5579	0.6503	0.7427
100.0	0.5651	0.6542	0.7433	0.6443	0.7171	0.7900	0.5529	0.6445	0.7361

Δ/eV / E/MeV	Aluminum			Copper			Lead		
	10^3	10^4	10^5	10^3	10^4	10^5	10^3	10^4	10^5
0.010	0.8441	1.0000	1.0000	0.8150	1.0000	1.0000	0.7541	1.0000	1.0000
0.015	0.8174	1.0000	1.0000	0.7867	1.0000	1.0000	0.7256	1.0000	1.0000
0.02	0.8002	1.0000	1.0000	0.7689	1.0000	1.0000	0.7082	1.0000	1.0000
0.03	0.7784	0.9689	1.0000	0.7465	0.9644	1.0000	0.6869	0.9560	1.0000
0.04	0.7642	0.9507	1.0000	0.7322	0.9440	1.0000	0.6736	0.9318	1.0000
0.05	0.7539	0.9371	1.0000	0.7219	0.9289	1.0000	0.6641	0.9141	1.0000
0.06	0.7459	0.9261	1.0000	0.7139	0.9168	1.0000	0.6568	0.9002	1.0000
0.08	0.7339	0.9092	1.0000	0.7020	0.8983	1.0000	0.6460	0.8792	1.0000
0.10	0.7250	0.8963	1.0000	0.6933	0.8843	1.0000	0.6381	0.8635	1.0000
0.15	0.7097	0.8735	1.0000	0.6783	0.8599	1.0000	0.6246	0.8365	1.0000
0.20	0.6994	0.8579	1.0000	0.6683	0.8432	1.0000	0.6158	0.8184	1.0000
0.30	0.6858	0.8368	0.9749	0.6553	0.8209	0.9724	0.6043	0.7944	0.9684
0.40	0.6769	0.8224	0.9589	0.6468	0.8059	0.9551	0.5971	0.7786	0.9488
0.50	0.6697	0.8114	0.9463	0.6401	0.7945	0.9415	0.5922	0.7671	0.9338
0.60	0.6635	0.8023	0.9359	0.6343	0.7851	0.9304	0.5886	0.7583	0.9217
0.80	0.6542	0.7885	0.9195	0.6257	0.7710	0.9128	0.5840	0.7456	0.9031
1.0	0.6474	0.7783	0.9070	0.6194	0.7607	0.8996	0.5812	0.7367	0.8895
1.5	0.6361	0.7612	0.8852	0.6091	0.7435	0.8766	0.5776	0.7228	0.8667
2.0	0.6288	0.7501	0.8707	0.6025	0.7324	0.8616	0.5754	0.7141	0.8521
3.0	0.6194	0.7359	0.8519	0.5941	0.7183	0.8421	0.5723	0.7032	0.8336
4.0	0.6133	0.7266	0.8397	0.5886	0.7091	0.8294	0.5701	0.6961	0.8218
5.0	0.6087	0.7198	0.8307	0.5844	0.7024	0.8202	0.5683	0.6908	0.8132
6.0	0.6051	0.7144	0.8237	0.5811	0.6971	0.8130	0.5667	0.6866	0.8065
8.0	0.5994	0.7063	0.8131	0.5759	0.6891	0.8021	0.5638	0.6802	0.7965
10.0	0.5951	0.7002	0.8052	0.5719	0.6830	0.7941	0.5614	0.6753	0.7891
15.0	0.5873	0.6894	0.7916	0.5645	0.6723	0.7801	0.5565	0.6663	0.7761
20.0	0.5817	0.6820	0.7823	0.5592	0.6649	0.7706	0.5526	0.6599	0.7672
30.0	0.5737	0.6716	0.7696	0.5515	0.6546	0.7576	0.5465	0.6507	0.7549
40.0	0.5680	0.6644	0.7608	0.5459	0.6473	0.7487	0.5418	0.6441	0.7464
50.0	0.5635	0.6588	0.7542	0.5416	0.6417	0.7418	0.5380	0.6389	0.7398
60.0	0.5598	0.6543	0.7488	0.5379	0.6371	0.7363	0.5347	0.6346	0.7345
80.0	0.5539	0.6472	0.7404	0.4322	0.6299	0.7277	0.5294	0.6278	0.7261
100.0	0.5494	0.6417	0.7339	0.5276	0.6244	0.7211	0.5252	0.6224	0.7197

2.2.4 Mass Radiative Stopping Power

The radiative electron interactions frequently result in large energy losses and electrons having undergone such energy losses contribute mainly to the low energy tail of the primary electron energy distribution (see Fig. 2.3). The mean energy loss of electrons due to radiative collisions cannot be given in a simple general form covering all energies and materials (Koch and Motz, 1959). To illustrate the general form of the mass radiative stopping power only the expression for high energies (complete screening: $\tau \gg 1/\alpha Z^{1/3}$) is given here:

$$(S/\rho)_{\text{rad}} = \frac{4r_e^2\alpha}{\beta^2} N_A \frac{Z(Z+1)}{M_A} (\tau+1)m_e c^2 \cdot \ln(183Z^{-1/3} + 1/18) \quad (2.4)$$

where α is the fine structure constant ($\alpha \approx 1/137$). It is evident that the mass radiative stopping power increases almost linearly with kinetic energy in the MeV region, whereas the mass collision stopping power has a weak logarithmic energy dependence in that region. This is of importance for interpolation between different energies in the stopping power tables, and also for determination of mean total energy losses. When more accurate values for a wider range of energies and materials are needed, the tabulations by Berger and Seltzer (1964, 1966, 1982) and Pages *et al.* (1972) and in the forthcoming ICRU Report 37 (1984) should be used.

In Table 2.4, values of the mass radiative stopping power for the elements and mixtures of Tables 2.1a and b are given. For electron energies (E) above 20 MeV, the mass radiative stopping power may be approximated with an accuracy of about 30% by

$$(S/\rho)_{\text{rad}} \approx \frac{E}{X_0} \quad (2.5)$$

where X_0 is the radiation length (Rossi, 1952) in the material in question. The accuracy improves as the energy is increased and it is about 15% at 50 MeV. The radiation length, as calculated by Tsai (1974), is given in the last line of Table 2.4. In addition, the close proportionality between $(S/\rho)_{rad}$ and E is very useful when interpolation in Table 2.4 is necessary.

TABLE 2.4—*Mass radiative stopping power*[a], $(S/\rho)_{rad}$, *in* MeV cm^2 g^{-1} *(Seltzer and Berger, 1982b) and radiation length,* X_0, *in g/cm*^{2} *(Tsai, 1974)*

		Elements									Elements								
E/MeV	Exp[b]	$_1$H	$_2$He	$_4$Be	$_6$C	$_7$N	$_8$O	$_{13}$Al	$_{14}$Si	Exp[b]	Exp[b]	$_{22}$Ti	$_{26}$Fe	$_{29}$Cu	$_{42}$Mo	$_{50}$Sn	$_{74}$W	$_{82}$Pb	$_{92}$U	Exp[b]
0.010	−4	9.702	9.885	1.815	3.150	3.711	4.267	6.559	7.255	−3	−3	9.835	1.138	1.213	1.524	1.645	1.977	2.045	2.101	−2
0.015		9.881	9.995	1.823	3.168	3.740	4.316	6.798	7.555		−2	1.056	1.235	1.307	1.709	1.869	2.320	2.421	2.516	
0.02	−3	1.004	1.010	1.831	3.176	3.753	4.336	6.926	7.720			1.099	1.296	1.399	1.832	2.021	2.563	2.693	2.822	
0.03		1.034	1.029	1.849	3.194	3.770	4.356	7.059	7.892			1.150	1.369	1.488	1.992	2.224	2.908	3.086	3.273	
0.04		1.061	1.048	1.870	3.215	3.790	4.376	7.133	7.988			1.180	1.414	1.543	2.099	2.364	3.160	3.376	3.612	
0.05		1.088	1.066	1.891	3.241	3.816	4.402	7.191	8.061			1.202	1.446	1.583	2.181	2.473	3.364	3.613	3.888	
0.06		1.113	1.084	1.914	3.270	3.846	4.434	7.243	8.123			1.218	1.471	1.615	2.247	2.564	3.539	3.817	4.127	
0.08		1.164	1.119	1.961	3.337	3.920	4.512	7.350	8.248			1.246	1.512	1.665	2.357	2.713	3.834	4.162	4.531	
0.10		1.216	1.157	2.014	3.414	4.005	4.607	7.476	8.389			1.272	1.548	1.710	2.449	2.836	4.084	4.454	4.875	
0.15		1.357	1.260	2.160	3.640	4.259	4.889	7.865	8.821			1.341	1.639	1.816	2.646	3.100	4.595	5.054	5.585	
0.20		1.511	1.375	2.326	3.896	4.550	5.215	8.344	9.349			1.419	1.736	1.926	2.826	3.328	5.021	5.555	6.184	
0.30		1.852	1.632	2.704	4.489	5.227	5.975	9.487	1.062	−2		1.600	1.956	2.172	3.192	3.776	5.797	6.460	7.263	
0.40		2.232	1.924	3.137	5.173	6.009	6.856	1.082	1.209			1.811	2.209	2.450	3.593	4.252	6.565	7.340	8.294	
0.50		2.648	2.245	3.618	5.935	6.882	7.838	1.230	1.374			2.044	2.489	2.757	4.032	4.766	7.353	8.228	9.316	
0.50		3.096	2.592	4.139	6.759	7.827	8.904	1.390	1.551			2.297	2.791	3.087	4.502	5.311	8.162	9.132	1.034	−1
0.80		4.076	3.352	5.277	8.559	9.889	1.122	1.739	1.938			2.848	3.448	3.803	5.510	6.472	9.841	1.098	1.241	
1.0		5.152	4.180	6.520	1.053	1.214	1.376	2.119	2.360			3.446	4.160	4.580	6.592	7.712	1.159	1.290	1.452	
1.5		8.190	6.515	1.000	1.602	1.842	2.084	3.177	3.533			5.107	6.137	6.733	9.550	1.108	1.624	1.792	1.995	
2.0	−2	1.162	9.132	1.388	2.213	2.540	2.869	4.350	4.833			6.940	8.315	9.103	1.276	1.472	2.117	2.319	2.559	
3.0		1.931	1.495	2.247	3.561	4.078	4.598	6.924	7.682		−1	1.094	1.306	1.425	1.967	2.251	3.158	3.427	3.732	
4.0		2.782	2.134	3.182	5.026	5.747	6.471	9.702	1.076	−1		1.523	1.814	1.976	2.699	3.075	4.248	4.582	4.955	
5.0		3.693	2.813	4.174	6.576	7.512	8.449	1.263	1.399			1.974	2.346	2.552	3.461	3.930	5.372	5.773	6.214	
6.0		4.651	3.523	5.211	8.193	9.352	1.051	1.567	1.735			2.440	2.896	3.146	4.246	4.808	6.523	6.991	7.504	
8.0		6.675	5.018	7.386	1.158	1.320	1.482	2.200	2.435			3.408	4.036	4.378	5.867	6.620	8.890	9.495	1.015	0
10.0		8.809	6.584	9.664	1.513	1.723	1.932	2.858	3.161			4.411	5.216	5.650	7.538	8.486	1.132	1.206	1.288	
15.0	−1	1.448	1.071	1.566	2.444	2.780	3.112	4.574	5.057			7.019	8.279	8.949	1.187	1.331	1.759	1.870	1.991	
20.0		2.046	1.505	2.194	3.417	3.884	4.343	6.357	7.023			9.721	1.145	1.236	1.634	1.829	2.406	2.554	2.717	
30.0		3.305	2.410	3.499	5.435	6.169	6.890	1.003	1.108	0	0	1.528	1.795	1.936	2.555	2.854	3.735	3.961	4.208	
40.0		4.615	3.346	4.841	7.508	8.515	9.502	1.379	1.523			2.096	2.460	2.650	3.497	3.902	5.096	5.402	5.733	
50.0		5.959	4.303	6.209	9.617	1.090	1.216	1.761	1.944			2.673	3.135	3.375	4.453	4.966	6.477	6.865	7.282	
60.0		7.326	5.272	7.595	1.175	1.332	1.484	2.147	2.369			3.255	3.816	4.107	5.419	6.041	7.873	8.345	8.847	
80.0	0	1.011	7.238	1.041	1.608	1.821	2.028	2.927	3.230			4.433	5.193	5.586	7.370	8.213	1.070	1.134	1.201	+1
100.0		1.295	9.229	1.325	2.046	2.315	2.577	3.714	4.099			5.623	6.584	7.079	9.339	1.040	1.355	1.436	1.521	
X_0	+1	6.305	9.432	6.519	4.270	3.799	3.424	2.401	2.182	+1	+1	1.617	1.384	1.286	9.803	8.817	6.763	6.369	5.999	0

		Tissues[c]				Liquids[c]				Gases[c]			Solids[c]					
E/MeV	Exp[b]	Adipose Tissue	Bone (cortical)	Muscle (skeletal)	Muscle (striated)	Water (H_2O)	Ferrous Sulphate Solution	Muscle Equiv. without Sucrose	Exp[b]	Exp[b]	Air	CO_2	Tissue Equiv with Methane	A 150	C 552	Glass (Pyrex)	M 3	MS 20	Exp[b]
0.010	−3	3.168	5.461	3.835	3.816	3.898	3.961	3.777	−3	−3	3.897	3.962	3.402	3.156	3.767	5.400	3.441	3.599	−3
0.015		3.194	5.664	3.880	3.862	3.944	4.011	3.818			3.937	4.003	3.433	3.188	3.812	5.548	3.487	3.646	
0.020		3.207	5.778	3.901	3.882	3.963	4.033	3.836			3.954	4.019	3.447	3.205	3.834	5.626	3.511	3.670	
0.030		3.227	5.907	3.924	3.905	3.984	4.057	3.857			3.976	4.039	3.467	3.232	3.860	5.707	3.543	3.701	
0.04		3.249	5.989	3.946	3.928	4.005	4.080	3.873			3.998	4.059	3.488	3.258	3.883	5.759	3.571	3.727	
0.05		3.275	6.054	3.973	3.955	4.031	4.107	3.904			4.025	4.085	3.514	3.287	3.909	5.803	3.600	3.756	
0.06		3.305	6.113	4.004	3.986	4.062	4.139	3.935			4.057	4.116	3.544	3.319	3.939	5.847	3.632	3.788	
0.08		3.373	6.230	4.079	4.061	4.138	4.215	4.009			4.133	4.192	3.614	3.388	4.010	5.943	3.703	3.860	
0.10		3.452	6.356	4.168	4.150	4.228	4.306	4.097			4.222	4.282	3.696	3.467	4.093	6.055	3.785	3.944	
0.15		3.681	6.719	4.431	4.412	4.494	4.576	4.357			4.485	4.548	3.937	3.697	4.347	6.393	4.027	4.193	
0.20		3.943	7.140	4.734	4.714	4.801	4.887	4.656			4.789	4.855	4.213	3.959	4.643	6.796	4.307	4.482	
0.30		4.547	8.129	5.438	5.415	5.514	5.610	5.350			5.495	5.570	4.851	4.563	5.336	7.749	4.956	5.152	
0.40		5.244	9.276	6.252	6.226	6.339	6.447	6.152			6.311	6.397	5.587	5.260	6.134	8.857	5.707	5.927	
0.50		6.020	1.055	7.158	7.129	7.257	7.379	7.047			7.223	7.319	6.407	6.036	7.020	1.009	6.541	6.789	
0.60		6.860	1.194	8.141	8.108	8.254	8.391	8.016			8.210	8.318	7.296	6.875	7.977	1.143	7.443	7.722	
0.80		8.692	1.495	1.028	1.024	1.043	1.059	1.013	−2	−2	1.036	1.050	9.233	8.706	1.006	1.434	9.412	9.756	
1.0	−2	1.070	1.824	1.262	1.257	1.280	1.300	1.244			1.271	1.288	1.135	1.071	1.234	1.751	1.156	1.193	−2

1.5		1.629	2.740	1.916	1.908	1.942	1.972	1.888			1.927	1.952	1.727	1.630	1.871	2.636	1.757	1.819	
2.0		2.522	3.755	2.642	2.632	2.678	2.719	2.605			2.656	2.690	2.385	2.252	2.581	3.617	2.426	2.509	
3.0		3.626	5.981	4.241	4.225	4.299	4.362	4.183			4.260	4.315	3.835	3.625	4.144	5.771	3.899	4.030	
4.0		5.120	8.386	5.977	5.954	6.058	6.146	5.896			5.999	6.077	5.411	5.116	5.840	8.102	5.499	5.681	
5.0		6.701	1.092	7.811	7.782	7.917	8.030	7.706			7.838	7.938	7.077	6.695	7.633	1.056	7.192	7.427	
6.0		8.350	1.355	9.722	9.686	9.854	9.993	9.593			9.754	9.877	8.815	8.341	9.501	1.311	8.956	9.246	
8.0	−1	1.181	1.904	1.372	1.367	1.391	1.410	1.354	−1	−1	1.376	1.394	1.246	1.179	1.341	1.844	1.265	1.305	−1
10.0		1.542	2.476	1.790	1.784	1.814	1.839	1.767			1.795	1.817	1.626	1.540	1.748	2.399	1.651	1.703	
15.0		2.492	3.971	2.887	2.877	2.926	2.966	2.850			2.895	2.930	2.626	2.488	2.817	3.850	2.664	2.747	
20.0		3.485	5.525	4.032	4.018	4.086	4.141	3.982			4.042	4.091	3.671	3.478	3.931	5.360	3.722	3.837	
30.0		5.544	8.735	6.403	6.381	6.489	6.574	6.324			6.417	6.493	5.835	5.532	6.235	8.477	5.913	6.093	
40.0		7.661	1.202	8.838	8.807	8.955	9.072	8.729			8.855	8.958	8.060	7.643	8.601	1.167	8.164	8.411	
50.0		9.815	1.537	1.131	1.127	1.146	1.161	1.118	0	0	1.133	1.146	1.032	9.792	1.101	1.491	1.045	1.077	0
60.0	0	1.200	1.875	1.382	1.377	1.400	1.418	1.365			1.384	1.400	1.261	1.197	1.344	1.819	1.277	1.315	
80.0		1.642	2.558	1.889	1.883	1.914	1.939	1.866			1.892	1.913	1.725	1.638	1.836	2.483	1.747	1.799	
100.0		2.089	3.249	2.402	2.394	2.434	2.465	2.373			2.405	2.432	2.195	2.084	2.335	3.153	2.222	2.287	
X_0	+1	4.176	2.657	3.635	3.671	3.608	3.568	3.697	+1	+1	3.661	3.620	3.983	4.193	3.763	2.821	3.931	3.830	+1

		Solids[c]									
E/MeV	Exp[b]	Polyamide (Nylon 6) ($C_3H_{11}ON$)	Polyethylene (C_3H_4)	Mylar ($C_{10}H_8O_4$)	PMMA ($C_5H_8O_2$)	Polystyrene (C_8H_8)	Teflon (C_2F_4)	Polyvinyl chloride (C_2H_3Cl)	Lithium Flouride (LiF)	Film Emulsion	Exp[b]
0.010	−3	3.164	2.837	3.431	3.332	2.982	4.211	5.953	3.678	1.310	−2
0.015		3.187	2.854	3.459	3.359	2.999	4.271	6.238	3.735	1.463	
0.020		3.199	2.864	3.471	3.372	3.008	4.300	6.369	3.762	1.565	
0.030		3.218	2.883	3.490	3.391	3.027	4.329	6.539	3.792	1.697	
0.04		3.239	2.905	3.511	3.413	3.048	4.353	6.641	3.815	1.786	
0.05		3.265	2.931	3.537	3.438	3.074	4.380	6.717	3.840	1.854	
0.06		3.295	2.960	3.567	3.468	3.103	4.410	6.783	3.867	1.910	
0.08		3.363	3.025	3.637	3.538	3.169	4.483	6.908	3.932	2.003	
0.10		3.441	3.099	3.719	3.619	3.244	4.571	7.040	4.011	2.081	
0.15		3.669	3.312	3.960	3.855	3.463	4.844	7.424	4.253	2.251	
0.20		3.930	3.553	4.235	4.126	3.711	5.167	7.877	4.540	2.405	
0.30		4.532	4.110	4.873	4.751	4.284	5.928	8.949	5.215	2.721	
0.40		5.226	4.750	5.610	5.474	4.945	6.805	1.020	5.992	3.066	
0.50		5.999	5.462	6.431	6.278	5.680	7.775	1.159	6.852	3.443	
0.60		6.836	6.233	7.320	7.149	6.475	8.823	1.310	7.779	3.846	
0.80		8.661	7.915	9.259	9.050	8.212	1.111	1.637	9.800	4.711	
1.0	−2	1.066	9.754	1.138	1.113	1.011	1.360	1.995	1.200	5.640	
1.5		1.623	1.490	1.730	1.693	1.541	2.057	2.990	1.818	8.177	
2.0		2.244	2.062	2.388	2.338	2.132	2.834	4.092	2.505	1.094	−1
3.0		3.612	3.327	3.838	3.761	3.435	4.544	6.507	4.021	1.687	
4.0		5.100	4.704	5.413	5.307	4.852	6.399	9.114	5.666	2.317	
5.0		6.674	6.162	7.079	6.943	6.353	8.357	1.186	7.402	2.973	
6.0		8.317	7.684	8.816	8.648	7.919	1.040	1.471	9.211	3.649	
8.0	−1	1.176	1.088	1.245	1.222	1.120	1.466	2.065	1.299	5.045	
10.0		1.536	1.422	1.626	1.596	1.464	1.910	2.683	1.693	6.485	
15.0		2.482	2.301	2.625	2.577	2.367	3.071	4.295	2.723	1.022	0
20.0		3.472	3.220	3.668	3.603	3.311	4.281	5.971	3.797	1.407	
30.0		5.523	5.129	5.830	5.728	5.270	6.781	9.428	6.014	2.202	
40.0		7.631	7.092	8.051	7.912	7.284	9.344	1.297	8.289	3.015	
50.0		9.777	9.092	1.031	1.013	9.334	1.195	1.657	1.060	3.840	
60.0	0	1.195	1.112	1.260	1.238	1.141	1.458	2.020	1.294	4.674	
80.0		1.635	1.522	1.723	1.694	1.562	1.991	2.756	1.767	6.358	
100.0		2.081	1.938	2.191	2.155	1.988	2.530	3.499	2.245	8.056	
X_0	+1	4.192	4.478	3.995	4.054	4.379	3.485	2.560	3.927	1.556	+1

[a] To convert the mass radiative stopping power values in MeV $cm^2 g^{-1}$ to coherent SI units (J $m^2 kg^{-1}$), multiply the values in the table by $1.602 \cdot 10^{-14}$.

[b] The lines enclose figures with the same value of the exponent; thus for hydrogen at 0.01 MeV, the exponent is −4 and the mass radiative stopping power is $9.702 \cdot 10^{-4}$ MeV $cm^2 g^{-1}$.

[c] The composition of the different compounds and mixtures is given in Table 2.1b.

2.2.5 The Continuous-Slowing-Down Range

A mean path length for an electron of initial energy E_0 can be defined by integrating the reciprocal of the total stopping power:

$$r_0 = \int_0^{E_0} \left(\frac{S(E)}{\rho}\right)_{tot}^{-1} dE \qquad (2.6)$$

This formulation is based on the continuous-slowing-down approximation (csda). It gives the path length which an electron would travel in the course of slowing down, in an unbounded uniform medium, if its rate of energy loss along the entire track was always equal to the mean rate of energy loss. In reality, the rate of en-

ergy loss fluctuates (see Fig. 2.2), but this is neglected in the continuous-slowing-down approximation. Furthermore, it should be noted that the csda range represents the path length and not the depth of penetration in a given direction. In Table 2.5 (Berger and Seltzer, 1982; and ICRU, 1984), the continuous-slowing-down range has been tabulated for the elements and mixtures in Tables 2.1a and b.

When the mean path length or the csda-range is known, the practical range (see Section 3.3.2.3) can be estimated by using a scaling law (see Fig. 2.22; Harder, 1970a). The mean path length is a practical parameter for scaling depth-dose curves and is used for this purpose in Sections 2.8.2 and 6.6.2.

TABLE 2.5—*Continuous-slowing-down range*[a], r_0, *in* g cm^{-2}

		Elements										Elements								
E/MeV	Exp[b]	$_1$H	$_2$He	$_4$Be	$_6$C[c]	$_6$C[d]	$_7$N	$_8$O	$_{13}$Al	$_{14}$Si	Exp[b]	Exp[b]	$_{22}$Ti	$_{26}$Fe	$_{29}$Cu	$_{42}$Mo	$_{50}$Sn	$_{74}$W	$_{82}$Pb	$_{92}$U	Exp[b]
0.010	−4	1.076	2.467	3.033	2.820	2.820	2.851	2.950	3.539	3.461	−4	−4	4.104	4.329	4.601	5.319	5.861	7.489	8.253	8.979	−4
0.015		2.245	5.098	6.226	5.767	5.768	5.825	6.009	7.111	6.946			8.157	8.539	9.028	1.029	1.124	1.387	1.502	1.611	−3
0.02		3.783	8.537	1.038	9.595	9.596	9.684	9.973	1.170	1.142	−3	−3	1.334	1.390	1.465	1.557	1.801	2.179	2.339	2.489	
0.03		7.878	1.764	2.134	1.966	1.967	1.983	2.037	2.367	2.308			2.677	2.774	2.914	3.264	3.528	4.181	4.444	4.694	
0.04	−3	1.322	2.945	3.551	3.267	3.268	3.293	3.378	3.900	3.802			4.390	4.536	4.754	5.296	5.705	6.681	7.066	7.433	
0.05		1.970	4.374	5.262	4.835	4.836	4.870	4.992	5.738	5.591			6.439	6.637	6.946	7.708	8.285	9.627	1.015	1.065	−2
0.06		2.724	6.029	7.241	6.648	6.650	6.694	6.856	7.855	7.653			8.793	9.050	9.459	1.047	1.123	1.298	1.365	1.429	
0.08		4.517	9.958	1.193	1.094	1.094	1.101	1.126	1.284	1.251	−2	−2	1.433	1.471	1.535	1.591	1.810	2.075	2.175	2.273	
0.10		6.650	1.462	1.749	1.602	1.603	1.611	1.647	1.872	1.822			2.083	2.136	2.225	2.445	2.612	2.977	3.113	3.249	
0.15	−2	1.322	2.891	3.451	3.156	3.158	3.169	3.235	3.659	3.561			4.056	4.149	4.314	4.714	5.021	5.668	5.905	6.149	
0.20		2.118	4.619	5.508	5.032	5.036	5.046	5.147	5.804	5.646			6.416	6.556	6.807	7.409	7.876	8.835	9.180	9.544	
0.30		4.007	8.702	1.037	9.462	9.474	9.462	9.642	1.083	1.054	−1	−1	1.194	1.218	1.263	1.367	1.448	1.611	1.668	1.730	−1
0.40		6.159	1.334	1.591	1.450	1.452	1.446	1.473	1.652	1.606			1.816	1.851	1.918	2.066	2.185	2.416	2.494	2.582	
0.50		8.480	1.833	2.188	1.993	1.997	1.982	2.018	2.260	2.197			2.481	2.528	2.617	2.809	2.965	3.265	3.361	3.475	
0.60	−1	1.091	2.355	2.814	2.561	2.567	2.542	2.586	2.894	2.812			3.173	3.231	3.345	3.578	3.772	4.137	4.250	4.389	
0.80		1.597	3.437	4.118	3.745	3.757	3.700	3.761	4.206	4.086			4.601	4.683	4.843	5.155	5.421	5.911	6.050	6.234	
1.00		2.116	4.547	5.460	4.964	4.981	4.883	4.961	5.546	5.386			6.055	6.159	6.367	6.748	7.083	7.686	7.843	8.068	
1.50		3.433	7.349	8.873	8.062	8.096	7.856	7.973	8.912	8.652			9.699	9.851	1.017	1.069	1.118	1.201	1.219	1.249	0
2.00		4.744	1.013	1.229	1.116	1.121	1.079	1.094	1.224	1.188	0	0	1.328	1.347	1.389	1.450	1.512	1.613	1.629	1.665	
3.00		7.316	1.557	1.903	1.727	1.736	1.649	1.671	1.869	1.812			2.019	2.042	2.101	2.170	2.251	2.372	2.381	2.425	
4.00		9.818	2.084	2.563	2.323	2.336	2.198	2.224	2.491	2.412			2.676	2.700	2.772	2.840	2.932	3.059	3.057	3.105	
5.00	0	1.226	2.597	3.210	2.906	2.923	2.728	2.758	3.092	2.991			3.304	3.325	3.408	3.466	3.564	3.687	3.673	3.721	
6.00		1.465	3.098	3.846	3.476	3.497	3.242	3.275	3.675	3.551			3.906	3.922	4.013	4.055	4.155	4.265	4.239	4.284	
8.00		1.931	4.070	5.091	4.585	4.614	4.231	4.267	4.795	4.624			5.042	5.042	5.143	5.140	5.234	5.301	5.249	5.287	
10.00		2.383	5.011	6.304	5.657	5.694	5.176	5.214	5.861	5.642			6.102	6.077	6.183	6.123	6.202	6.211	6.133	6.159	
15.00		3.470	7.258	9.221	8.202	8.260	7.388	7.421	8.328	7.992			8.481	8.374	8.472	8.239	8.258	8.094	7.954	7.945	
20.00		4.510	9.391	1.200	1.059	1.067	9.434	9.452	1.056	1.011	+1	+1	1.056	1.035	1.043	1.000	9.947	9.594	9.399	9.352	
30.00		6.485	1.341	1.720	1.498	1.510	1.315	1.312	1.450	1.383			1.408	1.365	1.365	1.282	1.262	1.190	1.161	1.149	+1
40.00		8.357	1.717	2.201	1.897	1.912	1.649	1.638	1.790	1.702			1.699	1.633	1.624	1.504	1.470	1.365	1.329	1.310	
50.00	+1	1.015	2.072	2.650	2.262	2.280	1.954	1.935	2.089	1.982			1.946	1.859	1.842	1.687	1.639	1.506	1.463	1.439	
60.00		1.188	2.410	3.069	2.598	2.619	2.235	2.207	2.356	2.231			2.162	2.054	2.029	1.841	1.783	1.623	1.574	1.546	
80.00		1.518	3.044	3.836	3.203	3.227	2.742	2.694	2.817	2.659			2.525	2.379	2.339	2.094	2.015	1.812	1.753	1.717	
100.0		1.831	3.631	4.524	3.735	3.762	3.189	3.120	3.205	3.019			2.822	2.643	2.591	2.296	2.200	1.960	1.894	1.851	

		Tissues[e]				Liquids[e]				Gases[e]			Solids[e]					
E/MeV	Exp[b]	Adipose Tissue	Bone (cortical)	Muscle (skeletal)	Muscle (striated)	Water (H_2O)	Ferrous Sulphate Solution	Muscle Equiv. without Sucrose	Exp[b]	Exp[b]	Air	CO_2	Tissue Equiv. with Methane	A 150	C 552	Glass (Pyrex)	M 3	MS 20	Exp[b]
0.010	−4	2.406	2.909	2.543	2.536	2.515	2.533	2.531	−4	−4	2.883	2.874	2.426	2.463	2.890	3.237	2.459	2.592	−4
0.015		4.940	5.911	5.205	5.190	5.147	5.183	5.181			5.886	5.868	4.984	5.054	5.897	6.540	5.042	5.304	
0.02		8.237	9.795	8.662	8.638	8.566	8.624	8.625			9.781	9.752	8.314	8.426	9.797	1.080	8.402	8.827	
0.03	−3	1.693	1.997	1.776	1.771	1.756	1.768	1.769	−3	−3	2.001	1.996	1.710	1.731	2.004	2.194	1.725	1.810	−3
0.04		2.818	3.308	2.951	2.944	2.919	2.937	2.939			3.322	3.313	2.846	2.880	3.326	3.624	2.869	3.008	
0.05		4.175	4.884	4.368	4.356	4.320	4.347	4.351			4.912	4.899	4.217	4.267	4.918	5.341	4.249	4.451	
0.06		5.745	6.703	6.006	5.991	5.940	5.976	5.983			6.750	6.732	5.805	5.871	6.758	7.321	5.846	6.121	
0.08		9.464	1.100	9.881	9.857	9.773	9.832	9.844		−2	1.110	1.107	9.564	9.669	1.111	1.199	9.625	1.007	−2
0.10	−2	1.387	1.607	1.447	1.443	1.431	1.439	1.441	−2		1.623	1.619	1.402	1.417	1.625	1.750	1.410	1.474	
0.15		2.734	3.155	2.848	2.841	2.817	2.833	2.838			3.193	3.184	2.764	2.792	3.196	3.427	2.778	2.903	
0.20		4.359	5.015	4.537	4.526	4.487	4.513	4.521			5.082	5.069	4.408	4.452	5.086	5.440	4.428	4.624	
0.30		8.190	9.386	8.513	8.494	8.421	8.468	8.485			9.527	9.504	8.282	8.362	9.535	1.016	8.315	8.677	
0.40	−1	1.253	1.433	1.302	1.299	1.288	1.295	1.297	−1	−1	1.456	1.452	1.268	1.280	1.457	1.549	1.272	1.327	−1
0.50		1.720	1.964	1.785	1.781	1.766	1.775	1.779			1.995	1.991	1.739	1.757	1.998	2.121	1.746	1.820	
0.60		2.209	2.519	2.290	2.285	2.265	2.277	2.283			2.558	2.552	2.232	2.258	2.564	2.717	2.242	2.335	
0.80		3.227	3.673	3.339	3.332	3.302	3.319	3.330			3.722	3.714	3.253	3.300	3.742	3.953	3.275	3.406	

1.00		4.275	4.857	4.418	4.409	4.367	4.390	4.406			4.912	4.900	4.297	4.375	4.953	5.239	4.339	4.508	
1.50		6.944	7.857	7.158	7.146	7.075	7.111	7.143			7.900	7.882	6.926	7.111	8.030	8.418	7.045	7.306	
2.00		9.621	1.085	9.903	9.886	9.785	9.835	9.885		0	1.085	1.083	9.527	9.856	1.111	1.160	9.756	1.011	0
3.00	0	1.491	1.671	1.532	1.530	1.514	1.521	1.530	0		1.658	1.654	1.459	1.528	1.717	1.782	1.511	1.563	
4.00		2.010	2.241	2.062	2.059	2.037	2.047	2.059			2.208	2.203	1947	2.059	2.310	2.384	2.035	2.102	
5.00		2.518	2.795	2.580	2.577	2.550	2.561	2.578			2.740	2.733	2420	2.579	2.888	2.970	2.548	2.630	
6.00		3.017	3.335	3.089	3.084	3.052	3.066	3.086			3.255	3.247	2879	3.090	3.454	3.539	3.051	3.147	
8.00		3.990	4.377	4.077	4.072	4.030	4.047	4.074			4.246	4.236	3765	4.084	4.554	4.638	4.030	4.153	
10.00		4.933	5.374	5.033	5.027	4.975	4.995	5.031			5.192	5.179	4614	5.048	5.614	5.689	4.979	5.126	
15.00		7.183	7.707	7.303	7.295	7.219	7.244	7.302			7.405	7.385	6613	7.348	8.125	8.145	7.239	7.438	
20.00		9.305	9.850	9.428	9.418	9.320	9.348	9.429			9.446	9.420	8474	9.515	1.047	1.040	9.364	9.606	
30.00	+1	1.324	1.369	1.333	1.332	1.317	1.320	1.334	+1	+1	1.315	1.311	1188	1.353	1.475	1.442	1.329	1.359	+1
40.00		1.683	1.707	1.685	1.684	1.665	1.668	1.687			1.646	1.642	1499	1.718	1.859	1.796	1.685	1.720	
50.00		2.013	2.008	2.006	2.005	1.983	1.986	2.010			1.948	1.945	1785	2.055	2.209	2.111	2.012	2.051	
60.00		2.320	2.280	2.302	2.301	2.276	2.277	2.307			2.227	2.223	2052	2.367	2.529	2.395	2.315	2.355	
80.00		2.875	2.757	2.832	2.832	2.799	2.799	2.839			2.727	2.723	2537	2.931	3.100	2.891	2.859	2.902	
100.00		3.366	3.164	3.296	3.297	3.258	3.256	3.306			3.167	3.163	2969	3.429	3.598	3.315	3.339	3.382	

		Solids[a]									
E/MeV	Exp[b]	Polyamide (Nylon 6) ($C_6H_{11}ON$)	Polyethylene (C_2H_4)	Mylar ($C_{10}H_8O_4$)	PMMA ($C_5H_8O_2$)	Polystyrene (C_8H_8)	Teflon (C_2F_4)	Polyvinyl chloride (C_2H_3Cl)	Lithium Fluoride (LiF)	Film Emulsion	Exp[b]
0.010	−4	2.458	2.308	2.712	2.580	2.545	3.105	2.974	3.181	4.664	−4
0.015		5.046	4.745	5.545	5.282	5.218	6.320	6.041	6.480	9.140	
0.02		8.414	7.921	9.224	8.792	8.694	1.048	1.001	1.076	1.482	−3
0.03	−3	1.729	1.630	1.890	1.803	1.785	2.140	2.040	2.198	2.945	
0.04		2.877	2.715	3.139	2.997	2.968	3.547	3.378	3.645	4.801	
0.05		4.263	4.025	4.645	4.436	4.395	5.239	4.987	5.386	7.011	
0.06		5.866	5.541	6.386	6.100	6.047	7.194	6.844	7.397	9.543	
0.08		9.662	9.134	1.050	1.004	9.955	1.181	1.123	1.215	1.547	−2
0.10	−2	1.416	1.339	1.537	1.470	1.458	1.727	1.641	1.777	2.242	
0.15		2.791	2.642	3.026	2.894	2.873	3.392	3.219	3.492	4.338	
0.20		4.450	4.215	4.819	4.610	4.579	5.395	5.117	5.555	6.833	
0.30		8.359	7.923	9.040	8.653	8.598	1.010	9.575	1.041	0.263	−1
0.40	−1	1.279	1.213	1.382	1.323	1.315	1.543	1.461	1.591	1.913	
0.50		1.757	1.667	1.896	1.815	1.805	2.114	2.001	2.183	2.604	
0.60		2.258	2.142	2.434	2.330	2.318	2.711	2.566	2.801	3.322	
0.80		3.301	3.133	3.554	3.401	3.385	3.952	3.738	4.086	4.797	
1.00		4.377	4.155	4.706	4.504	4.484	5.227	4.940	5.406	6.293	
1.50		7.116	6.759	7.635	7.308	7.281	8.462	7.980	8.756	1.001	0
2.00		9.865	9.375	1.057	1.012	1.008	1.169	1.100	1.210	1.363	
3.00	0	1.530	1.455	1.636	1.567	1.562	1.806	1.692	1.870	2.053	
4.00		2.062	1.963	2.201	2.109	2.104	2.426	2.265	2.515	2.699	
5.00		2.583	2.461	2.754	2.641	2.635	3.031	2.820	3.145	3.309	
6.00		3.095	2.950	3.296	3.162	3.156	3.622	3.360	3.761	3.886	
8.00		4.092	3.905	4.351	4.176	4.171	4.768	4.399	4.958	4.960	
10.00		5.058	4.833	5.370	5.158	5.155	5.870	5.391	6.113	5.942	
15.00		7.363	7.054	7.791	7.496	7.502	8.466	7.704	8.844	8.089	
20.00		9.536	9.157	1.006	9.693	9.717	1.087	9.819	1.139	9.909	
30.00	+1	1.356	1.307	1.424	1.375	1.382	1.523	1.359	1.602	1.288	+1
40.00		1.722	1.667	1.801	1.743	1.757	1.911	1.688	2.016	1.526	
50.00		2.060	2.000	2.147	2.081	2.103	2.262	1.981	2.392	1.724	
60.00		2.372	2.310	2.466	2.393	2.424	2.580	2.244	2.735	1.893	
80.00		2.937	2.874	3.038	2.955	3.004	3.144	2.703	3.346	2.173	
100.00		3.436	3.376	3.539	3.450	3.518	3.632	3.094	3.876	2.398	

[a] See forthcoming ICRU Report 37 (ICRU, 1984) or (Berger and Seltzer, 1982) for discussion of calculations.

[b] The lines enclose figures with the same value of exponent; thus, for hydrogen and an electron energy of 0.01 MeV, the exponent is −4 and the continuous-slowing-down range is $1.076 \cdot 10^{-4}$ g cm^{-2}.

[c] The density $\rho = 1.70$ g cm^{-3} was used in order to calculate the density effect correction.

[d] The density $\rho = 2.265$ g cm^{-3} was used in order to calculate the density effect correction.

[e] The composition of the different compounds and mixtures is given in Table 2.1b.

2.2.6 Mass Scattering Power

It can be shown that the mean square angle of scattering increases linearly with the thickness of the absorber (Rossi, 1952) because the scattering events in different layers are statistically independent and their respective mean square scattering angles thus add up linearly. Therefore, a mass scattering power, T/ρ, can be defined which expresses the increase in mean square angle of scattering ($\mathrm{d}\overline{\Theta^2}$) per unit of mass thickness ($\rho\,\mathrm{d}l$) in terms of mass traversed per unit cross sectional area (ICRU, 1972; Brahme, 1972), in close analogy with the mass stopping power (Eq. 2.1):

$$\frac{T}{\rho} = \frac{1}{\rho}\frac{\mathrm{d}\overline{\Theta^2}}{\mathrm{d}l} \tag{2.7}$$

This notation emphasizes that the scattering power is analogous to the stopping power. In the original work of Rossi (1952) the mass scattering power was symbolized by Θ_s^2. Several formulae have been derived for this quantity depending on the nucleon number, A, and on the ratio of the kinetic energy of the electron to its rest-mass energy, τ. The expression now used to calculate mass scattering power values differs slightly from that used in ICRU Report 21 (ICRU, 1972), because it includes a more accurate evaluation of screening effects (Rossi, 1952; Brahme, 1971).

$$\frac{T}{\rho} = \pi\left(\frac{2r_e Z}{(\tau+1)\beta^2}\right)^2 \frac{N_A}{M_A}\left\{\ln\left[1+\left(\frac{\Theta_m}{\Theta_\mu}\right)^2\right] - 1 + \left[1+\left(\frac{\Theta_m}{\Theta_\mu}\right)^2\right]^{-1}\right\} \tag{2.8}$$

In this expression, Θ_m is the cut-off angle due to the finite size of the nucleus. It is given by the ratio of the reduced de Broglie wave length of the electron to the nuclear radius and is

$$\Theta_m = \frac{2A^{-1/3}}{\alpha\beta(\tau+1)} \tag{2.9}$$

For Θ_m larger than unity, Θ_m should be set equal to 1 (Rossi, 1952). The screening angle, Θ_μ, is due to the screening of the nucleus by the orbital electrons. This angle is given by the ratio of the reduced de Broglie wave length of the electron to the atomic radius and can be written as

$$\Theta_\mu = 1.130\frac{\alpha Z^{1/3}}{\beta(\tau+1)} \tag{2.10}$$

Equation 2.8 yields mass scattering powers which are, generally, about 10% lower than those given in ICRU Report 21 (ICRU, 1972). The contribution from electron-electron scattering governed by the Møller cross section (Møller, 1932) is not included in Eq. 2.8 because of the considerable energy losses involved whereas it was included in ICRU Report 21 (1972). However, it could be taken into account in an approximate manner by replacing Z^2 by $Z(Z + 1)$ in Eq. 2.8.

In Table 2.6, the mass scattering power at energies from 10 keV to 100 MeV is given for a number of different elements, compounds and mixtures. The mass scattering power must be used with care for thin absorbers where single large-angle scattering events can be important. This is the case when the mean number of scattering events is less than about 20 (Moliere, 1947, 1948), i.e., when the thickness is less than approximately 1 mg cm^{-2}. In addition, for thick absorbers, the mean energy loss of the electrons must be considered. According to the experimental results (Fig. 2.8), the proportionality of the mean square scattering angle with thickness is useful over a fairly wide range of absorber thicknesses in low atomic number materials. However, the proportionality observed in Fig. 2.8 is not entirely due to the mass scattering power at the initial energy because the energy loss of electrons and the consequent gradual increase in scattering power has to be taken into account in thick absorbers. In the first approximation, this increase is given by (Eyges, 1948; Brahme, 1975)

$$\overline{\Theta^2}(l) = (T/\rho)\left\{1 - \left(\frac{S}{\rho}\right)_{\text{tot}} \rho l/(E_0 + m_e c^2)\right\}^{-1} \rho l \tag{2.11}$$

Furthermore, at larger depths, the angular distribution reaches an equilibrium shape (Bethe *et al.*, 1938), as is seen in Fig. 2.8, because electrons that are scattered at large angles are rapidly lost from the beam.

When the value of ρl in Eq. 2.11 is small, the equation reduces to $\overline{\Theta^2} = (T/\rho)\,\rho l$.

An approximate estimation of the mass scattering power for electrons of kinetic energy E can be made using the following formula (Rossi, 1952):

$$T/\rho \approx (E_s/E)^2/(\beta^4 X_0) \tag{2.12}$$

where E_s has a constant value of 21.2 MeV and X_0 in different materials is given in Table 2.4 and these values were calculated with the use of $Z(Z + 1)$ instead of Z^2 which was used in the expression for scattering power.

TABLE 2.6—*Mass scattering power, T/ρ, in* radian^2 cm^2 g^{-1}

		Elements									Elements								
E/Mev	Exp[a]	$_1$H	$_2$He	$_4$Be	$_6$C	$_7$N	$_8$O	$_{13}$Al	$_{14}$Si	Exp[a']	Exp[a]	$_{22}$Ti	$_{26}$Fe	$_{29}$Cu	$_{42}$Mo	$_{50}$Sn	$_{74}$W	$_{82}$Pb	$_{92}$U	Exp[a]
0.010	+3	2.13	1.96	3.16	5.02	5.71	6.39	9.21	101	+4	+4	1.35	1.56	167	2.14	2.36	3.04	3.23	3.44	+4
0.015		1.03	9.54	1.55	2.47	2.82	3.16	4.58	505	+3	+3	6.77	7.87	844	1.09	1.21	1.57	1.68	1.79	
0.02	+2	6.13	5.71	9.33	1.49	1.70	1.91	2.79	307			4.14	4.82	518	6.74	7.48	9.79	1.05	1.12	
0.03		2.97	2.78	4.56	7.32	8.37	9.41	1.38	152			2.07	2.41	259	3.40	3.78	4.99	5.34	5.73	+3
0.04		1.78	1.67	2.75	4.43	5.07	5.70	8.39	926	+2		1.26	1.48	159	2.09	2.33	3.09	3.31	3.55	
0.05		1.20	1.13	1.86	3.00	3.44	3.87	5.71	631		+2	8.61	1.01	109	1.43	1.60	2.13	2.28	2.45	
0.06	+1	8.67	8.18	1.36	2.19	2.51	2.83	4.18	462			6.32	7.40	798	1.05	1.18	1.57	1.69	1.81	
0.08		5.25	4.97	8.26	1.34	1.53	1.73	2.56	283			3.89	4.56	492	6.52	7.29	9.76	1.05	1.13	
0.10		3.58	3.39	5.65	9.16	1.05	1.19	1.76	195			2.68	3.15	339	4.51	5.05	6.77	7.28	7.85	+2
0.15		1.80	1.72	2.87	4.66	5.36	6.05	9.02	998	+1		1.38	1.62	175	2.33	2.62	3.52	3.79	4.10	*
0.20		1.12	1.07	1.80	2.92	3.36	3.80	5.68	628		+1	8.69	1.02	111	1.48	1.66	2.24	2.41	2.61	
0.30	0	5.87	5.61	9.44	1.54	1.77	2.00	3.00	332			4.61	5.44	588	7.87	8.86	1.20	1.29	1.40	
0.40		3.74	3.59	6.05	9.88	1.14	1.29	1.93	214			2.98	3.51	380	5.10	5.74	7.80	8.41	9.11	+1
0.50		2.66	2.55	4.31	7.04	8.11	9.18	1.38	153			2.13	2.51	272	3.65	4.12	5.61	6.05	6.55	
0.60		2.01	1.93	3.27	5.35	6.17	6.98	1.05	116			1.62	1.92	208	2.79	3.15	4.29	4.63	5.02	
0.80		1.30	1.25	2.12	3.47	4.01	4.54	6.85	758	0		1.06	1.25	136	1.83	2.06	2.82	3.04	3.30	
1.0	−1	9.25	8.92	1.51	2.48	2.87	3.25	4.91	543		0	7.60	8.99	974	1.31	1.48	2.03	2.19	2.38	
1.5		4.96	4.79	8.16	1.34	1.55	1.75	2.66	294			4.13	4.88	530	7.16	8.09	1.11	1.20	1.30	
2.0		3.15	3.05	5.21	8.57	9.90	1.12	1.70	189			2.65	3.14	340	4.61	5.21	7.15	7.74	8.40	0
3.0		1.64	1.59	2.72	4.48	5.18	5.87	8.92	990	−1		1.39	1.65	179	2.43	2.75	3.78	4.09	4.45	
4.0		1.02	9.87	1.69	2.79	3.22	3.66	5.57	618		−1	8.70	1.03	112	1.52	1.72	2.37	2.57	2.79	
5.0	−2	6.96	6.77	1.16	1.92	2.22	2.52	3.83	425			6.00	7.11	773	1.05	1.19	1.64	1.78	1.93	
6.0		5.08	4.95	8.50	1.40	1.62	1.84	2.81	312			4.40	5.22	567	7.71	8.74	1.21	1.31	1.42	
8.0		3.08	3.00	5.16	8.53	9.87	1.12	1.71	190			2.68	3.18	346	4.71	5.34	7.37	8.00	8.70	−1
10.0		2.07	2.02	3.48	5.76	6.66	7.57	1.16	128			1.81	2.15	234	3.19	3.62	5.00	5.42	5.90	
15.0		1.00	9.78	1.69	2.79	3.23	3.67	5.62	623	−2		8.83	1.05	114	1.55	1.76	2.44	2.65	2.88	
20.0	−3	5.92	5.79	1.00	1.66	1.92	2.18	3.34	371		−2	5.25	6.24	679	9.27	1.05	1.46	1.58	1.72	
30.0		2.81	2.75	4.75	7.89	9.14	1.04	1.59	177			2.51	2.98	325	4.43	5.07	6.89	7.43	8.04	−2
40.0		1.65	1.61	2.79	4.64	5.37	6.11	9.37	104			1.49	1.76	191	2.56	2.88	3.91	4.21	4.56	
50.0		1.09	1.07	1.84	3.06	3.55	4.04	6.23	691	−3	−3	9.59	1.13	123	1.64	1.85	2.51	2.71	2.93	
60.0	−4	7.71	7.58	1.31	2.18	2.55	2.89	4.34	481			6.68	7.90	854	1.15	1.29	1.75	1.89	2.04	
80.0		4.49	4.42	7.61	1.25	1.44	1.63	2.45	272			3.78	4.46	483	6.47	7.28	9.89	1.07	1.25	
100.0		2.95	2.90	4.88	8.03	9.25	1.05	1.57	174			2.42	2.86	310	4.15	4.67	6.35	6.85	7.41	−3

		Tissues[b]				Liquids[b]					Gases[b]			Solids[b]					
E/MeV	Exp[a]	Adipose Tissue	Bone (cortical)	Muscle (skeletal)	Muscle (striated)	Water (H_2O)	Ferrous Sulphate Solution	Muscle Equiv. without Sucrose	Exp[a]	Exp[a]	Air	CO_2	Muscle Equiv with Methane	A 150	C 552	Glass (Pyrex)	M 3	MS 20	Exp[a]
0.010	+3	5.01	7.93	5.84	5.82	5.91	5.99	5.77	+3	+3	5.94	6.01	5.30	5.01	5.74	7.79	5.35	5.55	+3
0.015		2.47	3.95	2.88	2.87	2.92	2.96	2.85			2.93	2.97	2.61	2.47	2.84	3.87	2.64	2.74	
0.020		1.49	2.40	1.74	1.74	1.77	1.79	1.72			1.77	1.80	1.58	1.49	1.71	2.35	1.60	1.66	
0.030	+2	7.31	1.19	8.57	8.54	8.69	8.81	8.47	+2	+2	8.73	8.84	7.76	7.32	8.44	1.16	7.85	8.15	+2
0.04		4.42	7.21	5.19	5.17	5.16	5.33	5.13			5.28	5.35	4.70	4.43	5.11	7.04	4.75	4.93	
0.05		3.00	4.91	3.52	3.51	3.57	3.61	3.48			3.59	3.63	3.19	3.00	3.47	4.79	3.22	3.35	
0.06		2.19	3.59	2.57	2.56	2.61	2.64	2.54			2.62	2.65	2.32	2.19	2.53	3.50	2.35	2.44	
0.08		1.34	2.20	1.57	1.57	1.59	1.62	1.55			1.60	1.62	1.42	1.34	1.55	2.14	1.44	1.49	
0.10	+1	9.15	1.51	1.08	1.07	1.09	1.11	1.06			1.10	1.11	9.73	9.16	1.06	1.47	9.85	1.02	
0.15		4.66	7.73	5.50	5.48	5.57	5.65	5.43	+1	+1	5.60	5.67	4.96	4.67	5.41	7.53	5.02	5.22	+1
0.20		2.92	4.86	3.45	3.44	3.50	3.55	3.40			3.51	3.56	3.11	2.93	3.40	4.73	3.15	3.27	
0.30		1.54	2.57	1.82	1.81	1.84	1.87	1.79			1.85	1.88	1.64	1.54	1.79	2.50	1.66	1.73	
0.40	0	9.88	1.66	1.17	1.16	1.18	1.20	1.15			1.19	1.21	1.05	9.90	1.15	1.61	1.07	1.11	
0.50		7.04	1.18	8.33	8.30	8.45	8.57	8.22	0	0	8.48	8.59	7.50	7.05	8.20	1.15	7.60	7.90	0
0.60		5.35	8.99	6.33	6.31	6.42	6.52	6.25			6.45	6.53	5.70	5.36	6.23	8.73	5.78	6.09	
0.80		3.48	5.86	4.12	4.10	4.17	4.24	4.06			4.19	4.25	3.70	3.48	4.05	5.68	3.75	3.90	

1.00		2.49	4.20	2.94	2.93	2.99	3.03	2.90		0	3.00	3.04	2.55	2.49	2.90	4.07	2.89	2.79	
1.50		1.34	2.27	1.59	1.58	1.61	1.64	1.57			1.62	1.64	1.43	1.34	1.57	2.20	1.45	1.51	
2.00	−1	8.57	1.45	1.02	1.01	1.03	1.05	1.00			1.04	1.05	9.14	8.59	1.00	1.41	9.27	9.65	−1
3.00		4.48	7.63	5.32	5.30	5.40	5.48	5.25	−1	−1	5.42	5.49	4.78	4.49	5.24	7.39	4.85	5.05	
4.0		2.79	4.76	3.31	3.30	3.36	3.41	3.27			3.37	3.42	2.98	2.80	3.26	4.61	3.02	3.14	
5.0		1.92	3.27	2.28	2.27	2.31	2.35	2.25			2.32	2.35	2.05	1.92	2.24	3.17	2.08	2.16	
6.0		1.41	2.40	1.67	1.66	1.69	1.72	1.65			1.70	1.72	1.50	1.41	1.64	2.32	1.52	1.58	
8.0	−2	8.53	1.46	1.01	1.01	1.03	1.05	1.00			1.03	1.05	9.11	8.56	9.99	1.41	9.24	9.62	−2
10.0		5.76	9.88	6.86	6.83	6.95	7.06	6.76	−2	−2	6.98	7.07	6.15	5.78	6.75	9.56	6.24	6.50	
15.0		2.79	4.80	3.32	3.31	3.37	3.42	3.28			3.38	3.43	2.98	2.80	3.27	4.64	3.03	3.15	
20.0		1.66	2.85	1.97	1.97	2.00	2.03	1.95			2.01	2.04	1.77	1.66	1.94	2.76	1.80	1.87	
30.0	−3	7.89	1.36	9.40	9.37	9.54	9.69	9.27	−3	−3	9.57	9.70	8.43	7.91	9.26	1.31	8.56	8.91	−3
40.0		4.64	8.00	5.53	5.51	5.61	5.70	5.45			5.63	5.70	4.95	4.65	5.44	7.73	5.03	5.24	
50.0		3.07	5.22	3.65	3.64	3.71	3.76	3.60			3.72	3.77	3.27	3.07	3.60	5.12	3.33	3.47	
60.0		2.18	3.66	2.58	2.57	2.65	2.69	2.57			2.67	2.69	2.34	2.19	2.56	3.61	2.36	2.46	
80.0		1.23	2.07	1.46	1.45	1.50	1.52	1.46			1.51	1.53	1.33	1.25	1.46	2.04	1.35	1.40	
100.0	−4	7.91	1.33	9.36	9.32	9.62	9.76	9.36	−4	−4	9.67	9.80	8.54	8.03	9.34	1.31	8.66	9.00	−4

		Solids[b]									
E/MeV	Exp[a]	Poly-amide (Nylon 6) ($C_6H_{11}ON$)	Poly-ethy-lene (C_2H_4)	Mylar ($C_{10}H_8O_4$)	PMMA ($C_5H_8O_2$)	Poly-sty-rene (C_8H_8)	Tef-lon (C_2F_4)	Poly-vinyl-chlo-ride (C_2H_3Cl)	Lithium Fluoride (LiF)	Film-Emulsion	Exp[a]
0.010	+3	5.01	4.60	5.35	5.22	4.79	5.28	8.51	5.53	1.85	+4
0.015		2.47	2.26	2.64	2.57	2.36	3.11	4.24	2.74	9.44	+3
0.020		1.49	1.36	1.59	1.55	1.42	1.88	2.58	1.66	5.82	
0.030	+2	7.32	6.69	7.83	7.64	6.98	9.26	1.28	8.15	2.93	
0.04		4.42	4.04	4.74	4.62	4.22	5.61	7.77	4.94	1.80	
0.05		3.00	2.74	3.21	3.13	2.86	3.81	5.29	3.35	1.23	
0.06		2.19	2.00	2.35	2.29	2.09	2.78	3.87	2.45	9.07	+2
0.08		1.34	1.22	1.43	1.40	1.27	1.70	2.38	1.50	5.61	
0.10	+1	9.15	8.35	9.82	9.57	8.72	1.17	1.63	1.03	3.88	
0.15		4.66	4.25	5.00	4.88	4.44	5.96	8.36	5.26	2.00	
0.20		2.92	2.66	3.14	3.06	2.78	3.74	5.26	3.29	1.27	
0.30		1.54	1.40	1.65	1.61	1.47	1.98	2.78	1.74	6.76	+1
0.40	0	9.88	8.99	1.06	1.03	9.40	1.27	1.79	1.12	4.38	
0.50		7.40	6.40	7.56	7.37	6.70	9.05	1.28	7.95	3.14	
0.60		5.35	4.87	5.75	5.60	5.09	6.88	9.75	6.05	2.40	
0.80		3.48	3.16	3.74	3.64	3.30	4.48	6.35	3.93	1.57	
1.0		2.49	2.26	2.67	2.60	2.36	3.20	4.55	2.81	1.13	
1.5		1.34	1.22	1.44	1.40	1.27	1.73	2.47	1.52	6.14	0
2.0	−1	8.57	7.78	9.22	8.98	8.15	1.11	1.58	9.72	3.95	
3.0		4.48	4.07	4.82	4.70	4.26	5.80	8.28	5.09	2.08	
4.0		2.79	2.53	3.00	2.92	2.65	3.61	5.17	3.17	1.30	
5.0		1.92	1.74	2.06	2.01	1.82	2.48	3.56	2.18	8.99	−1
6.0		1.40	1.27	1.51	1.47	1.33	1.82	2.61	1.60	6.61	
8.0	−2	8.53	7.74	9.19	8.94	8.10	1.11	1.59	9.71	4.03	
10.0		5.76	5.22	6.20	6.04	5.47	7.48	1.07	6.56	2.73	
15.0		2.70	2.53	3.01	2.93	2.65	3.63	5.22	3.18	1.33	
20.0		1.65	1.50	1.79	1.74	1.57	2.15	3.10	1.89	7.93	−2
30.0	−3	7.89	7.15	8.50	8.28	7.49	1.03	1.48	9.00	3.82	
40.0		4.64	4.20	5.00	4.86	4.40	6.03	8.70	5.29	2.19	
50.0		3.06	2.78	3.30	3.21	2.91	3.99	5.73	3.50	1.41	
60.0		2.19	1.98	2.36	2.29	2.07	2.83	4.01	2.49	9.85	−3
80.0		1.25	1.13	1.34	1.31	1.19	1.61	2.27	1.41	5.56	
100.0	−4	8.02	7.29	8.62	8.40	7.63	1.03	1.46	9.04	3.56	

[a] The lines enclose figures with the same value of the exponent. Thus, for hydrogen at 0.01 MeV the exponent is +3 and the mass scattering power is $2.13 \cdot 10^{+3}$ radian^2 cm^2 g^{-1}.

[b] The composition of the different compounds and mixtures is given in Table 2.1b.

2.3 Differential Electron Fluence

In the general transport theory, the field of high-energy charged particles is completely described by a time-dependent fluence rate, differential in coordinate and velocity space, which satisfies the general Boltzmann transport equation (Duderstadt and Martin, 1979). For relativistic particles, it is more convenient to use the particle direction, $\vec{\Omega}$ (unit vector), and the energy, E, instead of the velocity, $\vec{v}$. In this notation, the electron fluence differential in energy and angle at a point defined by $\vec{r}$ is written $\Phi_{E,\vec{\Omega}}(\vec{r})$ and satisfies the time-independent transport equation (Lewis, 1950; Beckurts and Wirtz, 1964; Harder, 1965c). $\Phi_{E,\vec{\Omega}}(\vec{r})\,dE\,d\Omega$ is the number of electrons at a point $\vec{r}$ with energy in the interval dE around E which cross a unit area, with the normal in the direction $\vec{\Omega}$, within the interval of solid angle $d\Omega$ around $\vec{\Omega}$.

When the differential electron fluence is known, all other generally useful quantities related to the electron field can be derived. For example, the particle fluence $\Phi(\vec{r})$ may be obtained from:

$$\Phi(\vec{r}) = \int_{4\pi}\int_0^\infty \Phi_{E,\vec{\Omega}}(\vec{r})\,dE\,d\Omega, \qquad (2.13$$

the vectorial particle fluence $\vec{\Phi}(\vec{r})$ from:

$$\vec{\Phi}(\vec{r}) = \int_{4\pi}\int_0^\infty \vec{\Omega}\Phi_{E,\vec{\Omega}}(\vec{r})dE\,d\Omega \qquad (2.14)$$

and the vectorial energy fluence $\vec{\Psi}(\vec{r})$ from:

$$\vec{\Psi}(\vec{r}) = \int_{4\pi}\int_0^\infty E\vec{\Omega}\Phi_{E,\vec{\Omega}}(\vec{r})\,dE\,d\Omega \qquad (2.15)$$

From an experimental point of view, the number of electrons which traverse a plane surface with the normal in the direction of a given unit vector $\vec{\omega}$, per unit area of that surface, is of great interest (see Section 2.4.1). This quantity, $\Phi^{p}(\vec{r},\vec{\omega})$, is called the planar fluence[1] (Roesch and Attix, 1968) in the direction $\vec{\omega}$, and is obtained from:

$$\Phi^{p}(\vec{r},\vec{\omega}) = \int_{4\pi}\int_0^\infty \vec{\omega}\cdot\vec{\Omega}\Phi_{E,\vec{\Omega}}(\vec{r})\,dE\,d\Omega$$
$$= \int_{4\pi}\int_0^\infty \cos\Theta\,\Phi_{E,\vec{\omega}}(\vec{r})\,dE\,d\Omega \qquad (2.16)$$

where Θ is the angle between the direction of motion of the electrons ($\vec{\Omega}$) and the normal ($\vec{\omega}$). The planar fluence can, therefore, be regarded as the component of the vectorial fluence in direction $\vec{\omega}$:

$$\Phi^{p}(\vec{r},\vec{\omega}) = \vec{\omega}\cdot\vec{\Phi}(\vec{r}) \qquad (2.17a)$$

The time derivative of the planar fluence is the number current density of particles or the planar particle radiance (particle radiance is defined in ICRU, 1980) in direction $\vec{\omega}$. The number of electrons passing through a plane of area, A, with the normal in a given direction, $\vec{\omega}$, is the surface integral of the planar fluence and is defined by

$$N(\vec{\omega}) = \int \Phi^{p}(\vec{r},\vec{\omega})\,dA \qquad (2.17b)$$

The absorbed dose, $D(\vec{r})$, at $\vec{r}$, can be obtained from the divergence of the vectorial energy fluences of the electrons ($\vec{\Psi}_e$) and photons ($\vec{\Psi}_x$) (Rossi and Roesch, 1962):

$$D(\vec{r}) = \frac{-1}{\rho(\vec{r})}\{\mathrm{div}[\vec{\Psi}_e(\vec{r}) + \vec{\Psi}_x(\vec{r})] - q(\vec{r})\} \qquad (2.18)$$

where $\rho(\vec{r})$ is the mass density at the point $\vec{r}$ and $q(\vec{r})$ is the volume density of all changes (decrease: positive sign) of rest mass energy of nuclei and elementary particles in nuclear transformations (including pair production) at the point $\vec{r}$. By using $\vec{\Psi}$ from Eq. 2.15, the absorbed dose contributed by the electron transport (first term inside the divergence operator of Eq. 2.18) may be rewritten as:

$$D(\vec{r}) = \frac{-1}{\rho(\vec{r})}\int_{4\pi}\int_0^\infty \{\vec{\Omega}\Phi_{E,\vec{\Omega}}(\vec{r})\cdot\mathrm{grad}E + E\vec{\Omega}\cdot\mathrm{grad}\,\Phi_{E,\vec{\Omega}}(\vec{r})\}dE\,d\Omega \qquad (2.19)$$

and when $\Phi_{E,\vec{\Omega}}$ is the differential fluence of the electrons only, Eq. 2.19 can be rewritten as:

$$D(\vec{r}) = -\int_{4\pi}\int_0^\infty \left\{\frac{dE}{ds}\Phi_{E,\vec{\Omega}}(\vec{r}) + E\frac{d\,\Phi_{E,\vec{\Omega}}(\vec{r})}{ds}\right\}dE\,d\Omega \qquad (2.20)$$

where the energy E of the electrons is regarded as a variable depending on the space coordinates and s is the mass traversed per unit surface area along the direction of the particle motion[2] (cf. Schulz, 1970). The second term of Eq. 2.20 can be interpreted as the contribution from those electrons that come to rest within an interval ds (the track-end term/see Section 4.3.3 and Burch, 1957; Nahum, 1976, 1978), whereas the first term is the contribution by electrons that pass through the interval ds and thus only deposit a fraction of their energy in that interval, as shown schematically in Fig. 2.1. The first term forms the basis for all theoretical formulations of stopping power ratios, whereas the second term may be treated as a correction.

[1] The designation "plane fluence" was used for this quantity by Whyte (1959) and Carlsson (1979).

[2] The minus sign in Eq. 2.20 compensates for the negative values of dE/ds and $d\Phi/ds$ obtained with a decreasing energy and fluence in the direction of s.

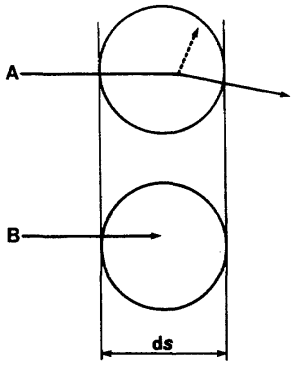

Fig. 2.1. Schematic representation of the two principal types of energy deposition in an interval ds along a particle track. Track A, and the first term in Eq. 2.20, represent the quasi-continuous loss of energy by ionizations and excitations along the track and loss of energy in the form of low energy delta rays (dashed line) set in motion by the primary particle. Track B, and the second term of Eq. 2.20, represent the change in particle fluence when a primary particle is no longer capable of leaving the interval under consideration. More complicated interactions in the volume defined by ds can, naturally, occur but they can always be divided into these two principal types.

Normally, it is difficult to find analytical solutions to the general transport equation except for the simplest geometries when continuous-slowing-down, small scattering angles or negligible energy loss are assumed. Some of these solutions are of a simple analytic form and will, therefore, be used in the sections that follow to describe the differential electron fluence in different materials.

2.4 Energy Spectra

2.4.1 General

The most important characteristic of an electron beam is normally its energy distribution or its energy spectrum. The yield of energy-dependent physical, chemical and biological radiation effects is a function of the energy spectrum and it influences the response of energy-dependent dosimeters.

The points of interest for a determination of the spectrum may be situated at the entrance or the exit surface of the medium or at some depth inside the medium. Contributions to the spectrum are made by (a) primary electrons, (b) secondary electrons including higher order δ-rays, and (c) electrons liberated in the interaction of photons and the medium that contaminate the beam or are produced within the medium.

When a monoenergetic electron beam enters an absorbing medium its energy distribution is rapidly broadened by numerous inelastic collisions with the atoms of the absorber. The spectral distribution expresses the number of electrons of a given energy crossing a sphere of unit cross-sectional area. This spectral distribution is of prime importance in dosimetric calculations and can be derived from the differential electron fluence discussed in Section 2.3:

$$\Phi_E = \int_{4\pi} \Phi_{E,\vec{\Omega}} \, \mathrm{d}\Omega \tag{2.21}$$

However, the spectral fluence Φ_E can rarely be measured experimentally in a simple way. A practical measurement at a plane reference surface yields, instead, the spectral distribution of the planar fluence of electrons (see Section 2.3). This quantity, $\Phi^{\mathrm{p}}_E(\vec{\omega})$, can be obtained from the spectrum of the vectorial electron fluence using the equation:

$$\Phi^{\mathrm{p}}_E(\omega) = \int_{4\pi} \Phi_{E,\vec{\Omega}} \cos\Theta \, \mathrm{d}\Omega = \vec{\omega} \cdot \vec{\Phi}_E \tag{2.22}$$

where Θ is the angle between the direction of motion of the electrons ($\vec{\Omega}$) and the normal to the reference surface, $\vec{\omega}$, (cf. Eq. 2.16). This situation is encountered when an absorber is divided in two parts and the net number of electrons, N^{p}, traversing the boundary plane is measured. If the measurement is performed with a detector which only measures the number of electrons crossing the surface in one direction and does not count the backscattered electrons, the spectrum of the unidirectional planar fluence is instead obtained:

$$\Phi^{\mathrm{p,u}}_E(\vec{\omega}) = \int_{2\pi} \Phi_{E,\vec{\Omega}} \cos\Theta \, \mathrm{d}\Omega \tag{2.23}$$

This situation is the most common in the measurement of electron spectra as part of the absorber normally has to be removed to allow extraction of the electrons for the energy analysis. It should be pointed out that this generally alters the electron fluence at the point of measurement. For example, those backscattered electrons that normally would be scattered forward again are not included in Eq. 2.23 due to the removal of backscattering material, but are included in Eq. 2.22. This difference is negligible in most dosimetric applications because the number of backscattered electrons is normally orders of magnitude smaller than the forward-directed electrons, particularly in low atomic number materials at relativistic energies (see Fig. 2.6a and Harder and Metzger, 1968). In some cases, only transmitted electrons from a small solid angle around the direction $\vec{\omega}$ are used due to limited acceptance of the spectrometric system. When this is the case, a fairly good approximation for the differential energy fluence can be obtained.

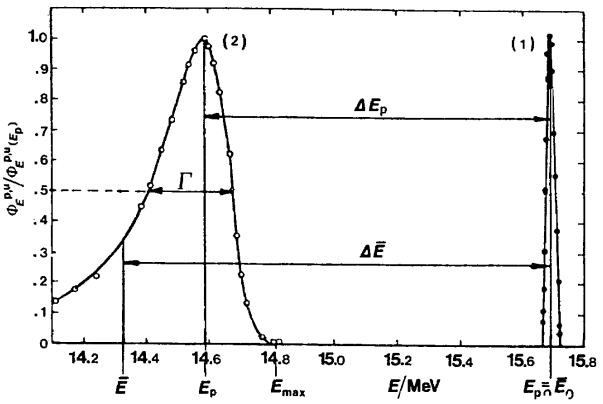

Fig. 2.2. Energy distribution of an "unobstructed" betatron beam (1) and of the electrons that have passed through 0.86 g cm^{-2} of aluminum (2). Experimental values are given by the points. The apparent width of the "unobstructed" electron beam is mainly due to the limited resolution of the spectrometer (Goldwasser *et al.*, 1952). The solid curve (2) agrees approximately with the energy distribution predicted theoretically by Landau (1944).

2.4.2 Spectrum of Electrons Traversing a Plane-Parallel Slab

One can consider electrons of any specified energy emerging from the thin window of an accelerator and assess the energy distribution after entry into a plane-parallel slab. Theoretical analysis and experimental measurements of the spectrum are readily carried out for this arrangement. The theoretical work is well developed and takes both collisional- (Landau, 1944; Blunck and Leisegang, 1950; Vavilov, 1957; Birkhoff, 1958; Badwar, 1973) and radiative-energy losses (Bethe and Heitler, 1934; Eyges, 1949, 1950; Blunck and Westphal, 1951) into account. In Fig. 2.2 the shape of the theoretical energy distribution according to Landau (1944) is compared with the experimental results of Goldwasser *et al.* (1952). Good agreement is generally obtained, particularly for low atomic number materials. The experimental spectrum was measured in the forward direction within a few degrees of the incident beam direction, but this spectrum should not differ much from that obtained from Eq. 2.23 because of the small foil thickness and consequent strongly forward-peaked angular distribution.

The most important energy parameters, E_{max}, E_p, $\bar{E}$, and Γ, of the energy straggling distribution are also indicated in this figure. E_{max} is the maximum energy of the electron spectrum, E_p the most probable energy, defined by the peak of the energy distribution, and $\bar{E}$ the mean energy of the spectrum of the planar fluence as obtained from

$$\bar{E} = \frac{\int E\, \Phi_E^p\, dE}{\int \Phi_E^p\, dE} \qquad (2.24)$$

The full width of the energy distribution at half its maximum value is designated Γ and is a measure of the energy spread in the beam after passage through a foil.

The spectra (cf. Eq. 2.23) of almost monoenergetic 20 MeV electrons after passage through carbon absorbers of different thickness are shown in Fig. 2.3. Figure 2.4 is based on the data of Fig. 2.3, and shows that the most probable electron energy, E_p, decreases linearly with the absorber thickness over practically the whole electron range (Harder, 1965a):

$$E_p(z) = E_p(0)\left(1 - \frac{z}{R_p}\right) \qquad (2.25)$$

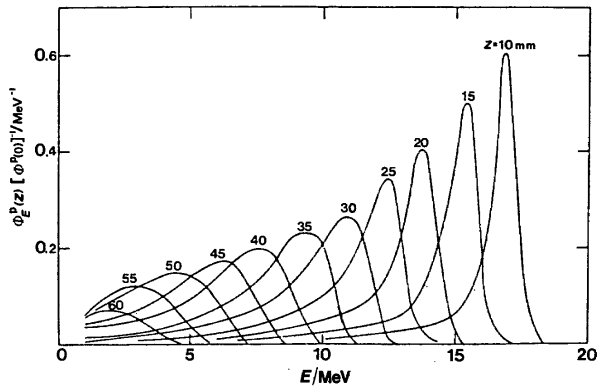

Fig. 2.3. Spectra of the planar fluence of primary electrons behind carbon layers of different thickness, z, normalized to the planar fluence of the incident plane-parallel beam; initial energy E_0 = 20 MeV. Data observed with a scintillation spectrometer and corrected for its finite resolution (from Harder, 1965, 1966).

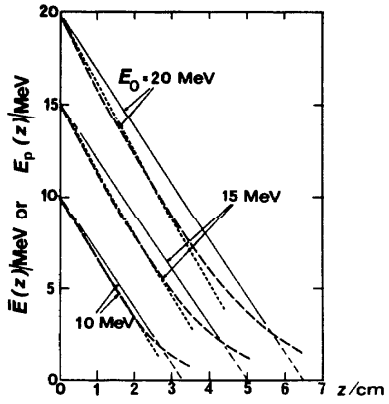

Fig. 2.4. Decrease with absorber thickness, z, of the most probable energy, $E_p(z)$, (the straight lines and their estimated extrapolations), and mean energy, $\bar{E}(z)$, (dashed curves) as measured by Harder (1965a, 1966) and as predicted by Eq. 2.28 (dotted lines). The measurements were made in carbon with different initial energies E_0 = 10, 15 and 20 MeV.

Here, $E_p(0)$ is the most probable energy at the surface, R_p the practical range (Section 3.3.2.3) and z the absorber thickness. This relation was investigated with a beam of negligible initial energy spread ($E_0 = E_p(0) = \bar{E}(0)$), but it is valid to a good approximation for a beam of small energy spread, when $E_p(0)$ is used as the initial value. In low atomic number materials, the most probable energy behind an absorber layer is approximately equal to

$$E_p(z) = E_p(0) - zS_{col}(E_p(0)) \tag{2.26}$$

where S_{col} is to be evaluated for energy $E_p(0)$. Eq. 2.26 gives values in good agreement with experiments except at high energies and large depths where range straggling cannot be neglected.

A theoretical estimate of the most probable electron energy in a material at a depth, z, when it is assumed that radiative energy losses can be ignored is due to Landau (1944) and Rohrlich and Carlson (1954) and results in an additional term, logarithmic in z. Due to the slow variation of the logarithm for most practical values of z, Eq. 2.26 can often be used as a first approximation. The value of the most probable energy decrease, containing the asymptotic value of the density effect, is particularly simple and was given by Hanson *et al.* (1952) and Goldwasser *et al.* (1952):

$$E_p(0) - E_p(z) = 2\pi r_e^2 m_e c^2 \frac{N_A Z \rho z}{M_A \beta^2}\left\{\ln\left(\frac{z m_e e^2}{\hbar^2}\right) + 0.37\right\} \tag{2.27}$$

where $\hbar$ is Planck's constant divided by 2π and $\hbar/m_e e^2$ is the radius of the hydrogen atom; other symbols as defined following Eq. 2.2. The numerical values derived from this equation are in good agreement with the experimental determinations of the most probable energy decrease in thin layers of matter by Hall *et al.* (1959), Schopka (1977) and Marbach and Almond (1981).

For many dosimetric applications, the mean electron energy, $\bar{E}(z)$, at a depth z may be approximated by $E_p(z)$ as derived from Eq. 2.25 (Harder, 1965a). However, Eq. 2.25 holds only approximately for $\bar{E}$, because the mean energy of high-energy electrons initially decreases more rapidly (see Fig. 2.4) due to their high initial radiative stopping power. That the mean energy of the electrons is lower than the most probable energy can also be seen from the skewed character of the energy straggling distribution (Figs. 2.2 and 2.3) caused by the long tails on the low energy side.

If it is assumed that the collision stopping power is constant and the radiative stopping power is directly proportional to the mean energy of the electrons, which is a good approximation over a wide energy range (see Section 2.2.4), it can be shown (Brahme, 1975) that the mean electron energy decreases in a simple exponential fashion:

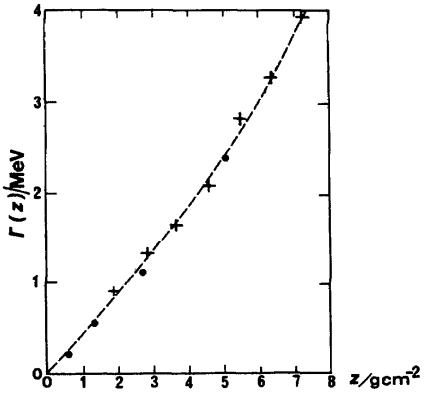

Fig. 2.5. Increase of the full width at half maximum of the energy distribution, $\Gamma(z)$, with the absorber thickness. Measurements in carbon at 20 MeV (+ Harder, 1965b, 1966) and 50 MeV (· Theissen and Gudden, 1966).

$$\bar{E}(z) = \bar{E}(0)\frac{S_{tot}\exp\{-zS_{rad}/\bar{E}(0)\} - S_{col}}{S_{rad}} \tag{2.28}$$

This relation gives a good approximation to the mean electron energy, at least over the first half of the electron range (see the dotted curves in Fig. 2.4 and Andreo and Brahme, 1981). The stopping power values to be used in Eq. 2.28 are those for the mean electron energy at the surface, $\bar{E}(0)$. At small depths, Eq. 2.28 simplifies to

$$\bar{E}(z) = \bar{E}(0) - zS_{tot}(\bar{E}(0)) \tag{2.29}$$

where S_{tot} is to be evaluated for $\bar{E}(0)$. Eq. 2.29 can be used with sufficient accuracy over the first quarter of the electron range (cf. Rassow, 1970). Eq. 2.29 is consistent with the experimental results of Markus (1978), who obtained an average value for S_{tot} between 5 and 15 MeV for water of 1.955 MeV cm^{-1} which agrees to within about 10% with the data in Tables 2.2a and 2.4.

The energy spread of the beam has been found to be nearly proportional to the absorber thickness (see Fig. 2.5) as should be expected from the simple theory (Landau, 1944). It is thus possible, for many practical purposes, to relate the energy spread, Γ, to the most probable energy loss in the absorber, ΔE_p, by a simple linear relation $\Gamma = \Delta E_p/\kappa$ or

$$\frac{1}{\rho}\frac{d\Gamma}{dl} = \left(\frac{S}{\rho}\right)_{col}/\kappa \tag{2.30}$$

A collection of experimental values of the dimensionless factor, κ, determined from published data for different materials, is presented in Table 2.7. It is observed that the increase in energy spread for a given most probable energy loss is considerably larger in high

TABLE 2.7—*The ratio, κ, between most probable energy loss, ΔE_p, and energy spread, Γ, as defined by Eq. 2.30*

Material	E_0/MeV	κ	Reference
Beryllium	10–15	4.7	Goldwasser *et al.* (1952)
	4–8	5.0	Lonergan *et al.* (1970)
Polystyrene	10–15	4.7	Goldwasser *et al.* (1952)
Carbon	50	4.1	Theissen and Gudden (1966)
	20	3.8	Harder (1965a, 1966)
Aluminum	10–15	4.2	Goldwasser *et al.* (1952)
	20–60	4.0	Breuer (1964)
	54	4.1	Bumiller *et al.* (1969)
Copper	10–15	3.5	Goldwasser *et al.* (1952)
	1.5–3.6	3.0	Van Camp and Vanhuyse (1965)
Gold	10–15	2.2	Goldwasser *et al.* (1952)

atomic number materials mainly due to the greater influence of radiative energy losses. All of the experimental values in Table 2.7 were obtained in measurements of the energy losses of electrons emerging from the absorber in a narrow cone in the forward direction, except for those of Harder (1965a, 1966) who used a scintillation spectrometer in a geometry for which Eq. 2.22 is applicable. However, because the electron distribution is strongly forward-peaked, the variations due to this difference are very small.

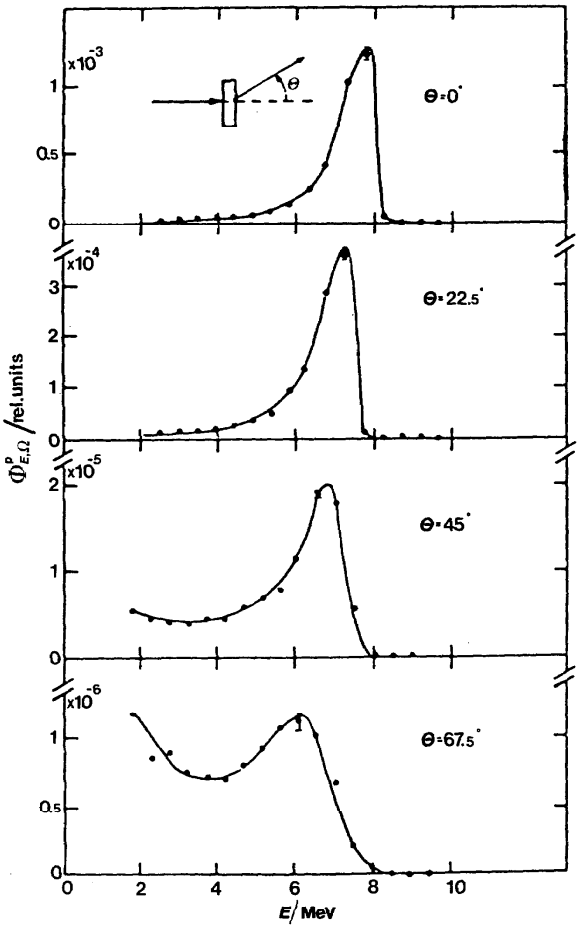

Fig. 2.6a. Spectra of the differential planar fluence of fast electrons with initial energy $E_0 = 10$ MeV after penetrating 1 cm of carbon as a function of electron energy, E. Measurements at different angles, θ (from Harder, 1966).

Several reports have been published on the spectral distribution at different angles from the incident beam and the experimental results have been compared to Monte Carlo calculations (Harder, 1965a, 1966; Berger, 1969; Lonergan *et al.*, 1970; Rester and Derrickson, 1971; Mikado *et al.*, 1976). Good agreement between calculated and experimental values has generally been obtained. The most probable energy decreases slowly, and the full width at half maximum of the energy distribution increases slowly with increasing angle from the incident beam (Fig. 2.6a). This is partly due to the fact that electrons leaving the scattering foils at a large angle generally have travelled a longer distance in the foil (Yang, 1951).

2.4.3 Energy Distribution of the Electron Fluence Inside an Absorber

Electrons may be extracted from a point of interest inside an absorbing medium and allowed to pass into a magnetic or scintillation spectrometer by inserting an evacuated tube into the absorber. The distribution of the fluence, differential in energy and angle, $\Phi_{E,\vec{\Omega}}$, in a medium is measured approximately by this method. From measurements at different angles, the distribution of the fluence in energy, Φ_E, may be obtained by integration over all angles.

The experimental results for water, obtained by several authors (Dolphin *et al.*, 1959; Feist, 1963; Epp *et al.*, 1965; Inada *et al.*, 1969) are closely similar to those obtained behind plane carbon layers (Section 2.4.2), because the contribution to the observed spectrum by backscattered electrons is very small for materials of low atomic number. Measurements of the electron spectrum inside absorbers down to energies as low as 15 eV have been performed by McConnell *et al.* (1968). Measurement of energy-loss spectra inside absorbers have been performed with semiconductor detectors by Olien and Holloway (1969).

Using the methods of electron transport theory or the Monte Carlo method, several authors have obtained calculated distributions of the electron fluence differential in energy (Kessaris, 1966; Hagemann, 1967; Laughlin, 1969; Berger and Seltzer, 1969a; Nahum, 1976; Abou-Mandour, 1978; and Andreo, 1980). An example of the calculated spectra is shown in Fig. 2.6b.

The contribution from the secondary electrons is evident in Fig. 2.6a. The presence of these are readily

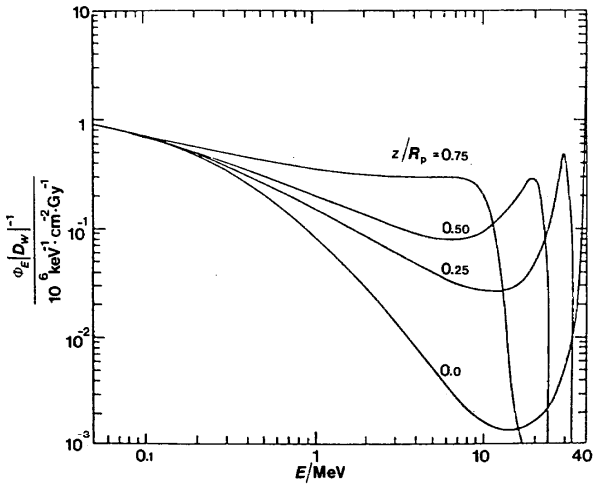

Fig. 2.6b. Calculated distributions of the electron fluence differential in energy, Φ_E, of primary and secondary electrons in water, normalized to absorbed dose for 40 MeV initial energy. The ratio z/R_p denotes the reference depth, z, for each spectrum, which is the average over a small interval of the depth close to z (from Berger and Seltzer, 1969a).

visible in the low-energy region of the spectra at large observation angles, where the contribution from the primary electrons is small. A more detailed experimental study of the low-energy region of the spectrum, ranging from 50 keV to a few MeV, was performed by Schulz and Harder (1969) which showed that the secondary electron fluence spectrum per unit absorbed dose was almost independent of absorber thickness (cf. Fig. 2.6b). The calculation of such spectra, based on the Monte Carlo method (Berger, 1963; Berger and Seltzer, 1969a; Patau *et al.*, 1969; Nahum, 1976; Abou-Mandour, 1978; Andreo, 1980), has been developed to a satisfactorily high degree of accuracy.

2.4.4 Slowing-Down Spectra Independent of the Space Coordinates

If the distribution of the fluence in energy, Φ_E, is integrated over an arbitrary volume V, one obtains the differential distribution of the track length in energy in this volume,

$$Y_E = \int \Phi_E \rho \, dV \qquad (2.31)$$

where ρ is the density and $Y_E dE$ is the sum of the path lengths expressed in mass traversed per surface area by electrons that have energies in the interval dE around E.

This quantity has been calculated for a volume in which complete slowing down of electrons of given initial energy, E_0, takes place (Spencer and Fano, 1954; McGinnies, 1959; Schneider and Cormack, 1959; Haynes and Dolphin, 1959; Rausche, 1963; Bruce *et al.* 1963; Markus, 1964; Harder, 1967a; Berger and Seltzer, 1969b; Sugiyama, 1970; Nahum, 1976; Hamm *et al.*, 1978; Morel and Halblieb, 1979). The production and proliferation of secondary electrons and higher-generation delta rays are followed in these calculations down to energies as small as 10 eV. In Fig. 2.7a, the variation of the tracklength distribution in different materials for electrons with an initial energy of 1.038 MeV is illustrated by the results of McGinnies (1959). A considerable increase in the fluence of low energy electrons is observed with increasing atomic number of the absorber. Of dosimetric and radiobiologic importance is the fact that the slowing-down spectra per unit absorbed dose of electrons of different initial energies approach a common asymptotic curve at energies below about 1/50 of the initial energy (Figs. 2.7b and 2.6b).

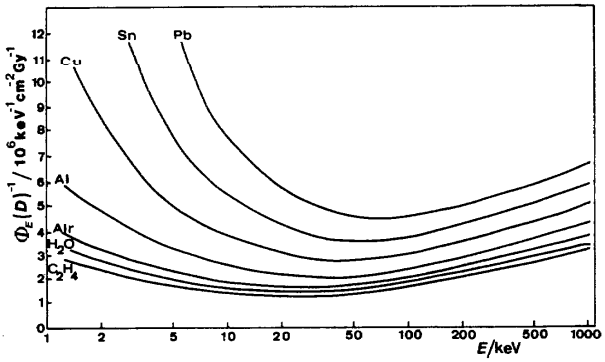

Fig. 2.7a. The slowing-down spectrum of 1.038 MeV electrons in different materials is characterized by the electron fluence differential in energy per unit absorbed dose which is equivalent to the differential distribution of track length in energy (from McGinnies, 1959).

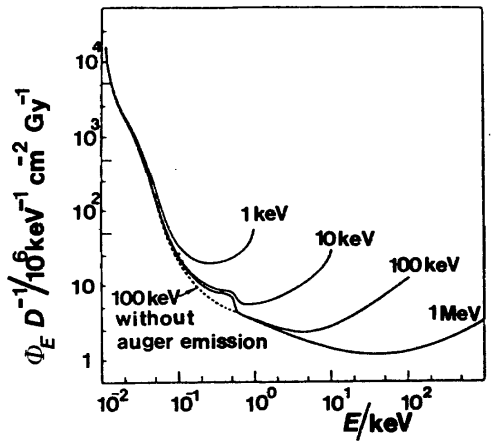

Fig. 2.7b. Electron slowing-down spectra in liquid water for electrons of initial energy 1 keV, 10 keV, 100 keV, and 1 MeV (Hamm *et al.*, 1978).

In Figs. 2.7 and 2.6b, the quantity Φ_E/D is shown on the ordinate; it is related to Y_E by

$$\frac{\Phi_E}{D} = \frac{Y_E}{E_0} \tag{2.32}$$

where D is the absorbed dose in the medium. This equation is valid for a homogeneous distribution of electron sources of energy E_0 within the slowing-down medium. Spectra of this kind have been used in the cavity theory of Spencer and Attix (1955).

2.5 Angular Distribution

2.5.1 General

The directional distribution of the electrons that have passed through a scattering foil or a certain thickness of phantom material depends on the scattering events that have taken place with the nuclei and, to a lesser extent, with the electrons of the material. These scattering events determine not only the angular distribution of the electrons at a given position but influence, also, the spatial distribution of the electron fluence (see Section 2.6 and 2.7). The angular distribution of the electrons is of dosimetric importance because, for example, it influences the shape of the absorbed-dose distribution in extended media (Section 3.2.4.3), the effective point of measurement of a dosimeter (Section 4.1.3), and the correction of the dose response of a dosimeter with a known angular dependence.

2.5.2 Angular Distribution of the Electrons Crossing a Plane Surface

There are several detailed theories which describe the multiple scattering of relativistic electrons to varying degrees of approximation, as reviewed by Scott (1963) and Marion and Zimmerman (1967). For most practical applications in radiation dosimetry, it is sufficient to use theoretical formulations which ignore the relatively few large-angle, single-scattering events and, therefore, result in purely Gaussian angular distributions of the multiply-scattered electrons (Fermi, 1940; Eyges, 1948; Zerby and Keller, 1967; Brahme, 1975). When this is the case, it is sufficient to use the scattering power concept (Eq. 2.7) to describe the angular distribution.

The angular distribution of the electrons transmitted through thin and thick targets has been measured by Lyman *et al.* (1951), Frank (1959), Tabata *et al.* (1967), Lonergan *et al.* (1970), Rester and Derrickson (1971), Kovaliev *et al.* (1972) and Roos *et al.* (1973). The increase of the mean square scattering angle with increasing absorber thickness has been studied by Tabata *et al.* (1967) and Roos *et al.* (1973) as shown in Fig. 2.8. It can be observed that the mean square scattering angle

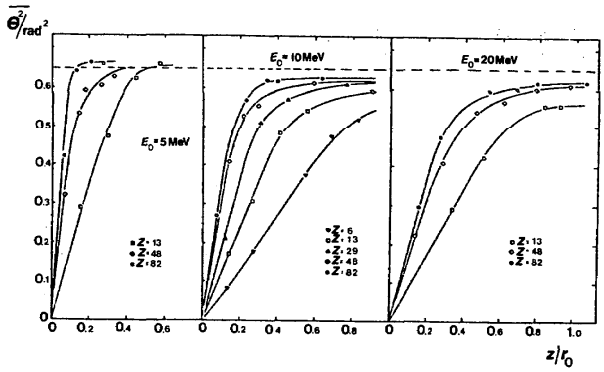

Fig. 2.8. The variation of the mean square scattering angle, $\overline{\theta^2}$, with depth (z) measured in fractions of the mean range (r_0) for materials of different atomic numbers (Z) according to Roos *et al.* (1973). The limiting value for full diffusion according to the distribution derived by Bethe *et al.* (1938) is also indicated by the horizontal dashed line.

first increases almost linearly with the absorber thickness (as should be expected from Eq. 2.7) but reaches an equilibrium value of approximately 0.6 radians^2 at large depths. At depths beyond 1/3 to 1/2 of the practical range, the electrons reach a state of full diffusion where the width of the angular distribution no longer increases. The explanation for this is that electrons scattered over large angles are rapidly lost from the beam so that the largest depths are mainly reached by electrons that have fairly straight initial paths.

In the small angle Gaussian approximation (Fermi, 1940; Eyges, 1948), it is possible to give a simple analytic expression for the angular distribution, irrespective of lateral position, of the primary electrons that have passed a given distance through plane parallel layers of constant or varying mass scattering power. A cylindrical coordinate system with the incident beam along the z direction is defined in Fig. 2.9. The angles Θ_x (in the x,z plane) and Θ_y (in the y,z plane) are treated as cartesian angular coordinates ($\Theta^2 = \Theta_x^2 + \Theta_y^2$) in the small angle approximation. In the small angle approximation, the

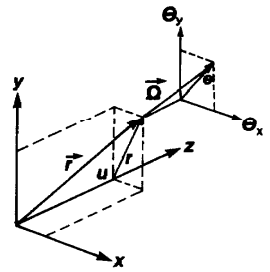

Fig. 2.9. The coordinate system used to describe the lateral and angular distribution of electrons in a cylindrical beam. The coordinates of the particle are $\vec{r} = (x,y,z)$ and the direction of motion $\vec{\Omega}$ The integration variable along the z axis is designated u.

fluence differential in angle in a beam with a narrow initial Gaussian distribution becomes (Eyges, 1948; Brahme, 1975):

$$\Phi_\theta(z) = \Phi(0)\,\frac{\exp\{-\theta^2/\overline{\theta^2}(z)\}}{\pi\,\overline{\theta^2}(z)} \qquad (2.33)$$

The mean square angular spread at depth z is obtained from

$$\overline{\theta^2}(z) = \overline{\theta_i^2} + \int_0^z T(u)\mathrm{d}u \qquad (2.34)$$

where $\overline{\theta_i^2}$ is the initial mean square angular spread of the beam when entering perpendicularly to the plane at $z = u = 0$, T is the linear scattering power (Eq. 2.7) and θ the angle with the initial beam direction (see Fig. 2.9). The integration of Eq. 2.33 over all directions yields $\int_0^\infty \Phi_\theta(z)\, 2\pi\theta\mathrm{d}\theta \equiv \Phi(0)$. The upper limit of integration is ∞ rather than π and θ is used instead of $\sin\theta$ due to the application of the small-angle approximation. Because this integral is constant at all depths, independent of the value $\overline{\theta^2}(z)$, Φ in Eq. 2.33 is more closely related to the planar fluence (see Fig. 2.13 and Eq. 2.16) than to the fluence (see Fig. 2.12 and Eq. 2.13) of primary electrons. The angular distribution of the fluence at small angles is, therefore, obtained with somewhat higher accuracy by dividing the Gaussian expression in Eq. 2.33 by $\cos\theta$ (cf. Eqs. 2.13 and 2.16).

As cylindrical symmetry and the small angle approximation are assumed, the projected distribution function in the x,z plane takes the form

$$\Phi_{\theta_x}(z) = \Phi(0)\,\frac{\exp\{-\theta_x^2/\overline{\theta^2}(z)\}}{(\pi\,\overline{\theta^2}(z))^{1/2}} \qquad (2.35)$$

The projected distribution is normalized such that $\int_{-\infty}^{\infty} \Phi_{\theta_x}(z)\mathrm{d}\theta_x \equiv \Phi(0)$. The total non-projected distributions function (Eq. 2.33) can be obtained as the product of the projected distribution in the x and y directions (Eq. 2.35), because, in the small angle approximation, $\theta^2 = \theta_x^2 + \theta_y^2$. Further differential and projected distributions of interest for electron penetration are given in the work of Rossi (1952), Zerby and Keller (1967), and Brahme (1975).

At small deflection angles, the magnitude of the true angular distribution is significantly lower than that of the Gaussian distribution, Eq. 2.33 (see dash-dot line of Fig. 2.10), whereas the reverse is true at large deflection angles due to the influence of large angle single scattering events. However, Eq. 2.34 still holds for the mean square deflection angle of the true angular distribution. In fact, it is possible to find a narrower Gaussian distribution (dotted line in Fig. 2.10) which fits the central portion of the true angular distribution better than Eq. 2.33. This reduced Gaussian distribution is obtained by replacing $\overline{\theta^2}(z)$ in Eq. 2.33 by $\theta_{1/e}^2(z) = \overline{\theta_{MG}^2}(1 - 1.330/B)$, where $\theta_{1/e}$ is the 1/e angle of the more exact Molière distribution (Scott, 1963) and $\overline{\theta_{MG}^2}$ is the mean square angle of the Gaussian part of the Molière distribution and B is the form factor in the Molière theory. In the first approximation $\overline{\theta_{MG}^2} = \overline{\theta^2}(z)/1.27$ for $B \approx 10$ (Brahme *et al.*, 1981). The parameter B increases logarithmically with thickness and is of the order of 10 at 1 g/cm^2 (cf. Scott, 1963). For large thicknesses and B values, the reduced Gaussian distribution and the Gaussian part of the Molière distribution approach each other.

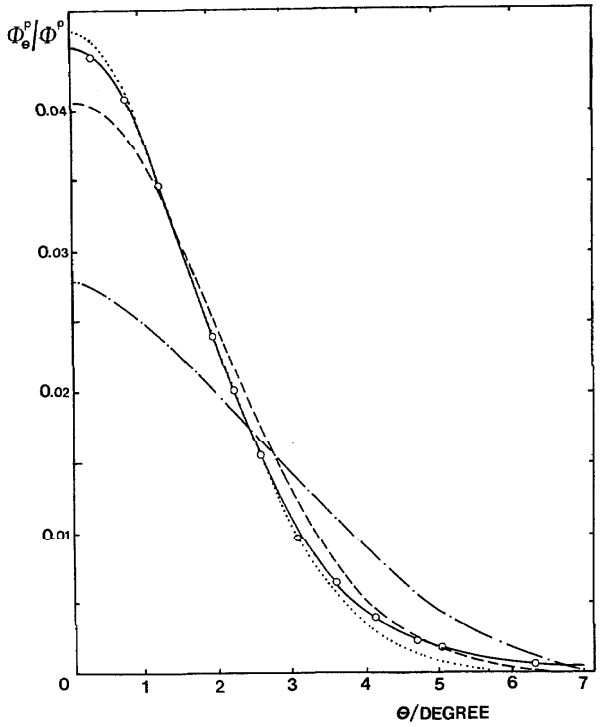

Fig. 2.10. The angular distribution of 15.7 MeV electrons scattered by 0.01 mm Au foil (Hanson *et al.*, 1951). The experimental data are represented by circles, the reduced Gaussian distribution by the dotted line, the more detailed Molière theory (cf. Scott, 1963) by the solid line, the Gaussian part in the Moliere theory by the dashed line (Molière 1947, 1948), and the Fermi-Eyges relationship (Eq. 2.33) using $\overline{\theta^2}$ from Table 2.6 by the dash-dot line. The distributions in this figure are normalized to one incident electron.

2.6 Lateral Distribution

2.6.1 General

The spatial electron distribution in a medium will be considerably influenced by the scattering properties of

the materials in the path of the beam. The spatial distribution of scattered electrons has been treated theoretically by a number of workers using the small angle approximation which results in Gaussian distributions in the lateral coordinates of sufficient accuracy for most applications in electron dosimetry (Fermi, 1940; Sternheimer, 1954; Zerby and Keller, 1967; Brahme, 1975; Kawachi, 1975).

2.6.2 Incident Narrow Gaussian Beams

With the same coordinate system and geometry as in Section 2.5 and Fig. 2.9, the depth dependence of the radial distribution of the planar fluence of primary electrons from an incident beam with a Gaussian distribution both in angle and position becomes:

$$\Phi^{\mathrm{p}}(r,z) = N(z)\,\frac{\exp\{-r^2/\overline{r^2}(z)\}}{\pi\overline{r^2}(z)}: \qquad (2.36)$$

where

$$\overline{r^2}(z) = \overline{r_i^2} + 2\overline{r\theta}_i z + \overline{\theta}_i^2 z^2 + \int_0^z (z-u)^2 T(u)\,du \qquad (2.37)$$

$\overline{r_i^2}$ is the initial mean square radial spread or variance of the radial distribution, $\overline{\theta}_i^2$ is the initial mean square angular spread (see Eq. 2.34) or the variance of the angular distribution, and $\overline{r\theta}_i$ is the initial covariance of the simultaneous radial and angular distribution (see Eq. 2.39, Section 3.2.4 and Table 3.1) of the beam incident on the plane $z = 0$. Eq. 2.36 has been given here for the planar fluence as discussed in the text after Eq. 2.34. This cannot be used for the planar fluence in Eq. 2.33 and 2.35 because, according to Eq. 2.17a, the angular distribution of the planar fluence is, by definition, cosine distributed when $\vec{\Phi}(\vec{r})$ is parallel to the beam direction. $N(z)$ is the number of electrons passing through a plane at z in the positive z direction and may be approximated by $N(0)\eta_T(z)$ where $\eta_T(z)$ is the transmission coefficient of the planar fluence taken from Eq. 2.44. This is a generalization of the basic Fermi-Eyges solution which takes the loss of primary electrons into account.

The integral in Eq. 2.37 is straightforward to evaluate when the positions, u, and scattering powers, $T(u)$, of the materials along the beam are known. In the special case of a uniform scattering medium, $T(u)$ may be assumed to have a constant value $T_0 = T(0)$ if z is smaller than the diffusion depth (see Fig. 2.8 and Section 2.2.6) and the integral in Eq. 2.37 becomes simply $T_0 z^3/3$ (cf. Table 3.1). This result may be interpreted to mean that an extended scatterer will only increase the mean square radius of the beam by a factor which is one third of that which the same scattering material would produce when condensed as a thin scattering layer at the origin ($z = 0$).

Another situation of practical interest was treated by Sternheimer (1954) and has been used by Harder and Abou-Mandour (1976) and Abou-Mandour and Harder (1978b) to obtain the dose distribution behind scattering foils or inhomogeneities of cylindrical shape. They divided the distance z into two parts, t and l, where the first part has a constant scattering power T and the second part has a negligible scattering power (because this part of the inhomogeneity was assumed to consist of air). The increase in mean square radius behind these layers can again be obtained from the integral in Eq. 2.37; it becomes simply $(l^2 + lt + t^2/3)\,Tt$, where the last term agrees with the simple expression above. In Section 3.2.4 the transport integrals (Eqs. 2.34, 2.37, and 2.39) are used to determine the effective irradiation geometry of therapeutic electron beams.

The projected distribution function, for example in the x,y-plane, is obtained in complete analogy with Section 2.5 for the angular distribution. This is true also for the complete distribution function Eq. 2.33, which may be expressed as the product of the projected distributions in the two orthogonal directions x and y (see Rossi, 1952; Zerby and Keller, 1967). Furthermore, the normalizing conditions of the radial distributions are analogous to those of the angular distribution.

The primary electron fluence, differential in both coordinate and direction space is of interest in many situations. This fluence can be given in a closed analytical form[3] when the small angle Gaussian approximation is used (Fermi, 1940; Eyges, 1948; Zerby and Keller, 1967; Brahme, 1975). This function can be used to describe the directional distribution at different points across an electron beam (see Section 3.2.4).

[3]
$$\Phi_{\theta_x}(x,z) = \Phi(0)\,\frac{\exp\{-(\overline{\theta^2}(z)x^2 - 2\overline{r\theta}(z)x\,\theta_x + \overline{r^2}(z)\theta_x^2)/B\}}{\pi B^{1/2}} \qquad (2.38)$$

where

$$\overline{r\theta}(z) = \overline{r\theta_i} + \overline{\theta_i^2} z + \int_0^z (z-u)T(u)\,\mathrm{d}u \qquad (2.39)$$

and

$$B = \overline{\theta^2}(z)\overline{r^2}(z) - (\overline{r\theta}(z))^2 \qquad (2.40)$$

The new transport integral in Eq. 2.39, the covariance of the simultaneous lateral and angular distribution, is proportional to the correlation coefficient between x and θ_x, and it is further discussed and used extensively in Section 3.2.4. It should be noted that Eq. 2.38 is the differential fluence in the x, z plane with $y \equiv 0$; $\theta_y \equiv 0$. When the total distribution in $x, y, z, \theta_x, \theta_y$ is needed, a second exponential analogous to the one in Eq. 2.38, but as a function of y and θ_y has to be multiplied by the right hand side of Eq. 2.38.

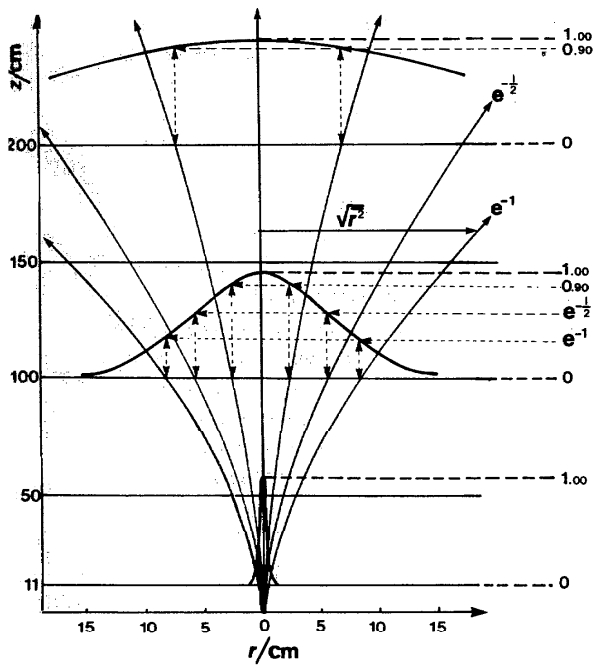

Fig. 2.11. The lateral electron fluence distribution of a 6 MeV initially nearly monodirectional and monoenergetic electron beam in air after 11–200 cm of travel (adapted from Brahme, 1971).

$$\Phi^{p}(x,y,z) = \frac{N(z)}{16ab}\left\{\mathrm{erf}\left(\frac{x+a}{r_{rms}}\right) - \mathrm{erf}\left(\frac{x-a}{r_{rms}}\right)\right\} \cdot \left\{\mathrm{erf}\left(\frac{y+b}{r_{rms}}\right) - \mathrm{erf}\left(\frac{y-b}{r_{rms}}\right)\right\} \quad (2.41)$$

where $N(z)$ is the number of electrons passing through a plane at depth z, the symbol erf denotes the error function (NBS, 1964) and $r_{rms} = \sqrt{\overline{r^2(z)}}$ is the root mean square radial displacement of the point monodirectional beam (see Fig. 2.17 and Eq. 2.37, with $\overline{r_i^2} = \overline{r\theta_i} = \overline{\theta_i^2} = 0$) at depth z. Instead of the symbol r_{rms}, other authors have used $\sqrt{\langle r^2 \rangle}$ (Fermi, 1940b; Brahme, 1975), $2\sqrt{A_2}$ (Eyges, 1948), r_0 (Sternheimer, 1954; Abou-Mandour and Harder, 1978a, 1978b), $\sqrt{2}\sigma$ (Brahme, 1975), $2\sqrt{\kappa\tau}$ (Kawachi, 1975; Steben *et al.*, 1979; Millan *et al.*, 1979) $2\sqrt{\tau}$ (Harder, 1965b; Nüsslin, 1979), $\sqrt{2}\sigma_x$ (Perry and Holt, 1980; Hogstrom *et al.*, 1981), and σ_r (Schröder-Babo and Harder, 1982). The same situation for a beam of circular cross-section was treated by Sternheimer (1954) and resulted in an expression containing the modified Bessel function which has been evaluated numerically by Abou-Mandour and Harder (1978b).

Because of the type of the quadratic form inside the curly bracket in Eq. 2.38, the fluence differential in angle is constant on ellipses in the x, θ_x-plane of the six dimensional $\vec{r}$, $\vec{\Omega}$ phase space. This is a general situation for beams that are influenced by stochastic processes and is often the case for the electron beam from an accelerator. This fact is further used in Section 3.2.1 to describe the properties of the electron beam from an accelerator in terms of its emittance (Eq. 3.1).

Several experimental investigations have been published on the spatial electron distribution that is produced by elementary narrow or pencil beams in uniform media (Berger and Paul, 1949; Jost and Kessler, 1963; Svensson *et al.*, 1968; Brahme, 1971; Lillicrap *et al.*, 1975; Osman, 1976; Yamazaki *et al.*, 1977). The agreement with the simple Gaussian theory is generally quite good (see Figs. 2.10 and 2.11), particularly over the first half of the electron range.

2.6.3 Rectangular and Circular Incident Beams

The spatial distribution for broad uniform beams can be obtained from an elementary Gaussian beam of zero initial width ($\overline{r_i^2} = 0$) by integration. The spatial distribution of a rectangular beam of initial width $2a \times 2b$ thus becomes:

2.7 Depth Distribution

2.7.1 General

During the slowing down of high-energy electrons in matter, secondary electrons are continuously generated and absorbed and, in addition, the primary electrons undergo multiple scattering and are lost at an increasing rate at depths beyond the diffusion depth due to range straggling (Section 2.5.2). These fundamental processes have a large influence on the variation of the electron fluence and the planar fluence with depth inside an absorber and, consequently, also on the distribution of absorbed dose. Due to the fundamental relation between electron fluence and absorbed dose (Eq. 2.20), a knowledge of the electron fluence distribution in electron beams is of interest.

2.7.2 Fluence and Planar Fluence

When the depth dependence of the differential electron fluence is known, the variation of the fluence and the planar fluence is obtained from Eqs. 2.13 and 2.16, respectively. Due to the cosine term in Eq. 2.16, the fluence will always be larger than the planar fluence.

The depth dependence of the fluence and the planar fluence calculated by the Monte Carlo method for broad, parallel and monoenergetic 20 MeV electron beams in water (Andreo, 1980), are given in Figs. 2.12

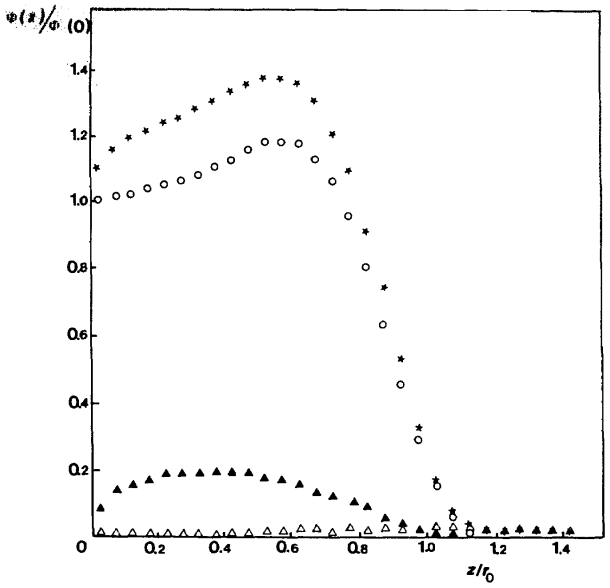

Fig. 2.12. The depth dependence of the fluence, computed for a broad 20-MeV beam, as a function of depth in water. The total fluence (stars) is the sum of the primary fluence (open circles), the secondary fluence (solid triangles) and the fluence due to the photon transport (open triangles) (Andreo, 1980). The fluence is normalized to the primary electron fluence at the entrance surface.

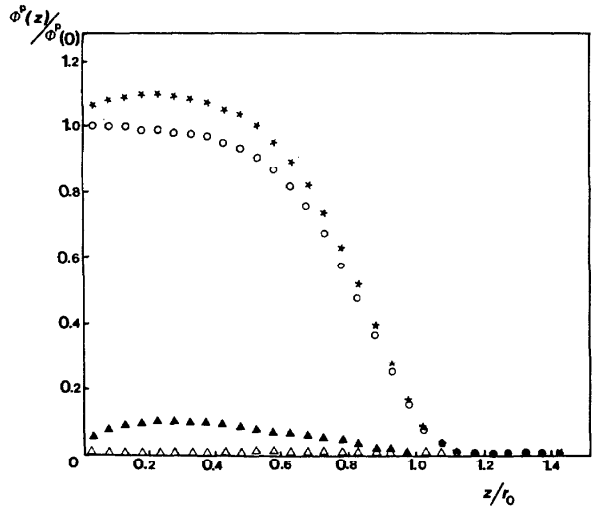

Fig. 2.13. The depth dependence of the planar fluence in the direction of the beam, for the same case as in Fig. 2.12 (Andreo, 1980).

and 2.13. Similar curves were obtained by the moments method (Kessaris, 1966). The total fluence has been divided into three parts, namely, that due to the primary electrons alone, that due to secondary electrons and higher order δ-rays set in motion by the primaries, and that due to photon-generated electrons.

It is seen from Fig. 2.13 that the planar fluence of primary electrons remains almost constant over the first half of the electron range and that the planar fluence of the secondary electrons, after a rapid build-up, reaches a constant value of approximately 10% of the primary planar fluence. Very few primary electrons are thus lost from the beam in the first half of the electron range in low atomic number materials like water. The fluence of primary electrons, on the other hand (Fig. 2.12), increases with depth and reaches a maximum before the increasing loss of electrons brings about a sharp reduction. This increase in primary fluence with depth is due to the increased obliquity of the electron tracks with depth (Harder *et al.*, 1961). Such an increase does not appear in the planar fluence due to the cosine factor in Eq. 2.16. The increase in fluence of primary electrons in a uniform medium becomes, in the first approximation (Brahme, 1975),

$$\frac{\Phi_z}{\Phi_0} = \frac{(\overline{\cos\theta})_0}{(\overline{\cos\theta})_z} \approx 1 + \frac{\overline{\theta^2}(z)}{2} \ldots \approx 1 + z\, T_0/2 + \ldots \tag{2.42}$$

In the first approximation, the fluence and the absorbed dose will thus increase at a rate equal to half the initial linear scattering power (Eq. 2.7) of the medium, in good agreement with the general shape of the depth-dose curves (see Figs. 2.21 and 2.22), and the fluence curve in Fig. 2.12. In Eq. 2.42, $\overline{\theta^2}(z)$ could be taken from Eq. 2.11 and a correction for the energy loss is directly obtained, showing that the real fluence increases are even steeper than linear. Owing to the small variation of the collision stopping power with energy in low atomic number materials, the shape of the absorbed-dose distribution will be very similar to that of the fluence distribution (Eq. 2.20 and Figs. 2.12 and 2.21).

The contribution from secondary electrons is almost a factor of two higher for the fluence than for the planar fluence according to Figs. 2.12 and 2.13. This effect is caused by the angular spread of the electrons which is broader for the secondaries than for the primaries. The high probability for low energy secondary electron production at right angles to the direction of the primary electrons (Møller, 1932) and the increase of scattering power with decreasing energy (Eqs. 2.8 and 2.12), are the reasons for this effect.

2.7.3 Particle and Charge Transport

When a parallel electron beam impinges on a thin slab of matter, a certain fraction of the incident planar fluence, η_B, will be backscattered from the surface and another fraction, η_T, will be transmitted through the

slab. The remaining fraction of the incoming planar fluence, η_A, is absorbed in the material. From the conservation of the total number of electrons, the three coefficients must be related by:

$$\eta_A + \eta_B + \eta_T = 1 \tag{2.43}$$

and, consequently, one of the coefficients can always be determined from a knowledge of the two others. This relation holds both for the primary electrons alone and for all the electrons (primaries, secondaries, etc., Ebert *et al.*, 1969). In the latter case, η_T may be larger than unity, but then η_A is negative due to the production of secondary electrons. The quantities η_A, η_B, and η_T are primarily defined for plane-parallel beams or point monodirectional beams (see Section 2.8.6), but they may be generalized to other types of beams.

2.7.3.1 **Transmission.** Early electron transmission measurements were reviewed by Katz and Penfold (1952). Later, measurements in a number of different elements were made by Seliger (1955) and Agu *et al.* (1958) at low energies and by Harder and Poschet (1967) and Ebert *et al.* (1969) at high energies. The general shape of the transmission of *primary electrons* as a function of depth is accurately described by a relation of the type:

$$\eta_T(z) = \exp\left\{-a\left(\frac{z}{R_{ex}}\right)^b\right\} \tag{2.44}$$

where b is a dimensionless constant[4] depending on material and energy of the absorber (Ebert *et al.*, 1969), R_{ex} the extrapolated range of the electron transmission curve and $a = (1 - 1/b)^{1-b}$ expresses the condition that the point where the tangent at the inflection point of the transmission curve crosses the abscissa coincides with R_{ex}. The extrapolated range of the transmission curve, R_{ex}, can be approximated for many practical purposes by the practical range of the depth versus absorbed dose or depth-ionization curves (Section 3.3.2.3).

The lower the atomic number, the steeper the decrease in number of transmitted electrons with depth, and the higher the value of b. Experimentally determined transmission curves from measurement in graphite by Harder (1965b) are shown in Fig. 2.14. The experimentally determined planar fluence of all electrons at a given depth was obtained with a Faraday cup and is compared with the planar fluence of the primary electrons measured with a scintillation spectrometer.

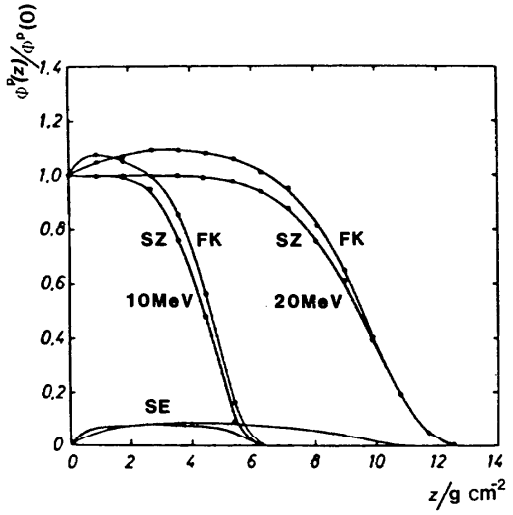

Fig. 2.14. Experimental determination of planar fluence of the secondary electrons (SE) at thickness z, from the difference between the signals from a scintillation counter (SZ) and a Faraday collector (FK). The absorber material is carbon of density 1.8 g cm^{-3} (Harder, 1965).

The scintillation counter indicates only one pulse for each primary and its associated secondary electron, but the Faraday collector indicates the sum of the electrical charges. The experimental data given here were obtained with a perpendicularly incident narrow beam of $N(0)$ electrons and the number of electrons crossing a plane at depth z was $N(z)$: The ratio $N(z)/N(0)$ is numerically equal to the plotted ratio, $\Phi^P(z)/\Phi^P(0)$, for a uniform broad beam perpendicularly incident on the surface (see Eqs. 2.17b and 2.46). Analytical expressions for the depth dependence of the primary and secondary electron fluences and planar fluences are also given by Spencer (1955), Kessaris (1966), and Tabata and Ito (1974, 1975).

2.7.3.2 **Backscattering.** Many experimental determinations of the backscattering coefficient have been reported (Wright and Trump, 1962; Cohen and Koral, 1965; Harder and Ferbert, 1964; Tabata, 1967; Harder and Metzger, 1968; Ebert *et al.*, 1969). The backscatter coefficient increases almost linearly with absorber thickness for thin absorbers and reaches a saturation value at about one third to one half of the electron range. The energy dependence of the saturated backscattering coefficient is depicted in Fig. 2.15. An almost constant value is obtained for a low or moderately high atomic number in the low energy region from 10 keV to 0.5 MeV, whereas a very marked decrease with energy is observed above this range. This energy dependence can be interpreted in terms of a competition between stopping and scattering effects. The decrease in the relativistic region is thus due to the approximate energy

[4] The constant b is a measure of the slope of the descending portion of the electron transmission curve. In fact, a normalized gradient of the transmission curve, G_T, may be defined in analogy with dose gradient, G, defined in Section 6.4.3 for the depth versus absorbed-dose curve. The transmission gradient is related to b according to the relation: $G_T = b/\exp(1 - 1/b)$.

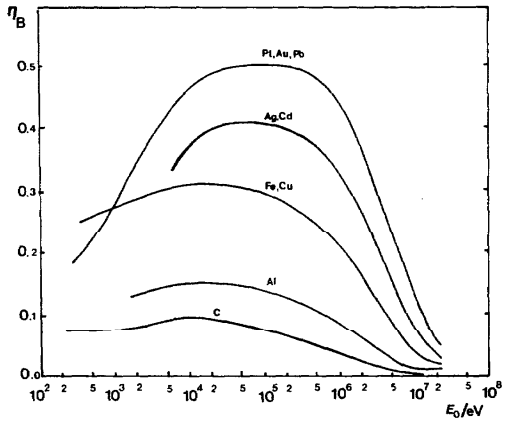

Fig. 2.15. Backscatter coefficients for monoenergetic electrons perpendicularly incident on a semi-infinite medium. Redrawn from a compilation by Harder (1970a) and added data from Ebert *et al.* (1969).

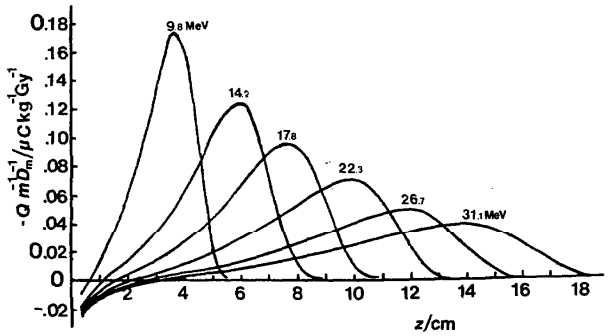

Fig. 2.16. Normalized charge deposition distributions measured with a charge collecting detector in water (Van Dyk and MacDonald, 1972). These distributions were obtained using a therapeutic betatron beam with a 9.7-cm diameter field and a source-to-surface distance of 110 cm.

independence of the stopping power, whereas in the plateau region, the scattering and stopping powers depend in a similar way on the energy. In the relativistic energy region, the saturated backscattering coefficient is approximately given by (Harder and Poschet, 1967):

$$\eta_B \approx 0.022\,(Z/\tau)^{1.3} \qquad (2.45)$$

A more accurate but less simple relation was given by Tabata (1967).

The high backscattering coefficient in the low energy region is significant in dosimetry, in particular, when the composition of the dosimeter and the medium are different. Differences in slowing-down spectra and backscattering properties between two materials can perturb the electron fluence and absorbed dose distribution at interface regions (Dutreix and Bernard, 1966; Ehrlich, 1971; Bertilsson, 1975, also see Section 4.3.1).

2.7.3.3 Charge Deposition. During the gradual slowing down of a high-energy electron beam, electrons come to rest and deposit their charge in the medium. Also, the secondary electrons, either generated by the incident electrons or by bremsstrahlung photons, take part in this process and contribute to the charge deposition. When the absorbing medium is an electrical conductor and the backscattering coefficient is negligible, it is possible to measure the locally deposited charge by simply insulating a small volume of the absorber and connecting it to an electrometer. This method has been used by several workers to measure the depth dependence of the charge deposition in high-energy electron beams (Laughlin, 1965; Gross and Wright, 1959; Tabata *et al.*, 1971a; Van Dyk and MacDonald, 1972; and Kato *et al.*, 1977).

The results of Van Dyk and MacDonald (1972) for clinical betatron beams in the energy range 10–30 MeV are shown in Fig. 2.16. The curves are normalized to allow calculation of the charge ($-Q$) collected in a region of interest of a given mass (m) and for a given absorbed dose at dose maximum (D_m). They may thus be used to estimate the charge deposition on the collecting electrode of an ionization chamber by multiplication by its effective mass (including that portion of the insulator mass which will be discharged through the collecting electrode).

From the shape of these curves, it is observed that charge deposition is of positive sign in the surface layer due to the net transport of energetic secondary electrons out of the surface region. The maximum of the charge deposition curve occurs on the steep fall-off section of the electron fluence curve where most primary electrons come to rest. The width of the charge deposition peak observed experimentally is somewhat broader than would be expected from theoretical calculations (Kessaris, 1966; Berger and Seltzer, 1969a). This is primarily due to the wider energy spectrum of the experimental beams which results in an increased range straggling in the absorber (Van Dyk and MacDonald, 1972).

The charge deposition distribution (Fig. 2.16) can be obtained from measurements of the charge transport across a plane interface (Fig. 2.14), simply by multiplying the gradient of the planar fluence with the electron charge.

2.8 Absorbed-Dose Distribution

2.8.1 General

This section is mainly concerned with absorbed-dose distributions obtained by numerical methods in uniform

materials and basic geometries of interest for the situations encountered in electron dosimetry. The few experimental dose distributions shown pertain to geometries of principally theoretical interest (e.g., point isotropic and plane parallel beams) and are, therefore, not typical for the dose distributions found in clinical electron beams (see Sections 6 and 7). When the distribution of absorbed dose in a medium irradiated by an electron beam is to be calculated, it is generally necessary to know the spatial variation of the electron fluence differential both in energy and angle, as seen from Eq. 2.20. Therefore, many of the elementary relations in the preceding sections are needed to give a detailed description of the distribution of absorbed dose. Some of these relations are incorporated in more general treatments like the moments method (Spencer, 1955; 1959; Adawi, 1957; Kessaris, 1966), the Monte Carlo method (Leiss *et al.*, 1957; Berger, 1963; Harder, 1965c; Berger and Seltzer, 1969b, 1978; Patau, 1972; Schulz and Harder, 1969; Nahum, 1976; Andreo, 1980), the phase-space-time evolution method (Cordaro and Zucker, 1971) and the discrete ordinates method (Bartine *et al.*, 1972; Prillinger, 1977).

2.8.2 Point Monodirectional Beam

The most elementary type of electron beam is the pencil beam or, more specifically, the monodirectional beam from a point source (Fig. 2.17a). This type of beam is of general interest for two reasons. It is the limiting case of a therapy beam when the field size is reduced to zero, and it can be used to derive dose distributions in more complex beams by direct summation of the elementary pencil beam distributions. This method is of special interest in dose-planning in the presence of tissue inhomogeneities (see Section 7.4).

In Fig. 2.18, the absorbed dose or energy deposition in water from a point monodirectional electron beam with an initial energy of 20 MeV is shown as calculated by Berger and Seltzer (1978) using the Monte Carlo method. The histogram in the upper right hand corner shows the total energy deposition per unit depth interval and, thus gives, approximately, the absorbed dose distribution in a broad beam. The histograms for the radial distributions show clearly how the initially narrow beam is broadened by multiple scattering interactions in the water medium. In these histograms, the area of each bin represents the fraction of the energy deposition per depth interval in the indicated ring around

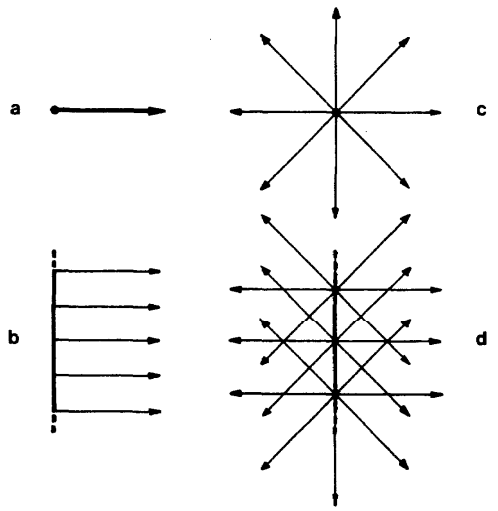

Fig. 2.17. The four principal types of ation source and beam geometries used in the calculation of ele n absorbed-dose distributions. (a) Point-monodirectional beam (point source, monodirectional emission), (b) Plane-parallel beam (plane source, parallel emission), (c) Point-isotropic source (point source, isotropic emission), (d) Plane-isotropic source (plane source, isotropic emission).

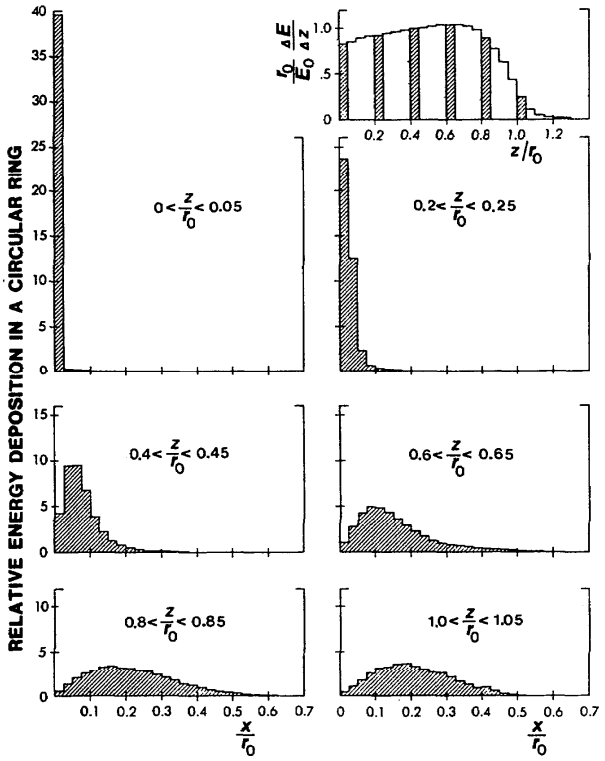

Fig. 2.18. Energy deposition in water from a point-monodirectional electron beam with energy E_0 = 20 MeV. All distances are expressed as fractions of the electron range r_0 = 9.21 g cm^{-2} in H_2O. The histogram in the upper right hand corner shows energy deposition per electron and unit depth. The other histograms show, for the six indicated (shaded) depth intervals, the radial distribution of deposited energy, as function of the scaled distance, x/r_0, from the beam axis. In these histograms, the area of each bin represents the fraction of the energy deposited in the indicated ring around the beam axis. Each histogram is normalized to unit area (Berger and Seltzer, 1978).

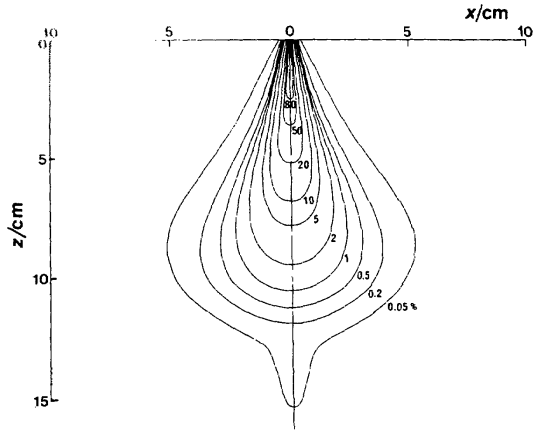

Fig. 2.19. The isodose contours measured on a nearly point-monodirectional and monoenergetic 22 MeV electron beam in water. The diameter of the incident beam was less than 5 mm, the initial angular spread of the electrons less than 3 degrees and the energy spread less than 50 keV (FWHM). The 100% value is at a depth of 2 cm on the beam axis (Brahme *et al.*, 1980).

the beam axis. The absorbed dose is obtained by dividing the energy deposition by the mass of each ring. This operation converts the shape of the radial histograms to a form which shows a steady increase towards the axis. This is also seen in the experimental isodose distribution of an almost point monodirectional electron beam in water (Fig. 2.19), as recorded by a small semiconductor diode (Brahme and Svensson, 1979). Most pronounced is the very steep dose fall-off on the central axis due to the rapid lateral scattering of electrons from the initial beam axis. This effect is masked in the upper right hand corner of Fig. 2.18, because in this histogram an integration was made over all radii so that the depth-dose curve of a plane parallel beam is obtained (see Section 2.8.6). In Fig. 2.19, the contribution of bremsstrahlung photons generated in the first few centimetres of depth shows up as the bump in the 0.05% isodose curve.

The primary electron fluence as given by Eqs. 2.33 and 2.36 will, in the limit, when $\overline{r_1^2}$ and $\overline{\theta_1^2}$ decrease to zero, approach that of a point monodirectional beam. Eq. 2.33 may, therefore, be used in Eq. 2.20 to calculate the absorbed dose due to primary electrons when continuous slowing down is assumed (Brahme, 1975). Because the mass stopping power for water varies slowly with energy for electron energies greater than 1 MeV, the shape of the electron fluence distribution and the absorbed dose distribution will be very similar as seen by comparing Figs. 2.12 and 2.21.

2.8.3 Plane-Parallel Beam

The plane-parallel beam is obtained when parallel point monodirectional beams are uniformly distributed over a plane surface (Fig. 2.17b). This is the most common geometry used for calculating absorbed dose distributions in uniform materials and it is also often used for comparison with measured dose distributions. The dose distribution of a plane parallel beam can be obtained either by integrating the contributions to the absorbed dose at a given point over a continuum of pencil beams, or by integrating the absorbed dose distribution of a single pencil beam at a given depth over all radii, as illustrated in Fig. 2.18. This has important consequences from an experimental point of view, because broad-beam dose distributions can be measured in a pencil beam by a broad detector or in a broad beam by a small detector (the reciprocity law, see Section 2.8.6). The first method was used by Harder and Schulz (1972) to obtain broad-beam dose-distributions and the results are compared with the Monte Carlo calculations of Berger and Seltzer (1978) in Fig. 2.20. Good agreement is obtained over the major part of the depth-dose curve. However, a more detailed analysis shows that the dose fall-off is steeper and the dose maximum is located somewhat deeper in the calculated distribution. Similar differences are obtained also at other energies, possibly due to the kind of treatment of multiple scattering in the Monte Carlo program (Abou-Mandour, 1978).

In Fig. 2.21, a more complete set of Monte Carlo generated, normalized depth-dose curves for plane-parallel electron beams in water are shown (Seltzer *et al*, 1978). It is clearly seen that the steepness of the build-up region and the total dose build-up are reduced with increasing beam energy. This should be expected

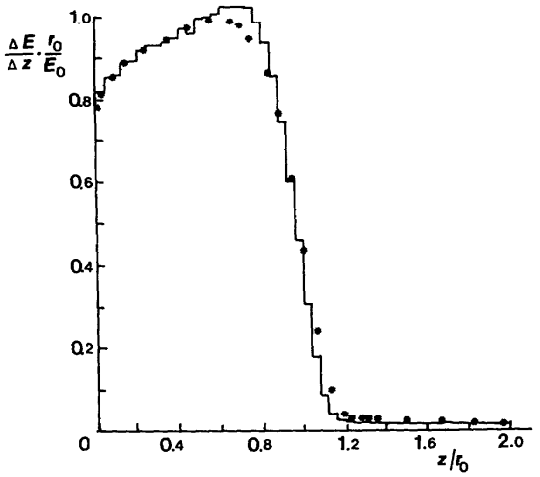

Fig. 2.20. Comparison of the calculated (Berger and Seltzer, 1978) depth distribution of energy deposition per electron in a 20 MeV uniform, plane-parallel beam (histogram) with experimental results of Harder and Schulz (1972). Here, $\Delta E/\Delta z$ is the energy imparted per electron and unit depth at depth z, and r_0 is the csda range of the electrons of incident energy E_0.

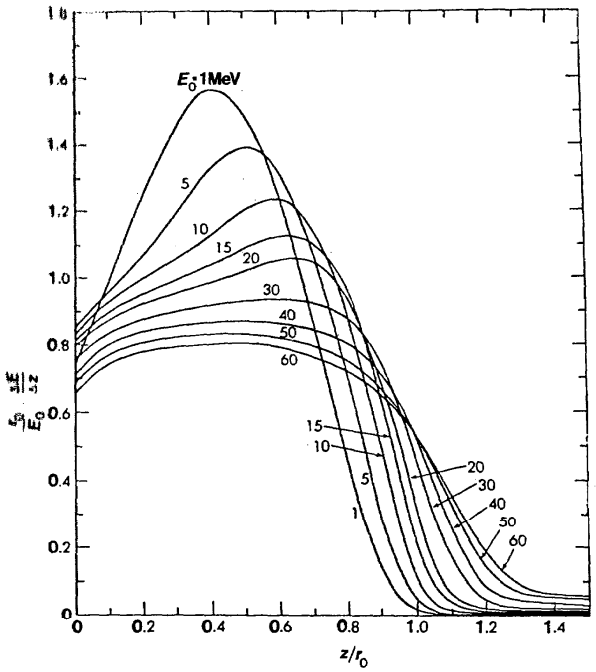

Fig. 2.21. Calculated distributions of energy deposition per electron with depth, z, in a water phantom for perpendicularly incident pencil beams of energy, E_0, of 1 to 60 MeV. Here $\Delta E/\Delta z$ is the energy imparted per electron and unit depth, and r_0 is the csda range (Seltzer *et al.*, 1978). (The values of the scaling factor, $\bar{Z}/\tau$, are, in order of increasing electron energy: 4.03, 0.81, 0.40, 0.27, 0.20, 0.13, 0.10, 0.081, and 0.067, respectively.)

because the mass scattering power is rapidly reduced with increasing energy (see Eq. 2.42, Table 2.6, and Section 6.4). This last fact is also one of the reasons for the increased penetration relative to the continuous-slowing-down range, r_0 because, with increasing energy, the electrons are less and less influenced by multiple scattering deflections. However, the increased range straggling due to bremsstrahlung production is also involved and explains a large part of the loss in dose fall-off gradient at high energies (Brahme and Svensson, 1976).

When energy deposition per electron and unit depth interval, $\Delta E/\Delta z$, in a given material divided by the quotient of the energy of the incident electron and the csda range in that material is plotted against the depth in the material expressed as a fraction of the csda range, the resulting shape is essentially determined by the value of $\bar{Z}/\tau$. Here $\bar{Z}$ is the mean atomic number and τ is the ratio of the kinetic energy of the incident electrons and the rest mass energy of the electron. Alternatively, the total stopping power, S_{tot} (E_0), in the material, for the incident electrons of energy E_0 may be substituted for the quotient of the energy of the incident electron and the csda range. The ordinate value for this alternative plot will be different from the other, but the same $\bar{Z}/\tau$ scaling relationship exists for such curves.

The general change in shape of the depth-dose curves from low to high energies seen in Fig. 2.21 is combined in Fig. 2.22a with the change due to the variation produced by varying the absorber material. In Fig. 2.22b, experimental values of $r_0/\rho R_p$ and other shape parameters are plotted as a function of the scaling parameter, $\bar{Z}/\tau$, for a number of different materials and energies. Good agreement between different materials and energies is generally obtained when the value of the scaling parameter is the same. The $r_0/\rho R_p$ curve may be used to estimate the practical range for different materials and energies by taking the continuous-slowing-down range from Table 2.5.

This scaling law (Harder, 1970a) works well at high initial energies relative to the rest energy of the electrons ($\tau \gg 1$) and for all atomic numbers (Fig. 2.22b), but with decreasing accuracy when bremsstrahlung production becomes important, even though bremsstrahlung is included in the first approximation.

In material mixtures and compounds, the mean atomic number,

$$\bar{Z} = \sum_i \left(p_i \frac{Z_i^2}{M_{A_i}} \right) \Big/ \sum_i p_i \frac{Z_i}{M_{A_i}} ,$$

is used instead of Z when calculating the scaling parameter, where p_i is the mass fraction, Z_i the atomic number, and M_{A_i} the molar mass of element i. The curves in Figs. 2.21 and 2.22 may, therefore, as a first approximation, be used for interpolation, to obtain the depth-dose curves in materials other than water, by applying the correct value of the scaling parameter. For example, the scaled depth-dose curve in bone at 15 MeV is similar to that of the depth-dose curve in water at about 10 MeV because $E_w = (\bar{Z}_w/\bar{Z}_b)$. $E_b \approx (7/10)$ 15 MeV $\approx$ 10 MeV.

2.8.4 Point Isotropic Source

The point isotropic source geometry (Fig. 2.17c) or, more exactly, a collimated point isotropic source, is probably the configuration which is most similar to the beam geometry used in radiation therapy (cf. Section 3.2.4) even though the effective radiation source (positioned near the scattering foil) is extended and the electron fluence is far from isotropic. Yet, very few calculations have been performed in this geometry, except for the work of Berger and Seltzer (1978). The dose distribution in a point isotropic beam can be obtained with a fairly high accuracy from that for the plane-parallel beam by a simple inverse-square correction for the divergence of the beam (see Section 6.4.3.3).

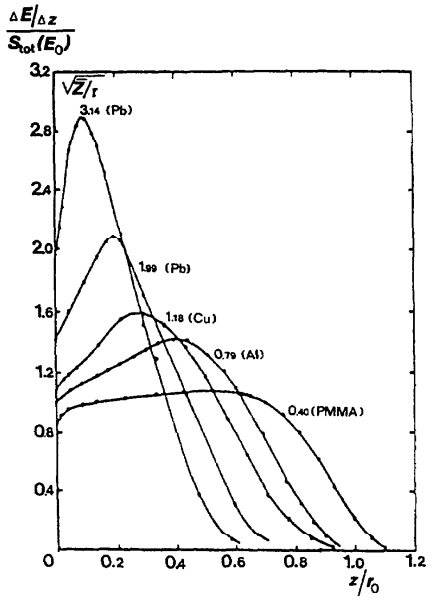

Fig. 2.22a. Energy deposition (normalized) as a function of remaining fractional csda range with $\sqrt{\bar{Z}/\tau}$ as a parameter. The material is indicated after each value of $\sqrt{\bar{Z}/\tau}$. The initial energy, $\bar{E}_0$, from the upper most curve to the lowest is 4.27, 10.62, 10.62, 10.62 and 21.13 MeV. Data for these curves are from Freyberger, 1964.

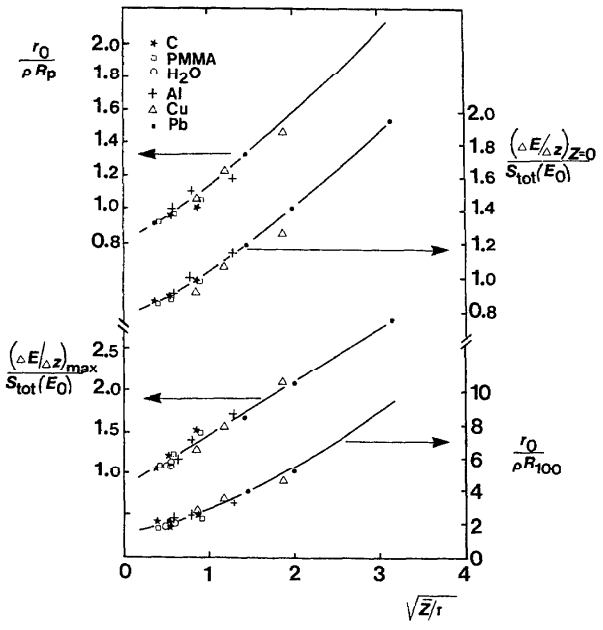

Fig. 2.22b. The $\bar{Z}/\tau$ dependence of the shape parameters of energy deposition versus depth curves for high initial energies (Harder, 1970a).

2.8.5 Plane Isotropic Source

At depth, the low energy part of the electron spectrum is often scattered over large angles due to the large scattering power at low energies. This means that at least this part of the electron spectrum can be described as a diffuse and nearly plane isotropic beam (Fig. 2.17d). A more detailed analysis shows that the equilibrium angular distribution is more like a cosine square distribution (Bethe *et al.*, 1938) with fewer electrons at large angles. In Fig. 2.23, the calculated depth-dose distribution in plane-isotropic and cosine-distributed electron beams are shown. The results are both from the Monte Carlo method (Berger, 1969) and the discrete ordinate method (Prillinger, 1977) which give results in very good agreement. The nearly linear spatial rate of dose decrease in the cosine distributed beam is typical for beams of large angular spread and explains the low

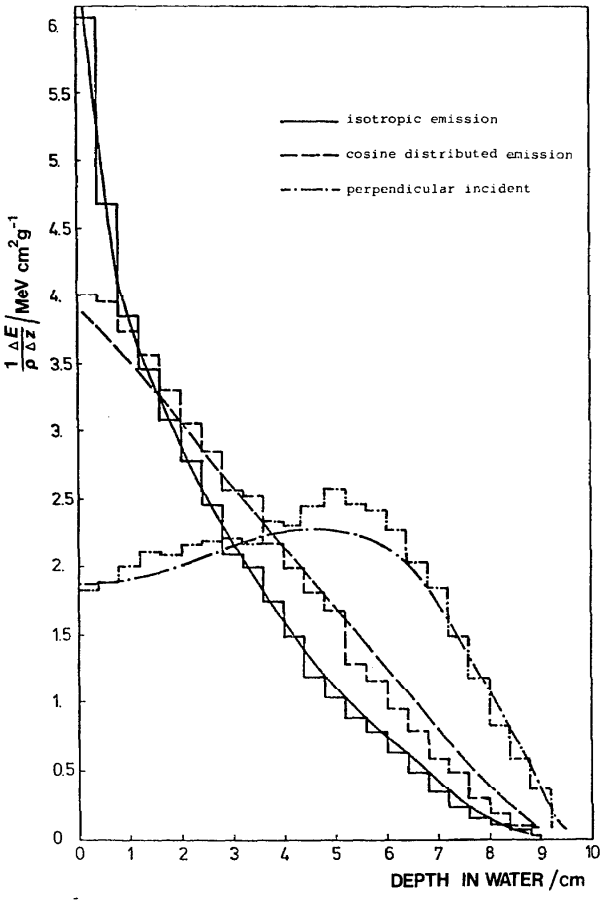

Fig. 2.23. Calculated depth-dose curves in water at 18 MeV for different angular distributions in plane beams. The smooth curves were obtained by the discrete ordinate method (Prillinger, 1977) and the histograms by the Monte Carlo method (Berger, 1969). The ordinate is the energy imparted ΔE in a layer of thickness $\rho\Delta z$.

dose build-up found in beams with a high contamination of low-energy electrons. The dose distributions with a cosine-distributed-emission source can be seen as the limiting case for a beam of Gaussian angular spread (compare Section 3.2.4.3 and Fig. 3.9).

2.8.6 Reciprocity

A simple mathematical relationship exists between point-monodirectional and plane-parallel beams (reciprocity relationship, Sternheimer, 1954). This relationship has been used to obtain the properties of plane-parallel beams from experiments or calculations on point monodirectional beams (Leiss *et al.*, 1957; Harder, 1965c; Kessaris, 1966; Berger, 1969; Andreo, 1980).

The absorbed dose at a depth z and radial distance r from the beam axis for an incident point monodirectional beam of N_{pm} particles impinging normally on a semi-infinite absorber, is denoted by $D_{pm}(z,r)$. The absorbed dose, $D_{pp}(z,0)$ at a depth z on the axis of a plane-parallel beam of radius R and fluence Φ_{pp} of identical particles incident normally on the same absorber is then given by the relationship:

$$\frac{D_{pp}(z,0)}{\Phi_{pp}} = \frac{\int_0^R D_{pm}(z,r)2\pi r dr}{N_{pm}} \qquad (2.46)$$

Perhaps the most important implication of this relationship for experimental electron dosimetry is that the depth-dose distribution in an infinitely broad plane-parallel incident beam can be determined by measurements with a point monodirectional beam and a laterally extended detector (crossection $2R \geqslant 2z_1$, where z_1 is the maximum lateral excursion of electrons—see Fig. 6.9 for values).

The reciprocity relationship can be generalized to describe the relationship between other transport characteristics such as the scalar, vectorial or planar fluence, produced by point and plane sources with arbitrary angular distributions.

2.9 Secondary Particle Production

2.9.1 General

Except for the case of propagation in a vacuum, all high-energy electron beams are accompanied by secondary particles. The production of secondary electrons in electron–electron collisions has already been discussed in detail in Sections 2.2.3 and 2.7.2.

Here, the generation of bremsstrahlung photons and the accompanying productions of positrons, neutrons, photons, etc. and also of new nuclides will be treated. These latter particles are predominantly produced in two-step processes via bremsstrahlung photons and pair production or photonuclear reactions, but also directly in electronuclear reactions.

In particular, the bremsstrahlung photons are of dosimetric importance not only as a contamination of the tail of the dose distribution, but also because their presence influences the choice of the true mean stopping-power ratio in a contaminated or mixed beam. A photon absorbed-dose contamination of 5% will, for example, increase the mean stopping power ratio in a high-energy electron beam by almost 1% in low atomic number materials, approximately independently of electron energy at the phantom surface. It should be noted that the electrons produced by the absorption of bremsstrahlung generated in the phantom are a part of the electron spectra and are normally included in tabulated stopping-power ratios.

2.9.2 Bremsstrahlung

The mean spatial rate of the energy loss of an electron beam due to the production of bremsstrahlung photons is given by the radiative stopping power as discussed in Section 2.2.4. In many practical applications, this information is insufficient as the angular distribution of the emitted bremsstrahlung quanta is also of importance.

The basic differential cross sections for bremsstrahlung production were reviewed by Koch and Motz (1959) and Tsai (1974). The production of bremsstrahlung in thin and thick targets, including effects of multiple scattering of the electrons in the target, has been treated by Sirlin (1956), Hisdale (1957), Berger and Seltzer (1970) and Matthews and Owens (1973).

Scattering foils constitute common sources of bremsstrahlung in electron beam therapy. The thin-target situation is most relevant because the foil thickness corresponds to only a small fraction of the electron range. (Exceptions occur when low atomic number decelerators are used for reducing the beam energy—see Section 7.5.1.)

The ratio of the angular distribution of thin target bremsstrahlung energy fluence, $\Psi(\theta)$, at an angle θ with the direction of the incident electron beam of energy, E_0, to that at zero angle was given by Schiff (1964, 1951) and is illustrated in Fig. 2.24, for three different target thicknesses. A useful, simple analytic approximation for the angular distribution of the energy fluence of photons is

$$\Psi(\theta) = \frac{\Psi(0)}{1 + \left(\frac{E_0\theta}{a}\right)^b} \qquad (2.47)$$

where a is the value of $E_0\theta$ when $\Psi(\theta)/\Psi(0)$ is 0.5 and

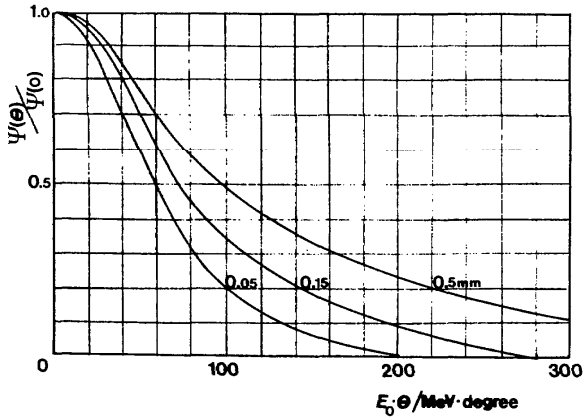

Fig. 2.24. The ratio of photon energy fluence at an angle Θ to that at $\Theta = 0$ as a function of the product of incident electron energy, E_0, and angle, Θ, of bremsstrahlung emission for tungsten foils of 0.05, 0.15, and 0.5 mm thickness, respectively (Schiff, 1946).

b is a constant (Brynjolfson and Martin, 1971; Brahme and Svensson, 1979).

The ratio of bremsstrahlung to electron dose rate in an electron beam depends on a number of factors. The photon dose rate in the forward direction increases with approximately the third power of electron energy due to the linear increase in radiative stopping power and the quadratic decrease in the effective solid angle of bremsstrahlung emission with electron energy. The production of bremsstrahlung per unit thickness of the scattering foil will, therefore, decrease rapidly and the electrons lose energy with increasing foil thickness. However, the electron fluence is simultaneously decreased due to the influence of multiple electron scattering in the foil. The resultant ratio of photon background dose to electron dose will, therefore, be approximately proportional to the foil thickness.

2.9.3 Positrons

A small fraction of the bremsstrahlung photons produced in scattering foils and other materials will be re-absorbed directly by the pair-production process and generate positrons. This process was studied theoretically by Katz and Lokan (1961) and experimentally by Tayurskii (1976). The most probable positron energy is only about ⅓ of the energy of the incident electron. A simple expression for the absolute yield of positrons was also given by Katz and Lokan (1961) and it is less than 10^{-3} positrons per electron even for high energies and relatively thick scattering foils (greater than $0.1X_0$).

2.9.4 Photonuclear Reactions

The cross section for interaction with an atomic nucleus that results in the ejection of one or more nucleons is larger for bremsstrahlung generated in the electron beam than for the electrons themselves. The cross section for such photonuclear reactions rapidly increases, and the energy at the maximum cross section decreases, with the atomic number. This so called "giant resonance" (see Fig. 2.25) is the dominating mode of photon absorption by the nucleus and it can be described as the excitation of an oscillation of the neutrons and protons of the nucleus. The theory of photonuclear reactions was reviewed by Levinger (1960), Hayward (1965) and Firk (1970). A very extensive bibliography of photonuclear reaction data are contained in NBS, 1973 and NBS 1982. More recent compilations of the energy dependence of the photonuclear reaction cross sections were published by Bülow and Forkman (1974) and Berman (1976).

Experimental data on absolute photoneutron production in different materials of interest for applications of electron beams were obtained by Barber and George (1959) and Brahme *et al.* (1980b). Theoretical calculations on the same subject have been published by Berger and Seltzer (1970), Seltzer and Berger (1973) and Swansson (1979).

The thresholds for photonuclear reactions are often very useful for energy determination on electron accelerators (Section 3.3.2.1). Photonuclear reactions may also be used to get a picture of the lateral photon distribution in an electron beam, as long as direct electron interactions are unimportant (Pohlit, 1965).

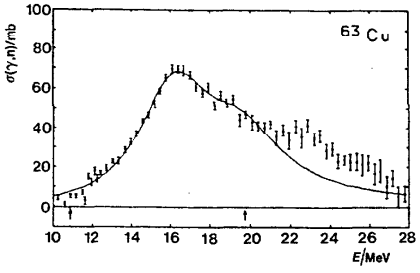

Fig. 2.25. The total photoneutron cross section for ^{63}Cu. The arrows indicate the thresholds for production of one and two photoneutrons, respectively. The curve is a two-line Lorentz profile fitted to the cross-section data (Berman, 1976).

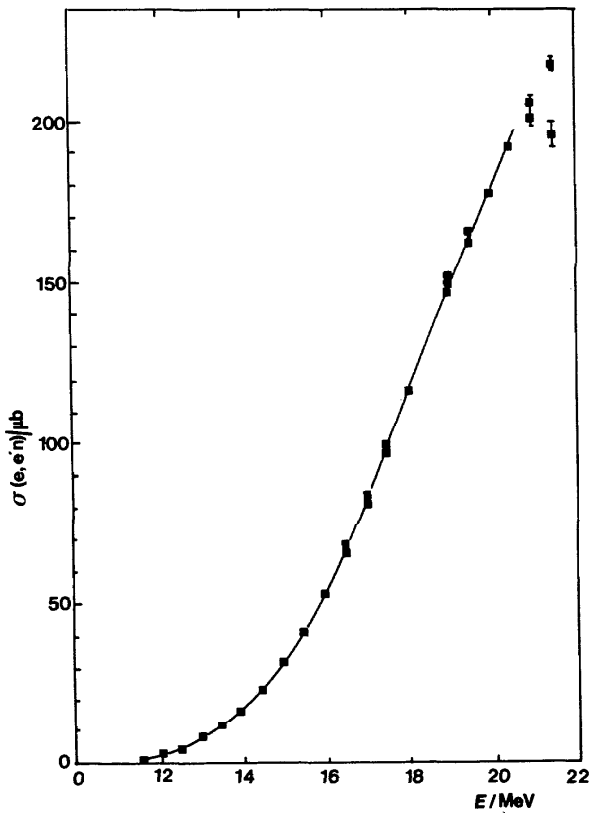

Fig. 2.26. The electroneutron cross section for ^{63}Cu. The cross section at 20 MeV is about three orders of magnitude lower than the photoneutron cross section—compare Fig. 2.25 (Scott *et al.*, 1955).

2.9.5 Electronuclear Reactions

The probability of an electron interacting directly with a nucleus is about two orders of magnitude ($\approx 1/\alpha$) smaller than the corresponding probability for a photon. In Fig. 2.26 the cross sections for electronuclear reactions in ^{63}Cu are shown. It is seen that the electronuclear cross section increases with energy whereas the photonuclear cross section has a broad peak, the giant resonance, about 6 MeV wide. This situation is important in the use of photonuclear reaction thresholds (Section 3.3.2.1) in energy determination. If a target is irradiated in an uncontaminated electron beam, the yield of electronuclear reactions increases with the first power of the target thickness, whereas that of photonuclear reactions increases with the second power due to the intermediate production of bremsstrahlung photons. The dominating reaction, therefore, depends on the target thickness. However, this has little relevance for the energy determination as the threshold energies are the same.

On the other hand, in electron beams contaminated with photons produced in windows, foils, etc., the maximum electron energy, because of energy loss in the intervening material, may well be lower than that of the photons. The energy determination using thresholds of nuclear reactions may thus give the maximum photon energy rather than the maximum electron energy (*cf.* Section 3.3.2.1).

3. Characteristics of Clinical Electron Beams

3.1 General

The properties of a clinical electron beam of relevance for its dosimetry are completely described by the differential electron fluence, $\Phi_{E,\vec{\Omega}}(\vec{r})$, as defined in Section 2.3. Such a complete description is useful as a physical basis for all practical applications including, e.g., absorbed dose measurement and computerized dose planning. For clinical use, however, a simplified description of the beam is generally more useful. This description contains the characteristics of dosimetric importance which are recommended for use when the beam is described in reports on radiotherapeutic procedures.

The shape of the absorbed-dose distribution obtained in a therapeutic electron beam normally depends more on the design parameters of the individual treatment unit than does that for a photon beam. Electrons are much more influenced by scattering and energy-loss interactions with the materials in and along the beam than are photons. However, variations in the quality of the intrinsic accelerator beam and in the design of the beam optical systems may also have a significant influence on the dose distribution (de Almeida and Almond, 1974a; Brahme *et al.*, 1975; Brahme and Svensson, 1979).

A schematic view of some of the important components of a typical electron-therapy accelerator is shown in Fig. 3.1. On its way from the vacuum chamber to the irradiated surface, the electron beam has to pass through several materials including a vacuum window, scattering foils, transmission monitors, a mirror, air and collimators. All these materials, which are used to shape and monitor the beam, will scatter the electrons and degrade their energy (Svensson, 1971) and consequently influence the position, size and energy distribution of the effective electron source.

In practice, there are two fundamentally different processes which complicate the design of broad uniform electron beams (Brahme, 1977). First, due to the high scattering power of the air and other materials in and along the beam, electron beam *collimation* is difficult at low energies. The scattering interactions tend to blur the directional and spatial distribution of the electrons which, in turn, results in a decrease in the effective source surface distance and makes it necessary to collimate the beam close to the irradiated surface. Secondly, for high energies, the combination of high radiative stopping power and low scattering power makes electron beam *flattening* with scattering foils difficult without excessive bremsstrahlung production. This combination can result in considerable energy loss, energy straggling and photon contamination, particularly when a single scattering foil is used to flatten the beam (Brahme and Svensson, 1979). The different parameters characterizing the geometry and energy distribution of clinical electron beams will be quantified and described in detail in the following sections.

3.2 Irradiation Geometry

A clinical electron beam is characterized by the spatial and angular distribution of the electron fluence. The electron fluence is determined by the properties of the initial electron beam, which depend on the emittance of the intrinsic accelerator beam and the beam optical system. In addition, the electron fluence is greatly influenced by the method of beam flattening and beam collimation because these will influence the amounts and locations of materials in and along the beam which, in turn, may contribute to the number of scattered electrons in the clinical beam.

3.2.1 Emittance and Beam Optics

In Section 2.6.2 it was pointed out that the spatial and angular distribution of electrons in the beam from an accelerator can generally be described by elliptic areas in the (x,θ_x) or (y,θ_y) planes (phase space). This is of particular importance because the emittance, ϵ, or the elliptical phase space area which encloses the beam, stays constant along the beam. More generally, it can be shown that as a consequence of the Liouville theorem (Steffen, 1965; Banford, 1966), the local phase space density is constant under the influence of macroscopic conservative fields like electromagnetic or gravitational fields (but not in the microscopic Coulomb fields in atomic collisions, which are responsible for the action of scattering foils). This implies that the emittance is a transport constant when the beam passes through beam optical components like quadrupoles or bending magnets. In Fig. 3.2, the motion of a slightly divergent beam through a quadrupole is shown both in real space (x, z plane) and in phase space (x, θ_x plane). It is observed that the phase-space ellipse is deformed in the x-direction (planes $z_2 \rightarrow z_3$ in Fig. 3.2) when the electrons are passing the field-free region and deformed in the θ_x-direction (planes $z_1 \rightarrow z_2$ in Fig. 3.2) when they are passing the quadrupole, but its area stays constant. Furthermore, at the focus or "waist" of the beam after the quadrupole, the emittance, ϵ, of the beam can be obtained simply from the major axes of the beam in coordinate space, Δx and direction space, $\Delta\theta_x$:

$$\epsilon = \Delta x \Delta\theta_x \pi \qquad (3.1)$$

Quite generally, it can be shown, using Eq. 2.38, that the condition for having a waist on a beam at a particular

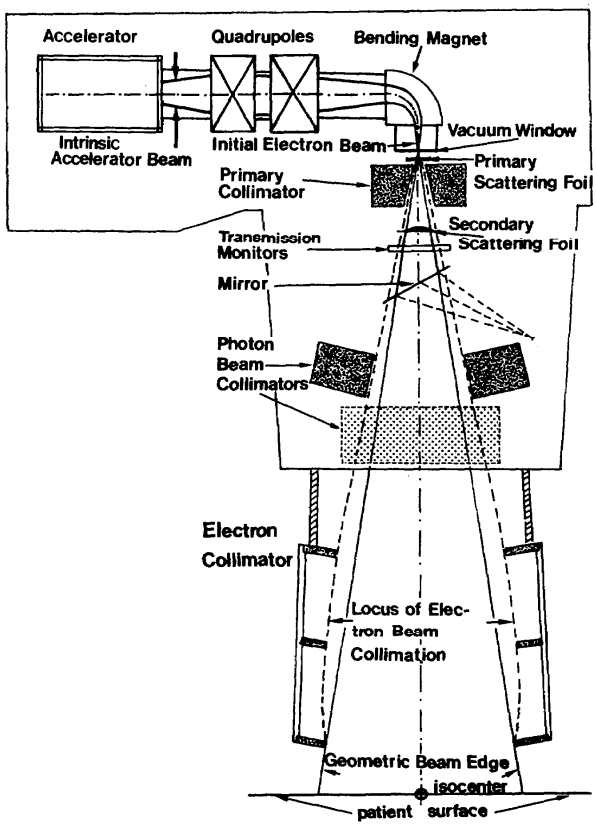

Fig. 3.1. The components of dosimetric importance in a typical electron-therapy accelerator. Also shown is the locus of closest recommended electron collimation, as discussed in Section 3.2.3.

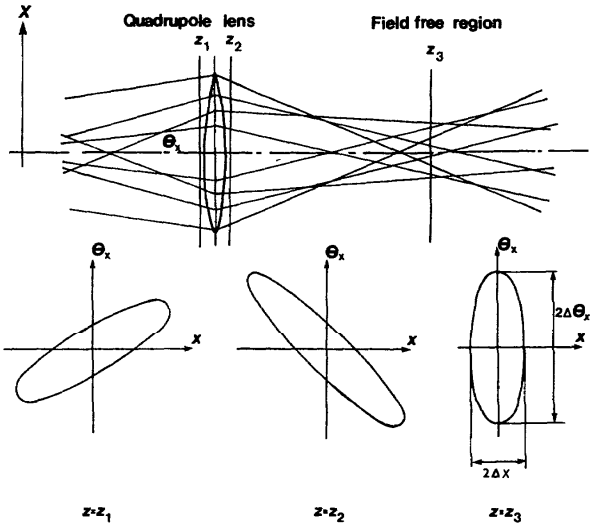

Fig. 3.2. The motion of a divergent electron beam through a quadrupole in real space (x, z) and in phase space (x, θ_x). The form of the elliptic area occupied by the beam in phase space is shown for three transverse sections through the beam in planes defined by z_1, z_2, and z_3. The ellipses in phase space indicate the possible combinations of θ_x and x values for electrons passing through each plane. For all points on such a curve, the fluence differential in angle is constant (see Section 3.2.4.1). The emittance (i.e., the ellipse area) stays constant.

location is that the covariance $\overline{r\theta}(z)$ in Eq. 2.39 is equal to zero (see Section 3.2.4). In the orthogonal plane of the beam (y,z plane), the action of the quadrupole is reversed (Banford, 1966) and the beam is instead defocused. However, the combined action of two or more quadrupoles may result in a net focusing in both planes.

When the focusing power of the quadrupole is increased in one plane to decrease the focal spot size, this can only be done at the cost of a larger divergence in the same plane, as the emittance is conserved. The emittance is, thus, a measure of the degree of deviation from point source beam optics, which would be obtained at the limit of zero emittance. The emittance of the intrinsic electron beam from a microwave-powered accelerator is normally of the order of 50π millimetre milliradians.

In accelerators where the electrons are confined by a magnetic field, as for the betatron and the microtron, the emittance can be different in the two orthogonal planes x,z and y,z. The focusing in quadrupoles and bending magnets may be different in the two planes, resulting in different angular spreads $\overline{\theta^2_{i,x}} \neq \overline{\theta^2_{i,y}}$ and radial spreads $\overline{r^2_{i,x}} \neq \overline{r^2_{i,y}}$ of the beam. It is, therefore, recommended that the shape of the initial electron beam be checked by a film near the vacuum window or by the methods of Section 3.2.4.5. When the focusing properties of a quadrupole or bending magnet are changed, the uniformity of the electron beam may be influenced, mainly due to the resulting change in angular spread of the initial electron beam.

In accelerators of the bent beam design, slightly different beam energies can be obtained at different locations in the bending plane of the beam. There are three principal types of bending magnets which have different characteristics in this respect (Fig. 3.3) and the differences will be more pronounced when the energy spread of the intrinsic accelerator beam is high. In the 90° magnets with a uniform magnetic field (Fig. 3.3a), the high and low energy electrons emerge from the magnet at different locations and at different angles. In the 270° magnets with a uniform magnetic field (Fig. 3.3b) and appropriate pole face angles, both low and high energy electrons emerge from the magnet converging to a point. In the 270° magnets with a certain magnetic field gradient (Enge, 1963), both high and low energy electrons emerge from the magnet at the same location and at the same angle (Fig. 3.3c).

The differences in the properties of the initial electron beam due to different beam optical components

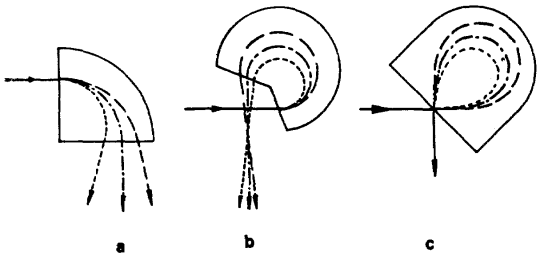

Fig. 3.3. The three principal types of bending magnets used in accelerators of the bent beam design. The nominal orbit for the most probable energy, E, is indicated by the dash-dot line, and the orbits for an energy less than E and more than E are indicated by short-dash lines and long-dash lines, respectively. (a) and (b) Uniform magnetic fields. (c) Magnetic field with a constant gradient normal to the field edge. Note that this is an achromatic magnet.

and different intrinsic accelerator energy distributions can often be reduced by slits or apertures which limit the width and energy or angular spread of the beam. Furthermore, the influence of the design and adjustment of the beam optical system and of the properties of the intrinsic accelerator beam on the characteristics of the therapeutic beam may also be reduced when scattering foils are used to flatten the beam. This effect is obtained when the scattering foils are so thick that the energy and angular distributions of the initial electron beam are substantially broadened.

3.2.2 Beam Flattening

In order to obtain high quality electron beams for radiation therapy, the initial electron beam delivered by the beam optical system must be flattened to give a broad uniform radiation field. Several methods of electron beam flattening are in use. The most common and straightforward one uses high atomic number scattering foils (Gund and Schittenhelm, 1953; Turano *et al.*, 1959; Loevinger *et al.*, 1961; Okumura *et al.*, 1969; Rassow, 1969; Brahme, 1972; Benedetti, 1973; Osman, 1976; Berger and Seltzer, 1978). Other more refined methods include magnetic defocusing of the beam by adjustable pole tips (Hsieh and Uhlmann, 1956), scanning magnets (Skaggs *et al.*, 1958), electromagnetic beam scanning quadrupoles (Aucouturier *et al.*, 1970), small-angle pendular movements of the accelerator (Rassow, 1970), defocusing beam diffusers (Shigematsu and Hayami, 1969), and depth dose flattening filters (Brahme and Svensson, 1976a). These latter methods have been developed to overcome the considerable energy loss, energy spread and photon contamination obtained when a single scattering foil is used to flatten an electron beam.

Since the 1960s, shaped scattering foils have been used on betatrons to improve the initial flattening obtained in the wall of the doughnut and the fringing field of the magnet (Cova *et al.*, 1967; Svensson, 1971; Kozlov and Shishov, 1976). The method of using two separate scattering foils can be improved considerably by selecting the appropriate thickness and radial profile of the scattering foils, particularly when the electron beam is of cylindrical symmetry (Brahme, 1972 and 1977, Sandberg, 1973; Bjärngard *et al.*, 1976; Abou-Mandour and Harder, 1978a; Brahme and Svensson, 1979). By using a secondary central scatterer (see Fig. 3.4), uniform beams can be produced with total foil thicknesses almost one order of magnitude thinner than when a single scattering foil is used. This is advantageous as the energy loss and spread (see Fig. 2.2) of the accelerator beam is decreased, with resultant improved depth-dose characteristics and a simultaneous increase in dose rate and energy uniformity (Brahme, 1972; Brahme and Svensson, 1979). In Fig. 3.4, the three principal types of electron beam scattering geometries are illustrated schematically. It is clear that only the double-foil techniques are capable of producing beams of perfect uniformity since they are not restricted to the simple Gaussian fluence distribution. Moreover, the double-foil techniques use the electron beam more effectively as fewer electrons are lost outside the useful beam, which, in turn, simplifies collimation.

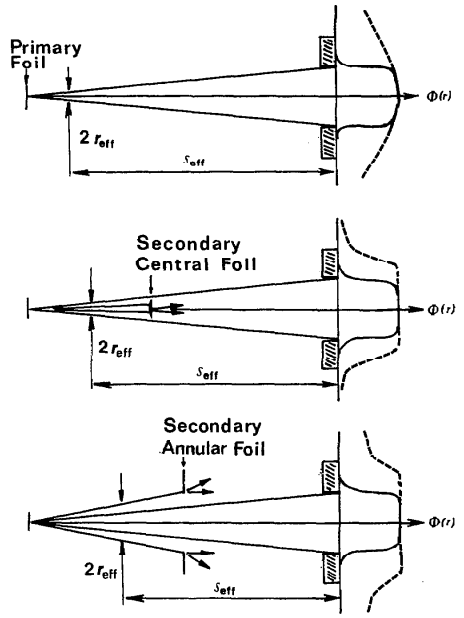

Fig. 3.4. Schematic representation of the three principal types of electron beam flattening geometries in which scattering foils are used. The approximate size and location of the effective electron source, as defined in Section 3.2.4, are also indicated (Svensson and Brahme, 1976; Brahme, 1977). The broken line indicates the distribution of the fluence in the absence of the collimator whereas the solid line shows the distribution of the fluence with the collimator.

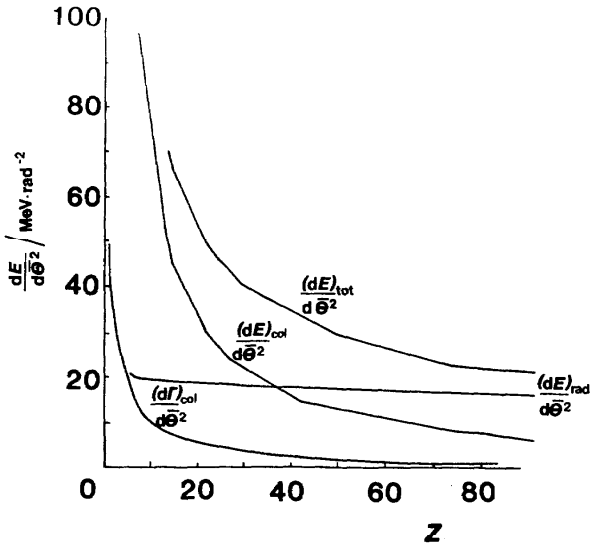

Fig. 3.5. The total energy loss $[(dE)_{tot}/d\overline{\theta^2}]$, the collision energy loss, $[(dE)_{col}/d\overline{\theta^2}]$, the radiative energy loss, $[(dE)_{rad}/d\overline{\theta^2}]$, and the energy straggling by collisions, $[(d\Gamma)_{col}/d\overline{\theta^2}]$, per unit mean square angle of scattering, as a function of the atomic number of the scattering material for 20 MeV electrons (Brahme, 1972).

The choice of material for the scattering foils and its thickness is of importance because they affect the amount of energy degradation obtained in the final therapeutic beam. Generally, the foil thickness is chosen to give a certain mean square angle of scattering of the transmitted electrons which will produce a beam of sufficient uniformity. Radiative and collision energy losses and increases in the electron energy spread also result from the use of foils. The amount of each such factor per unit mean square scattering angle is given in Fig. 3.5 as a function of the atomic number, Z, of the foil for 20 MeV electrons. Values for $dE_{col}/d\overline{\theta^2}$ and $dE_{rad}/d\overline{\theta^2}$ are the quotients of the 20 MeV values in Table 2.2 to those in Table 2.6, and those in Table 2.4 to those in Table 2.6, respectively, for each value of Z. $dE_{tot}/d\overline{\theta^2}$ is the sum of these two values for each value of Z. Determination of $d\Gamma_{col}/d\overline{\theta^2}$ is based on the theory of Landau (1944). The radiative energy loss per mean square scattering angle stays practically constant independent of the atomic number of the scattering foil, but the most probable energy loss and the energy straggling increase rapidly when low atomic number materials are used. The bremsstrahlung contamination will stay roughly constant under these conditions but the practical range and therapeutic range (see Section 6.4.3) will increase with increasing atomic number as the most probable energy loss and the energy straggling decrease (Gund and Schittenhelm, 1953; Loevinger *et al.*, 1961; Brahme and Svensson, 1979); compare also Fig. 3.14.

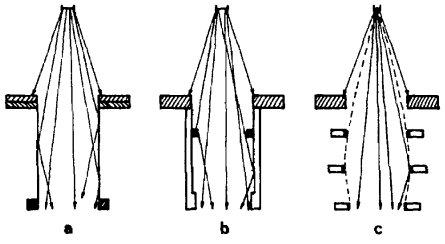

Fig. 3.6. Schematic illustration of the principal types of electron beam collimators: (a) cone or tube collimator, (b) modified tube collimator, (c) diaphragm collimator using a few discrete beam limiting plates (see Fig. 3.8) with high density material lining the collimator edge.

3.2.3 Beam Collimation

The primary function of the electron collimator is to limit the size of the flattened electron beam and thus to protect tissues outside the target volume from irradiation. Some collimator designs, particularly of the early cone or tube type, as shown in Fig. 3.6 a and b (Decken *et al.*, 1956; Wideroe, 1959; Loevinger *et al.*, 1961; Beattie *et al.*, 1962; Ward, 1964; Bradshaw and Maysent, 1964; Dahler, 1965), also have a secondary function as they often act as a source of scattered electrons which may improve the flattening of the beam near the surface (Fig. 3.7). For this type of collimator, the flattening of the beam can vary considerably with the field size and distance from the end of the collimator because a fraction of the real electron source is distributed along the collimator walls (see Abou-Mandour and Harder, 1975). Due to the broad angular distribution of the wall-scattered electrons, the point of maximum absorbed dose will be shifted closer to the surface and the dose gradient and therapeutic range of the beam will be decreased compared to a monodirectional beam (see Section 3.2.4.4 and Fig. 3.11). This has led to the development of plate or diaphragm collimators (Figs. 3.1 and 3.6c), with which the contribution of wall-scattered electrons is reduced considerably (Svensson and Hettinger, 1967; Svensson, 1971; Almond, 1975; Goede *et al.*, 1977; van der Laarse *et al.*, 1978).

Some of these diaphragm type collimators have also been designed to allow continuously-adjustable field sizes (Robinson and McDougall, 1966; Briot *et al.*, 1973; Bjärngard *et al.*, 1976; Brahme, 1977; Brahme and Svensson, 1979). Generally, the collimation of an electron beam cannot be treated simply as a ray-geometrical problem due to the considerable influence of air and, sometimes, also collimator wall scattering, particularly at energies below about 15 MeV. This is clearly seen in Fig. 2.11, where the measured electron fluence from an almost point monodirectional and monoenergetic electron beam is shown when passing through air of normal temperature and pressure. It is clear that the

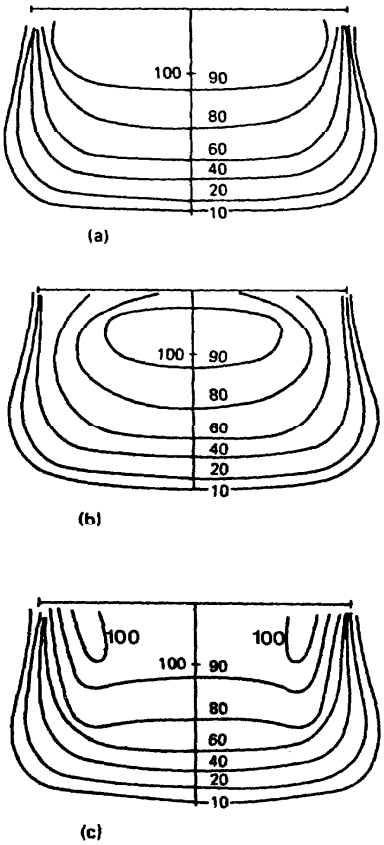

Fig. 3.7. The effects of collimator adjustment on the shape of the isodose curves for cone or tube-type collimators. (a) With correct adjustment of the collimator and the beam, a uniform distribution is obtained. (b) With the distal edges of the collimators farther apart than in (a), the isodose lines are pulled in from the field edge, resulting in more dose in the center of the field than towards the edge. (c) With the distal edges of the collimator closer together than in (a), too many electrons are scattered from the distal part of the collimator into the field, adding significantly to the dose around the edge and resulting in "hot spots" (Almond, 1975; see also Bradshaw and Maysent, 1964).

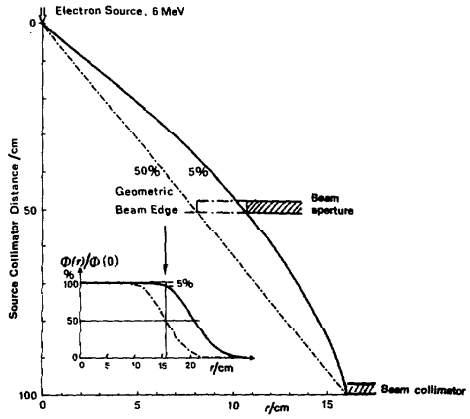

Fig. 3.8. The influence of electron scattering by air on the fluence uniformity of an electron beam at the irradiated surface. The insert indicates radial fluence, $\Phi(r)/\Phi(0)$, (at SSD = 100 cm) as a function of radial distance. Here the dot-dash curve indicates the fluence profile at 100 cm from the source when an aperture limits the electron beam to the straight dot-dash line from the source to a lateral distance of 16 cm at 100 cm from the source. A reduction of fluence by 50% at a lateral distance of 16 cm is obtained for this situation. The solid curve in the insert corresponds to the situation for the solid curve from the source to the 16 cm lateral position. Apertures edges should be located on this solid curve to reduce the fluence of the beam at 100 cm by 5%. The lateral scale is different from the vertical scale (Brahme, 1977).

width of the beam increases very rapidly due to the accumulated scattering interactions in the air. The root mean square radius at 6 MeV is almost 10 cm after only 1 meter of travel. A broad electron beam must, therefore, be collimated close to the irradiated surface and the beam cross-section should be significantly larger than that of the geometric beam in order to obtain a balance at the edge of the beam between electrons scattered into and out of the beam.

This phenomenon is further illustrated in Fig. 3.8. A constant fluence 6-MeV beam with a 16-cm radius at a distance of 100 cm from the source is desired. Two conditions are considered. In the first condition, a collimator is placed with its limiting edges on the straight dot-dash line labeled 50%. In Fig. 3.8 one of the limiting apertures is located at a distance of 50 cm from the source and this aperture has an 8-cm radius. The inserted drawing indicates the relative fluence as a function of distance from the central axis at the distance of 100 cm from the source. The dot-dashed line in that insert gives the relative fluence (beam profile) for the limiting aperture for this condition. It is seen that the electrons scattered out of the beam produce a marked reduction in the fluence from about 10–16 cm from the central axis of the beam. At a radial distance of 16 cm, the fluence is reduced to about 50% of its value on the central axis.

For the second situation, the limiting edges of the apertures are placed on the solid curve (labeled 5%) at any distance from the source. Now electrons scattered in the space between the straight dot-dashed line (labeled 50%) and the solid line (labeled 5%) contribute to the fluence in the region at a lateral distance of 16 cm from the beam axis. The solid line in the inserted figure gives the fluence (beam profile) for the condition as a function of distance from a central axis. It is seen that the relative fluence is only 5% smaller at a radial distance of 16 cm than that at a lateral distance of from 0- to, perhaps, 10- or 12-cm distance.

These relative fluence curves were calculated using the small angle approximation for the electron fluence (Brahme, 1977; see also Sections 2.5 and 2.6). It is seen

that in order to keep the dose reduction below 5%, the real beam cross-section at the aperture must be as much as 5 cm wider than the geometric beam at an energy of 6 MeV.

The locus of optimum electron beam collimation in the above sense is also indicated in Fig. 3.1 together with a collimator design according to Fig. 3.6 c, which will introduce a minimum of collimator-scattered electrons into the beam. Thus, in this type of collimator, the air is an integral part of the collimator system and scatters nearly the right amount of electrons back into the beam. Most of the beam-limiting apertures are placed in the beam penumbra (see the collimator plate in Fig. 3.8) where the electron fluence, and thus, the production of scattered electrons, is relatively small.

The choice of material for the collimator plates will have a considerable influence on the quality of the resultant therapeutic beam. The necessary thickness of a lead shielding and collimating plate was investigated by Giarratano *et al.* (1975). If, instead, a low atomic number material is used to minimize the bremsstrahlung production in the collimator, a considerable contamination by low energy electrons is obtained. This is because a much wider region near the edge of the source side of a low density collimator is hit by primary electrons, which are not stopped, but instead scattered back into the beam through the edge of the collimator (Lax and Brahme, 1980). There is, thus, an optimum material—osmium ($Z = 76$, $\rho = 22.48$ g cm^{-3}) that minimizes contamination of the beam by low-energy electrons produced by "out scattering" through the collimator edge.

The mean energy of those electrons scattered from the collimator back into the electron beam can be as low as 40% of the incident mean energy so that they will give rise to shallow "hot spots" along the edges of the field (Fig. 3.7c). These low energy electrons are particularly significant at small field sizes, and they are probably responsible for the increase in average stopping power ratio near the surface in some clinical beams (e.g., at 20 and 30 MeV in Fig. 4.11). However, their influence can be reduced considerably by using a high density material lining on the collimator edge (Fig. 3.6c). In the range 10–20 MeV, the "hot spots" are reduced by almost a power of ten by adding a 1-mm tungsten foil at the edge of an aluminum collimator (Lax and Brahme, 1980).

3.2.4 Irradiation Geometry Parameters

The characteristics of the initial electron beam delivered by the accelerator and the beam optical system, as well as the multiple scattering in all materials in and along the beam, determine the lateral and angular spread of the electron beam incident on the patient or phantom surface. A unified description of the whole irradiation geometry can generally be achieved by stating just three parameters. The most practical set of parameters contains the position, size and angular spread of that effective electron source which, when placed in a vacuum, would produce the same electron fluence at the patient or phantom surface as the real beam.

The location of the effective electron source (Section 3.2.4.2) or the virtual point source (Section 3.2.4.3) is of importance when the change in dose rate with the collimator-to-phantom distance has to be calculated, or when depth-dose curves have to be transferred from one effective source-surface distance to another (see Section 6.4.3.3). The size of the effective electron source is of major importance when the collimation geometry is analyzed because a large electron source will produce a much larger amount of wide-angle collimator-scattered electrons than will a small source. Such a larger electron source will also produce a broader angular spread at the irradiated surface. The widened angular distribution can have a substantial influence on the shape of the depth-dose curve (see Section 3.2.4.6) and on the width of the penumbra region (see Section 6.5.4). The angular spread of the effective source or the radial spread of the whole non-collimated beam is a measure of the uniformity of the dose distribution and can be used as a complement to the experimentally determined uniformity index (see NACP, 1980).

In the following subsections, the discussion of the relationships between the different geometric beam parameters is based largely on the multiple scattering formalism of Sections 2.5 and 2.6.

3.2.4.1 Three-parameter Description of the Beam. The combined lateral and angular distribution of the electron beam at the surface of the patient or phantom ($z = 0$), neglecting the lateral cut-off by the collimating system, can, for most purposes, be well described by the Fermi-Eyges distribution of the fluence differential in angle (Eq. 2.38). The three parameters of this function are the lateral and angular variances, $\overline{r^2}(0)$ and $\overline{\Theta^2}(0)$, and the covariance $\overline{r\Theta}(0)$, evaluated at the phantom surface, $z = 0$. These parameters can either be measured experimentally or can be calculated from the three transport integrals (Eqs. 2.34, 2.37, and 2.39 or Table 3.1), based on the characteristics of the initial electron beam (specified by the same set of parameters) and its multiple scattering in scattering foils, air, etc. In this approximation, only three independent parameters are thus needed to fully describe the spatial extension of a circularly symmetric beam. As mentioned in connection with Eq. 2.38, the fluence differential in angle has constant values on ellipses in the two-dimensional x, Θ_x plane of phase space (see also Section 3.2.1). For a clinical electron beam, this ellipse has been plotted in Fig. 3.9 by connecting all points at which the value of the fluence differential in angle has decreased to 1/e of its value on the central axis in the forward di-

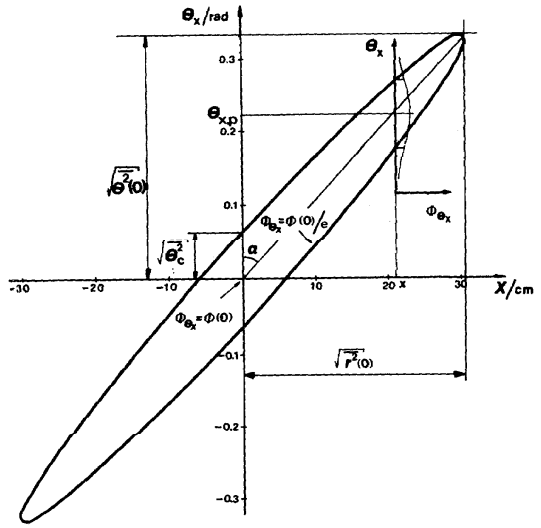

Fig. 3.9. The phase-space ellipse of a clinical electron beam. The ellipse shown connects all points in phase space where the fluence differential in angle has decreased to 1/e (the rms width for a Gaussian beam) of its value in the forward direction on the central axis (see Eq. 2.38). It is clearly seen that the angular spread at the central axis ($x = 0$) is only a small fraction of that of the whole beam, because the most probable direction of motion outside the central axis, $\Theta_{x,p}$, is inclined to the z-axis. The profile of the fluence differential in angle at a point x in the first quadrant is inserted for clarification. The actual numerical values of this beam are taken from the numerical illustration in Section 3.2.4.4.

rection ($x = 0$, $\Theta_x = 0$). The maximal extension of this ellipse projected on the x and Θ_x directions, therefore,

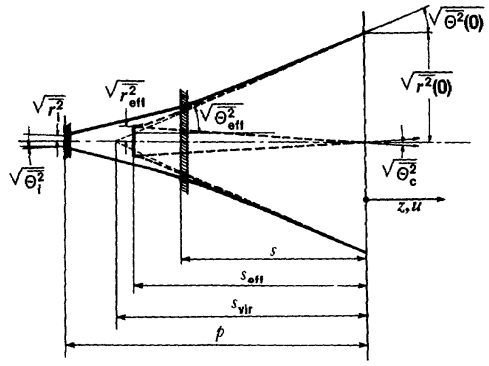

Fig. 3.10. Schematic representation of a simplified electron beam irradiation geometry illustrating the position (s_{eff}) and size ($\overline{r^2_{eff}}$) of the effective electron source and the central ($\overline{\Theta^2_c}$) and effective ($\overline{\Theta^2_{eff}} = \overline{\Theta^2}(0)$) mean square angular spread of the beam (see Table 3.1). The *mean square angular spread* ($\overline{\Theta^2_i}$) and *radial spread* ($\overline{r^2_i}$) of the initial electron beam are also shown. The distance to the virtual point source is s_{vir}. The distances to the primary foil (p) and secondary foil (s) are also indicated.

determines the rms radial and angular deviations, $\sqrt{\overline{r^2}(0)}$ and $\sqrt{\overline{\Theta^2}(0)}$, respectively. The angular spread at some point in the beam, for example at the central axis, is much more important for dosimetry (see Section 3.2.4.6) than the mean square angular spread of the whole beam, $\overline{\Theta^2}(0)$. For the center of the beam ($x = 0$), the mean square angular spread, $\overline{\Theta^2_c}$, is given by

$$\overline{\Theta^2_c} = \overline{\Theta^2}(0) - \frac{\{\overline{r\Theta}(0)\}^2}{\overline{r^2}(0)} \tag{3.2}$$

as can be derived from Eq. 2.38. In agreement with Eq. 3.2, Fig. 3.9 shows that the angular spread at the beam center is considerably smaller than $\overline{\Theta^2}(0)$. Figure 3.9 also illustrates that the same is true for each single point $x \neq 0$. In fact, a more detailed analysis of Eq. 2.38 shows that exactly the same mean square angular spread ($\overline{\Theta^2_c}$) is also obtained at other points in the beam. However, the most probable direction of motion is no longer along the central axis of the beam but at an angle[5].

Another relevant parameter that can be used to describe the beam is the tilt angle, α, of the phase space ellipse as defined in Fig. 3.9. The further away from the waist of the beam the more inclined is the ellipse (see also Fig. 3.2) and the larger is the angle α[6].

In conclusion, the three parameters $\overline{r^2}(0)$, $\overline{\Theta^2}(0)$, and $\overline{r\Theta}(0)$ characterize the incident beam within the limits of the Fermi-Eyges description. This description is valid when the initial beam can be characterized by the same set of parameters and when the beam is only influenced by small-angle multiple scattering. In the schematic drawing of the beam geometry encountered with essentially a dual scattering foil system (Fig. 3.10), some of these parameters are illustrated.

3.2.4.2 The Effective Extended Electron Source. In the presence of the various scattering materials which modify the lateral and angular distribution of an elec-

[5] The most probable direction of motion is given by $\Theta_{x,p} = x \cdot \overline{r\Theta}(0)/\overline{r^2}(0)$ which shows that $\overline{r\Theta}(0)$ is really a measure of the mean inclination of electrons outside the central axis. The greater the distance x from the central axis of the beam and the larger the covariance, $\overline{r\Theta}(0)$, the more inclined is the most probable direction of motion of the electrons for a given radial spread (see also Fig. 3.9). The distance to the mean center of divergence is thus given by $x/\Theta_{x,p} = \overline{r^2}(0)/\overline{r\Theta}(0)$.

[6] The tilt angle, α, of the main axis of the ellipse is given by the relationship

$$\tan 2\alpha = \frac{2\overline{r\Theta}(0)}{\overline{\Theta^2}(0) - \overline{r^2}(0)} \tag{3.3}$$

where the numerical values of r and Θ should be in the units chosen for the phase space diagram. A zero value of the covariance $\overline{r\Theta}(0)$, therefore, means that the ellipse is not tilted, which is the case when the angular distribution at each point of the beam is symmetrical with respect to the direction of the beam axis.

tron beam, it is possible to define an effective extended electron source. This source, when placed in vacuum at some distance s_{eff} from the phantom surface ($z = 0$), produces exactly the same electron fluence at $z = 0$ as the real beam. For practical use, for example in radiotherapy, it is more convenient to specify the electron beam in terms of such an effective radiation source rather than the variances and the covariance of the lateral and angular distribution at the phantom surface. The effective electron source is much less dependent on other parameters of the radiation geometry such as the distance to the phantom and the field size than are the variances and covariances of the distribution at the phantom surface. For a complete description of the effective electron source, four parameters are needed, namely, the location of this source and its lateral and angular variances and the covariance. This implies that at least one of these parameters can be arbitrarily chosen since only three independent parameters are needed to fully describe the beam (see Section 3.2.4.1).

The most natural choice is to locate the effective extended source at a waist of the beam, which is equivalent to assuming the covariance of the effective source to be zero.[6] Another useful approximation is to set the radius of the effective source to zero. However, this choice automatically sets the covariance to zero and thus does not allow an exact fitting to the real beam with regard to the radial variance and the covariance. This approximation is discussed in more detail in Section 3.2.4.3.

Therefore, in order to fully characterize the effective extended electron source, the following parameters are needed: $\overline{r^2_{eff}}$, the mean square radius of the source, $\overline{\theta^2_{eff}}$, the mean square angular spread of the source and s_{eff}, the effective source-to-surface distance. By definition, the covariance $\overline{r\theta}_{eff} \equiv 0$, which corresponds to an untilted phase-space ellipse and a symmetric angular distribution at each source point. Because the effective source is assumed to be located in vacuum, the effective angular spread must necessarily be identical to that of the real beam, i.e., $\overline{\theta^2_{eff}} \equiv \overline{\theta^2_0}$. The values of s_{eff} and $\overline{r^2_{eff}}$ are chosen so that the true beam is represented. The distance s_{eff} from the effective source to the plane $z = 0$ is calculated from the transport integral, Eq. 2.39: $\overline{r\theta}(0) = \overline{r\theta}_{eff} + \overline{\theta^2_{eff}} s_{eff}$. With the values of $\overline{r\theta}_{eff}$ and $\overline{\theta^2_{eff}}$ stated above, one obtains

$$s_{eff} = \frac{\overline{r\theta}(0)}{\overline{\theta^2}(0)} \tag{3.4}$$

The position of the effective electron source is illustrated in Fig. 3.10. In the present example, with a dual scattering foil system, the effective source is located between the two scattering foils. From Eq. 3.4, it can be concluded that the effective source-to-surface distance will decrease when the amount of scattering material near the irradiated surface is increased. It is also observed that at low electron energies, when the scattering power of air is appreciable, the position of the effective electron source will move somewhat towards the plane $z = 0$ when the collimator-surface distance is increased. Eq. 3.4 shows, together with Eq. 3.3, that s_{eff} depends on the tilt angle[6] of the phase space ellipse representing the incident beam. For $\overline{r\theta}(0) = 0$, one has $s_{eff} = 0$, i.e., the effective electron source lies in the plane $z = 0$. The size parameter, $\overline{r^2_{eff}}$, of the effective source is calculated from the transport integral for $\overline{r^2}(0)$ (Eq. 2.37), i.e., from $\overline{r^2}(0) = \overline{r^2_{eff}} + 2\overline{r\theta}_{eff} s_{eff} + \overline{\theta^2_{eff}} s^2_{eff}$. With $\overline{\theta^2_{eff}}$, $\overline{r\theta}_{eff}$ and s_{eff} as given above, one obtains

$$\overline{r^2_{eff}} = \overline{r^2}(0) - \frac{\{\overline{r\theta}(0)\}^2}{\overline{\theta^2}(0)} \tag{3.5}$$

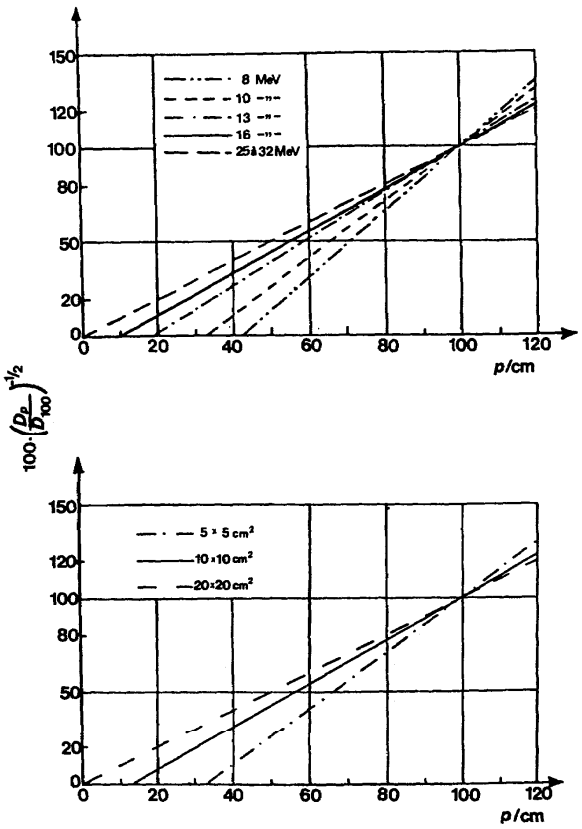

Fig. 3.11. Experimental determination of the influence of energy and field size on the variation of dose with distance, p, from the vacuum window. Measurements were made between $p = 80$ cm and $p = 130$ cm and all curves are normalized at a distance of 100 cm. Straight lines could be fitted to the experimental points. The intercept on the abscissa for a zero value of the ordinate gives approximately the distance between the window and the virtual point source. (a) Field size 5×5 cm^2 at 105 cm. (b) Energy 10 MeV. The location of the extrapolated virtual point source, as obtained by extrapolation to the horizontal axis, has a considerable dependence on the energy and the field size of the beam (Briot and Dutreix, 1976).

which shows that the effective source is smaller than $\overline{r^2}(0)$.

By comparison of Eqs. 3.2 and 3.5 it is observed that

$$\overline{\theta^2_c} = \overline{\theta^2}(0)\,\frac{\overline{r^2_{eff}}}{\overline{r^2}(0)} \tag{3.6}$$

The mean square scattering angle of the electrons at the center of the beam is thus only a fraction of the average value for the whole beam. The fraction is given by the ratio of the mean square radius of the effective electron source to the mean square radius of the whole beam. It can thus be concluded that it is of importance to have an electron beam with an effective electron source as small as possible in order not to broaden the angular distribution of the electrons at the irradiated surface because this will degrade the depth-dose curve (see Fig. 3.12).

The formalism necessary to calculate the properties of the effective electron source is summarized in Table 3.1. According to the general expressions for the parameters $\overline{r^2}(0)$, $\overline{\theta^2}(0)$, and $\overline{r\theta}(0)$, the three transport integrals (see Eqs. 2.34, 2.37, and 2.39) have to be taken from a point just inside the window through which the initial beam leaves the vacuum ($u = -p$ in the geometry of Fig. 3.10) and to be extended downstream to the plane $z = 0$. When the location of the effective source for the beam at a given depth z in the phantom is of interest, e.g., for dose planning with inhomogeneities, it is obtained simply by extending the range of integration down to that depth.

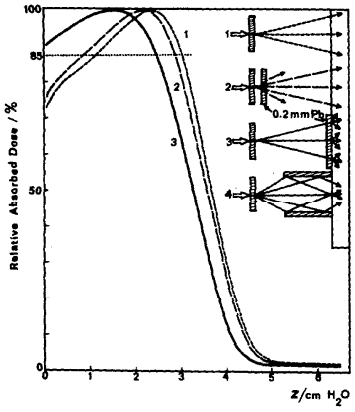

Fig. 3.12. The influence of the angular distribution of electrons on the central-axis depth-dose curves in water at 10 MeV. Curve No. 1 is a clinical beam using a thin scattering foil near the exit window of the accelerator tube. For curves Nos. 2 and 3, a 0.2-mm lead foil has been added so that the energy distributions are practically the same. However, the angular spread for curve No. 3 is much wider, which decreases the depth of the dose maximum, the therapeutic range (R_{85}), the dose gradient and the practical range. The dose distribution with the tube collimator (No. 4) is, in many respects, similar to that of curve No. 3 and is, therefore, not plotted separately (Brahme, 1978).

The last column of Table 3.1 is valid for the special case of a beam with a primary and a secondary scatterer and air (a volume scatterer) in the geometry of Fig. 3.10 as is further discussed in Section 3.2.4.4.

3.2.4.3 The Virtual Point Source. For the purpose of treatment planning (see Sections 7.3 and 7.4) or range measurement (see Section 3.3.2.3), it is desirable to represent, by approximate methods if necessary, the actual electron beam by a beam from a point source in vacuum, so that correction formulae based on the inverse square law can be applied. This source may be called the virtual point source (Pohlit, 1965).

Since a point source produces an incident beam represented by a phase space ellipse contracted to an inclined straight line, a point source cannot exactly represent the actual electron beam. In the cases where the effective electron source is small (i.e., when $\overline{r^2_{eff}} \ll \overline{r^2}(0)$), the virtual point source is, however, a good approximation. This situation can be realized at high beam energies, because the influence of the air and monitor chambers, etc. may be small, particularly if the distance between the scattering foil and the phantom surface is large.

In order to get the best possible fit to the geometrical shape of the real beam, the virtual point source should be chosen so that the radial variance and the covariance of the beams have the same value at the phantom surface. This means that the virtual point source distance, s_{vir}, and mean square angular spread, $\overline{\theta^2_{vir}}$, should be chosen to satisfy Eqs. 2.37 and 2.39 (i.e., $\overline{r^2}(0) = \overline{\theta^2_{vir}}\,s^2_{vir}$ and $\overline{r\theta}(0) = \overline{\theta^2_{vir}}\,s_{vir}$) since the approximation that s^2_{vir} is assumed to be zero automatically implies that $\overline{r\theta}_{vir}$ is zero due to the properties of a point source. From these two equalities, the distance to the virtual point source is directly obtained as

$$s_{vir} = \frac{\overline{r^2}(0)}{\overline{r\theta}(0)} \tag{3.7}$$

The angular spread of the virtual point source similarly becomes

$$\overline{\theta^2_{vir}} = \frac{\{\overline{r\theta}(0)\}^2}{\overline{r^2}(0)} = \overline{\theta^2}(0) - \overline{\theta^2_c} \tag{3.8}$$

where Eq. 3.2 has been used in the last equality. This choice of the virtual point source makes the radial variance and the covariance coincide for the real beam and the beam from the virtual point source, whereas the angular spread of the virtual beam is too small by the amount $\overline{\theta^2_c}$. This result is natural because for a point source, $\overline{\theta^2_c} = 0$ according to Eq. 3.6.

Of special interest is the fact that the mean center of divergence defined in Section 3.2.4.1 (footnote 5) exactly coincides with s_{vir}. This property has important con-

TABLE 3.1—*Geometrical electron beam parameters*

Parameter Name	Parameter Symbol	General Expression	Expression for a Primary (p), a Secondary (s) and a Volume (v) Scatterer (Figure 3.10)
Mean square angular spread of all electrons in the uncollimated beam	$\overline{\theta^2}(0)$	$\overline{\theta_i^2} + \int_{-p}^{0} T(u)du$	$\overline{\theta_i^2} + \overline{\theta_p^2} + \overline{\theta_s^2} + \overline{\theta_v^2}$
Mean value describing the most probable inclination of electrons off-axis	$\overline{r\theta}(0)$	$\overline{r\theta_i} + \overline{\theta_i^2}p + \int_{-p}^{0} (z-u)T(u)du$	$(\overline{\theta_i^2} + \overline{\theta_p^2})p + \overline{\theta_s^2}s + \overline{\theta_v^2}p/2$
Mean square radial spread of all electrons in the uncollimated beam	$\overline{r^2}(0)$	$\overline{r_i^2} + 2\overline{r\theta_i}p + \overline{\theta_i^2}p^2 + \int_{-p}^{0} (z-u)^2T(u)du$	$\overline{r_i^2} + (\overline{\theta_i^2} + \overline{\theta_p^2})p^2 + \overline{\theta_s^2}s^2 + \overline{\theta_v^2}p^2/3$
Angular spread of the electrons from the effective electron source	$\overline{\theta_{eff}^2}$	$\overline{\theta^2}(0)$	$\overline{\theta_i^2} + \overline{\theta_p^2} + \overline{\theta_s^2} + \overline{\theta_v^2}$
Angular spread of the electrons at the central axis of the beam	$\overline{\theta_c^2}$	$\overline{\theta^2}(0) - \frac{(\overline{r\theta}(0))^2}{\overline{r^2}(0)}$	$\frac{\overline{r_i^2}}{p^2} + \frac{\overline{\theta_v^2}}{3} + \overline{\theta_s^2}\left(1-\frac{s}{p}\right)^2 - \frac{\left(\overline{\theta_s^2}\left(1-\frac{s}{p}\right)\frac{s}{p} + \overline{\theta_v^2}\frac{1}{6}\right)^2}{\frac{\overline{r_i^2}}{p^2} + \overline{\theta_i^2} + \overline{\theta_p^2} + \overline{\theta_s^2}\left(\frac{s}{p}\right)^2 + \overline{\theta_v^2}\frac{1}{3}}, \left[(\overline{r_i^2} \ll \overline{\theta_s^2}s^2)\right]$
Distance from the effective electron source to the phantom surface	s_{eff}	$\frac{\overline{r\theta}(0)}{\overline{\theta^2}(0)}$	$s + \frac{\overline{\theta_p^2}(p-s) + \overline{\theta_v^2}(p/2-s)}{\overline{\theta_p^2} + \overline{\theta_s^2} + \overline{\theta_v^2}}$
Mean square radial spread of the electrons from the effective source	$\overline{r_{eff}^2}$	$\overline{r^2}(0) - \frac{(\overline{r\theta}(0))^2}{\overline{\theta^2}(0)}$	$\overline{r_i^2} + \overline{\theta_v^2}(p^2/3) + \overline{\theta_s^2}(p-s)^2 - \frac{(\overline{\theta_s^2}(p-s) + \overline{\theta_v^2}p/2)^2}{\overline{\theta_i^2} + \overline{\theta_p^2} + \overline{\theta_s^2} + \overline{\theta_v^2}}$
Distance from the virtual electron source to phantom surface	s_{vir}	$\frac{\overline{r^2}(0)}{\overline{r\theta}(0)}$	$s + p\frac{(\overline{\theta_i^2} + \overline{\theta_p^2})(p-s) + \overline{\theta_v^2}(p/3 - s/2)}{(\overline{\theta_i^2} + \overline{\theta_p^2})p + \overline{\theta_s^2}s + \overline{\theta_v^2}p/2}$

sequences for the experimental determination of the virtual point source (see Section 3.2.4.5).

The position of the virtual point source is illustrated in Fig. 3.10. The distance s_{vir} is generally larger than s_{eff}. As with the effective electron source, the virtual point source is frequently located between the two scattering foils, if there are two.

3.2.4.4 Application to a Simplified Geometry. The concepts of effective electron source and virtual point source will here be applied to a practical situation with two discrete scattering layers and a distributed volume scatterer in a geometry given by Fig. 3.10. The primary scattering layer produces the angular spread, $\overline{\theta_p^2}$, due to multiple scattering in the vacuum window and the primary scattering foil (see Fig. 3.1), since these are normally located fairly close together. Additional to this is the angular spread, $\overline{\theta_i^2}$, of the initial electron beam. The second layer could represent, to a reasonable approximation, the increase in mean square scattering angle, $\overline{\theta_s^2}$, produced in the transmission monitor, mirror and possible secondary scattering foil, because these components are also often placed close together (see Fig. 3.1). The third contribution, $\overline{\theta_v^2}$, represents the influence of the surrounding air volume which acts as a distributed volume scatterer. Under the above simplified assumptions, the expressions for the effective source-surface distance, the effective source size, the effective angular spread and the angular spread in the center of the beam are given in Table 3.1.

The expressions in the last column of Table 3.1 show that the virtual electron source is placed somewhere between the two scattering layers. It is closer to the second layer when that layer's contribution to the mean square scattering angle is increased. It may be seen that the effective source size and the angular spread in the center of the beam can increase considerably if the mean square scattering angles are large and the distance between the layers is large. From the expressions for $\overline{r_{eff}^2}$ and $\overline{\theta_c^2}$ it follows that the angular spread of the initial electron beam and that produced in the primary foil will have no first order influence on these parameters. Instead, the volume scatterer (air) and the secondary foil are the principal contributors to $\overline{r_{eff}^2}$, $\overline{\theta_c^2}$ and to obliquely scattered electrons. At low energies, and when $p - s \ll p$ (small distance between scattering foils or when only a single foil is used) the volume scatterer can even become the predominant contributor. These influences on $\overline{r_{eff}^2}$ and $\overline{\theta_c^2}$ show that all scattering materials in the downstream part of the beam are responsible for a large part of the deterioration of the beam quality (see Section 3.2.4.6).

If the thickness of the secondary scatterer is not uniform, the relationships in Table 3.1 are no longer strictly valid, but they can be employed as a first approximation if an average value of the mean square scattering angle, $\overline{\theta_s^2}$, is used. Moreover, it should be pointed out that the relationships are also less accurate when the fraction of collimator scattered electrons is high (see Section 3.2.3).

To give a numerical illustration of the influence of the scattering materials in an electron beam, the following fairly realistic data for a 10 MeV beam are assumed (see Fig. 3.10): Initial beam: $\overline{\theta_i^2} = 0.002$ rad^2 ($\theta_{rms} \approx 2.5°$) and $\overline{r_i^2} = 0.1$ cm^2 ($r_{rms} \approx 0.3$ cm); primary foil: 0.1 mm of lead, $p = 100$ cm; secondary foil: 1 mm of aluminum (made up, for example, of the transmission monitor walls and the secondary scattering foil), $s = 80$ cm; volume scatterer: 100 cm of air. From these values and the scattering power data from Table 2.6, the mean square scattering angles of the three scattering materials are obtained:

$$\overline{\theta_p^2} = l \cdot \rho \cdot T/\rho = 0.01 \text{ cm} \times 11.35 \text{ g cm}^{-3} \times 0.542 \text{ rad}^2 \text{ cm}^2 \text{ g}^{-1} = 0.0615 \text{ rad}^2$$

$$\overline{\theta_s^2} = 0.1 \text{ cm} \times 2.7 \text{ g cm}^{-3} \times 0.116 \text{ rad}^2 \text{ cm}^2 \text{ g}^{-1} = 0.0313 \text{ rad}^2$$

$$\overline{\theta_v^2} = 100 \text{ cm} \times 1.2\ 10^{-3} \text{ g cm}^{-3} \times 0.0698 \text{ rad}^2 \text{ cm}^2 \text{ g}^{-1} = 0.0084 \text{ rad}^2$$

The mean square angular spread of the whole beam (which is equal to that of the effective electron source) thus becomes $\overline{\theta^2}(0) = \overline{\theta_i^2} + \overline{\theta_p^2} + \overline{\theta_s^2} + \overline{\theta_v^2} = 0.1032$ rad^2, which corresponds to a root mean square angle of 18.4°. The mean square radial spread of the whole beam at the surface 100 cm from the primary foil becomes $\overline{r^2}(0) = \overline{r_i^2} + p^2(\overline{\theta_i^2} + \overline{\theta_p^2}) + s^2\overline{\theta_s^2} + (p^2/3)\overline{\theta_v^2} = 950.0$ cm^2, which, due to the properties of the Gaussian distribution, corresponds to a 1/e radius of $\sqrt{\overline{r^2}} = 29.4$ cm or a diameter of 19.1 cm inside which the dose variation is less than ±5%. The value of $\overline{r\theta}(0)$ similarly becomes $p(\overline{\theta_i^2} + \overline{\theta_p^2}) + s\overline{\theta_s^2} + (p/2)\overline{\theta_v^2} = 9.3$ cm·rad.

The effective source surface distance can now be obtained from $s_{eff} = \overline{r\theta}(0)/\overline{\theta^2}(0) = 9.3$ cm/0.1032 = 90.1 cm which means that the effective source is located about 10 cm downstream from the primary foil. For comparison, the distance of the virtual point source, s_{vir} (see Section 3.2.4.3), becomes $\overline{r^2}(0)/\overline{r\theta}(0) = 93.1$ cm which is fairly close to s_{eff}. The mean square radius of the effective electron source is obtained from $\overline{r_{eff}^2} = \overline{r_0^2} - \{\overline{r\theta}(0)\}^2/\overline{\theta_0^2} = 27.4$ cm^2 which corresponds to a root mean square radius of 5.2 cm. This shows that in this case the effective electron source is far from a point source. Finally, the angular spread at the center of the beam becomes: $\overline{\theta_c^2} = \overline{\theta_0^2} \cdot \overline{r_{eff}^2}/\overline{r_0^2} = 0.0033$ rad^2 corresponding to a root mean square angle of 3.3°, which is considerably less than the value for the whole beam. The resultant clinical electron beam is further described by its phase-space ellipse in Fig. 3.9.

It should be pointed out that the analysis in Sections 3.2.4.1 to 3.2.4.4 holds strictly only for non-collimated electron beams of Gaussian cross-section. However, the general form of the results is also approximately valid

for collimated, nearly uniform beams if the opening angle of the collimator, as viewed from the source, is used instead of $(\overline{\theta_p^2})^{1/2}$.

3.2.4.5 Experimental Determination of Irradiation Geometry Parameters. Quite generally, it is recommended that a method should be used which simulates, as closely as possible, the situation in which the determined parameter is later going to be used, e.g., in clinical practice. When, therefore, the source-surface distance is to be determined experimentally so that the dose rate can be corrected for the air space between the collimator and the patient, it is advisable to use the actual measured dose-rate variation with the distance in air between the end of the collimator and the patient (Briot and Dutreix, 1976; Khan *et al.*, 1978). Experimental results from such measurements are shown in Fig. 3.11. The position of the virtual point source can be estimated from the dose-rate reduction with distance. The virtual source-to-surface distance can be seen to decrease with decreasing energy and field size, in general agreement with theoretical relations given for the effective source in Table 3.1.

These results may also be used for comparison with the multiple scattering theory because this theory gives a good description of the variation of the planar fluence differential in angle and, consequently, of the absorbed dose with the distance along the beam. According to Eq. 2.36, the dose at the central axis of an uncollimated electron beam should, therefore, decrease in a manner that is inversely proportional to the mean square radial spread, $\overline{r^2}(z)$. By inserting the parameters of the effective extended electron source in Eq. 2.37, the mean square radial spread may be expressed as $\overline{r^2}(z) = \overline{r_{eff}^2} + \overline{\theta^2}_{\text{eff}} s_{\text{eff}}^2$, which shows that the simple inverse square law is not strictly valid for extended electron sources unless $\overline{r_{\text{eff}}^2}/\overline{\theta^2}_{\text{eff}} \ll s_{\text{eff}}^2$. If, instead, the parameters of the virtual point source are used in Eq. 2.37, $\overline{r^2}(z)$ becomes simply $\overline{\theta^2}_{\text{vir}} \cdot s_{\text{vir}}^2$. The distance to the virtual point source should, therefore, be used in expressions of the inverse square law type (see Eqs. 3.9 and 7.2) in order to take the extension of the effective electron source into account in an approximate manner. Note that multiple scattering in air produces slight changes in $\overline{r_{\text{eff}}^2}$, $\overline{\theta^2}_{\text{eff}}$ and the position of the effective source. The experimental finding (see Fig. 3.11) that the dose rate on the beam axis decreases with the inverse square of the distance from some virtual point source is, therefore, due to the combined influences of air scattering and an extended effective source. This explains why the curves in Fig. 3.11 are surprisingly linear, even for low energies and small field sizes, and cross the abscissa downstream from the vacuum window. When accurate results over a larger interval are needed, the basic expressions in Eqs. 2.36 and 2.37 should be used.

A number of other experimental techniques have been used to determine the position of the virtual electron source. Pohlit (1965) used the image of a grid of wires projected by the electron beam on to a photographic film to determine the position of the electron source in three dimensions (see ICRU, 1972). However, this method is only applicable when the size of the effective source is so small that a readable shadow is obtained from the wires. The method is, therefore, useful at higher energies beyond about 15 MeV. In principle, this method determines the mean center of divergence (see footnote 5). However, according to the analysis in Section 3.2.4.3, this center exactly coincides with the virtual point source. Therefore, s_{vir} determined by the wire-grid method could, at least at high energies, be used to approximate the variation of dose rate with distance from the accelerator. Schröder-Babo and Harder (1981) further developed Pohlit's method by using a multipinhole with, e.g., five double-conical holes in a metal plate. From the projection of the holes on a film, about 15 cm behind the pinhole plate, the location of the virtual electron source can be readily determined.

The variation of field size with distance from the end of the collimator (Fehrentz *et al.*, 1976 and Khan *et al.*, 1978) is sometimes used for determination of the virtual point source, but this method should be used with care when the effective source size is large, because it is strictly only a field size determination. Furthermore, these methods can be influenced by the varying contribution of electrons scattered from the collimator end plate (see Fig. 3.7 and Section 3.2.3). Another systematic error of this method can arise from the fact that the full width at half maximum of the transverse dose distribution increases in a nonlinear fashion with depth. According to Eq. 2.41, this is the case for field sizes (2a × 2b) and depths for which

$$\operatorname{erf}\frac{a}{r_{\text{rms}}} \cdot \operatorname{erf}\frac{b}{r_{\text{rms.}}} < 1.$$

It should also be pointed out that in betatrons and other accelerators, where the beam optical properties of the initial electron beam are different in two orthogonal directions (parallel and perpendicular to the orbital plane, see Section 3.2.1), different virtual source-surface distances can be obtained in the two planes. When this is the case, the dose rate variation will no longer be of the simple inverse square law type (see Eq. 3.18 below), but becomes instead

$$\dot{D}_d = \frac{\dot{D}_0 s_{\text{vir},\parallel} \cdot s_{\text{vir},\perp}}{(s_{\text{vir},\parallel} + d)(s_{\text{vir},\perp} + d)} \qquad (3.9)$$

where $s_{\text{vir},\parallel}$ is the virtual source distance in the orbital plane, $s_{\text{vir},\perp}$ is the virtual source distance in the plane perpendicular to the orbital plane, and $\dot{D}_d$ is the absorbed dose rate at a distance d from the normal treatment distance where the absorbed dose rate is $\dot{D}_0$.

The effective source size and angular spread at a point in the beam are more difficult to determine experimentally. One possibility is to measure the distribution of electrons transmitted through a narrow pinhole camera (Lax and Brahme, 1980). However, it is essential that the pinhole aperture be in a material of high density like tungsten or gold to minimize the contribution from aperture scattered electrons.

3.2.4.6 Influence of Angular Spread on Depth-Dose Curve. The influence of a certain angular spread, $\overline{\theta}_c^2$, of an almost monoenergetic electron beam on the shape of the depth-dose curve is clearly demonstrated in Fig. 3.12. Curve No. 1 is the central axis depth-dose distribution of an almost parallel 10-MeV clinical electron beam. In curve No. 2, the scattering foil thickness has been increased by 0.2 mm of lead, which has decreased the practical range due to energy loss, and decreased the therapeutic range, R_{85} (see Section 6.4.3), even more due to energy loss straggling in the foil. The angular distribution of the electrons in these two beams are almost identical because the extra lead foil added to yield curve No. 2 was placed very near to the normal scattering foil used for curve No. 1.

For curve No. 3, the extra scattering foil has been moved and placed at the phantom surface. The energy distributions in curves No. 2 and No. 3 are thus almost identical. However, the angular distributions of the electrons that reach the phantom are completely different. The directions of the electrons incident on the phantom in curves No. 1 and No. 2 are essentially parallel to the axis, as they represent the central 10 cm of a divergent beam from a point source at 100-cm distance. For curve No. 3, the angular spread of the electrons reaching the surface of the phantom is very broad ($\overline{\theta}_c^2 = 0.13$, or $\theta_{rms} = 20°$) due to the foil at the surface. This results in a decreased practical range because the mean angle of incidence of the electrons is increased (see Eq. 3.5). For high electron energies, the reduced practical range, R'_p, can be estimated from (Brahme, 1978)

$$R'_p = R_p \overline{\cos\theta} \approx R_p(1 - \overline{\theta}_c^2/2) \qquad (3.10)$$

where R_p is the practical range in a plane parallel beam of normal incidence. The loss in therapeutic range is even larger than that given by this correction factor because the electrons reach a state of full diffusion more quickly when they already have a wide angular spread at the surface. For the same reason, the surface dose is higher as the dose build-up is mainly due to the increase in obliquity of the electrons as they penetrate into the medium (see Eq. 2.42).

The above results, therefore, explain why collimators of the tube type illustrated in Fig. 3.6a and b and insert No. 4 of Fig. 3.12 produce depth-dose distributions with a small therapeutic range and a high surface dose.

3.3 Energy

3.3.1 Energy Parameters

The dosimetric properties of clinical electron beams depend significantly on the electron fluence spectrum differential in energy, Φ_E. In some situations, it is sufficient to characterize Φ_E with one energy parameter, but in many cases, two or more parameters are needed. The following energy parameters, defined in Section 2.4.2, are in current use: the maximum energy, E_{max}, the most probable energy, E_p, the mean energy, $\overline{E}$, and the full width of the energy distribution at half maximum, Γ. Some or all of these parameters are needed, depending on the situation. Indices a, i, 0, or z are used to indicate if the energy is specified for the intrinsic accelerator beam (a), for the initial electron beam at the inner side of the vacuum window of the beam transport system (i), for the beam at the surface of the phantom or the patient (0) or, at a depth inside the phantom or the patient (z). It should be pointed out that the energy distribution of the intrinsic accelerator beam can differ from that of the initial electron beam when vacuum windows and slits (see Fig. 3.1) are used in the beam transport system. Therefore, the initial electron beam, (i), delivered to the treatment head is generally the most relevant in clinical applications.[7]

3.3.1.1 Energy Distribution of the Intrinsic Accelerator Beam and the Initial Electron Beam. The distribution of electrons in energy before passing through possible beam handling systems depends on the type of accelerator and the method of injection and extraction. Generally, the energy distribution of the intrinsic accelerator beam is very narrow for betatrons, $\Gamma_a < 20$ keV (Goldwasser *et al.*, 1952), and microtrons $\Gamma_a < 40$ keV (Brahme *et al.*, 1975). It is broader for linear accelerators, particularly of the standing wave type, where Γ_a is about 10% of the most probable energy, $E_{p,a}$, and the travelling wave type, where Γ_a is about 5% (Dolphin *et al.*, 1959; Telford *et al.*, 1967; Wessels *et al.*, 1979). The energy spread of some linear accelerators is reduced in the beam handling system, for instance, by a slit system in combination with a bending magnet (Brown, 1956; Aucouturier *et al.*, 1970). This will normally increase the mean energy and decrease the energy spread of the initial electron beam compared to that of the intrinsic accelerator beam, but it usually leaves the most probable energy unchanged. Other beam handling systems are specially designed to accept quite large energy variations (e.g., the 270° achromatic deflection system, see Fig. 3.3c), making the

[7] In betatrons, the intrinsic accelerator beam and the initial electron beam have the same meaning because no slits are used. For such machines, $E_a = E_i$. It should be noted that the notations $\overline{E}(z)$ and $\overline{E}_z$, for example, are used interchangeably in the text.

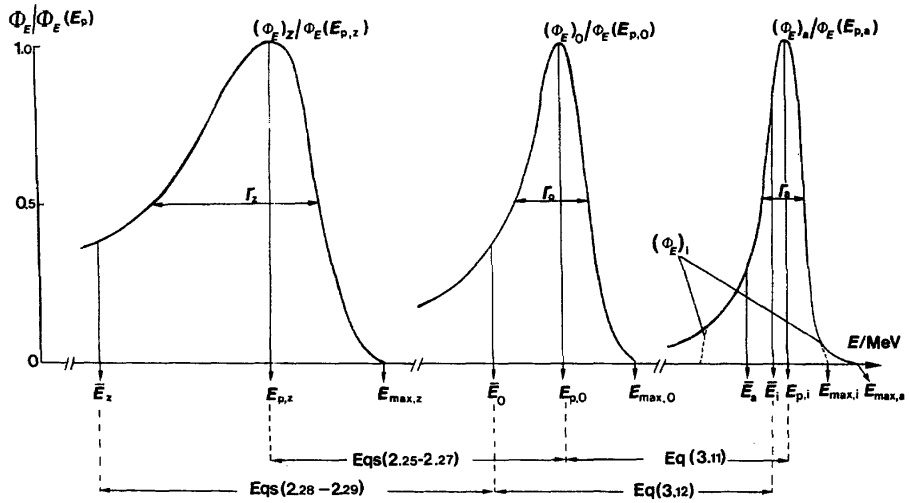

Fig. 3.13. Energy parameters and their relationship. The index, a, indicates the energy distribution of the intrinsic accelerator beam and the index, i, that for the initial electron beam. The two energy distributions differ because of possible energy cutoffs by slits in the beam optical system. The slit modification is shown by the broken lines. The indices 0 and z indicate the distributions at the phantom surface ($z = 0$) and at a depth $z = z$ below the surface, respectively.

energy distribution of the initial electron beam and the intrinsic accelerator beam practically equal. Information on bending magnets for medical electron linear accelerators is given by Karzmark and Pering (1973).

It has already been shown that the difference in the amount of energy spread of the intrinsic accelerator beams from different accelerators may influence the shape of the depth-dose curve (Lillicrap and Rosenbloom, 1972; Brahme and Svensson, 1976a, 1979). A description of the initial electron beam ought, therefore, to include at least one of the energy parameters, $E_{p,i}$, $\overline{E}_i$, or $E_{max,i}$, together with the energy spread Γ_i (Fig. 3.13).

3.3.1.2 Energy Distribution at the Phantom Surface. Energy losses of the electrons in matter between the inner surface of the vacuum window and the patient shift the energy distribution to lower energies, and energy loss fluctuations broaden the energy spectrum (Fig. 3.13). The energy parameters at the phantom surface can be evaluated from the energy parameters of the initial electron beam if the atomic compositions and thicknesses of the materials in the beam are known and vice versa. $E_{p,0}$ is obtained by subtracting from $E_{p,i}$ the most probable energy loss in the layers of matter traversed by the beam. Since the most probable energy loss in layer n is fairly well approximated by the mean collisional energy loss, $(\Delta E)_{col,n}$, in layer n (see Section 2.4.2), the relation

$$E_{p,0} = E_{p,i} - \Sigma(\Delta E)_{col,n} \qquad (3.11)$$

is often used as an approximation to obtain $E_{p,0}$.

$\overline{E}_0$ can be obtained from $\overline{E}_i$ by subtracting the total mean energy losses in the intervening material layers

$$\overline{E}_0 = \overline{E}_i - \Sigma(\Delta E)_{tot,n} \qquad (3.12)$$

where $(\Delta E)_{tot,n}$ is the mean total energy loss in layer n, i.e., the sum of collision and radiative energy losses. In Eq. 3.12, the filtration of the low-energy region of the electron spectrum by electron scattering in the air volume has not been considered. This filtration is due to the rapid increase of the scattering power with decreasing electron energy, which results in a large number of low-energy electrons disappearing out of the beam and then being stopped by the collimator (Brahme, 1977). In some accelerator-beam geometries, this effect is not present as these low-energy electrons are scattered from the collimator walls back into the beam. Equation 3.12 is, therefore, approximate, but its accuracy is sufficient for most dosimetric purposes in the calibration of electron therapy beams.

$E_{max,0}$ may be estimated from

$$E_{max,0} \approx E_{max,i} - \Sigma(\Delta E)_{col,n} \qquad (3.13)$$

which should be regarded only as a lower limit for $E_{max,0}$ because some electrons will suffer lower energy losses than ΔE_{col}.

The energy spread at the phantom surface, Γ_0, is made up of several contributions and can be estimated from the relationship (Brahme and Svensson, 1976a, 1979)

$$\Gamma_0 = \Gamma_i + \Sigma\Gamma_n \qquad (3.14)$$

where Γ_i indicates the energy spread of the initial electron beam and Γ_n indicates the energy spread due to foils, air and other materials in the beam. Γ_n can be taken from Eq. 2.30 by using ΔE_{col} as an approximation to ΔE_p

$$\Gamma_0 = \Gamma_i + \sum \frac{(\Delta E)_{col,n}}{\kappa_n} \qquad (3.15)$$

Numerical values of κ_n for different material layers (n) can be estimated from Table 2.7. When the energy parameters at the phantom surface are known, the corresponding parameters at a depth in the phantom can be obtained directly from the relationships given in Section 2.4.2.

3.3.1.3 Statement of Electron Energy. Absorbed dose distributions and other beam data can only be meaningfully compared if the energy parameters used are clearly specified. A summary of the different energy parameters and their relationships is given in Fig. 3.13.

When a radiotherapeutic irradiation procedure is reported, the energy at the phantom surface should be given; $E_{p,0}$ is usually used, as this quantity is simple to measure from the energy-range relationships. Therefore, for uniformity, $E_{p,0}$ is recommended for use in the specification of depth-dose and isodose curves. When the deep penetration of an electron beam is to be specified in more detail, it is not sufficient to use a single parameter like $E_{p,0}$ because the slope of the depth-dose curve may vary considerably for a given $E_{p,0}$. The most probable energy at the surface must be complemented by the therapeutic range, R_t, i.e., the useful range of depths for radiation treatment by the beam, which is related to a certain absorbed dose level (see Section 6.4). Alternatively, Γ_0 or $\overline{E}_0$ may be used as they, together with $E_{p,0}$, can be used to estimate R_t (see Section 6.4).

In dosimetry, the energy dependent calibration factors are generally best related to the mean energy. For this purpose, the mean energy at the surface, $\overline{E}_0$, is most useful because it can be used to calculate the mean energy, $\overline{E}_z$, at the depth of interest in the phantom (see Eq. 2.28), where dosimetric measurements are to be carried out. As dosimetric constants often are slowly varying functions of the energy, it is sometimes sufficient to estimate $\overline{E}_z$ by $E_{p,z}$, i.e., by the most probable energy at the depth z (see Section 6.3.2.1); $E_{p,z}$ can be calculated from $E_{p,0}$.

It is often convenient to give a single accelerator energy parameter at the console of the accelerator facility. A parameter indicating the energy of the initial electron beam, e.g., $E_{p,i}$, is often convenient to use as this quantity is independent of the choice of scattering foil. When the scattering foil can be varied for a given setting of the accelerator energy, different values of $E_{p,0}$ and $\overline{E}_0$ are obtained for the same accelerator energy setting.

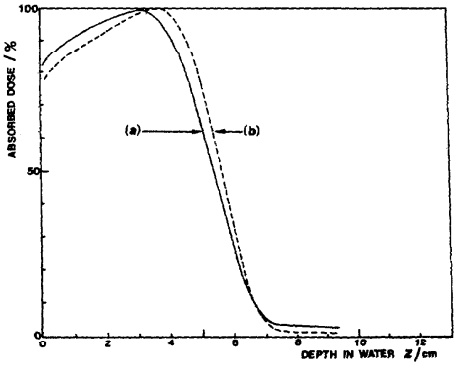

Fig. 3.14. Experimentally determined central-axis, relative, depth versus absorbed-dose distributions with the same most probable energy at the phantom surface ($E_{p,0}$ = 13.6 MeV), but with different energy spreads. All other parameters, such as field size, angular spread and divergence of the beams, were approximately the same and should not contribute to the difference in absorbed dose distributions. Other characteristics of the beams are: (a) Γ_0 = 1.6 MeV, $\overline{E}_0$ = 12.4 MeV, and G = 2.5, (b) Γ_0 = 0.2 MeV, $\overline{E}_0$ 13.3 MeV, and G = 3.3. (G is a measure of the fall-off of the descending part of the depth-dose curve defined in Section 6.4.3.) [Data recalculated from Brahme and Svensson, 1979.]

3.3.1.4 Influence of Energy Distribution on Depth-Dose Curve. Electron beams with the same field size, source-surface distance, and angular spread may have differently shaped absorbed dose versus depth distributions even if the most probable energy at the surface is the same (see Fig. 3.14), due to differences in other energy parameters. For example, a large energy spread will result in a low dose gradient of the decreasing part of the depth dose curve (see Section 6) because the energy spread in the beam results in a spread of penetration in the phantom. Differences in the energy distribution may appear even in the initial electron beam (see Section 3.3.1.1), and these can be increased further due to energy degradation in the materials in the beam (e.g., in scattering foils) and outside the beam (by collimators). The collimator may give a considerable low-energy contribution, which may degrade both the reference-axis depth versus absorbed-dose relationship and the uniformity of the beam, particularly, at small field sizes. Well constructed collimators will reduce this low-energy contamination (Section 3.2.3). The combined influence of the angular and energy spread on the absorbed-dose distribution is described in Section 6.

3.3.2 Determination of Electron Energy

The general methods used to measure spectra of high-energy electrons are the magnetic spectrometer (see Siegbahn, 1965) and the total-absorption scintillation spectrometer (see, for example, Feist *et al.*, 1968)

having energy resolutions of about 0.1 and 5%, respectively. For electrons below a few MeV, the semiconductor detector may be used as a total-absorption spectrometer with energy resolution of the order of 1%. At electron energies lower than 0.1 MeV, the electrostatic analyser is the method used currently to measure electron spectra.

Energy parameters of the beam can also be measured from thresholds for nuclear reactions (3.3.2.1) or for emission of Cerenkov radiation (3.3.2.2). In dosimetric procedures used for calibration of radiation treatment beams, empirical range-energy relationships are sufficient. A value of I_0 can be estimated from a measurement of the normalized dose gradient under standardized conditions, as shown by Brahme and Svensson (1979). In Section 3.3.1 it is shown that the energy parameters at the accelerator window and at the phantom surface are related by simple equations, and in Section 2.4.2 that the energy parameters at the phantom surface are related to parameters at a depth in the phantom. Measurement of one energy parameter is, therefore, often sufficient for input in the calculation of other parameters of interest; for example, $E_{p,0}$ can be determined from the range-energy relation and $E_{p,i}$ calculated from Eq. 3.11, or $E_{p,z}$ from Eqs. 2.25 to 2.27 (see Fig. 3.13).

3.3.2.1 Nuclear Reaction Thresholds. The interaction of a photon or electron with an atomic nucleus can result in the emission of one or more nucleons and the creation of a radioactive nucleus. The nuclear reaction can be detected through the decay of this nucleus. The energy threshold, E_{th}, for a nuclear reaction is given, approximately, by the difference between the rest energy of the target nucleus and that of the residual nucleus and the emitted nucleon(s). By careful evaluation of mass spectroscopic data and of nuclear reaction energies (Everling *et al.*, 1960; Mattauch *et al.*, 1965; Wapstra and Gove, 1971; Lederer and Shirley, 1978), the rest energies of many nuclei are known to a very high accuracy. For large threshold energies, a correction term, $E_{th}^2/2m_Tc^2$, (where m_T is the mass of the target nucleus) becomes important and should be added to E_{th}. Such threshold values can then be used to determine the maximum energy of a photon or electron beam (Bendel *et al.*, 1958; Geller *et al.*, 1960; Lanzl, 1969).

In a sample irradiated with electrons of energy exceeding E_{th}, nuclear reactions are induced either directly by the electrons [e.g., by the (e, e'n) reaction] or by the bremsstrahlung photons produced in the sample [e.g., by the (γ,n) reaction]. The relative contributions of these processes to the reaction rate depend on the electron energy, and on the atomic number and thickness of the sample. Both reactions, however, have the same energy threshold, and it is not necessary to eliminate one or the other in measurements of the electron energy.

The electron beam incident on the activation sample may be contaminated with bremsstrahlung from the accelerator window and also, in some accelerators, from the foils and other materials in the beam. The maximum energy of photons generated in the window can be a few MeV higher than the maximum electron energy at the activation sample due to the energy losses of electrons in the intervening materials (Svensson and Hettinger, 1971). Thus, it is often the peak energy of these photons, i.e., $E_{max,i}$, that is determined from (γ,n) thresholds, rather than the maximum energy of the electrons at the activation sample. However, the central axes of the electron beam and of the beam of photons generated in the accelerator window have different directions for some betatrons because the deflection due to the magnetic field influences the electron beam outside the window. In this case, the (γ,n) threshold measurement may give a lower energy than $E_{max,i}$, as the source of the photon generation, seen by the activation sample, may be some material between the window and the sample. By making threshold measurements in different parts of the beam inside the treatment head, it is possible to determine which energy parameter has been measured.

Table 3.2 contains values of threshold energy for some common materials often used for energy determinations. In addition, abrupt changes of the activation curve ("breaks") are also given. Such "breaks" can be determined when the energy distribution is narrow, but may be missed for a broad distribution. Moreover, the maximum photon and electron energies at the activation sample may differ, as discussed above, giving rise to "apparent breaks." Caution should be exercised, so that a "break" energy is not interpreted as the threshold energy.

The practical procedure requires that a number of identical samples be made from the target material. Each of the samples is irradiated by the same fluence, as indicated by the monitor, but with a different electron energy and the induced radioactivity of each sample is measured. The times for irradiation and for counting, as well as that for sample transfer, are kept constant throughout the experiment. The threshold is indicated by the point at which the net number of counts, i.e., the count rate minus background, falls to zero.

Several ways of increasing the precision of this measurement can be used: (a) Changes in the beam intensity will produce changes of the count rate due to varying decay of the induced activity during irradiation. This effect can be compensated for by shunting the charging condenser of the monitor instrument with a resistor of such a value that the decay time of the electric charge on the condenser equals the decay time of the induced activity. (b) When counting the annihilation photons from the irradiated positron-emitting samples, back-

TABLE 3.2—*Physical data for threshold of nuclear reactions*

Relevant Feature of Reaction	Reaction			
	$^{63}Cu(\gamma,n)^{62}Cu$	$^{16}O(\gamma,n)^{13}O$	$^{13}C(\gamma,n)^{11}C$	$^{16}O(\gamma,2n)^{16}O$
Threshold energy (nuclear mass data,[a] corrected to laboratory system)	10.855 (±0.005) MeV	15.678 (±0.001) MeV	18.737 (±0.001) MeV	28.916 (±0.001) MeV
"Breaks" of activation curve[b]	—	15.86 MeV 15.99 MeV 16.22 MeV 17.27 MeV	18.79 MeV 18.86 MeV 19.00 MeV	—
Induced radioactive transformation	$^{62}Cu \xrightarrow{\beta^+} {}^{62}Ni$	$^{15}O \xrightarrow{\beta^+} {}^{15}N$	$^{11}C \xrightarrow{\beta^+} {}^{11}B$	$^{14}O \xrightarrow{\beta^+} {}^{14}N$
Half-life	9.73 min[c]	124 s[e]	20.5 min[d]	70.48 (±0.15)s[g]
Radiation	β^+, annihilation photons (0.511 MeV)	β^+, annihilation photons (0.511 MeV)	β^+, annihilation photons (0.511 MeV)	β^+, γ(2.3 MeV), annihilation photons (0.511 MeV)[d,e]
Probe material	Copper	Water	Benzene[d]	Water[f]

[a] Wapstra and Gove, 1971.
[b] Geller *et al.*, 1960.
[c] Hawkins *et al.*, 1961.
[d] Pohlit, 1965.
[e] O'Connell *et al.*, 1959.
[f] Breuer and Pohlit, 1962.
[g] Alburger, 1972.

ground may be reduced by using a scintillation counter with a single channel analyser tuned to the total absorption peak (0.511 MeV). (c) The square root of the net number of counts may be plotted against the reading of the panel energy meter as this will give a nearly straight line which is suitable for extrapolation to zero net counts. The panel meter reading for zero net counts corresponds to the threshold energy (SCRAD 1966, NACP 1972).

The nuclear activation threshold method is particularly suitable with betatrons because the energy can be varied continuously.

3.3.2.2. Measurement of Cerenkov Emission Threshold. The onset of Cerenkov radiation emission can be used for the determination of the electron energy (von Arx *et al.*, 1970; Svensson, 1970). For this purpose, a gas-filled tube is positioned lengthwise in the electron beam. A mirror is fixed at the far end of the tube to reflect the Cerenkov photons produced inside the tube through a window mounted on the side wall to a photomultiplier (Fig. 3.15).

The number of Cerenkov photons detected is given by (Frank and Tamm, 1937):

$$N = \text{const}\ \Phi\left(1 - \frac{1}{\beta^2 n^2}\right) \qquad (3.16)$$

where Φ = electron fluence
β = ratio between velocity of the electron and light in vacuum
n = mean refractive index for the measured wavelength of emitted light.

The energy of the electrons is kept constant and the refractive index of the gas is decreased by reducing the gas pressure until no Cerenkov photons are detected (Fig. 3.16). At this threshold, β becomes β_{th} and is equal to $1/n$ as can be seen from Eq. 3.16. Because the refractive index for gases at different pressures is known, β_{th}, the relative velocity of the electrons at the threshold

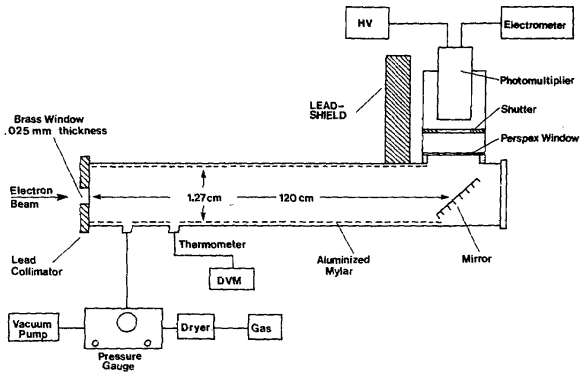

Fig. 3.15. Apparatus used for Cerenkov threshold measurements (Svensson, 1970; de Almeida and Almond, 1974b). The uncertainty due to energy losses in the air is directly proportional to the pressure and tube length. Therefore, in the low energy range, where high pressures are necessary, shorter tubes than the above should be used.

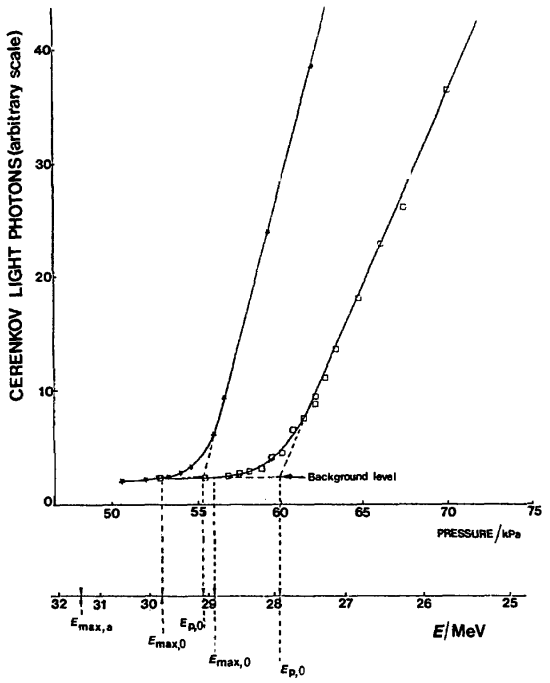

Fig. 3.16. Two Cerenkov light output curves measured at the same maximum accelerator energy, $E_{max,a}$ = 31.4 MeV (determined by the activation method, see Section 3.3.2.1). Curve A is measured with the standard foils in the beam and curve B with an extra 0.99 mm Cu foil. The nonlinear part of the curves depends mainly on the energy spread in the beam. This spread is largest in Curve B (Svensson, 1970).

can be determined. The kinetic energy of the electrons at the threshold, E_{th}, follows from the relation

$$E_{th} = m_e c^2\{(1 - \beta_{th}^2)^{-1/2} - 1\} \qquad (3.17)$$

where $m_e c^2$ is the rest energy of the electron. The refractive indices may vary somewhat over the spectral sensitivity region of the photomultiplier. Liesem and Pohlit (1978) showed that for their experimental set-up, a systematic error of up to 0.3% was obtained in the determination of E_{th} in the energy range of 20–55 MeV if the variation of n with wavelength was disregarded. A narrow-band optical filter in front of the multiplier, having maximum transparency in the range of the maximum multiplier sensitivity, could be used, but would decrease the sensitivity of the Cerenkov tube assembly, which might influence the uncertainty. Liesem and Pohlit (1978) gave correction factors to be used for their multiplier in the absence of a filter.

The light intensity generated by a monoenergetic electron beam increases linearly with the pressure above that of the threshold, $p - p_{th}$, for a large pressure range; a departure from linearity of 0.1% for air at room temperature is obtained at a value of $p - p_{th}$ of about 250 kPa (Liesem, 1976). For an electron beam of broad spectral distribution, the Cerenkov light intensity will instead increase faster than linearly as more and more electrons exceed the threshold when the pressure is raised (Fig. 3.16). The Cerenkov method could be used in that case as an approximate method for the determination of the relative distribution in energy of the high energy part of the electron spectrum (von Arx *et al.*, 1970).

The Cerenkov method can be used for the measurement of $E_{max,0}$ from the determination of the pressure for the onset of Cerenkov radiation. A linear part of the curve is obtained for pressures above that where all of the incident electrons have passed their threshold values. A well-defined point is obtained from the extrapolation of the linear part of the light intensity curve to the background reading (Fig. 3.16). For an electron beam with a broad energy distribution, but without a "tail" of low energy electrons, the extrapolation will give $\overline{E}_0$ (von Arx, 1970; Liesem *et al.*, 1974). For this type of distribution, $\overline{E}_0 \approx E_{p,0}$. Electron beams that have passed through foils or other materials will have an increased Γ (see Fig. 3.13) and a low energy tail due to energy straggling and secondary electrons. Such distributions may yield an approximately linear increase of the light intensity at large pressures, as only a small fraction of the tail has an energy sufficient to generate Cerenkov light in the pressure range normally used for extrapolation. The low energy tail may, however, contribute significantly to the reduction of the true mean energy of the electrons, $\overline{E}_0$. Svensson (1970) showed experimentally that the energy parameter determined with the Cerenkov extrapolation method in this case was well related to $E_{p,0}$ because the tail is disregarded. Thus, experiments with and without foils in the beam resulted in differences in the energy closely corresponding to ΔE_{col} (see Eq. 3.11). This experiment also explains the very good agreement between the energy, as determined

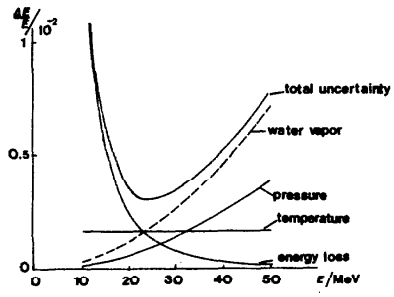

Fig. 3.17. The influence of different variables on the total uncertainty in the energy when basing the determination on Cerenkov threshold measurements in air. The largest contribution in the low-energy range is obtained from the energy loss in air. The tube length was relatively short (30 cm) in order to minimize this influence. The total uncertainty was determined by taking the square root of the sum of squares of all the separate uncertainties (modified from Liesem, 1976). The contribution from water vapor can be eliminated by using dry air.

TABLE 3.3—*Suitable gases for Cerenkov threshold measurements in energy determinations.*

Gas	Threshold/MeV
Helium	59.5
Hydrogen	29.5
Air	20.2
Methane	16.5
Carbon dioxide	16.0
Pentane	8.0

The threshold is valid at STP, i.e., p = 101.3 kPa and T = 273.15 K, and at a wavelength of about 420 nm, which is at the maximum sensitivity region of many photomultipliers. The refractive index is relatively insensitive to changes in wavelength; thus, a change of the sensitivity maximum of the photomultiplier of 50 nm at 30 MeV would change the threshold by about 0.2 MeV (Liesem *et al.*, 1974).

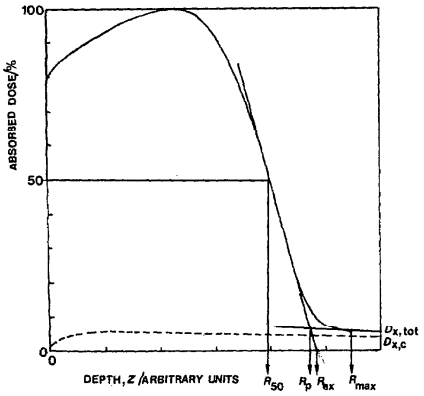

Fig. 3.18. Definition of different range parameters. $D_{x,tot}$ is the bremsstrahlung background from (1) photons generated in the absorber and (2) photon contamination in the electron beam incident on the absorber. $D_{x,c}$ is the absorbed dose from the contaminating photons only. The definitions of R_{50}, R_p, R_{ex}, and R_{max} are given in the text.

by the practical range-energy relationship (de Almeida and Almond, 1974b), and the Cerenkov method, as both methods give an approximate value for $E_{p,0}$ (see Sec. 3.3.2.3).

Air can be used as the gas in the Cerenkov tube in the energy range between approximately 14 and 50 MeV. The uncertainty increases due to energy loss in the air of the tube at low energies whereas, at high energies, uncertainties are mainly due to the influence of water vapor. The total uncertainty can be estimated from Fig. 3.17. Other gases can be used at lower and higher energies (Table 3.3).

The Cerenkov threshold determination method is particularly valuable as the measurements can be made at a constant energy setting of the accelerator; the energy of many clinical accelerators (linear accelerators and microtrons) cannot be varied continuously in a simple way.

3.3.2.3 Range Measurements. Absolute determinations of the kinetic energy of electrons by the use of nuclear reactions or the Cerenkov threshold are rather laborious and need special equipment. There is, however, a much simpler indirect method of energy determination which uses empirical relationships between the kinetic energy and range parameters of the penetration of electrons in various materials. Several range parameters are in common use (Fig. 3.18), measured from depth dependence of absorbed dose, ionization or planar fluence curves. Slightly different ranges are obtained from these curves with the largest differences at high energies. The range definitions which follow apply to depth versus absorbed-dose curves, but analogous definitions can be written for ionization and transmission curves (see Section 2.7.3). Range parameters of special importance in describing the quality of an absorbed dose distribution are defined in Section 6.4.3.

The *maximum range*, R_{max}, is defined as the depth at which extrapolation of the tail of the central-axis depth versus absorbed-dose curve meets the bremsstrahlung background. A linear relationship between the electron energy and maximum range measured in PMMA and aluminum at the phantom surface was demonstrated for 10–25 MeV electrons by Breuer *et al.* (1958) and Pohlit (1965). The maximum range does not depend on the irradiation geometry, but it has the drawback of not giving a very well-defined measurement point.

The *practical range*, R_p, is defined as the point where the tangent at the steepest point (the inflection point) on the almost straight descending portion of the depth versus absorbed dose curve meets the extrapolated bremsstrahlung background[8] (Fig. 3.18). Most measurements of R_p are based on depth-ionization curves determined with gaseous detectors (e.g., Markus, 1961; Nüsse, 1969; Harder and Schulz, 1972). Due to the variation of the stopping-power ratio with depth, the practical range determined from depth versus absorbed-dose curves is about 1 mm larger at 30 MeV (Svensson and Hettinger, 1971) for water and tissue equivalent materials than would be so if the stopping power ratio was constant. The difference is even larger at higher energies and for beams contaminated with x rays. For the determination of central axis depth versus ionization or absorbed-dose curves, the methods described in Section 6.4 can be used. In the determination of depth ionization curves, the effective point of measurement (see Section 4.1.3) of the chamber must be

[8] Some investigators make the extrapolation down to the depth axis (e.g., Tabata *et al.*, 1971a; Seltzer *et al.*, 1978) as they do not have any background contamination. The symbol R_{ex} is used here for this range.

TABLE 3.4—*Energy-range relations*

Equation	Quantity Measured	Quantity Calculated	Recommended Constants	Recommended Energy Range
3.19	R_p in H_2O phantom[a] by depth versus ionization or depth versus absorbed dose	$E_{p,0}$	$C_1 = 1.95$ MeV cm^{-1} $C_2 = 0.48$ MeV	3 MeV $\leq E_{p,0} \leq$ 25 MeV
3.19	R_p in Al phantom by depth versus ionization	$E_{p,0}$	$C_1 = 5.09$ MeV cm^{-1} $C_2 = 0.20$ MeV	5 MeV $\leq E_{p,0} \leq$ 25 MeV
3.21	R_p in H_2O phantom[a] by depth versus ionization or depth versus absorbed case	$E_{p,0}$	$C_3 = 0.22$ MeV $C_4 = 1.98$ MeV cm^{-1} $C_5 = 0.0025$ MeV cm^{-2}	1 MeV $\leq E_{p,0} \leq$ 50 MeV
3.22	R_{50} in H_2O phantom by depth versus absorbed dose	$\bar{E}_0$	$C_6 = 2.33$ MeV cm^{-1}	5 MeV $\leq \bar{E}_0 \leq$ 35 MeV

[a] R_p can also be measured in other low atomic number phantoms by making use of Eq. 3.20.

known. In order to reduce the uncertainty, plane-parallel chambers with only a small distance between the plates are recommended, because these have a well defined effective measurement point at the inner surface of the entrance window. The practical range can either be measured by a broad detector in a narrow beam (designated as geometry a) or a narrow detector in a broad beam (designated as geometry b) (Harder, 1965c; Nüsse, 1969), i.e., (a) using a detector with a diameter larger than the practical range in a beam whose diameter is very small compared to the electron range or (b) using a beam with a diameter larger than the practical range and a detector diameter very small compared to the beam diameter.

The beam divergency in geometry b must be corrected for by the inverse square law

$$D_{m,z} = D'_{m,z}\left[\frac{s_{vir} + z}{s_{vir}}\right]^2 \qquad (3.18)$$

where s_{vir} is the virtual source-to-phantom surface distance and $D'_{m,z}$ is the absorbed dose to the medium (m) at a depth z for the uncorrected curve. Approximate corrections are adequate as R_p is not very sensitive to changes in s_{vir} (see Brahme and Svensson, 1976a).

The following empirical range and energy relationships are valid for a broad electron beam incident perpendicularly on a semi-infinite phantom. Their coefficients are given in Table 3.4. The range-energy relationship determined by Markus[9] (1961), based on magnetic spectrometer energy measurements and depth-ionization curves determined in low atomic number materials, is recommended in several national protocols (SCRAD, 1966; DIN, 1976; NACP, 1980)

$$E_{p,0} = C_1 R_p + C_2 \qquad (3.19)$$

Equation 3.19 can also be used for aluminum (Katz and Penfold, 1952) but with constants C_1 and C_2 differing from those for water (Table 3.4).

The general scaling law of Section 2.8.3 may also be used to calculate the most probable energy from range measurements in an arbitrary material (m). The value of the water-equivalent (w) practical range R_p to be inserted in Eq. 3.19 and also in Eq. 3.21 below can be estimated from

$$R_p = R_{p,m}\frac{\rho_m}{\rho_w}\frac{r_{0,w}}{r_{0,m}} \qquad (3.20)$$

where r_0 is the continuous-slowing-down range (Table 2.5). This relationship is very accurate in low atomic number phantom materials or for materials with $(\bar{Z}/\tau)_m$ not too different from that for water, $(\bar{Z}/\tau)_w$. When this is no longer the case, the dependence of $r_0/\rho R_p$ on $\bar{Z}/\tau$ has also to be taken into account (compare Fig. 2.22) and the simple Eq. 3.20 is not valid.

Nüsse (1969) and Harder and Schulz (1972) showed that Eq. 3.19 can be used for monoenergetic electrons from a few MeV up to 30 MeV both for aluminum and water, with an uncertainty not exceeding 2%. A nonlinearity caused by the increasing importance of the radiative energy losses is observed beyond about 30 MeV and increases with energy. A modified equation for water which takes this effect into account is

TABLE 3.5—*Materials for practical range determinations* (adapted from DIN 6809, 1976)

Material	$\left(\frac{Z}{A}\right)_{eff}$	$\left(\frac{Z^2}{A}\right)_{eff}$	ρ/g cm^{-3}
Water	0.555	3.67	1.00
Perspex, Lucite (PMMA)	0.540	3.16	1.15 – 1.20
Polystyrene	0.538	2.84	0.98 – 1.11
Polyethylene	0.571	2.71	0.92 – 0.97
Graphite	0.500	3.00	1.7 – 1.9

[9] Markus' relation was originally determined in the energy range 3–15 MeV for broad beams with narrow energy distributions (I'_0 = 1.6% at 3.2 MeV and 0.6% at 14.2 MeV) as $R_p\rho(Z/A)_{eff} = k_1 E_0 - k_2$, provided that $(Z^2/A)_{eff} < 4$ (Markus, 1961; DIN, 1976). In this equation, $(Z/A)_{eff} = \sum_i p_i Z_i/A_i$, where p_i is the fraction by mass of the constituent element of nuclear charge, Z_i and atomic mass, A_i. Numerical values for some commonly used materials are given in Table 3.5. The value of the physical constants are, $k_1 = 0.285$ g cm^{-2} MeV^{-1} and $k_2 = 0.137$ g cm^{-2}.

$$E_{p,0} = C_3 + C_4 R_p + C_5 (R_p)^2. \quad (3.21)$$

This relationship agrees from 1 to 50 MeV within ±1% with practical ranges extracted from Monte Carlo calculated depth versus absorbed-dose curves between 1 and 60 MeV by Berger and Seltzer (1969a), and with experimental data between 1 and 20 MeV from Tabata *et al.* (1971b), between 3 and 15 MeV by Markus (1961), and extended to 25 MeV by Nüsse (1969), between 4 and 30 MeV by Freyberger (1964), between 30 and 60 MeV by Harder and Schultz (1972), and between 10 and 50 MeV by Brahme *et al.* (1980a).

Equations 3.19 and 3.21[10] were originally determined for beams with a very small energy spread. Measurements by Svensson and Hettinger (1971) of R_p from clinical accelerator beams with various energy spectrum widths gave a consistent relationship between the most probable energy at the phantom surface, $E_{p,0}$, and the practical range, R_p, in agreement, within the uncertainty of measurement, with Markus' equation.[9] Equations 3.19 and 3.21 are, therefore, valid not only for monoenergetic beams, but also for beams with some energy spread, provided the energy distribution is of the straggling type (see Figs. 2.2, 3.13, and Section 3.3.1.2). The energy calculated from R_p should thus be very close to the most probable energy at the surface if the energy spread is produced in foils or other materials in the beam. This is also the case if the energy distribution of the electrons from the accelerator is broad, but of a similar shape to the straggling distribution (Fig. 2.2), which is the case with most linear accelerators (see Section 3.3.1.1).

The angular spread of the electrons at the phantom surface has not always been taken into account in experimental determinations of the energy-range relationships. From Eq. 3.10 it is obvious that a mean square angular spread ($\overline{\theta^2}$) of only 0.01 radian^2 will decrease the practical range by about 0.5%. The experimental arrangements of Nüsse (1969), who used a broad, slightly divergent beam and small detector with a correction for beam divergence according to Eq. 3.18, and of Harder and Schulz (1972), who used a broad detector and narrow pencil beam, in effect had a beam of insignificant angular spread, so that the numerical values of the constants of Eqs. 3.19 and 3.21 given in Table 3.4 are precisely valid for a very small angular spread. For electron beams where the angular spread is appreciable, the range-energy relationship can only be used with a good precision if the correction supplied by Eq. 3.10 is applied. Only rough values for the most probable energy are, however, obtained where the scattering in collimators and air is large (see Section 3.2.4.3 and Table 3.1).

The *half-value depth*, R_{50}, is defined as the depth at which the absorbed dose has decreased to 50% of its maximum value. Brahme and Svensson (1976a) showed from measurements on different medical accelerator beams that R_{50} in water is approximately related to the mean electron energy at the phantom surface by

$$\overline{E}_0 = C_6 R_{50} \quad (3.22)$$

The recommended numerical value of C_6 is given in Table 3.4. The equation is valid in the energy range 5–35 MeV for broad beams perpendicularly incident on a water phantom if R_{50} is determined from depth versus absorbed-dose curves and if the energy distribution is of the Landau-Vavilov straggling type (Section 2.4.2). Geometries a and b above give somewhat different R_{50} values according to measurements by Pohlit (1965). The constant in Eq. 3.22 was determined in geometry b and consequently is strictly valid only for this geometry.

3.4 Time Structure

Most high energy electron accelerators produce beams with some kind of time structure due to inherent acceleration principles (exceptions may be found among the electrostatic machines).

In induction accelerators like betatrons, the beam is generally pulsed with the same repetition frequency as the line voltage, i.e., 50 or 60 Hz, with a pulse separation of about 20 ms. However, some betatrons run at higher pulse repetition frequencies extending up to 500 Hz. The length of each betatron pulse generally lies in the range 1–20 μs depending on the method of extraction.

For microwave-powered accelerators like the linear accelerator and the microtron, the pulse repetition frequency can vary from values as low as 10 Hz up to about 500 Hz for the highest photon dose rates. The length of each such macropulse is generally in the range 1–5 μs with a fine structure depending on the microwave frequency. The most common frequency range is the S-band, with frequencies around 3 GHz, or wavelengths close to 10 cm.

The time structure of the electron beam current [$I(t)$] from a typical microwave accelerator may, therefore, look like that shown in Fig. 3.19. Each macropulse consists of a large number of micropulses of about 30-ps duration, separated by a pulse interval of 0.3 ns or, expressed differently, the electrons are grouped in about 1-cm long micropulses which are 10-cm apart. The figure illustrates the situation for photon therapy. For electron therapy, the average current is reduced by two to three orders of magnitude from that employed in

[10] The inverse relation to Eq. 3.21 may sometime be of interest and is given, to a good approximation, by $R_p = C_7 + C_8 E_{p,0} + C_9 (E_{p,0})^2$, where $C_7 = -0.11$ cm, $C_8 = 0.505$ cm MeV^{-1} and $C_9 = -0.0003$ cm MeV^{-2}.

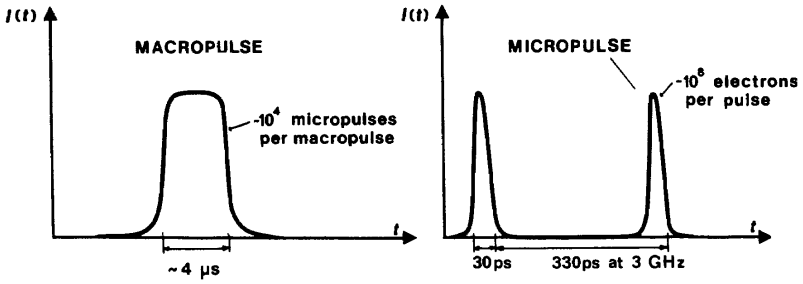

Fig. 3.19. Typical time structure of the electron beam from a microwave-powered accelerator used for photon therapy.

photon therapy to obtain the conventional dose rate of a few gray per minute (2 Gy min^{-1} corresponds to a mean current density of about 15 pA cm^{-2}). This is done either by reducing the peak current, the macropulse length or the pulse repetition frequency or a combination of these three parameters.

4. Determination of Absorbed Dose

4.1. Relationship Between Absorbed Dose in the Detector and in the Medium

4.1.1 General

In order to measure the absorbed dose, D_m, to a medium (phantom), m, at a point of interest, P, a small piece of the medium surrounding this point is replaced by a detector. Generally, the detector consists of a radiation-sensitive material, i, and, in many cases, also of a wall, container, or cover, w, surrounding it (see Fig. 4.1). The dimensions of such a detector should be small enough to give the required spatial resolution and to minimize—as far as possible for the given requirements of sensitivity and precision—the perturbation of the particle fluence that occurs when the detector is inserted into the medium. When the radiation-sensitive material is so large that the dose varies within it, its response is a measure of the *mean* absorbed dose in it.

This general description of the detector applies to all kinds of dosimeter systems: gas-filled ion chambers as well as calorimeters, chemical, photographic, thermoluminescent, radiophotoluminescent and other solid state dosimeters. Ion chambers containing air as the radiation-sensitive material, surrounded by air-equivalent or other non-medium equivalent walls, are examples of "walled" detectors. The charge-collecting electrodes and the insulator form parts of the wall for both cylindrical ("thimble") and for flat ("coin-shaped") ionization chambers. Solid-state detectors such as LiF rods or chips, when inserted without a cover into a phantom material, m, are examples of "wall-less" detectors. Air-filled ion chambers with water-equivalent walls, when used in a water phantom, can be described as wall-less, air-filled cavities in water.

A determination of the absorbed dose at a specified location in a medium normally consists of two principal steps, namely: (1) the determination of the mean absorbed dose to the radiation-sensitive material, i, of the detector surrounding the specified location by using either an appropriate calibration factor or performing an absolute measurement, (2) the determination of the absorbed dose to the medium at the point of interest in the undisturbed medium by calculations based on knowledge of the mean absorbed dose to the radiation-sensitive detector material and the stopping and scattering properties of the medium and the detector material.

The second step is the main subject of this section, whereas the first step is treated in detail in Section 5.

4.1.2 Small Detector

For a detector which is so small that the electron fluence with the detector in place is the same as that existing at the point of interest in the undisturbed medium, the Bragg-Gray relationship

$$D_m = D_i \, s_{m,i} \tag{4.1}$$

can be used for calculating the absorbed dose, D_m, to the medium at the point of interest. In this equation D_i is the absorbed dose to the radiation-sensitive material and $s_{m,i}$ is the mass collision stopping power ratio which accounts for the differences in energy deposition per unit mass in materials m and i. For such a small detector, it is sufficient to evaluate $s_{m,i}$ for the electron spectrum at the point of interest (where this is the same as the center of the detector) in the uniform medium. This problem is treated in detail in Section 4.3.

4.1.3 Large Detector

In practical dosimetry, it is often not possible to construct a sufficiently small detector with adequate sensitivity. Most practical detectors contain a radiation-sensitive material which is so large that the electron fluence rate, and thus the absorbed dose rate, may vary appreciably within it. The detector will consequently "sense" the electron fluence rate not at a point, but over a *spatially extended region.* Furthermore, the material of the detector often differs from that of the medium, so that the electron fluence rate in the radiation-sensitive material will be different from that at the point of interest in the undisturbed medium.

Although the Bragg-Gray conditions are no longer applicable, one may use an equation similar to Eq. 4.1 by replacing D_i there by the measured $\overline{D}_i$ in the large detector and making adjustment for the effects of the spatial extension of the detector and of its perturbing action on the electron fluence rate.

The characteristics of the radiation field in an electron-irradiated material, i.e., the rapid change of the electron fluence rate and of the electron energy and angular distribution with depth, have led to a two-step approach: First, the perturbation of the electron fluence rate due to the presence of the detector material (i) in the medium (m) is corrected by using the "perturbation correction factor", $p_{m,i}$ (Harder, 1968). Second, the effect of the spatial extension of the detector is overcome by the introduction of the concept of an "*effective point of measurement*", P_{eff} (Skaggs, 1949). The location of P_{eff} may be different from that of the center of the detector. The detector is placed so that P_{eff} is at the point of interest. The effective point of measurement is treated separately for a gas-filled detector (Section 4.2.1) and for a solid or liquid (Section 4.2.2.2).

After the introduction of the effective point of measurement and the perturbation correction factor, $p_{m,i}$, Eq. 4.1 takes the form

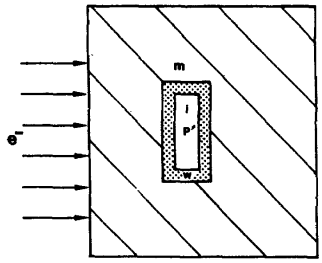

Fig. 4.1. Schematic representation of a detector for absorbed dose measurements. The detector is placed with its center at a point P′ (this may or may not be the "point of interest, P") within the electron irradiated medium (phantom), m. The detector consists of the radiation-sensitive material, i, and, often, a surrounding wall, w. "Wall-less" detectors have either no wall or a medium-equivalent wall.

$$D_m\,(P_{eff}) = \overline{D}_i\, s_{m,i}\, p_{m,i} \qquad (4.2)$$

where $\overline{D}_i$ is the mean absorbed dose to the radiation sensitive material and $s_{m,i}$ is the mass collision stopping-power ratio for the materials m and i, calculated for the electron spectrum existing in the undisturbed medium at P_{eff}.

4.2 Location of Effective Point of Measurement and Values of Perturbation Correction Factor

4.2.1 Gas-Filled Detectors

4.2.1.1 Flat Ion Chambers. A coin-shaped cavity ion chamber with a guard-ring provides a means of essentially eliminating perturbation effects in the determination of absorbed dose in a uniform medium. Figure 4.2 shows schematically such a chamber placed in a beam with its axis parallel to the incident beam and located, respectively, at positions in a uniform medium where the fluence is increasing, constant, and decreasing (Svensson, 1981). In the chambers, C represents the ion collector plate, G the guard-ring (coplanar with the collector plate), and F the other parallel plate of the ion chamber. The relative absorbed dose to photographic film placed in the GCG plane is given in the figure. At each depth, a relative dose of 1.0 represents the absorbed dose at that depth, but removed from any fluence perturbation produced by insertion of the chamber. For all three cases, as the location of the chamber is approached laterally, the dose to the film decreases because of lack of electrons scattered from the uniform medium that has been replaced by gas in the cavity. This is followed under G by an increase due to electrons entering the cavity through the periphery of the circular part of the cavity. Finally, under C, the relative absorbed dose is equal to that at the depth corresponding to the location of F, whether the ion chamber is in place or not. Thus, the absorbed dose obtained from the ion charge collected on C is constant throughout the region of collection and equal to the absorbed dose to the gas at F in the uniform medium. The center of the front surface, F, of the gas-filled cavity can, therefore, be considered as a good approximation to the effective point of measurement.

The guard-ring serves two purposes. It is wide enough so that the lines of force from the electrical collecting

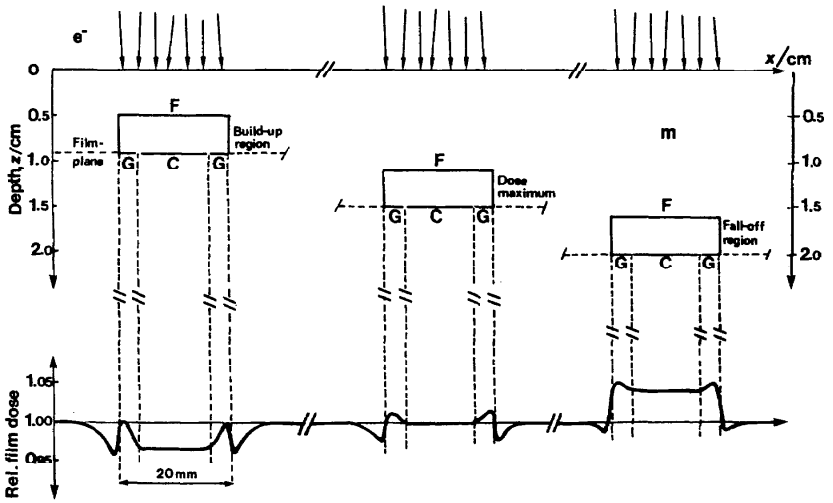

Fig. 4.2. The relative absorbed dose distribution in the GCG plane behind a 4-mm thick coin-shaped air cavity with surface F at depths, z, of 0.5, 1.1 and 1.6 cm in a polystyrene phantom when irradiated by a 6.3 MeV electron beam. Note that the 20-mm diameter and the 4-mm thickness of chamber have different scales (Svensson, 1981). The film location for the relative dose determination in the GCG plane is indicated by the horizontal dashed lines; the relative film dose at each depth is indicated at the bottom of the figure.

field are perpendicular to planes C and F over the entire area of C. The guard-ring is also wide enough so that electrons entering the cylindrical periphery of the flat chambers do not produce a significant number of ions in the collecting region.

4.2.1.2 Cylindrical Ion Chambers. Cylindrical chambers are often used to determine the absorbed dose distribution in the uniform phantom. Such devices are used with their axes perpendicular to the direction of the electrons incident upon the uniform phantom. The absorbed dose is generally not constant throughout the collecting region as it is for the coin-shaped chamber. Thus, the determination of the effective point of measurement is not as simple as it is for the coin-shaped chambers, nor is the perturbation effect eliminated. Generally, these cannot be readily separated, but measuring conditions may be set so that each can be measured independently.

The magnitude of the perturbation correction factor, $p_{m,g}$, when the radiation sensitive material is a gas is obtained experimentally from a comparison of data obtained with the cylindrical chamber and the flat coin-shaped chamber at or near the broad dose maximum of the depth-dose curve. In this region, the location of the effective point of measurement is unimportant because the absorbed dose in the uniform medium is constant.

Johansson *et al.* (1978) made measurements of the perturbation correction for thin-walled (0.5 mm) cylindrical chambers with their axes perpendicular to the electron beam for mean electron energies between 2.5 and 22 MeV at the depth-dose maximum in polymethyl methacrylate (PMMA). Their results (Fig. 4.3 and Table 6.4) show that the perturbation correction factor decreases with increasing chamber diameter and decreasing electron energy. It may be noted that the perturbation correction factor for a chamber cavity radius of 2.5 mm in PMMA given here is nearly 2% lower at $\bar{E}$ = 4 MeV than that in water given in ICRU Report 21 (ICRU, 1972), but that the factors are nearly equal at 20 MeV.

The strong variation of the perturbation correction factor with energy implies that relative dose measurements are also affected when made at different depths in a phantom with a given incident electron beam. However, the variation of $p_{m,g}$ with depth, z, and hence with $\bar{E}_z$, for a specified electron beam, is not necessarily given by the results of Johansson *et al.*, which were obtained at the depth-dose maxima in beams of different initial energy.

The numerical values for the perturbation factor that Johansson *et al.* obtained, strictly apply only in PMMA, but as the linear scattering power (Section 2.2.6) of water differs from that of PMMA by only a few percent, their values may also be used in a water phantom. It should be noted that thin-walled (0.5 mm) chambers of similar diameter but with walls made of various commonly-used materials (e.g., graphite, A 150, PMMA) have been experimentally shown to have the same perturbation correction factor (Nahum and Svensson, 1981).

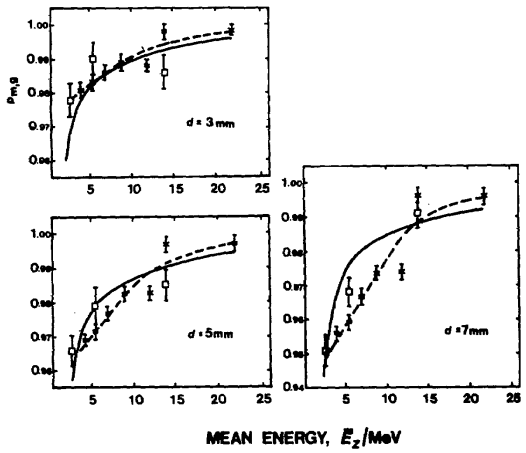

Fig. 4.3. The perturbation correction factor, $p_{m,g}$, for cylindrical ionization chambers with the cylinder axis perpendicular to the beam axis. The diameters were d = 3, 5, and 7 mm, respectively. Experimental data: from Johansson *et al.* (1978) measured at the depth of dose maximum in PMMA (□ from comparison with a flat chamber; x using an extrapolation to d = 0). The dashed curve is fitted to the experimental data; the values in Table 6.4 are taken from these curves. The full curve was calculated using Eq. 4.3 with T_m values from Table 2.6.

Harder (1968) carried out a theoretical evaluation of $p_{m,g}$. Applying his method, but using a better approximation for the cross-section of the thimble chamber, Harder (1980) obtained the relationship

$$p_{m,g} = 1 - 0.096\sqrt{r\,T_m} \qquad (4.3)$$

where r is the chamber radius and T_m is the linear scattering power for the medium, m (Section 2.2.6). This gives fairly good agreement with the measured data of Johansson *et al.* (1978) (see Fig. 4.3). However, they found that at a given $\bar{E}_z$, $(1 - p_{m,g})$ was proportional to the chamber radius, and not to the square root of the radius as predicted by Eq. 4.3. This emphasizes the approximate nature of the theoretical treatment.

The effective point of measurement for a cylindrical chamber may be determined at depths other than that of the broad maximum by first applying the perturbation correction factor to the reading from the cylindrical chamber and then finding the depth where the same absorbed dose is measured with the coin-shaped chamber. Experimental results have been reported in the energy range from 3 MeV to 34 MeV (Dutreix and Dutreix, 1966; Hettinger *et al.*, 1967; Weatherburn and Stedeford, 1977; Johansson *et al.*, 1978). The effective point of measurement was found to be a distance of 0.5r

$\pm$ 0.1r nearer the phantom surface than the geometric center of the cylindrical chamber, where r is the chamber cavity radius. When the uncertainty of 0.1r is unacceptable, a cylindrical chamber of smaller radius or a flat coin-shaped chamber should be used.

Theoretical calculations have also been made for the effective point of measurement (see, for example, Skaggs, 1949; Dutreix and Dutreix, 1966; and Harder, 1977), but because of the convention used, the assumptions made and the approximations inherent to the calculations, exact comparisons with the experimentally derived location of the effective point of measurement given above can not be made.

4.2.2 Solid and Liquid Detectors

The rationale for the modification of the Bragg-Gray relationship to make it appropriate for extended volume solid and liquid radiation-sensitive materials differs from that used for gaseous materials. Interactions with the solid or liquid radiation-sensitive material will appreciably modify the fluence of electrons in that material and this must be taken into account in the treatment of the perturbation effects (Section 4.2.2.3) and in determining the effective point of measurement (Section 4.2.2.2).

4.2.2.1 Reference Volume. For simplicity, only the most common case of flat detectors with negligible lateral scattering effects is treated here, even though a generalization to more complex detector shapes is conceivable. It is convenient to define a *reference volume* as a first step in determining the effective point of measurement in the undisturbed medium, P_{eff}, and the perturbation correction factor, $p_{m,s}$, (where the radiation sensitive material is s) as well as D_m (P_{eff}), the corresponding absorbed dose which is related by Eq. 4.2 to the mean absorbed dose in the radiation-sensitive material.

The reference volume (Fig. 4.4) is located in the uniform medium in such a way that the shape of the electron spectrum (i.e., the relative electron energy distribution, irrespective of absolute normalization), averaged over the reference volume in the unperturbed medium, is as similar as possible to the spectrum averaged over the volume of the radiation-sensitive part of the detector. It is most important that the mean energy of electrons and their energy spread in the reference volume be as similar as possible to that in the radiation-sensitive part of the detector because existing tabulations of mass collision stopping power ratios may then be used (see Table 6.3 or Eq. 4.11). The thickness of the reference volume is then related to that of the radiation-sensitive part of the detector by the ratio of the linear total stopping power of the sensitive material in the detector to that of the uniform medium (Gray, 1936, used a similar scaling law for the spectrum of

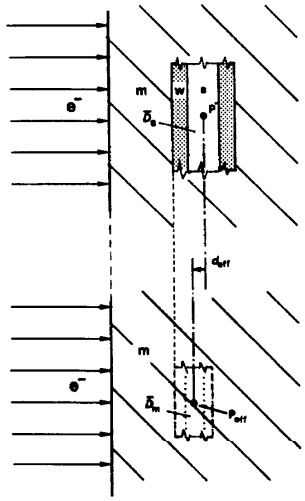

Fig. 4.4. Definition of the reference volume in the uniform medium (indicated by the area within dotted lines in the lower half of the figure), the effective point of measurement, P_{eff}, and the shift, d_{eff}, of P_{eff} from P′ for solid and liquid detectors. In this figure, it is assumed that the radiation-sensitive material (s) of the detector is surrounded by a wall (w) of the same material, and that the linear total stopping power at P′ in the radiation-sensitive material is less than that for the unperturbed medium (m) at that point. The mean absorbed dose inside the radiation-sensitive material of the detector is $\bar{D}_s$ and that inside the dotted reference volume is $\bar{D}_m$. Under the assumption of a linear dose variation with depth in the detector, the effective point of measurement will be close to the center of the reference volume.

photon-generated electrons). For wall-less detectors, the front face of the reference volume is located in the same plane as that of the front face of the radiation-sensitive part of the detector (cf. Fig. 4.4). In the case of a medium-equivalent detector (with respect to atomic composition and density, cf. Section 6.2.2), such as the ferrous sulphate dosimeter in a water phantom, the radiation-sensitive part of the detector volume and the reference volume coincide, and the perturbation correction factor is unity.

However, the requirement that the mean energy and energy spread be the same in the detector material and the medium, m, does not necessarily mean that the electron fluence in the two are equal. Thus the mean dose in the radiation-sensitive material, $\bar{D}_s$, as indicated by the detector is related to the mean dose in the reference volume of the medium, $\bar{D}_m$, by

$$\bar{D}_m = \bar{D}_s \, s_{m,s} \, p_{m,s} \qquad (4.4)$$

where $s_{m,s}$ is the mass collision stopping power ratio of the medium (m) to that of the material (s), and $p_{m,s}$ is the perturbation correction factor, which corrects for the differences in mean fluence in the detector and the reference volumes.

4.2.2.2 Effective Point of Measurement. Rather than the mean value of the absorbed dose in the refer-

ence volume, the absorbed dose at a point in the uniform medium is usually desired. The effective point of measurement, P_{eff}, in the reference volume is the point at which the absorbed dose, D_m (P_{eff}), is equal to the mean absorbed dose in the reference volume, $\overline{D}_m$. Thus

$$D_m(P_{eff}) = \overline{D}_s s_{m,s} p_{m,s} \tag{4.5}$$

When the absorbed dose variation with depth in the solid or liquid radiation-sensitive device is approximately linear, the center of the reference volume is close to the effective point of measurement. For flat detectors, the shift, d_{eff}, of P_{eff} from P′ is then given by

$$d_{eff} = \left(1 - \frac{S_{tot,s}}{S_{tot,m}}\right)\frac{t}{2} \tag{4.6}$$

where t is the thickness of the detector and S_{tot} is the sum of the linear collision and radiative stopping powers.

The effective point of measurement may be significantly shifted from the center of the reference volume if the dose distribution is varying in a strongly nonlinear fashion over the dosimeter volume. A method of determining the shift of P_{eff} from the geometric center of extended medium-equivalent detectors has been given by Brahme (1981). When the thickness, t, of the detector in the direction of interest in the phantom is constant, the measured dose profile may be corrected in a simple way for the finite detector size by using the measured data. The corrected dose distribution is given by

$$D_{corr}(x) = \overline{D}_{meas}(x) - \frac{t^2}{24}\overline{D''}_{meas}(x) + \ldots \tag{4.7}$$

where $\overline{D}_{meas}(x)$ is the measured mean absorbed dose with the detector center at a point x in the medium and x is the variable along the direction of measurement, e.g., parallel or perpendicular to the direction of the beam and $\overline{D''}_{meas}(x)$ is the second derivative of the absorbed dose with x. The resultant upstream shift of the effective point of measurement from the center of the radiation sensitive volume of the detector (P′) is therefore given in the first approximation by

$$d_{eff} = -\frac{t^2}{24}\frac{\overline{D''}_{meas}(P')}{\overline{D'}_{meas}(P')} \tag{4.8}$$

The first and second derivatives of the measured dose distribution, $\overline{D'}_{meas}(x)$ and $\overline{D''}_{meas}(x)$, may be obtained by fitting any three consecutive data points by a second order polynomial.

It is possible, in principle, to apply the reference volume approach also to a flat gas-filled ionization chamber inserted into a liquid or solid medium. Because then $S_{tot,g}/S_{tot,m} \ll 1$, Eq. 4.6 shows that the shift d_{eff} is from the center to the upstream surface of the coin-shaped cavity, in accordance with the definition of the effective point of measurement given in Section 4.2.1.1 for flat ionization chambers.

4.2.2.3 Perturbation Correction. The perturbation of the primary electron fluence by solid or liquid detectors has been investigated by Svensson and Brahme (1979). Their work treated the case of an arbitrary detector material (s) in a uniform medium (m), and was restricted to flat circular detectors with the axes parallel to the beam axis. Scattering within the radiation-sensitive material was treated in detail as it was dominant in this application, in comparison to the radiation scattered through the circular periphery which was only treated in an approximate manner. The perturbation correction factor derived by these authors has been modified here to make it applicable for use with the reference volume concept and also to take the lateral scattering effect (last term in the curly bracket of Eq. 4.9) into account in a more accurate fashion[11]

$$p_{m,s} = 1 + \frac{T_m t}{4}\left\{\frac{S_{tot,s}}{S_{tot,m}} - \frac{T_s}{T_m} - 0.43\frac{t}{r}\left(1 - \frac{T_s}{T_m}\right)\left[\frac{\sqrt{3\overline{\theta^2}(z)} + 1/\sqrt{3\overline{\theta^2}(z)}}{2}\right]\right\} \tag{4.9}$$

where t is the thickness and r the radius of the cylinder, $\overline{\theta^2}(z)$ is the mean square angular spread of the electrons in the uniform medium at the entrance surface of the cylinder at depth z, and $S_{tot,m}$ and $S_{tot,s}$ are the total linear stopping powers of the medium and the detector respectively. The expression is valid for $\overline{\theta^2}(z) > T_m t/3$, which is always fulfilled provided that $z > t/3$. Furthermore, the depth should be less than the therapeutic range (see Section 6.4.3) so that full diffusion (Section 2.5.2) has not been reached, and the planar fluence (Section 2.7.2) has not begun to decrease. The term within the square brackets in Eq. 4.9 is close to unity provided that the electrons are appreciably scattered ($\overline{\theta^2}(z) > 0.15$). It is seen that the perturbation of the primary electron fluence due to scattering within the radiation-sensitive material (first two terms inside the curly brackets) is negligible when the linear stopping power ratio equals the linear scattering power ratio. If, instead, the linear scattering powers are identical ($T_s = T_m$), no perturbation due to laterally scattered electrons should be expected.

[11] In their original paper, Svensson and Brahme (1979) do not use the reference volume concept. They take into account the perturbation of the electron fluence by means of alternative methods using either (1) a perturbation correction factor (without displacement of the measuring point) or (2) an effective point of measurement (without applying a perturbation correction). In the approach presented here, which uses the reference volume concept, two corrections have to be applied simultaneously according to Eq. 4.5: $D_m(P_{eff}) = \overline{D}_s s_{m,s} p_{m,s}$, with $p_{m,s}$ given by Eq. 4.9 and d_{eff} as given by Eqs. 4.6 or 4.8 used to obtain P_{eff} from P′.

From the general expression for the perturbation correction for a flat cylindrical dosimeter (Eq. 4.9), it can also be concluded that thin, disc-shaped detectors such as TLD will introduce a negligible effect due to scattering into the periphery of the detector. However, the effect of scattering within the detector may become significant if the difference between the linear stopping- and scattering-power ratios is large. For a 0.4 mm thick LiF-teflon TLD disc near the surface in a polystyrene phantom, $p_{m,s} \approx 0.995$ for a 5 MeV electron beam, as calculated from Eq. 4.9.

4.3 Stopping Power Ratio

4.3.1 Fundamentals

An accurate knowledge of the stopping power ratio, $s_{m,i}$, is essential for the application of the Bragg-Gray relationship (Eq. 4.1). In discussing $s_{m,i}$ it is assumed that the effects treated in Sections 4.1 and 4.2 are either negligible or corrections for them have been made. The detector material can then be considered to be exposed to the same electron fluence (both number and spectrum) as the medium m at the effective point of measurement. The quantity that $s_{m,i}$ expresses is, therefore, the ratio of the absorbed dose to the medium, D_m, to the absorbed dose to the material in the cavity, D_i, for the same primary electron fluence.

Under the idealized assumption that the electrons are dissipating their energy continuously and locally, this absorbed dose ratio is given exactly by (NCRP, 1961)

$$s_{m,i}^{BG} = \frac{\int_0^{E_{max}} (\Phi_E)_m \, (S/\rho)_{col,m} \, dE}{\int_0^{E_{max}} (\Phi_E)_m \, (S/\rho)_{col,i} \, dE} \qquad (4.10)$$

where $(\Phi_E)_m$ is the primary electron spectrum at the point of interest in medium m and $(S/\rho)_{col}$ denotes the *unrestricted* mass collision stopping power for an electron with kinetic energy E in media m and i. The word "primary" in "primary electron spectrum" is used because it is assumed, under the continuous slowing down approximation, that secondary electrons deposit their energy where they are generated so they do not contribute to the electron fluence. The secondary electrons are not absorbed at the point of their generation. However, under equilibrium conditions, secondary electrons generated upstream contribute approximately the same amount of absorbed energy as that of the secondary electrons leaving the point of generation. Thus, the assumption of local deposition of secondary electron energy at their point of production may be justified for this situation. The upper limit of the integrals is given by the maximum energy, E_{max}, of the electrons in the fluence spectrum and the lower limit corresponds to the lowest energy in the spectrum, here indicated by a zero. It should be noted that this spectrum also includes any electrons set in motion by bremsstrahlung photons. The stopping power ratio calculated from Eq. 4.10 is denoted by $s_{m,i}^{BG}$ because it applies to a cavity where it is valid to calculate the stopping power ratio from the unrestricted mass collision stopping power, a fundamental assumption in the Bragg-Gray theory (Burlin, 1968).

The assumption of "local" energy dissipation by the primary electrons is, in practice, invalidated by the relatively few large energy transfers that give rise to secondary electrons with ranges that are non-negligible compared to the physical dimensions of the detector. However, D_m is accurately given by the numerator of Eq. 4.10 if full secondary electron equilibrium has been established. This means that there is a balance between the energy carried into and out of the volume of interest by the secondary electrons (equivalent to assuming that the second term of Eq. 2.20 is negligible).

The effects of the "long-range" secondaries, or delta rays, can be seen experimentally in the dependence of the stopping power ratio on the size of a wall-less cavity within an arbitrary medium (Spencer and Attix, 1955). The original Bragg-Gray cavity theory did not consider this effect. Spencer and Attix (1955) extended the cavity theory to take account of the finite ranges of the secondary electrons. They introduced the parameter Δ, an electron energy cut-off value, that can be related to cavity size. The Spencer-Attix stopping power ratio, $s_{m,i}^{SA}$, for high-energy electron beams is treated in detail in Section 4.3.3.

An important assumption of the Bragg-Gray theory is retained in the Spencer-Attix extension to all electrons with initial energy larger than Δ, namely that the cavity does not disturb the electron fluence in any way. Transition effects in the low-energy part of the electron spectrum at the cavity edges are thus not taken into account. Such effects can be significant when the "wall" and "cavity" are made of materials with very different atomic numbers, and detectors of this nature are to be avoided if at all possible (Bragg, 1912; Holthusen, 1919; Harder, 1965b; Burlin, 1968; Bertilsson, 1975). A general method for modifying such detectors so that it becomes valid to calculate the stopping power ratio from Eq. 4.10 is described in Section 4.3.2.

In the case of electron beams, the most common application of the Bragg-Gray relationship (Eq. 4.1) is to an air-filled ionization chamber with a wall that is nearly air- or water-equivalent in a water or water-equivalent phantom. In such a situation, the polarisation or density effect (Sternheimer, 1952 and 1956; Sternheimer and Peierls, 1971) enters into the mass collision stopping power ratio and causes $s_{m,i}$ to be strongly dependent on electron energy (Laughlin, 1956, and Figs. 4.5 and 4.6). The main sources of uncertainty in the $s_{m,i}$-values to be

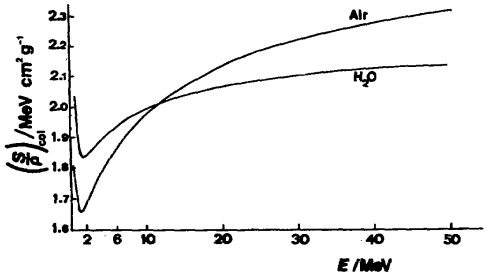

Fig. 4.5. Variation of mass collision stopping power $(S/\rho)_{col}$ for water (I = 75.0 eV) and air (I = 85.7 eV) with the density effect evaluated according to Sternheimer and Peierls (1971).

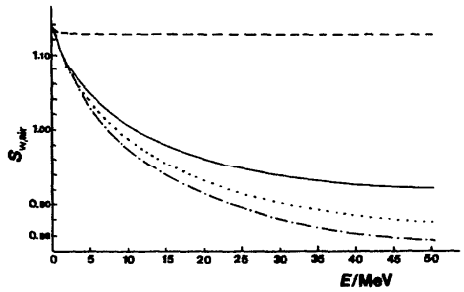

Fig. 4.6. The water/air stopping power ratio, $s_{w,air}$, evaluated at single electron energies with I-values as in Fig. 4.5: using unrestricted mass collision stopping powers and assuming zero density effect (- - - -); using unrestricted collision stopping powers and including density effect (—); using restricted stopping powers, Δ = 100 keV (·····) and Δ = 10 keV (· · · · ·) and including density effect.

used in converting the absorbed dose in the cavity gas to that in water are then the uncertainties in the electron energy distribution at the depth of interest and in the mass collision stopping-power values for each energy.

4.3.2 Transition Material Between Wall and Radiation Sensitive Material of a Detector

Most air-filled ionization chambers used in electron dosimetry for measurements in water or other tissue-like phantoms have a chamber wall which is either entirely made from graphite or has a graphite lining on its inner side. Graphite is similar to air with regard to mean atomic number which is important for electron slowing-down—the mean ionization potentials differ by less than 10 eV—and, therefore, such chambers have nearly air-equivalent walls for electrons generated in the wall. Due to the fact that the ranges of most secondary electrons in condensed materials are extremely small (less than 0.1 mm for 0.1 MeV electrons in carbon), even a relatively thin inner lining is sufficient for the primary electron beam to build up a secondary electron spectrum that is characteristic of the atomic number of the lining for all but the relatively few high-energy secondaries. The rapid change in the secondary electron spectrum near an interface is illustrated in Fig. 4.7. This, in turn, means that for an air cavity with a thin air-equivalent lining, there exists an equilibrium in the fluence of low energy electrons, i.e., a zero net energy transport, across the cavity-wall interface. Harder (1965) concluded that this is a close approximation to the condition for which it is valid to evaluate the stopping power ratio from Eq. 4.10.

An experimental demonstration of the effect of a very thin detector-equivalent lining on the secondary electron transport has been carried out by Harder (1970b). The variation of the ionization per unit mass of air with cavity size (simulated by varying the air pressure) was significantly reduced by lining the lead walls with graphited paper (Fig. 4.8). This indicated that the transition from the secondary electron spectrum of the surrounding lead to the secondary electron spectrum of the radiation-sensitive material occurred in the paper wall. Further theoretical and experimental work on the effect of graphite linings in air-filled chambers has been reported by Harder (1965b and 1970b), Harder and Schulz (1972) and Markus (1978).

For detectors where a complete build-up of the secondary electron spectrum can be assumed, the Bragg-Gray stopping power ratio (Eq. 4.10) was further used

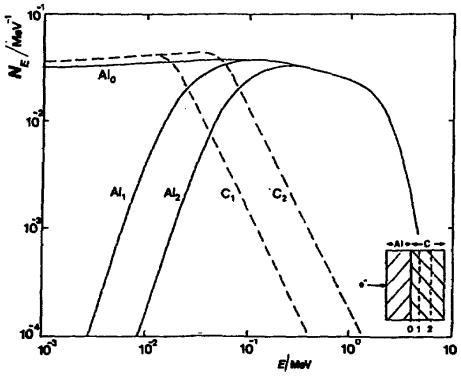

Fig. 4.7. The number of secondary electrons, differential in energy, crossing a reference plane (i.e., the surface integral of planar fluence, differential in energy, Ψ_E^E) in the vicinity of an aluminum-carbon interface. The spectra are given for one initial electron and plotted for reference planes No. 0, 1, and 2, as shown in the inset; contributions of electrons originating from aluminum are denoted by Al_0, Al_1, and Al_2; contributions of electrons originating from carbon are denoted by C_1, and C_2. Thickness of aluminum layer, 2.7 g cm^{-2}; of carbon layer between planes 0 and 1, 0.25 mg cm^{-2}; of carbon layer between planes 0 and 2, 2.5 mg cm^{-2}. Initial electron energy: 20 MeV. Insert not to scale. The spectra were obtained by diffusion-model calculation (from Schulz, 1970, and Harder and Schulz, 1972).

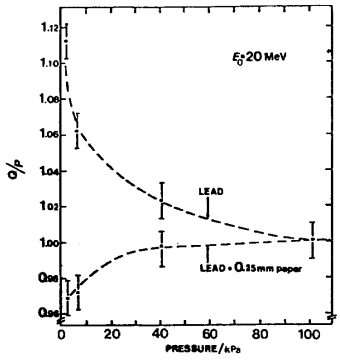

Fig. 4.8. Pressure dependence of the quotient of charge, Q, by pressure, P, in relative units for a flat air-filled ionization chamber with flat lead walls, which were lined with graphited paper in one case. Thickness of lead walls: front 1 mm, back 2 mm; thickness of air layer 12 mm; electron energy: E_0 = 20 MeV (Harder, 1970b).

by Harder (1965b) to derive a very simple approximation of $s^{BG}_{m,i}$ namely

$$s^{H}_{m,i} = \frac{\{S[\overline{E}(z)]/\rho\}_{col,m}}{\{S[\overline{E}(z)]/\rho\}_{col,i}} \qquad (4.11)$$

where $\overline{E}(z)$ is the mean energy of the primary electron spectrum at depth z, and the collision mass stopping powers are evaluated at this single energy. This expression is exact for a linear variation of $(S/\rho)_{col}$ with E, over the range of the primary electron spectrum at a given depth. It is also a good approximation even for spectra of the type shown in Fig. 2.3. In the case of water to air, the non-linearity of the variation of $(S/\rho)_{col}$ with E results in, at most, a 1% error at large depths for a 30 MeV beam, and no more than 0.5% for initial beam energies of 10 MeV and below (see Fig. 4.11). The stopping-power ratio $s^{H}_{m,i}$ can be recommended for general use with solid and liquid detectors, as $s^{H}_{m,i}$ then varies very slowly with $\overline{E}(z)$. However, the mean energy in the detector may differ from that in the medium. This effect could be taken into account by using slightly different mean energies in Eq. 4.11 for the detector and the medium (see Svensson and Brahme, 1979).

The simple method of obtaining $\overline{E}(z)$ by using Eq. 2.25 for $E_p(z) \approx \overline{E}(z)$ is sufficiently accurate to be used in calculating $s^{H}_{m,i}$ for gas-filled cavities at small depths and electron beam energies up to 10 MeV, as was demonstrated in a comparison between $s^{H}_{w,a}$ and $s^{BG}_{w,a}$ by Nahum (1978). However, the range of validity of $s^{H}_{m,i}$ can be extended to greater depths and higher energies by calculating $\overline{E}(z)$ from the more accurate Eq. 2.28 (Brahme, 1975) or by using Monte Carlo or experimental methods to determine $\overline{E}(z)$—see, for example, Andreo and Brahme (1981).

At small depths, a systematic error is introduced into the computations of $s^{BG}_{m,i}$ and $s^{H}_{m,i}$ (Eqs. 4.10 and 4.11) if the unrestricted collision stopping power is used, as the equilibrium slowing-down spectrum of secondary electrons is not yet fully built up. This can be taken into account in an approximate manner by replacing $(S/\rho)_{col}$ in Eqs. 4.10 and 4.11 by (L_Δ/ρ) (Brahme, 1975), where Δ is equal to the energy of the secondary electron whose range is equal to the depth in question[12]. If this adjustment is not made, the numerator and denominator in Eq. 4.10 overestimate the absorbed dose to the medium and to the detector material for small z. Numerically, $s^{BG}_{w,air}$ is lowered by about 1.5% at a depth of 0.05 R_p, independent of electron beam energy, but beyond 0.1 R_p, there is almost no change compared to using the unrestricted stopping powers because $(L_\Delta/\rho) = (S/\rho)_{col}$ at all depths greater than that for which $\Delta = \overline{E}/2$. This adjustment has been made in the values of $s^{BG}_{w,air}$ and $s^{H}_{w,air}$ shown in Fig. 4.11.

The existence of the polarization or density effect in condensed materials for electron energies above about 0.5 MeV gives rise to an appreciable difference in mass collision stopping power between wall and gas even when their atomic compositions are identical. This will, however, only affect the assumption of partial secondary electron equilibrium across the solid-gas boundary for extremely low electron energies, much less than 1 keV, as it is only the "distant collisions" (which correspond to the smallest energy losses) that are reduced in number in a solid compared to gas of equivalent atomic composition (Nahum, 1976). Since the ranges of these low-energy secondaries are extremely small, the influence of this effect is negligible for practical cavity sizes.

4.3.3 Wall-Less Detectors

A "wall-less" detector may consist of one material, e.g., a thermoluminescent dosimeter or an ionization chamber whose walls are of nearly the same atomic composition as the phantom material.

Spencer and Attix (1955) derived an expression for the stopping power ratio to apply to "wall-less" chambers. Their theory attempted to account for the experimentally observed deviations of $s_{m,i}$ from the predictions of the Bragg-Gray theory. They introduced the consideration of secondary electrons into cavity theory and divided them into two groups, with the dividing energy Δ set equal to the energy of an electron whose range in the cavity material (usually air) is equal to the mean chord length across the cavity. Those electrons with energy greater than Δ are assumed to originate

[12] In Eq. 4.10, the integration is over a spectrum of energies E and one simply replaces $(S/\rho)_{col}$ with (L_Δ/ρ) for those energies for which Δ is less than the maximum energy loss $(E/2)$, permitted by convention.

entirely in the wall material (i.e., the surrounding medium) and to deposit their energy "locally" in the cavity in energy losses up to Δ in size. This "local" energy deposition is calculated from the total electron fluence spectrum by the use of the restricted mass collision stopping power $(L/\rho)_\Delta$. The Spencer-Attix stopping-power ratio is given by

$$s^{SA}_{m,i} = \frac{\int_{2\Delta}^{E_{max}} (\Phi_E)_m (L/\rho)_{\Delta,m} dE + \int_{\Delta}^{2\Delta} (\Phi_E)_m (S^{SA}/\rho)_m dE}{\int_{2\Delta}^{E_{max}} (\Phi_E)_m (L/\rho)_{\Delta,i} dE + \int_{\Delta}^{2\Delta} (\Phi_E)_m (S^{SA}/\rho)_i dE} \tag{4.12}$$

where $(\Phi_E)_m$ is the distribution of the *total electron fluence* (primary and secondary electrons) in energy at the point of interest in medium m and $(L/\rho)_\Delta$ is evaluated from Eqs. 2.2 and 2.3. For $2\Delta > E > \Delta$ it becomes possible for an electron to drop below Δ as a result of a collision with an atomic electron. Spencer and Attix employed a special form of stopping power, here denoted by S^{SA}, to automatically include the residual energy of such "track-ends" in the energy dissipation. This is an important point as the energy dissipation by these "track-ends" accounts for between six and eight per cent of the total absorbed dose to the cavity (Burch, 1957; Nahum, 1976 and 1978).

The evaluation of s^{SA} involves an integration over the Møller cross-section which becomes increasingly complicated as E approaches Δ. An approximate expression for $s^{SA}_{m,i}$ which avoided this problem was developed (Eq. 3b in Spencer and Attix, 1955) but it is not particularly suited for use with high-energy electron beams. Nahum (1976) derived a simpler expression for $s^{SA}_{m,i}$ involving only a very slight approximation with respect to the energy dissipation in the 2Δ to Δ region

$$s^{SA}_{m,i} = \frac{\int_{\Delta}^{E_{max}} (\Phi_E)_m (L/\rho)_{\Delta,m} dE + (\Phi_E(\Delta))_m (S(\Delta)/\rho)_m \Delta}{\int_{\Delta}^{E_{max}} (\Phi_E)_m (L/\rho)_{\Delta,i} dE + (\Phi_E(\Delta))_m (S(\Delta)/\rho)_i \Delta} \tag{4.13}$$

where $(\Phi_E(\Delta))_m$ and $(S(\Delta)/\rho)$ are, respectively, the total electron fluence, differential in energy, and mass collision stopping power evaluated at energy $E = \Delta$. The product of these two quantities is very close to the number, per unit mass, of electrons that drop below Δ in energy. Thus, the second term in the numerator and in the denominator of Eq. 4.13 is equal to the total energy dissipated by the track-ends (Nahum, 1976 and 1978). This form of the track-end dissipation in the Spencer-Attix stopping power ratio was first discussed by Burch (1957).

The absorbed dose to a thin layer of water at various depths was computed by Nahum (1976), using electron spectra determined by Monte Carlo Techniques, from the integral in the numerator of Eq. 4.13 for Δ = 1, 10, and 100 keV. The absorbed dose was also computed by simply adding up all the separate energy depositions by the electron interactions in the same water layer. These two methods yield values that agree to within 1% for 5, 10, 20, and 30 MeV electron beams and thus verify that the numerator in Eq. 4.13 accurately gives the absorbed dose in the medium, m. Tabulations of $(\Phi_E)_m$ which can be used for the evaluation of $s^{SA}_{m,i}$ from Eq. 4.13 have been given by Nahum (1976) for 5, 10, 20 and 30 MeV electron beams.

The two-group schematization for energy losses on which the Spencer-Attix theory is based, is an approximation to the actual physical situation with the merit that it introduces a single parameter Δ that can be related to cavity size. The theory has had considerable success in predicting the variation of stopping power ratio with plate separation for parallel-plate ionization chambers (Spencer and Attix, 1955; Attix *et al.*, 1958; NCRP, 1961). It should be noted, however, that the radiation qualities in question were cobalt-60 gamma radiation and lower energy photon sources.

Computations of $s^{SA}_{w,a}$ for electron beams by Laughlin (1956) and Kessaris (1970) were limited by incomplete information on (Φ_E). Monte Carlo computations by Berger and Seltzer (1969) and Nahum (1976) have yielded the total electron fluence spectrum at different depths for a wide range of initial beam energies (Section 2.4.3). The comprehensive computation of $s^{SA}_{m,i}$ for water to air and carbon to air by Berger and Seltzer (1969a) and Berger *et al.* (1975), neglected to take into account track-end dissipation[13]. Nahum (1978) showed that for the water to air case, using the I-values of either Berger and Seltzer (1964) or Dalton and Turner (1968), such an omission results in values that are between 0.5% and 1.5% too low for Δ = 10 keV, depending on electron energy and depth. Berger (1980) has re-calculated $s^{SA}_{m,i}$, taking account of the track-end dissipation (see Section 4.3.4 and 4.3.5). These calculations also incorporate changes in I-values and the net result is that the new $s^{SA}_{m,i}$ are very close to the values given by Berger *et al.* (1975).

[13] Berger *et al.* (1975) computed $s^{SA}_{m,i}$ from

$$s^{SA}_{m,i} = \frac{\int_{\Delta}^{E_{max}} (\Phi_E)_m (L/\rho)_{\Delta,m} dE}{\int_{\Delta}^{E_{max}} (\Phi_E)_m (L/\rho)_{\Delta,i} dE}$$

where $(L/\rho)_\Delta$ was evaluated in the conventional manner (cf. Eqs. 4.12 and 4.13) for $2\Delta > E > \Delta$.

The Spencer-Attix stopping power ratio varies only very slowly with Δ when the detector material and the medium have similar atomic numbers (Spencer and Attix, 1955; NCRP, 1961). Nahum (1978) found that $s^{SA}_{w,air}$ for Δ = 1 keV was generally about 1.5% higher than the corresponding value for Δ = 100 keV when using I-values of 71.3 and 92.9 eV for water and air, respectively. Such a range of Δ-values corresponds to an enormous range of air cavity sizes. Using the new I-values for water and air (75.0 eV and 85.7 eV, respectively) this small dependence of $s^{SA}_{w,air}$ on Δ is reduced to under 1%; such a weak cavity-size dependence would be almost impossible to detect experimentally. The reason for this reduced dependence is that the quantity ($I_{air} - I_{water}$) has been significantly decreased (from 21.7 eV to 10.7 eV).

Another consequence of the decreased I-value difference in the water to air case is that the difference between the Bragg-Gray stopping power ratio, $s^{BG}_{w,air}$ evaluated from Eq. 4.10, or $s^{H}_{w,air}$ from Eq. 4.11, and $s^{SA}_{w,air}$ with Δ = 10 keV (equivalent to a realistic cavity size of about 2 mm) is now reduced to under 0.5% at all electron energies and depths (see Figs. 4.10 and 4.11).

The Spencer-Attix theory is not rigorous, being limited by the inherent assumption that the cavity material does not disturb the total electron flux above energy Δ (NCRP, 1961; Burlin, 1968). In practice, this will never be exactly true because, for energies close to Δ, an appreciable number of the electrons in the cavity originate from interactions in the cavity material. There will, therefore, be a gradual transition of the fluence spectrum in the cavity from that characteristic of the medium, m, for energies much larger than Δ, to being totally characteristic of the cavity material, i, for energies much lower than Δ (see Fig. 4.7).

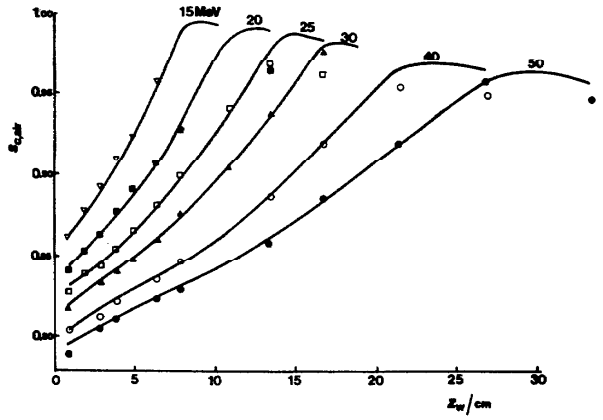

Fig. 4.9. Carbon/air stopping power ratios at depth in water (z_w) and various energies: individual values experimentally determined by Domen and Lamperti (1976); the full lines computed by Berger (1980) for Δ = 10 keV, (for carbon, I = 78.0 eV and for air, I = 85.7 eV; the density effect correction has been evaluated according to Sternheimer and Peierls, 1971). Note that a density of 2.25 g cm^{-3} for crystalline graphite was used to evaluate the density effect (see Section 5.3.2.3).

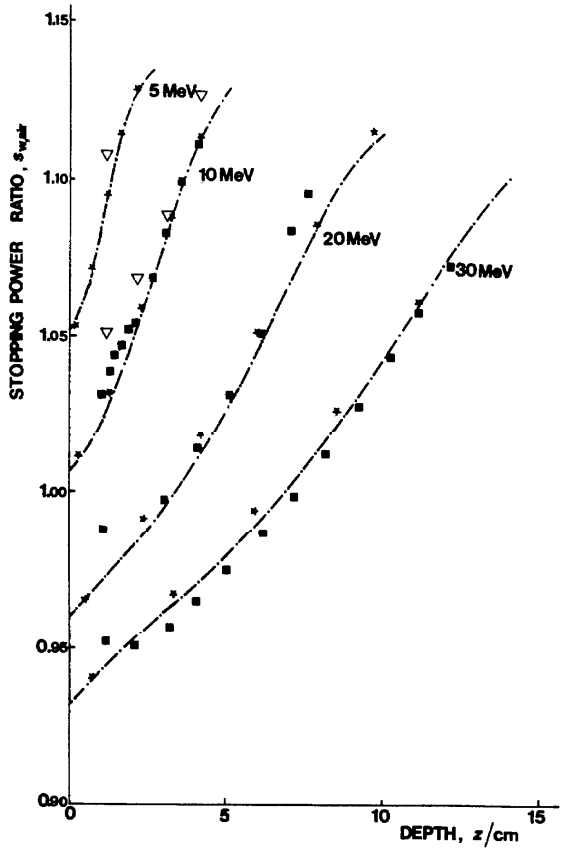

Fig. 4.10. Calculated water/air stopping power ratios, using I (water) = 75.0 eV and I (air) = 85.7 eV, with the density effect correction evaluated according to Sternheimer and Peierls (1971): $s^{SA}_{w,air}$ from Berger (1980) for Δ = 10 keV (- - - -), $s^{SA}_{w,air}$ from Nahum and Svensson (1980) for Δ = 10 keV (*); experimental values by Svensson (1971) and adjusted by Svensson and Brahme (1981) (■), and by Markus (1978) (▽). [$\epsilon_m \cdot G$ was assumed to be 352·10^{-6} m^2 kg^{-1} Gy^{-1} for both sets of experimental values; see Section 5.3.2.3.]

4.3.4 Comparison of Calculated and Experimental Values

A considerable amount of experimental work has been carried out on the response of air-filled ionization chambers in electron beams. The most direct determinations of $s_{m,i}$ have been made using a graphite calorimeter to determine the absorbed dose, and a graphite-walled ionization chamber to determine the carbon to air stopping power ratios (Bradshaw, 1965; Pinkerton, 1969; Domen and Lamperti, 1976).

The work of Domen and Lamperti is, by far, the most comprehensive; they determined the absorbed dose at different depths in a carbon block for electron beams

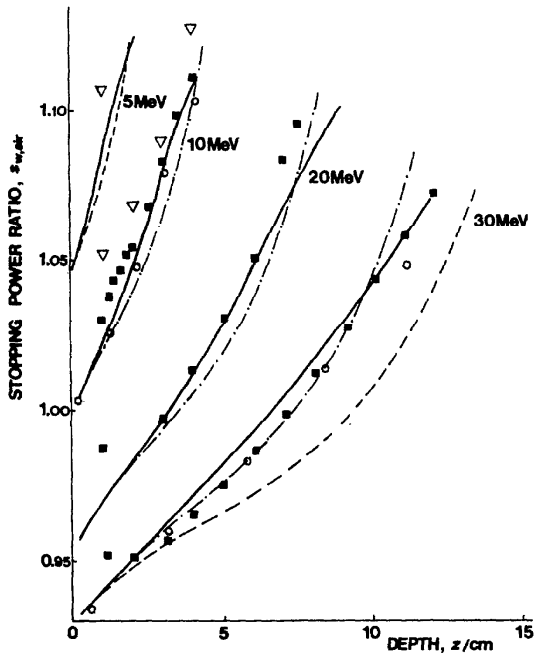

Fig. 4.11. Comparison between experimental and calculated water/air stopping power ratios: Measurements by Svensson (1971) and adjusted by Svensson and Brahme, 1981 (■); Measurements by Markus, 1978 (▽); $s^{BG}_{w,air}$ calculated by Nahum and Svensson, 1980 (—); $s^{H}_{w,air}$evaluated using a single mean electron energy: (a) from a Monte Carlo computation (Nahum, 1980) (○), (b) from Eq. 2.28 (- · - ·), (c) from Eq. 2.25 (- - -). The experimentally-derived $s_{w,air}$, ■ and ▽, were recalculated by means of $\epsilon_m \cdot G = 352 \cdot 10^{-6}$ m^{-2} kg^{-1} Gy^{-1}.

of initial energy between 15 and 50 MeV. They replaced the calorimeter with a carbon-walled parallel plate ionization chamber of known volume at exactly the same depth and hence could determine the mass ionization, J_{air}, corresponding to a given absorbed dose. (W/e) was taken to be equal to 33.85 J C^{-1} (Section 5.4.2) and it was assumed that the perturbation of the electron fluence by the detectors was negligible (see Section 4.2). Carbon to air mass stopping power ratios were derived from the measurements using Eq. 4.1. These $s_{C,air}$ values are compared in Fig. 4.9 to values of $s^{SA}_{C,air}$ (with Δ = 10 keV and carbon density of 2.25 g cm^{-3}) calculated by Berger (1980). Except at very large depths, which are of minimal practical dosimetric interest, the agreement between experiment and theory is very good, the difference being always within 1% and on average very much less than this.

Two conclusions can be drawn from this comparison. First, the Monte Carlo computations of total electron fluence spectra at different depths in the carbon medium must be reasonably accurate, and hence considerable confidence can be attached to similar calculations when the medium is water instead of carbon. Second, experimental results support the theory behind the evaluation of the stopping power ratio $s^{SA}_{m,i}$ from Eq. 4.12, or $s^{BG}_{m,i}$ from Eq. 4.10 and $s^{H}_{m,i}$ from Eq. 4.11 which give very similar results in this case. The direct transfer of these conclusions to theoretical water-to-air stopping power ratios is complicated, however, by uncertainties in the knowledge of the mean excitation potential for water, which has been increased by as much as 15% (Berger, 1980) compared to the Berger and Seltzer (1964) values.

Independent experimental determinations of $s_{m,i}$ for carbon and air have been performed by Harder (1965b, 1966) who measured energy deposition in sheets of reactor graphite (mean density 1.8 g cm^{-3}) by use of a scintillation spectrometer. He confirmed Eq. 4.11 to within 1% in the energy range of 4–20 MeV.

Experimental work on the determination of water-to-air stopping power ratios is complicated by the practical difficulties of determining the absorbed dose at a depth in water or water-equivalent phantoms. All the experimental determinations (Loevinger *et al.*, 1961; Liesem and Pohlit, 1962; Svensson and Pettersson, 1967; Almond, 1970; Rassow, 1970; Svensson, 1971; Wambersie *et al.*, 1971; Markus, 1978) are based on ferrous sulphate dosimetry (Section 5.3.2) and thus involve the uncertainty of the radiation chemical yield and of the molar extinction coefficient (Section 5.3.2.3). The determinations also involve an uncertainty in the calibration of the ionization chamber in terms of mass ionization (Section 5.4.1). It has been shown both theoretically and experimentally (Almond and Svensson, 1977; Nahum and Greening, 1978; Johansson *et al.*, 1978) that the composition of the inner wall of the chamber has a significant influence on this calibration if it is carried out in a photon beam. This has been the case in most experiments (see Section 5.4.5). A further complicating factor is that the perturbation correction (Section 4.2) has not been taken into account in most of the experiments cited above. Considerable spread in the water-to-air stopping-power ratios is thus obtained if the results of the various determinations are compared, including that due to uncertainties in the mean electron energy at the depth of measurement (Section 3.3.2).

The quantity $s^{SA}_{m,i}$ for water to air has been computed from Eq. 4.13 by both Berger (1980) and Nahum and Svensson (1980) using the new I-values. A comparison between the two sets of theoretical $s^{SA}_{w,a}$ for a Δ-value of 10 keV has been made in Fig. 4.10. The differences, which are solely due to minor differences in $(\Phi_E)_w$ derived from two completely independent Monte Carlo electron transport computations, are never more than 0.6% and mostly very much smaller. The Bragg-Gray stopping power ratio evaluated by Nahum and Svensson (1980) using Eq. 4.10 is shown in Fig. 4.11. The difference between $s^{SA}_{w,air}$ and $s^{BG}_{w,air}$ calculated by these authors

is less than 0.5% (compare Figs. 4.10 and 4.11), and it is, thus, largely immaterial which of these sets of stopping power ratios is used in experimental ionization dosimetry. The very small difference between the two stopping power ratios result from the selected small difference in mean ionization potentials for water and air (see Sections 4.3.2 and 4.3.3). Physically, this implies the existence of a close approximation to secondary electron equilibrium in a small air cavity in water.

Comparisons between $s^{BG}_{w,air}$ and $s^{H}_{w,air}$ (see Section 4.3.2) values are shown in Fig. 4.11. The full line is the computation by Nahum and Svensson (1980) from Eq. 4.10. The approximate, but very simple method due to Harder (Eq. 4.11) has been evaluated using $\overline{E}(z)$ from (a) the Monte Carlo calculation by Nahum (1980), (b) the continuous-slowing-down expression (Eq. 2.28) for the mean energy of primary electrons at depth z, and (c) the simpler Eq. 2.25. It can be seen that $s^{H}_{w,air}$ with $\overline{E}(z)$ from the Monte Carlo calculation is in excellent agreement with the experimental values and with $s^{BG}_{w,air}$. With $\overline{E}(z)$ from Eq. 2.28, $s^{H}_{w,air}$ lies very close to $s^{BG}_{w,air}$ except at large depths, which is to be expected from the inaccuracy of Eq. 2.28 at these depths as indicated in Fig. 2.4 (see also the discussion in Section 4.3.2). Note that all the Bragg-Gray values have been adjusted at depths near the surface using the method described in Section 4.3.2.

The experimentally-derived water-to-air stopping-power ratios of Svensson (1971) and Markus (1978), recalculated to $\epsilon_m \cdot G = 352 \cdot 10^{-6}$ m^2 kg^{-1} Gy^{-1} (see Section 5.3.2.3), are included in Fig. 4.11. The measurements by Svensson have also been corrected by Svensson and Brahme (1981) for bremsstrahlung contamination in the initial electron beams from the accelerator, the non-air equivalence of the build-up cap for cobalt-60 gamma rays (Almond and Svensson, 1977) and perturbation of the electron fluence by the cylindrical air cavity (see Section 4.2.2.3). It can be noted that the ionization chamber used had an approximately water-equivalent wall (actually PMMA) with a graphite inner lining. As graphite is very close to air-equivalent, such a chamber can be expected to behave as a detector with walls equivalent to air (Section 4.3.2). The measurements by Markus were carried out with a parallel-plate chamber with a thin front window of polyethylene coated with graphite to yield mass ionization by comparing it with a standard, graphite walled extrapolation chamber.

4.3.5 Recommended Stopping Power Ratios

The recommended values of $s_{w,air}$ to be used for an ionization chamber with a water-equivalent wall (Section 4.3.3) are given in Table 6.3 (Section 6.3). These values have been computed by Berger (1980) from Eq. 4.13 taking $\Delta = 10$ keV, I (water) = 75.0 eV, and I (air) = 85.7 eV.

A useful general method, applicable to the water/air combination but also to all other phantom/dosimeter combinations, is to use a detector lined with walls equivalent to the detector material (Section 4.3.2) and to calculate the appropriate stopping power ratios from Eqs. 4.10 or 4.11. For the water/air combination, this approach leads to practically the same results as the Spencer-Attix stopping power calculation (compare Figs. 4.10 and 4.11). Most ionization chambers have walls that are close to air-equivalent. Using this method, a TLD disk could be used for absorbed-dose determination in a phantom, when surrounded by one disk on each side. With most solid and liquid detectors, it is sufficient to estimate $\overline{E}(z)$ in Eq. 4.11 from Eq. 2.25, because $s_{m,i}$ often varies fairly slowly with mean electron energy in these cases. With gas detectors, however, the absence of the polarisation effect in the gas causes $s_{m,i}$ to vary rapidly with energy (Fig. 4.6) and makes it important to use the more accurate Eq. 2.28 or Monte Carlo- or experimentally-derived values for an estimate of $\overline{E}(z)$ (Andreo and Brahme, 1981). Mass collision stopping powers can be taken from Table 2.2.

5. Absorbed Dose Measurement Techniques

5.1 General

The general principles of absorbed dose determinations are discussed in Section 4. These principles can be applied when different kinds of dosimeters are to be used in the determination of absorbed dose. Dose measurements can be divided into two main categories:

(i) The determination of absorbed dose at a given location in a phantom; and
(ii) The determination of relative absorbed dose values at a given location in a phantom with respect to the absorbed dose at a standard position in the phantom.

This section describes systems that are used to carry out both kinds of measurements. The first three systems described, calorimeters, chemical dosimeters and ionization chambers, are those that can be used for the absolute determination of the absorbed dose at a given location, while the last three, liquid ionization chambers, solid-state dosimeters and film dosimetry, are generally used for relative absorbed dose measurements.

5.2 Calorimetry

5.2.1 Introduction

Calorimetry is a basic method for the determination of absorbed dose in a small volume of an irradiated medium. If a small volume of the medium is thermally isolated from the remainder, the mean absorbed dose in this volume (the absorber) is given by

$$\overline{D}_i = \frac{\Delta\bar{\epsilon}}{\Delta m} = \frac{\Delta E_h}{\Delta m} + \frac{\Delta E_s}{\Delta m} \qquad (5.1)$$

where $\overline{D}_i$ is the mean absorbed dose in the absorber of material, i, and mass, Δm; $\Delta\bar{\epsilon}$ is the mean energy imparted to the absorber by the ionizing radiation; ΔE_h is the energy appearing as heat; and ΔE_s is the chemical defect which may be positive or negative. An example of ΔE_s is the energy produced or absorbed in induced radiochemical reactions. If there is no change of state,

$$\frac{\Delta E_h}{\Delta m} = c_p \cdot \Delta T \qquad (5.2)$$

where c_p is the specific heat capacity at constant pressure and ΔT the change in temperature.

General reviews of radiation calorimeters have been carried out by Gunn (1964, 1970, and 1976). There are fewer reports on the use of calorimeters to measure absorbed dose from electron beams than from x-ray beams. However, most of the calorimeters constructed for x rays could be used for electron radiation as well and the general principles, described in ICRU Report 14 (ICRU, 1969) are, therefore, also applicable to electron beams. The main causes of differences in the use of the calorimeters with the two radiations arise from the different form of the depth vs. absorbed-dose distributions in the calorimeter material and from the more readily scattered electrons.

In the case of electron beams, the absorbed dose at different depths inside the absorber of the calorimeter may vary considerably, especially at low energies, and cannot be represented by simple analytical expressions as accurately as in the photon case. The thickness of the calorimeter absorber may be as large as 1 g cm^{-2} in order to reduce the relative influence of foreign materials in the absorber such as thermistors and wires. Corrections to zero absorber thickness, made in order to determine the absorbed dose to a point of interest in a uniform phantom of calorimeter material, could introduce large uncertainties at low electron energies, especially in the fall-off part of the depth-dose curve (see Section 4.2.2.2). Foreign materials in the calorimeter, inside or around the absorber, such as air gaps, may change the electron fluence in the absorber due to multiple scattering of the electrons.

5.2.2 Experimental Work with Calorimeters

Carbon calorimeters have been used by Geisselsoder *et al.* (1963), Bradshaw (1965), Pinkerton (1969), Domen and Lamperti (1976), and Cottens (1979) in electron beams. Geisselsoder *et al.* used a calorimeter to calibrate an ionization chamber and a ferrous sulphate dosimeter with 10-MeV and 20-MeV electron beams. Bradshaw used a calorimeter in a 15-MeV electron beam to calibrate an ionization chamber. Pinkerton compared the absorbed dose measured in a carbon calorimeter with the charge collected in a carbon-walled ionization chamber at a number of depths in carbon for a 20-MeV electron beam. He also used the calorimeter to calibrate ferrous sulphate dosimeters and TLD systems. Domen and Lamperti measured the quotient of absorbed dose to graphite and charge collected per unit mass of air in the cavity of a graphite chamber at different depths in graphite with 15-MeV to 50-MeV electron beams. Cottens compared the response of a carbon calorimeter and iron sulphate dosimeter to determine the radiation chemical yield for the ferrous sulphate dosimeter at different energies and depths in graphite (see Table 5.3). An aluminum calorimeter was used by Almond (1967) to calibrate ferrous

sulphate dosimeters at energies between 6 MeV and 18 MeV at the dose maximum.

Thermocouples attached to thin absorbers made of graphite or metal have been used to measure absorbed dose to the absorber from single high-dose pulses of electrons with energies between 0.3 MeV and 2 MeV by Willis *et al.* (1971), Miller *et al.* (1974), and Lockwood *et al.* (1976). For the particular problems in measurement of high-dose pulses, the reader is referred to ICRU Report 34 (ICRU, 1982).

When a graphite or metal calorimeter is used to determine absorbed dose to water at a point of interest inside a water phantom, a transfer dosimeter must be used which is calibrated at the position of the absorber inside the calorimeter or a phantom of the same material and size as the calorimeter. The calibrated transfer dosimeter is then used in the water phantom at a depth where the spectral distribution of the electrons is as similar as possible to that obtained in the calibration geometry. Such a depth could be found by using the scaling law of Section 6.2.2. Stopping-power ratios, as well as correction factors for electron fluence perturbation, must be applied when calculating the absorbed dose to water (see Section 5.2.4).

To minimize the uncertainty in the stopping-power ratios and in the scattering correction factors, aqueous calorimeter systems can be used which utilize the change of different physical properties as a function of temperature rise in the liquid. Pettersson (1967) used a calorimeter based on the expansion of water with temperature. He determined the energy imparted to water in a spherical volume of about 1 liter inside a water phantom irradiated by 33-MeV electrons. The water was then replaced by ferrous sulphate solution to determine the radiation chemical yield. Schmidt and Buck (1969) used the change of electrical conductivity with temperature. They used cells with liquid layers of about 7 mm. The liquid could then be replaced with ferrous sulphate dosimeter solution. A similar calorimeter was also developed by Hohlfeld and Reich (1978). The change in refractive index with temperature in water or other transparent liquids can be measured by means of holographic interferometry, as used by Hussman and McLaughlin (1971) and Miller and McLaughlin (1975, 1976). This method is particularly suitable for pulsed, high fluence-rate beams; see ICRU (1982). In this method, the local temperature change is determined with a very high spatial resolution without the introduction of any temperature sensors that may disturb the radiation field to be measured. Domen (1980) used an ultra-small thermistor sandwiched between two thin polyethylene films inside a water phantom. In its present, preliminary state, it is capable of a precision of 0.5% mean error of the mean (10 runs) at a dose rate of 66 $mGy \cdot s^{-1}$. Further development is being directed toward a standard instrument that can be used in a medical therapy beam.

A portable tissue-equivalent (A-150) calorimeter was used in cobalt-60 gamma and neutron beams by McDonald *et al.* (1976). There appears to be no difficulty in extending this method to electron beams (Holt *et al.*, 1978). The chemical defect due to endothermic radiochemical effects introduces the largest uncertainty in this method. The chemical defect of A-150 plastic has been measured to be 3.6–4.1% in photon beams between 30 kV and 7 MV and in a proton beam at 1.7 MeV; no systematic quality dependence was found (Fleming and Glass, 1969; Bewley *et al.*, 1972; Säbel *et al.*, 1972; and McDonald *et al.*, 1976). Therefore, a value of 4% would be expected also for electron radiation with an uncertainty of ±2% (Bewley *et al.*, 1972). This calorimeter would be particularly suitable for calibration of transfer instruments, e.g., tissue equivalent ionization chambers at different depths in tissue-equivalent plastic. However, the water to A-150 stopping-power ratio (see Section 5.2.4) will appear in the calibration because it is generally the absorbed dose to water that is required.

5.2.3 Uncertainty in the Determination of Absorbed Dose in a Reference Material

The carbon calorimeter is the most thoroughly investigated system and the principal uncertainties have been carefully investigated. Particular attention should be given to those experiments carried out at different national standardizing laboratories. At the National Bureau of Standards in the United States, Domen and Lamperti (1974, 1976) estimated an uncertainty of 0.1% in the determination of mean absorbed dose, $\overline{D}_i$, to the carbon absorber. At the Physikalisch-Technische Bundesanstalt in West Germany, Engelke and Hohlfeld (1971) found a value of 0.3%. Both groups considered the chemical defect and the fluence perturbation to be insignificant. Heat loss from the calorimeter absorber can be accurately corrected for by suitable extrapolation of the cooling curves. Irradiation and calibration times should be kept small (≈100 s) to minimize the uncertainty of such extrapolation.

A calorimeter of the same construction as that of Domen and Lamperti was recently employed by Cottens (1979). He gave special attention to the uncertainty due to perturbation (caused by the gaps between the various components of the calorimeter) in the determination of absorbed dose, $\overline{D}_m$, to graphite in a uniform block of graphite—at the position of the absorber. By simulating the calorimeter geometry using ferrous sulphate irradiation cells and surrounding the cells with thin sheets of paper, he measured perturbation effects as large as −0.7% for 8 MeV ($E_{p,0}$) to +0.6% for 16 MeV in the dose maximum regions of the electron beams. He gave an

TABLE 5.1—*Uncertainty in a determination of absorbed dose at a point in carbon with a carbon calorimeter*
[Absorbed dose rate of about 0.5 Gy s^{-1}, Cottens, 1979; see also Domen and Lamperti, 1974 and 1976]

Source	Uncertainty[a] (%)
1. Temperature gradients	0.03
2. Electrical power dissipation	0.02
3. Inhomogeneous absorbed dose distribution	0.1
4. Perturbation	0.4
5. Mass inhomogeneities	0.1
6. Heat loss corrections	0.04
Total (Quadratic sum)	0.43

[a] 99% confidence limit.

uncertainty of 0.4% for the perturbation correction, assuming that careful experimental investigations are carried out for the geometry used for calorimetric measurements. The perturbation correction factor is the dominating uncertainty in the determination of the mean absorbed dose, $\overline{D}_m$, as can be seen from Table 5.1.

5.2.4 Transfer of Absorbed Dose Calibration to Different Dosimetric Systems and to a Point in Water

A dosimeter which is to be calibrated for measurement of electrons can be placed in a cavity in a block of material similar to that of the calorimeter. The cavity should preferably be at a depth such that the mean energy of electrons and their energy spread in the dosimeter is the same as in the absorber of the calorimeter. The mean absorbed dose in the dosimeter, $\overline{D}_i$, is given by (see Eq. 4.2)

$$\overline{D}_m = \overline{D}_i \, s_{m,i} \, p_{m,i} \tag{5.3}$$

where the subscript (i) refers to the dosimeter instrument under calibration and (m) to the calorimeter material. The evaluation of the stopping-power ratio, $s_{m,i}$, is discussed in detail in Section 4.3. The perturbation factor $p_{m,i}$, which corrects for change of the primary electron fluence obtained by replacing a volume of the calorimeter material (m) by the dosimeter (i), is dealt with in Section 4.2.1 for gaseous detectors, and in Section 4.2.2 for solid and liquid detectors. It should be noted that if the dosimeter exactly replaces the calorimeter absorber, the evaluation of $p_{m,i}$ is often more involved; see the discussion in Section 4.2 and Svensson and Brahme (1979).

A general expression for $p_{m,i}$, correcting both for spatial and angular changes of the electron fluence, was given by Svensson and Brahme (1979) for a coin-shaped detector or absorber (see Section 4.2.2.3). It was assumed that the detector was placed with its axis parallel to the beam axis and surrounded by calorimeter medium. The correction increases with the difference in linear scattering power (equals the product of mass scattering power—see Eq. 2.7—and density) between dosimeter and calorimeter materials and is, therefore, of greatest importance at low electron energies, where the scattering power is large. This correction is dealt with for the special case of the calorimeter absorber being replaced by a ferrous sulphate dosimeter in Section 5.3.2.3.

There will be a change in the spectrum of low energy secondary electrons at the interface between the calorimeter material and the dosimeter to be calibrated, as discussed in Section 4.3. A thin coating of dosimeter material may be needed around the sensitive volume in order to achieve the highest possible accuracy (Section 4.3.2).

The absorbed dose at a point in water (D_w) can now be found by exposing the dosimeter in water at a depth where the mean electron energy is the same as in the absorber of the calorimeter. The absorbed dose at this point in water, in the absence of the dosimeter, is given by

$$D_w = \overline{D}_i \, s_{w,i} \, p_{w,i} \tag{5.4}$$

where the subscript, w, refers to water. The remarks made above about the perturbation correction and the interface also apply here. Equations 5.3 and 5.4 give

$$D_w = \overline{D}_m \frac{s_{w,i} \, p_{w,i}}{s_{m,i} \, p_{m,i}} \tag{5.5}$$

In ICRU Report 14 (ICRU, 1969) it was recommended that an ionization chamber be used as the transfer instrument for photons owing to its high stability and precision. With electron beams, however, there are additional considerations. In general, the absorbed dose will be needed at a point where the electron energy is not the same as at the absorber in the calorimeter. Ionization chambers for electrons show a greater variation of absorbed-dose sensitivity with electron energy than do some other dosimetric systems. Furthermore, the evaluation of the perturbation factors may involve considerable uncertainties, particularly for cylindrical (thimble) chambers. Laboratories with the necessary facilities may, therefore, prefer to use other dosimetric methods such as chemical dosimetry (Section 5.3) or solid-state dosimetry (Section 5.6) to determine the absorbed dose under practical conditions where a variety of electron energies might be encountered. In this case, the use of an ionization chamber as transfer instrument introduces an unnecessary link in the chain, and it is better to calibrate the chemical or solid-state dosimeter directly by comparison with the calorimeter according to Eq. 5.5.

The uncertainty in the determination of the absorbed dose in water using an ionization chamber as a transfer

TABLE 5.2—*Uncertainty in a calorimetric determination of absorbed dose at a point in water at which the mean energy of the electrons is the same as at the calorimeter absorber, using a plane-parallel ionization chamber as transfer instrument*

Source	Uncertainty[a] (%)
1. Calorimetric measurement of absorbed dose in calorimeter material, $\overline{D}_m$	0.4
2. Ionization measurement in transfer	0.2
3. Stopping power ratio	1.5
4. Perturbation corrections, $p_{w,i}/p_{m,i}$	0.6
5. Wall and stem effects	0.1
Total (Quadratic sum)	1.7

[a] 99% confidence limit.

instrument is given in Table 5.2. The uncertainties are similar to those given for photons in Table 4.2 of ICRU Report 14 (ICRU, 1969).

The uncertainty in the ratio of the mass stopping powers of water to graphite, at any one energy is about 1.5% (see Section 2.2.2). In the more general case, where another dosimetric system is calibrated directly against the calorimeter, the uncertainty depends on the system used and on the differences in energy between calibration and use.

5.3 Chemical Methods

5.3.1 Introduction

Although several chemical systems for determining absorbed dose are available, only the ferrous sulphate dosimeter (Fricke and Morse, 1927, 1929) has been extensively used and is discussed here. Much effort has been invested in determining its response to different qualities of ionizing radiation and it is now well understood and can be used for accurate measurements of absorbed dose. The use of the ferrous sulphate dosimeter for the determination of absorbed dose in photon beams was fully discussed in ICRU Report 14 (ICRU, 1969) and ICRU Report 17 (ICRU, 1970). The principles and recommendations outlined in those reports are also applicable to electron beams.

5.3.2 Ferrous Sulphate Dosimeter

The standard dosimeter solution is composed of 1 mol m^{-3} ferrous sulphate (or ferrous ammonium sulphate) and 1 mol m^{-3} NaCl in either 400 mol m^{-3} or 50 mol m^{-3} sulphuric acid. Upon exposure to radiation, the oxidation of ferrous ions is directly proportional to the absorbed dose if certain conditions are met (see ICRU Report 14—ICRU, 1969). The most reliable way of determining the ferric ion concentration is by direct spectrophotometric analysis of the irradiated solution (Hardwick, 1953). The measured difference in absorbance is related to the absorbed dose in the dosimeter solution according to the equation

$$\overline{D}_i = \frac{\Delta A_t}{\rho\, l (\epsilon_m)_t \cdot G_{t'}} \tag{5.6}$$

where $\overline{D}_i$ = mean absorbed dose to the dosimeter solution;
ΔA_t = increase in absorbance due to irradiation at a temperature t during the spectrophotometric measurement;
ρ = density of dosimeter solution;
l = length of the light path in the photometer cell;
$(\epsilon_m)_t$ = difference of molar linear absorption coefficient for ferric ions and for ferrous ions at temperature t;
$G_{t'}$ = radiation chemical yield of ferric ions at the irradiation temperature, t', and at the dose $\overline{D}_i$.

By convention, the values of $G_{t'}$ and $(\epsilon_m)_t$ are for an irradiation temperature (t') and spectrophotometric measurement temperature (t) of 25°C.

5.3.2.1 Absorbed Dose Rate and Absorbed Dose. The range of absorbed doses that may be determined with adequate accuracy is 30 to about 350 Gy with the commonly employed 1 mol m^{-3} ferrous sulphate solution; the measurements are made at the ferric ion absorption maximum at 304 nm using 1 cm absorption cells. For absorbed dose rates up to 2×10^6 Gy s^{-1}, the radiation chemical yield is independent of absorbed dose rate, but above this value, the yield decreases with increasing absorbed dose rate (Glazunov and Pikayev, 1960; Rotblat and Sutton, 1960; Anderson, 1962; Thomas and Hart, 1962). In closed irradiation cells, the yield decreases at high doses due to oxygen depletion. Typically, the yield at 350 Gy is 0.7% smaller than at low doses (Cottens, 1979). By increasing the ferrous concentration to 50 mol m^{-3} and bubbling oxygen or air through the solution during the irradiation, the dose range can be extended up to 10^4 Gy (Fricke and Hart, 1966).

It is possible to increase the sensitivity by a factor of 2 by measurement at another absorption maximum at 224 nm because of the higher molar linear absorption. However, impurities from plastic containers are reported to be more troublesome at 224 nm (Pettersson and Hettinger, 1967). The lower limit of the acceptable absorbed dose range can be reduced by using longer measuring cells—up to 10 cm. However, the longer cells require more dosimeter solution and this may not be practicable. A method of increasing the sensitivity by a factor of 8 involves adding potassium or ammonium

thiocyanate after the irradiation, as suggested by Frigerio (1962). In general, however, only limited success has been obtained with this system (Shalek and Smith, 1969; Oller *et al.*, 1969).

5.3.2.2. Molar Linear Absorption Coefficient and Factors Affecting the Determination of the Radiation Chemical Yield. Factors affecting the radiation chemical yield, such as impurities, types of irradiation cells, etc., are discussed in ICRU Reports 14 and 17 (ICRU, 1969, 1970).

Measurement of the molar linear absorption coefficient with different spectrometers indicates an agreement of better than 1% at a wavelength of 304 nm (Pettersson and Hettinger, 1967; Wambersie, 1967; Bryant and Ridler, 1968; Shalek and Smith, 1969; Law and Svensson, 1972; Law *et al.*, 1975; Eggermont *et al.*, 1978). However, the scatter of published molar linear absorption coefficients is much larger than the reported differences in spectrophotometer response. Broszkiewicz and Bulhak (1970) stressed the importance of using pure metallic iron rather than iron compounds in the determination of the molar linear absorption coefficient, because the amount of water of crystallization can change in the compounds. They showed that reported measurements of ϵ_m based on metallic iron are significantly lower than those based on ferrous or ferric compounds. Eggermont *et al.* (1978) investigated the oxidation of metallic iron with H_2O_2 and found that the residual H_2O_2 gave an increase in extinction; evidence was given that some of the published values of ϵ_m could be too high by 3% or even more. As a result of many measurements with pure iron samples from different manufacturers, Cottens (1979) reported $(\epsilon_m)_t = 217.3 \pm 0.6$ m^2 mol^{-1}, including random and systematic uncertainties at the 99% confidence level, to be compared with a mean of 220.5 ± 0.3 m^2 mol^{-1} following the review of 83 determinations by Broszkiewicz and Bulhak (1970). These values refer to 400 mol m^{-3} sulphuric acid and a temperature $t = 25$°C.

The molar linear absorption coefficient is also dependent on sulphuric acid concentration and temperature, as described in ICRU Reports 14 and 17 (ICRU, 1969, 1970). Although most of the investigations have been done with 400 mol m^{-3} sulphuric acid dosimeter solution, there are some advantages in using 50 mol m^{-3} sulphuric acid solution. Storage effects in polystyrene are less marked for the weaker solution (Pettersson and Hettinger, 1967), and there is less chance of introducing impurities due to sulphuric acid (Fregene, 1967). However, a concentration of 50 mol m^{-3} sulphuric acid is the lowest that should be used for reproducible dosimetry.

5.3.2.3 Radiation Chemical Yield. Table 5.3 gives a summary of radiation chemical yield determined for various electron energies. Earlier determinations with the ionization chamber method have not been included,

TABLE 5.3—*Values of the radiation chemical yield, G, for the ferrous sulphate dosimeter at different energies*

[The author's original values are, in some cases, corrected. The difference between the corrected and the author's values are given. Mean values of ϵ_m and G, with the same weight given to each investigator independent of number of experiments carried out, are given]

Reference	Energy $E_{p,0}$/MeV	Energy $\bar{E}_z$/MeV	Calorimeter Type	ϵ_m/m^2 mol^{-1} [a]	G/mol·kg^{-1}Gy^{-1} [b] (corrected)	Correction[c] percent	$\epsilon_m \cdot G$/ m^{2}kg^{-1}Gy^{-1}
Schuler and Allen (1956)	2	1	Total absorbing	219.4	$1.601 \cdot 10^{-6}$	—	$351.2 \cdot 10^{-6}$
Cottens (1979)	8	3.5	Graphite absorber	217.3	$1.597 \cdot 10^{-6}$	—	$347.0 \cdot 10^{-6}$
	16	13		217.3	$1.603 \cdot 10^{-6}$	—	$348.3 \cdot 10^{-6}$
		9		217.3	$1.605 \cdot 10^{-6}$	—	$348.7 \cdot 10^{-6}$
		7		217.3	$1.605 \cdot 10^{-6}$	—	$348.7 \cdot 10^{-6}$
	26	14.5		217.3	$1.602 \cdot 10^{-6}$	—	$348.1 \cdot 10^{-6}$
Giesselsoder *et al.* (1963)	10	6	Graphite absorber	220.0	$1.585 \cdot 10^{-6}$	−0.2	$348.7 \cdot 10^{-6}$
	20	16		220.0	$1.559 \cdot 10^{-6}$	−0.8	$343.0 \cdot 10^{-6}$
Pinkerton (1969)	20	16.5	Graphite absorber	220.0	$1.592 \cdot 10^{-6}$	−0.9	$350.2 \cdot 10^{-6}$
Almond (1967)	13.3	9	Aluminum absorber	217.7	$1.608 \cdot 10^{-6}$	+0.4	$350.0 \cdot 10^{-6}$
	15.9	12		217.7	$1.601 \cdot 10^{-6}$	+0.3	$348.5 \cdot 10^{-6}$
	24.0	20		217.7	$1.594 \cdot 10^{-6}$	+0.2	$347.0 \cdot 10^{-6}$
Anderson (1962)	15	7	Water absorber	222.5	$1.575 \cdot 10^{-6}$	—	$350.4 \cdot 10^{-6}$
Pettersson (1967)	30	20	Water absorber	219.6	$1.613 \cdot 10^{-6}$	—	$354.2 \cdot 10^{-6}$
Mean values				219.5	$1.594 \cdot 10^{-6}$		$349.8 \cdot 10^{-6}$ [d]

[a] To convert ϵ_m-values stated in coherent SI units (m^2 mol^{-1}) to the sometimes used unit dm^3·mol^{-1}·cm^{-1}, multiply the values by 10.

[b] To convert radiation chemical yield stated in coherent SI units (mol kg^{-1}Gy^{-1} or mol·J^{-1}) to the formerly often used unit (100 eV)$^{-1}$, multiply the values by $9.648 \cdot 10^6$.

[c] Corrections are made for the difference between the electron fluence in the dosimeter solution and in the calorimeter absorber due to different scattering properties in the media (Svensson and Brahme, 1979) and for the difference between the stopping power values from Berger and Seltzer (1964) and from Berger (1980) (i.e., Sternheimer—Peierls density effect correction and the crystallite density of 2.25 g cm^{-3}).

[d] The value recommended for $\epsilon_m G$ is $352 \cdot 10^{-6}$ m^2 kg^{-1} Gy^{-1} (see the text).

as the knowledge of stopping-power ratios and perturbation corrections may have been inadequate and consequently introduced large uncertainties in earlier publications. The values of the radiation chemical yield based on the ionization method reported in ICRU Report 21 (ICRU, 1972) were all larger than those from calorimetric or charge input measurements. However, recent investigations (Svensson, 1971; Ellis, 1974; Nahum and Greening, 1978; Svensson and Brahme, 1979) show consistency between ferrous sulphate and ionization chamber dosimetry if calorimetrically-determined radiation chemical yields (or $\epsilon_m G$ products) are used.

Radiation chemical yield based on calorimetric measurements in which the absorber is replaced by a ferrous sulphate dosimeter must be corrected not only for the difference in stopping-power between absorber and dosimeter, but also for the different fluence of electrons in the two materials (see Eq. 5.3 and Section 4.2.2.3). This latter effect has been considered in calorimetric determinations of radiation chemical yields by Cottens (1979), but not by other workers; it will give a somewhat larger radiation chemical yield in some of the reported measurements (Table 5.3; Svensson and Brahme, 1979). Corrections for the change in stopping-powers in tables from Berger and Seltzer (1964) to those from Berger (1980) have been carried out. The change for graphite is particularly large as the density effect calculations here are based on a density of 2.265 $g \cdot cm^{-3}$ instead of the mean density which is about 1.70 $g \cdot cm^{-3}$ [14].

There is now considerable support for an almost constant radiation chemical yield, i.e., within 1% from low to high electron energies. Cottens (1979) carefully measured the radiation chemical yield between $\overline{E}_z = 3.5$ and $\overline{E}_z = 14.5$ MeV and found a 0.5% lower value at the lowest energy, which was not quite significant at the 99% confidence level (0.55% total uncertainty). A variation of the same magnitude was obtained by using a semi-empirical method (Nahum, 1976; Nahum *et al.*, 1981). Pinkerton (1969) measured the yield as a function of depth at 20 MeV and found no significant variation. Furthermore, Pettersson (1967) and Pinkerton (1969) made measurements in both cobalt-60 gamma-rays and high-energy electron beams and found no significant difference in yield between these two qualities, which is also in agreement with the calculations by Nahum (1976). A constant radiation chemical yield is, therefore, recommended for mean electron energies, $\overline{E}_z$, from 1 MeV up to at least 30 MeV.

[14] The lower density of 1.70 g cm^{-3} may still be valid for amorphous graphite at high energies if the crystalline grains are small compared with the interaction distance of the relativistic electric field of the moving electron.

Several authors have measured the effect of the sulphuric acid concentration upon the yield of the dosimeter. Some investigators (Pettersson and Hettinger, 1967; Shalek and Smith, 1969; Day and Law, 1969) have noted a 1% to 3% decrease in sensitivity and consequently of the radiation chemical yield with decrease in concentration from 400 to 50 mol m^{-3} of sulphuric acid.

The product $\epsilon_m G$ has been calculated in Table 5.3 because it is assumed that experimental uncertainties in the determination of ϵ_m, by some of the investigators, give larger errors than would be obtained assuming the same response for all the spectrophotometers (see Section 5.3.2.2). A systematic error in the measured ϵ_m would give a corresponding error in G. This error does not, however, appear in the product, provided that the spectrophotometer is correctly calibrated. The mean value of this product for 400 mol m^{-3} sulphuric acid dosimeter solution at 304 nm, giving the same weight to each experimenter independent of the number of beam qualities investigated, is $349.8 \cdot 10^{-6}$ m^2 kg^{-1} Gy^{-1}. This value of $\epsilon_m G$ may, however, be slightly low for the following reasons:

(a) The effective density (see footnote 14) of the graphite used in the density effect correction to the stopping-power, 2.25 g cm^{-3}, represents an upper limit; a decrease of the density to 1.7 g cm^{-3}, which is the average density of the commonly-used reactor-grade graphite, would decrease the graphite collision stopping power by 1.2% at 20 MeV and thus increase the experimental graphite-calorimeter radiation chemical yield by this percentage, at the same time decreasing the spread in experimental data in Table 5.3 (Svensson and Brahme, 1979).

(b) Theoretical and experimental evidence has been given above that the radiation chemical yields are approximately the same for cobalt-60 gamma-rays and high-energy electrons; in fact, there are indications that G should be slightly larger for the electron beams. However, the mean value from Table 5.3 is somewhat smaller than that generally accepted for cobalt-60 gamma-rays which is $1.606 \cdot 10^{-6}$ mol kg^{-1} Gy^{-1} (equal to 15.5 per 100 eV; ICRU Report 14–ICRU, 1969).

(c) A somewhat better agreement is obtained between ionization chamber dosimetry and ferrous sulphate dosimetry with a higher value for $\epsilon_m \cdot G$ (see Section 4.3.4 and Fig. 4.10).

Considering all of these aspects, a value of $\epsilon_m \cdot G$ equal to $352 \cdot 10^{-6}$ m^2 kg^{-1} Gy^{-1} is recommended in the energy range 1 MeV up to at least 30 MeV at an irradiation temperature, t', of 25°C, and a spectrophotometer measurement temperature, t, of 25°C. A correction for temperatures differing from 25°C should be made

$$(\epsilon_m)_t G_{t'} = (\epsilon_m)_{25°} G_{25°}[1 + k_1(25 - t)] \times [1 + k_2(25 - t')] \quad (5.7)$$

The temperature coefficient, k_1, is approximately $0.007°C^{-1}$ and k_2 is $0.0015°C^{-1}$ which are the mean values evaluated from a literature study by Pettersson and Hettinger (1967).

5.3.2.4 Determination of Absorbed Dose in Water and its Uncertainty. The mean absorbed dose in water, $\overline{D}_w$, can be determined from the mean absorbed dose in the ferrous sulphate solution, $\overline{D}_i$, using the principles outlined in Section 4

$$\frac{\overline{D}_w}{\overline{D}_i} = s_{w,i} p_{w,i} \quad (5.8)$$

where $s_{w,i} = 1.004$ for $\overline{E}$ between 3 and 50 MeV (see Table 2.2 and Eq. 4.11). The perturbation effect of the dosimeter in a water phantom expressed by $p_{w,i}$, is generally negligible, at least when a single plastic cell is used (see Eq. 4.9). However, corrections may have to be performed when dosimeters are placed in a stack in a water phantom for measurements of depth-dose distributions (Svensson, 1971). This correction can be minimized by using plastic with linear stopping-power and scattering-power values somewhat less than those for water, thus compensating for the larger values in the ferrous sulphate solution as compared to water. Pettersson and Hettinger (1967) obtained an optimum combination using polystyrene irradiation cells. They showed that their dosimeters, used at small phantom depths, did not disturb the electron fluence in the water phantom at larger depths. However, much care is needed with polystyrene cells because the storage effect may be fairly large.

Storage of the dosimeter solution in the irradiation vessel may give yields, for some plastic wall materials, which are too high. An investigation of this effect must, therefore, be made for the irradiation cells in use (Svensson and Pettersson, 1967; Ellis, 1974). Pre-irradiation of the plastic irradiation cells filled with ferrous sulphate solution, using a high absorbed dose in order to eliminate or reduce this effect, has been recommended by several authors (Shalek *et al.*, 1962; Davies and Law, 1963; Wambersie, 1967). Alternatively, glass irradiation vessels which have a negligible storage effect can be used, but then the perturbation effect is larger and there may also be difficulties in choosing an appropriate value of the stopping-power ratio which accounts for the difference between δ-ray spectra in glass and that in $FeSO_4$ solution or water (see Section 4.3.2). Because of their smaller storage effect, glass cells are preferred for dosimetry whenever there will be delays before reading, for example, in intercomparison exercises (Nagel and Sanielevici, 1967; Ehrlich and Lamperti, 1969). A purity check of the dosimeter solution can be made by irradiating the solution with and without NaCl. The addition of 10 mol m^{-3} NaCl should yield a 1.5% decrease of the radiation chemical yield (Cottens, 1979). A larger value would be expected for a solution containing small traces of foreign materials—from the plastic walls of the irradiation cells for example.

TABLE 5.4—*Uncertainty in the determination of the absorbed dose at a point in water using the ferrous sulphate dosimeter*

Source	Uncertainty[a] (%)
Measurement of net absorbance (for 30 to 350 Gy)	0.1
Calibration of the spectrophotometer	0.5
The reference value of $\epsilon_m \cdot G$, i.e., $352 \cdot 10^{-6}$ m^2 kg^{-1} Gy^{-1}	1.7
Storage effect	0.2
$s_{w,i}$	0.2
$p_{w,i}$	0.2
Total (Quadratic sum)	1.8

[a] 99% confidence limit.

The estimated uncertainties in the determination of the absorbed dose in water using the ferrous sulphate system based on 400 mol m^{-3} H_2SO_4 are given in Table 5.4. It is assumed that the spectrophotometers and cells are of high quality and that they have been checked by absorbance intercomparisons, for instance using KNO_3 (303 nm) or $K_2Cr_2O_7$ (313 nm) solutions (Bruke and Maurodineanu, 1977) in order to exclude systematic errors for an individual instrument.

The fact that $\epsilon_m G$ is, at the most, only very weakly dependent on radiation quality can be exploited because many departments have well established dosimetry for cobalt-60 gamma radiation which can be used for the calibration of a ferrous sulphate dosimeter for electron beam dosimetry. This method is particularly useful when ϵ_m-value determinations or absorbance intercomparisons have not been undertaken (Wambersie *et al.*, 1975). It also has the advantage of giving consistency in dosimetry over the whole range of beam qualities used in a department.

5.4 Gas Ionization Chambers

The air ionization chamber is the most common form of dosimeter and has been the method of choice for determining the absorbed dose at a point in a phantom (AAPM, 1966; HPA, 1971; NACP, 1972, 1980, 1981; ICRU, 1972; and DIN, 1975). The method is universally available, simple to use both for dose rate and dose measurement, precise and quite rugged.

An ionization chamber may be either, one for which all necessary parameters are known so that its sensitivity can be computed, or one for which the sensitivity is determined by comparison of its response with that of an instrument (standard or reference instrument)

whose sensitivity is known. The former is sometimes called an absolute ionization chamber and the latter a calibrated ionization chamber. For the absolute device, the sensitivity is given (for present purposes) in terms of the absorbed dose, at the effective position of the chamber, per unit quotient of electrical charge of one sign produced in the cavity and the mass of gas in the cavity; the same may be true for the calibrated device. Alternatively, the sensitivity of the calibrated device may be expressed in terms of absorbed dose, at the effective position of the chamber, per unit value of some other parameter, such as the meter reading.

A local standard or reference ionization chamber may be either an absolute or a calibrated device. Generally, it will be used to calibrate other instruments that may be termed "working" or "field" instruments.

5.4.1 Gas-Ionization Chamber for Absolute Determinations

Equation 4.2 provides a starting point for the consideration of the absolute gas-ionization chamber. The radiation-sensitive material, i, in that equation, becomes gas (subscript g, in the present context) but the other symbols are the same.

$$D_m(P_{eff}) = \overline{D}_g \, s_{m,g} \, p_{m,g}$$

The mean absorbed dose, $\overline{D}_g$, in the cavity is given by

$$\overline{D}_g = (W/e)(Q_g/\rho_g V_g)$$

and, because the charge per unit mass of gas, $Q_g/\rho_g V_g$, is frequently symbolized by $\overline{J}_g$, Eq. 4.2 becomes

$$D_m(P_{eff}) = \frac{W}{e}(Q_g/\rho_g V_g) s_{m,g} \, p_{m,g} \qquad (5.9)$$

$$= \frac{W}{e} \overline{J}_g \, s_{m,g} \, p_{m,g}$$

where W is the average energy expended in the gas per ion pair formed; e is the elementary charge of the electron; Q_g is the charge of one sign produced in the volume V_g, filled with gas of density, ρ_g; $s_{m,g}$ is the stopping-power ratio; and $p_{m,g}$ is the electron fluence perturbation correction factor. Of the terms on the right side of Eq. 5.9, $s_{m,g}$ and $p_{m,g}$ have been discussed in Section 4 and the others, with the exception of ρ_g, are treated below.

5.4.1.1 Experimental Values of W/e for Electrons. Air is the gas normally used for electron or photon dosimetry with ionization chambers. Experimental values of W in air for electrons are listed in Table 5.5. It can be seen that such values are rather scarce. There is some indication that W will increase at electron energies above about 10 MeV due to additional energy losses by production of Cerenkov radiation (Barber, 1955). These additional energy losses might be about two percent of the total energy loss of 40 MeV electrons in noble gases, but should be much less than 1% in air. The mean value obtained by Kretschko (1960) and Ovadia *et al.* (1955), when readjusted for recent stopping-power values and humidity is not significantly different from the ICRU value (ICRU, 1979) for the lower energy region. Therefore, this lower energy value, W = 33.85 eV, or W/e = 33.85 J/C, is also recommended for use with high energy electron beams up to 50 MeV. This value is for dry air. When water vapor is present, the number of ions produced is larger than for dry air. An increase by 0.3% for a relative humidity between 20 and 70% at 20°C and 101 kPa was obtained with a cobalt-60 gamma-ray beam (ICRU, 1979). This difference results from a variation of both the stopping power and W with the amount of water vapor present. The same increase should be expected with high-energy electron radiation. Therefore, the collected charge in dry air (Q) should, in most practical situations, be obtained from the measured charge in humid cavity air, Q', by $Q = c_{hum} \cdot Q'$, where c_{hum} has a value of 0.997.

TABLE 5.5—*Energy expended by electrons in air per ion pair formed (W)*

Type of Radiation	W/eV Values and estimated error given by the authors	Author
Beta rays and photons at or below 2 MeV	33.85 ± 0.15[a]	ICRU (1979)
Electrons, 17.5 MeV	34.3 ± 1[b]	Ovadia *et al.* (1955)
Electrons, 10 MeV	33.3 ± 0.5[b]	Kretschko (1960)
Electrons, 15 MeV	33.6 ± 0.5[b]	
Electrons, 20 MeV	34.0 ± 0.5[b]	
Electrons, 25 MeV	34.0 ± 0.5[b]	

[a] Value recommended for dry air and based on 13 experiments using electrons generated by ^{137}Cs, ^{60}Co and 2 MV x-ray photons and by some β emitters of maximum energies between about 0.17 and 2.2 MeV.

[b] These values are for humid air. They should be adjusted to correspond to dry air by taking into account the ratio of stopping powers for humid and dry air, and the W ratio for dry and humid air as given in Fig. 5.15 of ICRU Report 31 (ICRU, 1979). They should also be adjusted by considering stopping power values calculated with a more recent I-value for air (Table 2.1b) than that used by the authors. These adjustments have been estimated for Kretschko's values and lead to an increase of his W-values of about 1%.

5.4.1.2 Determination of $\overline{J}_g$. Several investigators (Rase and Pohlit, 1962; Markus, 1975; Holt *et al.*, 1977) have described ionization chambers designed so that J_g and $p_{m,g}$ may be accurately determined. These chambers are flat extrapolation-type chambers with well-defined sensitive volumes that can be varied either in thickness or radius or both. The perturbation factor is always very close to unity for such flat chambers (see Section 4.2.1.1) and may, if the chamber wall is gas-equivalent (see Section 4.3.2), be precisely determined by varying the chamber volume, both in thickness and in radius and extrapolating the measured values of

TABLE 5.6—*Estimated uncertainty of determination of D_m in an extrapolation chamber*

Source	Uncertainty[a] (%)
Measurement of V_g	
Measurement of area, a	0.1
Measurement of distance, l	0.1
c_{pot}	0.0
c_{field}	0.01
Measurement of Q_g	
Capacitance for charge measurements	0.1
Voltage measurement	0.0'
c_{sat}	0.1
c_{hum}	0.05
c_{sc}	0.1
W/e (for dry air)	0.5
Stopping power ratio, $s_{m,g}$	1.5
Perturbation correction factor, $p_{m,g}$	0.4
Total (Quadratic sum)	1.7

[a] 99% confidence limit.

$Q_g/\rho_g V_g$ to zero cavity size. Not only does such extrapolation provide unity for the perturbation factor, but the extrapolation provides the value of $\bar{J}_g p_{m,g}$. The value of ρ_g is determined from the pressure and temperature of the gas in the cavity. If the chamber is used in a phantom of material which differs from that of the chamber wall, a correction factor, c_{ec}, must be applied to allow for changes in the electron radiation scattered back into the air volume (Markus, 1975). The uncertainty in this factor is given in Table 5.6. When an extrapolation chamber is not available, Q_g and V_g are measured separately.

5.4.1.3 Measurement of Charge Collecting Volume, V_g. V_g is determined for a coin-shaped chamber having the geometry indicated in Fig. 4.2. With an adequate guard plate, the electric field between C and F is constant throughout the collecting region. Then ions are collected over the volume defined by the product of the separation distance of F from C and the effective area of the collector plate. The effective diameter of the collector is the sum of the collector diameter plus one-half the insulating gap between C and G

Collecting field uniformity is obtained only if the collecting electrode is maintained at the same potential as that of the guard (ground potential) and the electric field lines are perpendicular to the plane of the collecting electrode. Both conditions can be fulfilled to a very good approximation and only small correction factors c_{pot} and c_{field}, correcting for deviation from ground potential of the collecting electrode and for electric field inhomogeneity respectively, are necessary (Boag, 1964, 1966). These correction factors can be determined by making ionization measurements with various configurations (Rase and Pohlit, 1962). The uncertainties in the various parameters used in the determination of V_g are summarized in Table 5.6

5.4.1.4 Measurement of Charge, Q_g, Released in the Volume, V_g. As indicated above, when an extrapolation chamber is not available, the charge, Q_g, of one sign produced in the gas volume, V_{gal}, must be measured. However, a small proportion of this charge is always lost due to recombination of ions, especially in pulsed beams. Therefore, an experimentally determined correction factor, c_{sat}, has to be applied, which is dependent on the collecting potential used, the distance, l, and the absorbed dose rate in the gas (Boag, 1956; Rase and Pohlit, 1962; Scott and Greening, 1961; Greening, 1964; Niatel, 1967; Ellis and Read, 1969; ICRU, 1981).

The measurement of Q_g in an electron beam has to be made both with positive and negative high voltage applied to the high voltage electrode. In general, these two values will differ somewhat due to electrons that are stopped in the collecting electrode or in insulators and transported to the collecting electrode or its electrical connections (Pohlit and Teich, 1962; Johns *et al.*, 1968). This effect depends on the depth in the phantom where the measurement has been carried out, and on the energy of the electrons (see Fig. 2.16 and Rase and Pohlit, 1962). For a given absorbed dose, the number of stopped and collected electrons increases with the mass of the collecting electrode and its irradiated insulator. These masses can be minimized by using, for example, chamber designs described by Markus (1975), and Svensson and Nahum (1981)—see Fig. 5.1.

The quantity, Q_g, can be obtained from the measured value of Q'_g

$$Q_g = c_{sc} c_{sat} c_{hum} Q'_g \qquad (5.10)$$

with c_{sc} = backscattering correction factor;
c_{sat} = correction factor for lack of saturation voltage;
c_{hum} = correction factor for humidity of the air (Niatel, 1975);
Q'_g = mean value of the charge measured with positive and negative high voltage.

5.4.1.5. Uncertainties in the Parameters. The uncertainties of absorbed-dose determination in a medium, m, usually graphite, are summarized in Table 5.6. The transfer of absorbed-dose calibration from a point in medium m to a point in water may be carried out with a transfer ionization chamber as described in Section 5.2.4. The transfer results in additional uncertainties which are shown in Table 5.2. However, the stopping power ratio appears only once because the transfer chamber is calibrated in terms of $\bar{D}_{g,c}/M_c$ ($=N_D$, see Section 5.4.4.1, Eq. 5.15; g is assumed to be air), where M_c is the meter reading of the transfer instrument when irradiated in a phantom material, m, in a position corresponding to that of the cavity of the calibrating

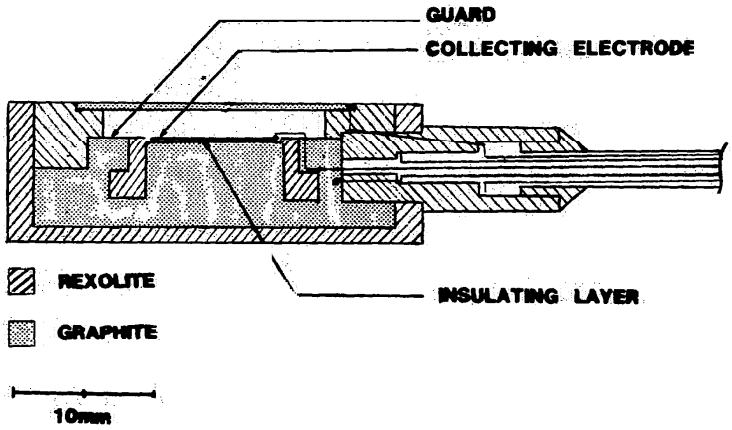

Fig. 5.1. Cross-sectional view of a plane-parallel air ionization chamber designed for use in high-energy electron beams, especially for $\bar{E}_0 \geq 10$ MeV (Mattsson *et al.*, 1981; Svensson and Nahum, 1981). The very narrow (2 mm) air gap and the presence of the guard-ring minimize perturbation effects (see Fig. 4.2). The collecting electrode is very thin (<0.1 mm) and is mounted on a thin insulating layer (≈0.2 mm) in order to give a negligible polarity effect. The front and back walls are made of one single material (in this case graphite). Rexolite® is a polystyrene copolymer with a density of 1.05 g cm^{-3} and a chemical composition very similar to that of polystyrene.

chamber. $D_{g,c}$ is the mean absorbed dose to the gas which would have been obtained if the irradiation had been of the standard chamber.

5.4.2 Field Instruments

The instruments discussed in 5.4.1 are complicated because they must be used to determine correction factors with high accuracy. Simpler versions of this type of instrument have been made and may be used as field or reference chambers. Ionization chambers used as field instruments in high-energy electron beams should have small dimensions, especially in the direction of the beam.

For electron beams of mean energy above 10 MeV, cylindrical ionization chambers (thimble type) can be used because the perturbation correction is small and has been experimentally determined (see Section 4.2.1.2), but their internal diameter should preferably not exceed 6 mm and their length should be no greater than 25 mm (NACP, 1980). As far as possible, the chamber, i.e., the wall, build-up cap and central electrode, should be made of a single known material with specified composition and good dimensional stability (Loevinger, 1980). If the wall is of a material that is not phantom-equivalent, e.g., graphite or air-equivalent plastic, it should be thin (about 0.5 mm thick). Leakage and stem effects should be negligible and the ratio between measured charge with negative and positive polarizing voltage should differ from unity by less than 0.5% so that corrections for charge deposition can be avoided; these performance criteria are met by most commercially available cylindrical ionization chambers (Mattsson *et al.*, 1981).

For electron beams below 10 MeV, a plane-parallel (coin-shaped) chamber should be used because the perturbation correction for cylindrical chambers is large and uncertain. The radial dimensions of the collecting volume should be defined by a guard-ring (Fig. 5.1). The entrance window should be thin so that measurements at the surface of the phantom can be made. The plate separation should be small in order to minimize the perturbation effect (see Section 4.2.1.1). The charge deposition in the collecting electrode and insulators of a coin-shaped chamber is generally larger than that for a cylindrical chamber of similar dimensions. Furthermore, the charge deposition (at the depth of its maximum) per unit absorbed dose increases with a decrease of the electron energy (see Fig. 2.16). If possible, the collecting electrode should be sufficiently thin so that the charge deposition has minimal effect on the collected ion charge (Markus, 1976), i.e., a ratio that departs from unity by less than 0.5% for the lowest electron energy in use. If this is not possible, then readings should be taken with both negative and positive polarity and averaged (Morris and Owen, 1975).

For both types of chambers, the saturation characteristics should be adequate for the dose rates from pulsed electron beams used in clinical practice. For a polarization voltage of 300 volts or more, and using the coin-shaped or cylindrical chambers with maximum dimensions given above, the losses due to ion recombination can be less than 1% for an absorbed dose to air in the chamber cavity of less than 0.1 mGy per pulse. Correction for recombination losses can be made either by calculation or measurement. For pulsed radiation, the measured charge is plotted against the inverse of the

polarizing voltage in the region of losses below 5%. The correct charge is determined by linear extrapolation of this plot to infinite polarizing voltage. The Hospital Physicists Association (HPA, 1971) suggests the following test to determine if sufficient voltage has been applied. A reading, R_1 is obtained, for a given monitored dose, using a polarizing voltage V. The measurement is then repeated for the same monitor units but only half of the polarizing voltage, $V/2$, to yield a reading, R_2. If the change in the reading, $X = 100\,(R_1 - R_2)/R_1$ is less than 5%, the efficiency at the full polarizing voltage V is $(100 - X)\%$. If X is greater than 5%, the polarizing voltage must be increased (see ICRU, 1982, Section 2.2.6).

Irradiation of the stem and cable may cause an unwanted current to be collected. This must be checked and the necessary precautions should be taken (either shielding the cable or placing the stem and cable out of the beam). This effect may be dependent upon the electron-beam energy and should be checked at the various energies used.

5.4.3 Calibration of Field Instrument Against a Chamber of Known Sensitivity

The most direct way of calibrating a field instrument is against a chamber of known sensitivity. This can be done by placing each instrument, in turn, in a phantom at a depth corresponding to the maximum of the depth ionization curve (for recommended depths for such calibration, see Section 6.2.3). Small variations from this depth then have negligible influence on the measurement. To assure that the two chambers are equally exposed, a transmission ionization chamber (see Section 8) can be used as a beam monitor. The readings of the field instrument and the instrument of known sensitivity are then normalized to a common monitor reading. The quotient of the normalized reading for the chamber of known sensitivity to that for the field instrument gives the absorbed dose per unit reading of the field instrument. However, when chambers of the thimble type are used, two problems arise. First, the perturbation correction for a thimble chamber when used with its axis perpendicular to the electron beam, is much greater than that for a coin-shaped chamber of similar volume. Although the perturbation correction is included in the calibration against a standard chamber, the variation in this correction, when the thimble chamber is used in electron beams of other energies, may be significant. The perturbation correction is discussed in Section 4.2.1.2 and typical values are given in Table 6.4. Second, the position of the effective point of measurement (Section 4.2.1.2) must be considered; the point of measurement will be displaced from the center of the chamber towards the source of the electron beam.

5.4.4 Calibration of a Thimble Chamber as a Field Instrument in a Cobalt-60 Gamma-Ray or 2 MV X-Ray Beam

An important problem for many users has been the lack of access to a laboratory able to provide the calibration for high energy electrons or the lack of access to a chamber of known sensitivity as described in Section 5.4.3. However, in most centers equipped with high-energy accelerators, an ionization chamber calibrated as an exposure meter for cobalt-60 gamma-rays or 2 MV x-rays is available, and several investigators have shown how the absorbed dose from electron beams can be obtained using such chambers (Almond, 1967, 1970; Svensson and Pettersson, 1967). An energy dependent factor, C_E, was introduced in ICRU Report 21 (ICRU, 1972), such that the absorbed dose in water, D_w, was obtained from $D_w = C_E N_c M$, where N_c is the cobalt-60 exposure calibration factor of the chamber, and M is the meter reading when the irradiation is made with electron radiation. This method has been the basis for absorbed-dose calibration methods recommended by various groups (HPA, 1971, 1975; NACP, 1972; ICRU, 1972; DIN, 1975).

There are some problems with this method and the similar method for photon beam calibration, as pointed out by various investigators (Matsuzawa *et al.*, 1974; Greening, 1974; Nahum and Greening, 1976, 1978; Almond and Svensson, 1977; Johansson *et al.*, 1978; NACP, 1980). ICRU Report 14 (ICRU, 1969) gives absorbed dose conversion factors (C_λ) to be used for measurement of high-energy x rays and valid for an ionization chamber with a *water equivalent wall*, while ICRU Report 21 (ICRU, 1972) gives factors (C_E) for electron radiation which are valid for an ionization chamber with a wall that is effectively *air equivalent* at the calibration quality.

The composition of the wall material influences the mass ionization corresponding to a given exposure in free air during calibration with cobalt-60 gamma radiation. The C_λ and C_E values are, therefore, dependent on the wall materials, and systematic errors are introduced if this is disregarded.

A new formulation is recommended below, which takes the materials of the chamber walls into account. Sections 5.4.4.1 and 5.4.4.2 describe the steps by which the exposure (or air kerma) produced by cobalt-60 gamma radiation is converted into absorbed dose to the air of the chamber. Section 5.4.4.3 deals with the next step—the conversion of the absorbed dose produced by the electron beam in the air of the chamber into the absorbed dose to the medium.

5.4.4.1 Derivation of the Absorbed Dose to Air Conversion Factor From the Exposure Calibration Factor. A calibration by a standards laboratory results in an exposure calibration factor N_X,

$$N_X = X_c/M_c \tag{5.11}$$

where X_c is the exposure at a point P in air, in the absence of the chamber, and M_c is the chamber meter reading when the chamber is centered at P and is corrected to standard temperature and pressure, and for humidity and recombination. The index c denotes that the radiation calibration of the ion chamber is involved (the quality of the calibration beam should be specified). The total chamber wall thickness, including build-up cap, should be equal to the thickness necessary for the production of transient charged particle equilibrium. For cobalt-60 gamma-rays, a thickness of 0.45 ± 0.05 g cm^{-2} can be used. The response of the chamber will ordinarily vary by less than 1% when using build-up caps of different low atomic number materials (plastic or graphite), provided the thicknesses, in g cm^{-2}, are the same (Almond and Svensson, 1977). This possible variation is eliminated if the material of the build-up cap is the same as that of the chamber wall.

The exposure can also be related to the mean charge per unit mass of air in the chamber $\overline{J}_{air}$ by,

$$\overline{J}_{air,c} = X_c k_m k_{att} k_{stem} \cdots \tag{5.12}$$

where the various correction factors, k, indicated in the equation, are applicable to the particular ionization chamber and the conditions existing at the time of the in-air exposure calibration at the standardizing laboratory. Specifically, k_m takes into account the lack of air equivalence of the ionization chamber material, k_{att} is a factor that takes into account the attenuation of the photons in the ionization chamber material, and k_{stem} takes into account the fractional increase in the ionization current due to scatter from the stem. The product of the correction factors, denoted by Πk_i, is discussed in detail below.

As the energy required to form an ion pair, W, has been considered to be constant for electrons in the energy range under consideration, the measurement of ionization in a known mass of air is directly proportional to the absorbed dose to the air, i.e.,

$$\overline{D}_{air,c} = \overline{J}_{air,c} W/e \tag{5.13}$$

where $\overline{D}_{air,c}$ is the mean absorbed dose to air inside the air cavity of the ionization chamber. W is the mean energy expended in air per ion pair formed; a (W/e) value of 33.85 JC^{-1} is recommended for dry air (see Section 5.4.1). From Eqs. 5.11, 5.12, and 5.13

$$D_{air,c} = N_X M_c \Pi_i k_i W/e \tag{5.14}$$

A calibration factor, N_D, giving the absorbed dose to air in the cavity can then be defined:

$$N_D = \overline{D}_{air,c}/M_c \tag{5.15}$$

where

$$N_D = N_X \Pi_i k_i W/e \tag{5.16}$$

N_D is a constant for each ionization chamber. Because (W/e) is experimentally determined to be independent of electron energy within the electron energy range of interest here, the calibration factor, N_D, can also be used for the determination of the absorbed dose to air in the cavity for other electron energies, i.e.,

$$N_D = \overline{D}_{air,c}/M_c = \overline{D}_{air,E}/M_E \tag{5.17}$$

where E denotes the electron beam energy. According to Eq. 5.16, when N_X is x C kg^{-1} per scale division, N_D is x $\Pi_i k_i$·33.85 Gy per scale division. When N_X is y R per scale division, N_D is y $\Pi_i k_i$·0.87 rad per scale division.

N_D can thus be determined from an exposure calibration in a cobalt-60 gamma-ray beam using Eq. 5.16 and applying the appropriate factors. The most important factors, k_m and k_{att} are discussed below.

k_m. This factor takes into account the lack of air equivalence of the ionization chamber wall material and the build-up cap for the radiation used for the calibration (cobalt-60 gamma-rays or 2 MV x rays). Theoretical values for wall material and build-up cap of the same material (m) can be calculated from the expression

$$k_m = (\overline{\mu}_{en}/\rho)_{m,air}\, s_{air,m} \tag{5.18}$$

k_m values, using recent $(\overline{\mu}_{en}/\rho)$ values from Hubbell (1977) and $s_{air,m}$ values from Berger (1980) are given in Table 5.7 for several materials used for chamber walls. It should be noted that the change in I-values incorporated in Berger (1980) has increased the value of k_m for water and PMMA by 2% from those used previously.

According to most protocols, ionization chambers should be calibrated with additional plastic caps to give a total thickness of about 0.5 g cm^{-2}. A common combination is a chamber with a graphite (or air-equivalent) wall of approximate thickness 0.5 mm fitted with a plastic cap. Equation 5.18 does not apply when the chamber wall and build-up cap are made of different materials. However, the experimental work by Almond and Svensson (1977) indicates that the composition of the inner wall is much more important than that of the build-up cap. Thus, it is a reasonable approximation to use Eq. 5.18 even for a heterogeneous chamber, though experimental determinations of k_m for the particular chamber in question are to be preferred (Mattsson *et al.*, 1981).

k_{att}. This factor takes account of the attenuation of photons in the ionization chamber material at the time of calibration in the cobalt-60 gamma-ray (or 2 MV x-ray) beam. In the determination of the attenuation of the photons in the cap and wall material, it is important to remember that the electrons producing ions in the cavity are generated at different depths in the materials in front of the cavity and, thus, that not all of the at-

TABLE 5.7—*The factor k_m which takes into account the lack of air-equivalence of the chamber wall and cap material at the exposure calibration in cobalt-60 gamma-ray beams*

Chamber Wall and Cap Material, m	$(\mu_{en}/\rho)_{m,air}$[a]	$s_{air,m}$[b]		k_m	
		St&P[c]	St-C[d]	St&P[c]	St-C[d]
Air equivalent	1.000	1.000	1.000	1.000	1.000
Graphite	1.002	0.988[e]	1.000[f]	0.990[e]	1.002[f]
			0.999[g]		1.001[g]
Water	1.112	0.885	0.885	0.984	0.984
PMMA	1.081	0.910	0.909	0.984	0.983
Polystyrene	1.079	0.904	0.904	0.975	0.975
A-150	1.103	0.880	0.879	0.971	0.970

[a] Values taken directly from, or calculated using Hubbell (1977).
[b] Calculated assuming effective electron energy of 0.3 MeV for the slowing-down spectrum of the generated electrons.
[c] Sternheimer and Peierls (1971) density effect corrections were applied; data from Berger (1980).
[d] Sternheimer (1952)—Carlson (1975) density effect corrections were applied; data from Berger and Seltzer (1982).
[e] A density of 2.25 g cm^{-3} was used for graphite (see Section 2.2.2).
[f] A density of 2.265 g cm^{-3} was used for graphite (see Section 2.2.2).
[g] A density of 1.7 g cm^{-3} was used for graphite (see Section 2.2.2).

tenuation in the front wall should be included in k_{att}—only the attenuation from the wall's outer surface to the mean location of electron production that produces ions in the cavity.

The factor k_{att} or its inverse has been discussed by several investigators (e.g., Burlin, 1959; Whyte, 1959; Barnard *et al.*, 1962; Boutillon and Niatel, 1973; Loftus and Weaver, 1974; Johansson *et al.*, 1978; Almond *et al.*, 1978; Nath and Schulz, 1979). Fairly good agreement is obtained between experimental and Monte Carlo calculated values (Nath and Schulz, 1979). The factor is dependent on the size and shape of the chamber and varies between 0.98 and 1.00 for "practical chambers". A value of 0.990 ± 0.010 can be used for cylindrical chambers of the sizes recommended in Section 5.4.2 (Johansson *et al.*, 1978).

A graphite wall and a PMMA build-up cap have often be used. Johansson *et al.* (1978) and Almond *et al.* (1978) determined $k_m \cdot k_{att}$ for this combination by comparison with a graphite chamber with a graphite build-up cap, for which k_m was obtained from Eq. 5.18 (see also Table 5.7). They showed that a value of 0.975 ± 0.005 can be recommended for this type of cylindrical chamber. Henry (1979) carried out an experimental determination of $k_m \cdot k_{att}$ for a Tufnol-walled Baldwin-Farmer chamber with a perspex build-up cap by determining the geometrical volume of the chamber and then comparing the chamber response with the exposure standard established by a national standards laboratory. His result was 0.971 ± 0.008.

5.4.4.2 Use of other Calibration Factors. The possibility now exists of obtaining calibration factors from the standards laboratories for quantities other than exposure. These include calibrations of ionization chambers in terms of air kerma or absorbed dose to water in a cobalt-60 gamma-ray beam. In principle, it is also possible to use such calibrations to derive a chamber conversion factor, N_D. This is explained below for the example of an air kerma calibration. The procedure using an absorbed dose to water calibration has been analyzed in detail by Loevinger (1980, 1981).

The air kerma calibration factor, N_K, is defined by

$$N_K = K_{air,c}/M_c \tag{5.19}$$

where $K_{air,c}$ is the kerma in air for the calibration radiation quality and at the center of an ionization chamber (with a wall thick enough for transient electron equilibrium to be established) without the perturbing influence of the chamber, and M_c is the meter reading at calibration, corrected for recombination losses, temperature, pressure, humidity etc. There are now international recommendations (Jennings, 1982) for primary standards laboratories to derive air kerma from exposure measurements. The relationship between air kerma (K_{air}) and exposure (X) is

$$K_{air,c}(1-g) = X_c W/e \tag{5.20}$$

where g is the fraction of the energy of the charged particles that is lost to bremsstrahlung in air. From Eqs. 5.20 and 5.14

$$\bar{D}_{air,c} = K_{air,c}(1-g)\Pi_i k_i \tag{5.21}$$

and from Eqs. 5.15, 5.19, and 5.21

$$N_D = \bar{D}_{air,c}/M_c = N_K(1-g)\Pi_i k_i \tag{5.22}$$

In order to obtain N_D from the air kerma calibration, the $\Pi_i k_i$ factors are required (Section 5.4.4.1) as well as the fraction g of energy lost to bremsstrahlung. For cobalt-60 gamma-rays, $g = 0.004$ (Boutillon, 1977).

5.4.4.3 Determination of the Absorbed Dose in Water in the Electron beam. The second step is to use the Bragg-Gray relationship (Eq. 4.2) to calculate the

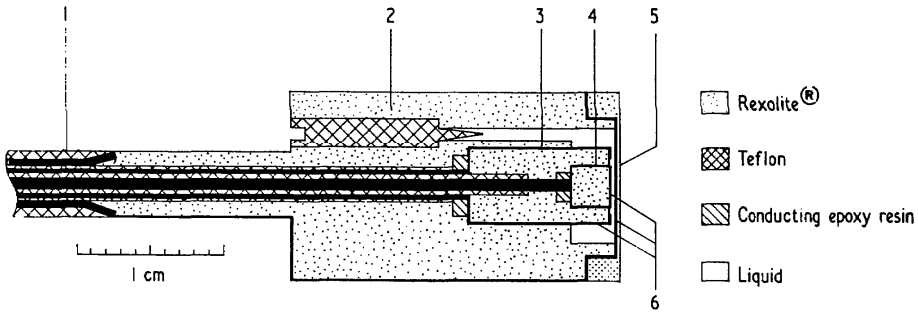

Fig. 5.2. Cross-sectional view of a liquid ionization chamber. (1) Teflon insulated low noise triaxial cable. (2) Teflon needle valve. (3) Guard electrode. (4) Central electrode. (5) Front window with HT electrode. (6) Thin layers of beryllium. From Wickman (1974a). Rexolite® is a polystyrene copolymer with a density of 1.05 g cm^{-3} and a chemical composition very similar to that of polystyrene.

dose to water from the dose to the air in the cavity. If one assumes that the cavity is "wall-less" (Section 4.3.3), the stopping power ratio, $s_{w,air}$, can be calculated from the Spencer-Attix theory (Spencer and Attix, 1955) with an appropriate value of Δ determined by the size of the cavity (Eq. 4.13). This assumption is acceptable if the surrounding medium is not too dissimilar from air in atomic composition. If the atomic composition of the medium is greatly different from that of air, a thin air-equivalent lining may be necessary (Section 4.3.2). For the case of water, there is no problem in this respect and the absorbed dose can be evaluated using Eq. 5.9. The complete practical procedure for absorbed dose determination with an ionization chamber is described in detail in Section 6.3.2.

5.5 Liquid Ionization Chambers

Dielectric liquids have been used instead of air as the sensitive medium in ionization chambers for electron dosimetry for measurements of relative dose distributions (Mathieu, 1968; Mathieu *et al.*, 1969; Casanovas *et al.*, 1971; Wickman, 1974a, 1974b). The properties of ten different liquid hydrocarbons for use in ionization chambers were studied in detail by Casanovas (1975). The response of the liquid chamber, expressed as the quotient of collected charge and absorbed dose to the liquid, was shown to increase slowly with temperature and rapidly with electric field strength, and to decrease with an increase in mean LET.

The walls of liquid ionization chambers have been made from perspex (Mathieu *et al.*, 1970; Casanovas, 1975) and from Rexolite® (a styrene copolymer with a chemical composition very similar to that of polystyrene) with an evaporated thin layer of beryllium as the conducting electrode material (Wickman, 1974a; Fig. 5.2).

Some characteristic data for a 2,2,4-trimethylpentane-based liquid ionization chamber used for measurements in electron beams are given by Wickman (1974a, 1974b): the polarizing potential was 900 V over a liquid thickness of 0.3 mm; the general recombination for irradiation at a pulse repetition frequency of 50 Hz, with a mean absorbed dose rate to the liquid of about 20 mGy s^{-1}, was 1%; the sensitivity of the chamber increased by 0.3% per °C in the temperature region 20–40°C and no quality dependence was found when measuring at depths in water larger than 10 mm for electron energies between 8 and 32 MeV and using the $FeSO_4$ dosimeter as a reference. No significant energy dependence was expected as the stopping-power ratio of 2,2,4-trimethylpentane to water varies by only 0.2% in the energy range 1–50 MeV, and as the LET distribution is almost independent of incident energies and phantom depth (Berger and Seltzer, 1969a).

The liquid chamber is particularly suitable for measurements in high-dose gradient regions at small phantom depths (Hultén and Svensson, 1975), at the fall-off part of the depth-dose curve (Casanovas, 1975), and behind inhomogeneities in the phantom (Wickman, 1974a). It may also be possible to use the chamber as a transfer instrument of absorbed dose calibrations as it has high reproducibility and small quality dependence in an electron beam.

5.6 Solid State Dosimetry

5.6.1 Introduction

There are several types of solid state dosimeters which may be used with electron beams. They are not absolute and require calibration to determine absorbed dose. These dosimeters can be divided into two classes: (a) integrating dosimeters such as thermoluminescent crystals, and plastic optical density dosimeters, and (b) dose rate measuring devices such as semiconductor junction detectors.

Thermoluminescent dosimeters (TLD) have been widely used in the absorbed dose range from fractions of a milligray to tens of grays and above. The radiation induced optical changes in polymethylmethacrylate (PMMA) have been used in the 10^3 to 10^5 gray absorbed dose range. Silicon diode junction detectors are finding increasing application in scanning devices to map

electron beam field distributions. Thermoluminescent dosimeters, optical density systems and silicon diode detectors will be briefly discussed in the following sections.

5.6.2 Thermoluminescent Phosphors

Thermoluminescent dosimeters (TLD) are now widely used in radiation therapy to measure the patient absorbed dose (Rudén, 1971; Suntharalingam and Mansfield, 1971; Rudén and Nilsson, 1975; Lindskoug, 1974).

Suntharalingam (1980) has noted that lithium fluoride continues to be the most commonly-used phosphor for clinical dose measurements. "Throw-away" LiF is a radiation-sensitized powder available as a pre-encapsulated dosimeter. If allowance is made for the mass of the powder in each dosimeter, a measurement precision of 1–2% is possible. Solid TL dosimeters are available as extruded or heat-pressed ribbons, rods or chips which have greatly facilitated the use of TLD in the clinical environment. The thin Teflon-impregnated discs are best suited for such purposes as skin-dose measurements, although they have not been as widely used as the other forms of the phosphor. A detailed evaluation of the clinical use of TLD, including its use with electrons and a discussion of the electron-beam energy dependence, has been made by Rudén (1975) and Rudén and Bengtsson (1977).

The light sensitivity of LiF is only of practical importance when low doses are measured. Several investigators (Bjärngard and Jones, 1968; Freewick and Shambon, 1970) have shown that 2 days of exposure to a normal fluorescent laboratory light produces a response in LiF-Teflon discs equal to an absorbed dose of 0.3 mGy from gamma-rays. Lippert and Mejdahl (1967) found that a 2-hour exposure of powdered LiF MgTi to daylight resulted in an apparent exposure of 300 mR. TLD materials are particularly sensitive to ultraviolet light so exposure to sunlight or fluorescent light should be avoided. It should also be pointed out that Teflon itself may exhibit some phosphorescence. It has also been found that there is an increase in the intrinsic response of ^{7}Li MgTi powder (TLD 700) to 207 nm ultraviolet light after exposure to gamma radiation (Mason, 1971).

Since LiF is slightly soluble in water but very toxic, care must be taken when using LiF for in vivo measurements. Unprotected matrix-imbedded LiF dosimeters exhibit a loss in sensitivity and extruded LiF also reacts with tissue fluid resulting in a loss of sensitivity which is initially very rapid.

Several of the factors which make solid-state TL dosimeters suitable for electron beam studies are listed below:

(a) The large response of TLD per unit volume enables one to use small sizes. Since there are often steep absorbed-dose gradients in the electron beam fields, TL dosimeters can be used there to good advantage (Almond *et al.*, 1967a).
(b) Trapped electrons or holes may persist for long periods with the advantage that total absorbed dose may be determined at a convenient time after irradiation.
(c) Higher absorbed dose rates (sensitivity independent of absorbed dose rate up to 10^{9} Gy s^{-1}) can be measured with TL dosimeters than with other systems such as ionization chambers and chemical dosimeters (Fowler, 1963, 1966).
(d) Ruggedness.
(e) Adaptability to various sizes and shapes.
(f) Useful absorbed dose range from milligrays to grays.

It is necessary to calibrate the response of the thermoluminescent dosimeter. This calibration should be done with a particular read-out instrument, because each instrument will have a different response to the light emitted, due to geometric considerations, photomultiplier response, etc. It is advisable to calibrate the dosimeter in an electron beam which is as similar as possible to the beam to be investigated, and at approximately the same absorbed dose level as that to be measured. Such procedures will eliminate energy-dependent effects and variation of sensitivity with absorbed dose (see below). Some of the dosimeters should be re-calibrated after each annealing as a check of their reproducibility. The relative response between individual solid dosimeters should be determined, and it is often possible to select groups of solid dosimeters with equal response.

Energy Response and LET Dependence. TL dosimeters are generally insensitive to changes in electron energy over the range of interest in radiation therapy. Care must be taken, however, in calculating the energy absorbed in the phosphor (see below). The TL response shows a marked LET dependence with the response decreasing with increasing LET above approximately 10 keV/μm (Tochilin *et al.*, 1968).

There has been extensive discussion in the literature concerning the energy dependence of TLD for electron beams relative to cobalt-60 gamma rays. Decreased responses of greater than 10% have been reported, although some investigators have found no dependence (Gantchew and Toushlekova, 1976; Shiragai, 1977). Various explanations have been put forward to explain this decrease in response, including the dependence on size and shape, and the composition of the phosphor. The effect is probably related to interface effects as indicated by Rudén (1975) and Bankvall and Lidén (1977). It is, therefore, always advisable to calibrate at

the same energy a TL dosimeter of the same size and shape as those being used in the investigation.

Absorbed Dose Response. Ideally, a dosimeter should have a linear response over the full range of absorbed doses to be measured. However, most TL phosphors do not respond linearly (Cameron *et al.*, 1967) and require careful calibration in the absorbed dose range of interest. The change from a linear response to a "supralinear" response (i.e., the response increasing more rapidly than the first power of the absorbed dose) may occur at or below 10 Gy. The departure from linearity is generally gradual and the response can often be approximated as linear over a limited range.

For very high absorbed doses, the dosimeter becomes saturated and the TL output remains constant with further increases in absorbed dose. TL read-out instruments may also demonstrate non-linearity of response, complicating the determination of the phosphor response. The calibration should, therefore, always be carried out on the instrument to be used in the investigation.

Fading. Due to shallow electron trap depth or to light sensitivity, the total TL output will decay with time. Care should be taken to take this decay into account or to eliminate it (Cameron *et al.*, 1968; Mårtensson, 1969) by careful selection of the temperature range over which the TL output is recorded or by special post-irradiation annealing or both.

5.6.3 Optical Absorption in Clear Polymethyl Methacrylate (PMMA)

Clear PMMA has been used as a dosimeter in the kilogray range and has been studied by a number of investigators (Boag *et al.*, 1958; Orton, 1966; Berry and Orton, 1966; Berry and Marshall, 1969). Berry and Marshall found that, with spectrophotometers in good condition, readings with a standard deviation of less than 2% may be achieved from 1-mm thick material exposed to 25 kGy. Care should be taken in cleaning the material and measuring its thickness, and all determinations of optical density should be done with reference to an unirradiated control sample at 304 nm. Fading of the induced change in optical density should also be taken into account.

5.6.4 Silicon Diode Detectors

Radiation detectors utilizing silicon p-n junction diodes offer the advantages over conventional ionization chambers of enhanced sensitivity, instantaneous response, ruggedness, and small size. Since the determination of the actual collecting volume (depletion region) of a diode is difficult, if not impossible, to achieve, they cannot be used for absolute measurement of absorbed dose. However, they are very suitable for relative measurements in steep dose gradients. They can be used directly to measure relative absorbed dose in electron beams if certain precautions are taken. In general, no systematic differences between diode measurements and measurements made with the other systems are seen for depths larger than the dose maximum (Hultén, 1975; Gager *et al.*, 1977; Johansson and Svensson, 1982). At smaller depths, the diode measurements may be too low by a few per cent because of energy and particle direction dependence (Brahme and Svensson, 1976). In general, great care must be exercised in using diodes because they may exhibit a large temperature dependence, cumulative radiation damage, including that caused by neutrons, as well as dependence on electron energy and direction. Systematic errors can also be introduced for some accelerators (especially betatrons) due to the radiation pulse shape. When using diodes, the distributions should be checked against ionization chamber measurements or iron-sulfate dosimeter measurements and, if the diode agrees with the fully-corrected ion chamber data, then it can be used to measure relative dose distributions directly.

5.7 Film Dosimeters

Photographic dosimetry is a convenient and rapid method of obtaining a complete set of isodose curves in the plane of the film for high energy electrons (Dutreix, 1958; Breitling and Seeger, 1963; Dutreix and Dutreix, 1966; Hettinger and Svensson, 1967). However, it is an empirical method. The radiation-sensitive medium, the photographic emulsion, does not meet the general requirements for the atomic composition of the biological tissues, and the complex mechanism that transforms the absorption of energy into blackening involves many steps of a physical and chemical nature that are not thoroughly understood.

The variation of optical density as a function of dose is represented by the sensitometric curve, the shape of which depends upon the type of emulsion used (Fig. 5.3) (Rassow, 1970; Marinello and Sliwinski, 1974; Dutreix, 1979). For some emulsions, the net density, i.e., the total density minus the fog, is proportional to the dose. For others, the proportionality between density and dose does not exist. For a given film, the shape of the sensitometric curve, together with the absolute sensitivity itself, may change with time because of new manufacturing methods. The shape of the sensitometric curve and the response of certain films have changed at least seven times during the last 20 years. In 1975, for example, the response of a particular type of film was reduced by a factor of 2 (Dutreix, 1979). Therefore, published curves may not be reliable and should not be used in place of actual calibrations. Also, film characteristics may vary from batch to batch.

Whenever possible, films that have a linear sensitometric curve should be used because the net optical density can be used directly to give the relative absorbed dose distribution in a single film or in several films processed simultaneously. The optical density corresponding to the fog is the optical density of a nonirradiated film of the same batch that is processed under the same conditions as the measured film. It is common practice to determine the fog density on the edge of the measured film; this procedure leads, in general, to an overestimation of the fog density and to large errors in regions of low densities.

The processing conditions do not critically affect the shape of the sensitometric curve, but the value of optical density corresponding to a given dose depends strongly upon the bath temperature and developing time (Dutreix, 1958; Rassow, 1970). It is essential that the processing conditions be exactly reproduced if comparisons are made between series of films that are processed separately—a variation of 0.1°C in the bath temperature or of 2–3 sec in developing time, for usual processing conditions, leads to a variation of 1% in optical density. The films should all come from the same batch. In automatic processing devices, the temperature is usually very high and a very small variation in temperature may lead to a large variation in density even between the various parts of a single film. It is, therefore, recommended that the film be processed manually. The reproducibility in density that can be expected can be summarized as follows:

Different areas of the same film	2%
Films processed simultaneously	3%
Films processed separately (nominally identical processing conditions)	5%

The density is generally considered to be dose rate independent in the range encountered in radiotherapy, even for pulsed beams.

The response of the film (net optical density per unit absorbed dose to the film) must depend in some way on the electron fluence spectrum in the emulsion layer, which, in its turn, depends on the electron fluence spectrum in the surrounding medium. Harder (1967), Berger and Seltzer (1969a) and Nahum (1976) have shown that the low energy part of the electron spectrum, where the LET depends strongly on the electron energy, has an almost constant shape per unit absorbed dose, irrespective of electron beam energy and depth (see Figs. 2.6b and 2.7b). As can be seen in Table 2.2, the LET (collision stopping power) varies relatively slowly with energy in the high energy region. This means that the total LET distribution for electron beams and, hence, the film response, changes little with energy and depth even though film response is LET dependent.

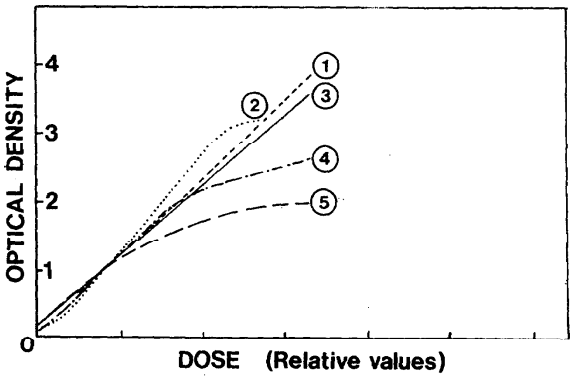

Fig. 5.3. Optical density versus dose for selected films (Dutreix, 1979). The values of the doses are normalized in such a way that the curves coincide for an optical density of unity, which corresponds roughly to the following doses in water: (1) Kodak M—0.1 to 0.2 Gy; (2) Kodalite—1 Gy; (3) Gevaert Structurix double-coated—0.24 Gy; Gevaert Structurix single-coated—0.58 Gy; (4) Gevaert Rapidoline (FQ71P)—1 Gy; (5) Dupont (RIF)—1 Gy.

The absorbed dose in the phantom is related to the absorbed dose in the film dosimeter through the phantom-film mass collision stopping-power ratio, and can be further complicated by electron scattering differing in phantom material and film material. The for-

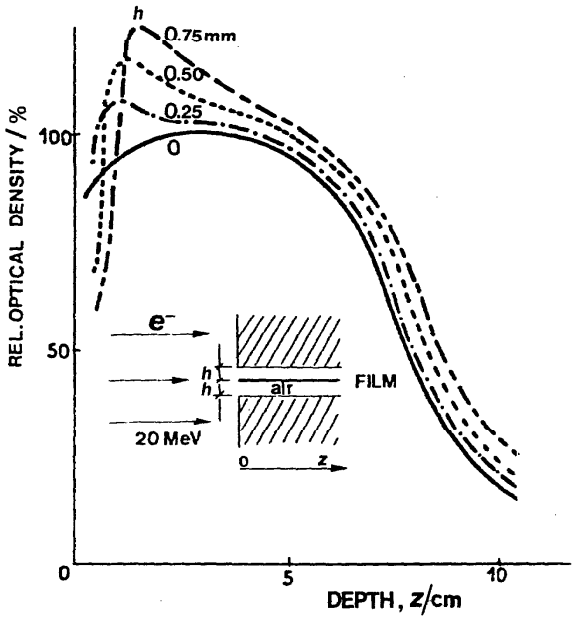

Fig. 5.4. Influence on the depth-density curve of thin air gaps along the film surface. Air gaps are produced on both sides of the film by strips of paper of thickness h. Significant modifications of the depth-density curve are noticed even for very thin air gaps (Dutreix and Dutreix, 1969).

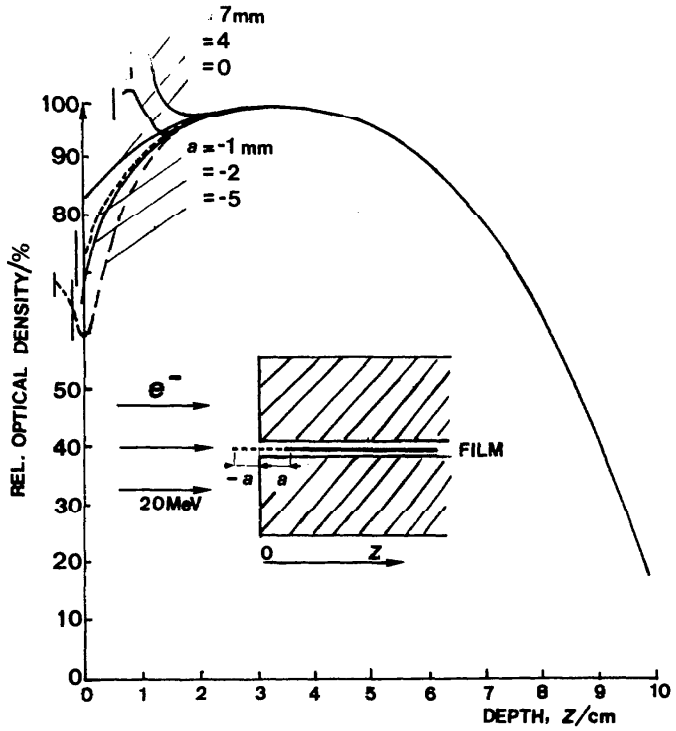

Fig. 5.5. Influence on depth-density curve of maladjustment of the film edge to the phantom surface (Dutreix and Dutreix, 1969).

mer varies only slowly with mean primary electron energy whereas the latter can be extremely complicated and is best investigated experimentally.

Breitling and Seeger (1963) and Rassow (1970) have studied, experimentally, the variations of film blackening with absorbed dose as a function of the energy at the phantom surface and the depth in the phantom. Breitling found a 12% variation in the net optical density per unit of absorbed dose to the phantom between 4 and 16 MeV electrons. Rassow found a variation of 2 to 10% for 5- to 45-MeV electrons depending upon the type of film and the processing conditions. Breitling and Rassow concluded that in the fall-off region of the depth-dose distribution, such variations could often be neglected due to the high dose gradient (a 10% error at the level of 10% depth dose leads to only a 1% displacement of the depth-dose curve) and that the relative net optical density could generally be used directly for depth-dose determination after correction for nonlinearity of the sensitometric curve, if necessary. This was confirmed by Wambersie *et al.* (1965) and Hettinger and Svensson (1967) who found excellent agreement between depth-dose curves measured by film and by ferrous sulphate. Film dosimetry can be used, therefore, without further corrections, to measure complete dose distributions and the agreement between film readings and absorbed dose is adequate even in the regions near the edges of the beam.

Some authors (Markus and Paul, 1953; Loevinger *et al.*, 1961) have reported discrepancies between films exposed perpendicular or "parallel" to the beam axis, particularly in the build-up region where the "parallel" film underestimates the dose received. This discrepancy was attributed by Markus and Paul (1953) to the increased scatter associated with the high atomic number of the emulsion. Another reason for this effect may be a misalignment of the film edge with the surface of the phantom or the presence of thin layers of air on both faces of the film. The artifacts that result from a thin air layer along the film surface were demonstrated by Loevinger *et al.* (1961), and were investigated systematically by Dutreix and Dutreix (1969), see Fig. 5.4. The figure shows the distortion of the depth-density curve when thin paper spacers are placed on both sides of the film to create air gaps. The explanation is that the electrons are more easily scattered into than out of an air volume; thus there is a tendency for the electrons to concentrate in any "tunnel" parallel to the beam direction. To avoid the influence of such strips of paper as the foldings of the envelope, the film must be exposed bare or under a single paper sheet.

The influence of the nonalignment of the film edge with respect to the phantom surface is shown in Fig. 5.5. In the case with $a < 0$, the edge of the film extends outside the phantom, giving rise to an initial underestimation of the dose due to scatter of electrons by the

film out of the plane of the film. When the film edge lies slightly back within the phantom, $a > 0$, an artifact appears due to the air gap in front of the film.

In both cases, the distortion of the electron beam is limited to the first few centimetres below the surface and vanishes at larger depths. To avoid any distortion of the beam by the film itself, the film should be irradiated between two accurately flat phantom surfaces which are tightly pressed together. Under these conditions, no significant differences are found between films irradiated perpendicular or parallel to the beam axis (Dutreix and Dutreix, 1966; Rassow, 1970; Marinello and Sliwinski, 1974). However, as the setting of films parallel to the beam axis requires great care, it is recommended that agreement between perpendicular and parallel films be checked carefully.

Since film is very sensitive to Cerenkov radiation, an opaque phantom material must be used or the film must be wrapped in an opaque cover. In practice, the film can either be loaded directly into cassettes made of the phantom material, or placed in the phantom in ready-packed containers.

Film dosimetry has some practical advantages over other systems in measuring isodose distributions: a complete dose distribution in a plane can be obtained during one exposure and films have a high spatial resolution which is very useful in the regions where the dose gradients are very steep.

6. Absorbed Dose in a Phantom Irradiated with an Electron Beam

6.1 General

Each radiotherapy department must have absorbed dose distributions in water available for each beam quality to be used. Standardized reference absorbed-dose distributions for a given energy can generally not be used as extensively with electrons as with photon beams, because the shape of electron beam isodose curves can vary considerably between different treatment units. The dose distributions depend on several factors such as the quality of the initial electron beam when it meets the accelerator window and the scattering and energy degradation in window, foils, transmission chambers, air, etc. These factors may also differ for accelerators of the same type and manufacturer and, therefore, a complete set of absorbed-dose distributions should be measured for each accelerator. All the data supplied by the manufacturer of the accelerator must be checked to confirm their applicability. This usually involves carrying out extensive measurements and must be done with great care. The number of absorbed-dose distributions needed for radiation treatments is often large because several combinations of nominal energies, field sizes, scattering foils, etc. may be used. Therefore, much emphasis must be given to rapid methods of absorbed-dose distribution determinations.

6.2 Phantoms

6.2.1 Standard Phantom

Water is recommended as the standard medium for absorbed-dose measurements because the absorbed-dose distributions in water and human soft tissue are very similar for electron beam irradiations. Furthermore, the constant chemical composition and density of water present a great advantage. However, slabs of solid material are more easily handled. Furthermore, they are more convenient than water for measurements at small depths. When a material other than water is used, it is recommended that the solid phantom data be converted into "in-water data" (Section 6.2.2).

The size of the phantom used should be larger than the field size so that none of the primary electrons can leave it laterally. The standard size recommended is, as for photon beams, a 30-cm cube. Such a phantom is convenient for any energy used and for most of the clinical situations (Fig. 6.1). For low energies, shallower phantoms may be used; a total depth 5 cm greater than the practical range is adequate.

6.2.2 Material Equivalence

The condition for two phantom materials to be considered as exactly equivalent is that the following three physical quantities should be identical for the whole electron energy range under consideration: linear collision stopping power, S_{col}, linear radiative stopping power, S_{rad}, and linear scattering power, T. These quantities can be obtained from Tables 2.2a, 2.4, and 2.6, respectively. Table 6.1 gives the ratios of these values to those for water for various phantom materials and the values given may be used as figures of merit in the choice of water equivalent phantom materials. Any material used as a phantom material for photon beams can also be used for electrons.

It is often necessary to convert absorbed-dose distribution data determined in one material into data for a different material, e.g., plastic to water. The *scaling* law (Section 2.8.3) can be used for this purpose. However, a simplified procedure is often desirable and may be used when the mean atomic numbers, $\overline{Z}$ (see Section 2.8.3), of the materials are similar. The linear continuous-slowing-down range, r_0/ρ (r_0 is the csda range in units of mass per area) is a convenient scaling factor. The ratios $(r_0/\rho)_m/(r_0/\rho)_w$, evaluated from Table 2.5, are, therefore, included in Table 6.1. As csda ranges are calculated by integrating the reciprocal of the linear total stopping power, they should be identical for two materials if the linear total stopping powers are identical for the two materials for all energies between $\overline{E}_0$ and 0. As the linear total stopping powers of two different materials never are strictly identical for every energy, the linear csda range allows the scaling of depths by means of an "average" linear total stopping power value.

Assuming the linear depths $z_w(P)$ and $z_m(P)$ along the central axis, corresponding to a certain percentage absorbed dose P in water (w) and in medium (m), are proportional to the csda ranges in the two materials; then

$$\frac{z_m(P)}{z_w(P)} = \frac{(r_0/\rho)_m}{(r_0/\rho)_w} \tag{6.1}$$

When this ratio is known, the depth of the percentage dose P in water, $z_w(P)$, can be calculated from measurements of the depth, $z_m(P)$, of the same percentage dose P in medium m.

Equation 6.1 was shown by Mattsson *et al.* (1981) to be a fairly good approximation for some commonly-used materials (graphite, polystyrene, A-150 plastic, and PMMA) in the energy range ($\overline{E}_0$) from about 5 MeV to at least 30 MeV, but a relatively large difference was obtained with aluminum below 10 MeV. This is also to be expected from the more general scaling law in Section 2.8.3 because $\sqrt{\overline{Z}}/\tau$ is very different for water and aluminum, when τ is fixed. When a plane-parallel ionization chamber was used to measure the radiation at the

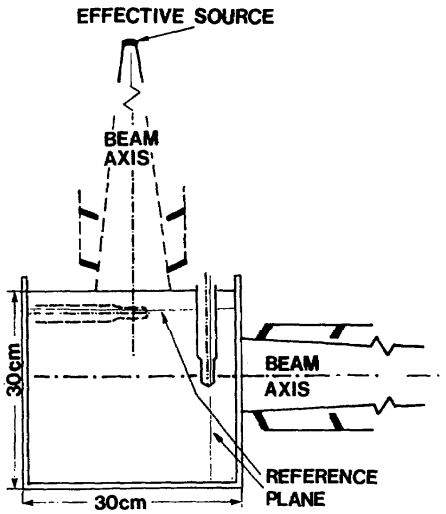

Fig. 6.1. The standard water phantom for absorbed dose determination. In this example, the use of a thimble ionization chamber for absorbed dose determination at the reference point in the phantom is shown. The effective point of measurement of the chamber should be placed at the reference point in the phantom (Section 6.3).

maximum of the depth-ionization in water and in the four materials mentioned above, the results were identical to within 1%. The "relative depth versus ionization curves" for depths beyond the dose maximum region for these four materials, recalculated using Eq. 6.1, were displaced less than 1 mm from the curves measured in water.

In a divergent beam, a correction factor should be applied for the relative influence of the inverse square law in the two media. It can be neglected when the difference in depths for a given percentage absorbed dose is small, i.e., for nearly water-equivalent materials or for low electron energies where the depths are always small compared with the distance to the source.

The scaling factor in the direction perpendicular to the beam axis could, in the first approximation, also be taken from Eq. 6.1, even though more accurate scaling is obtained by using the method described in Section 2.8.3 (see Fig. 2.22). However, problems due to lack of lateral scattering equilibrium, particularly for small fields in low density materials, should be kept in mind. The approximation represented by Eq. 6.1 is significantly better than assuming that the right hand side of Eq. 6.1 is the reciprocal of the mass densities of the two materials.

6.2.3 Reference Plane and Reference Point

The reference plane is a plane perpendicular to the beam (reference) axis at a specified depth. The intersection between the reference plane and the beam axis is the reference point. Its depth must be large enough to minimize any possible influence from low-energy electrons scattered into the phantom from air at large angles of incidence or scattered from machine accessories, especially the collimator device. At the same time, in order to increase the accuracy of dose measurements at the reference point, the reference point should be located in a region with a small dose gradient.

The depth of the maximum absorbed dose, R_{100}, along the beam axis for a 10 cm × 10 cm field is recommended as the depth of the reference plane, except when this maximum absorbed dose occurs at an un-

TABLE 6.1—*Ratios of linear collision stopping powers, linear radiative stopping powers, linear total stopping powers, linear continuous-slowing-down ranges, and linear scattering powers for different phantom materials*[a] *and tissues to the corresponding values for water (calculated from Tables 2.2a, 2.4, 2.5 and 2.6)*

	PMMA/Water					Polyethylene/Water				
Energy MeV	$\frac{S_{col,m}}{S_{col,w}}$	$\frac{S_{rad,m}}{S_{rad,w}}$	$\frac{S_{tot,m}}{S_{tot,w}}$	$\frac{(r_0/\rho)_m}{(r_0/\rho)_w}$[b]	$\frac{T_m}{T_w}$	$\frac{S_{col,m}}{S_{col,w}}$	$\frac{S_{rad,m}}{S_{rad,w}}$	$\frac{S_{tot,m}}{S_{tot,w}}$	$\frac{(r_0/\rho)_m}{(r_0/\rho)_w}$[b]	$\frac{T_m}{T_w}$
0.1	1.159	1.019	1.158	0.863	1.04	1.001	0.689	1.001	0.995	0.72
0.2	1.159	1.023	1.158	0.864	1.04	0.999	0.696	0.998	1.000	0.71
0.5	1.159	1.029	1.157	0.864	1.04	0.984	0.707	0.992	1.003	0.71
1.0	1.154	1.035	1.153	0.865	1.03	0.984	0.720	0.982	1.010	0.71
2	1.149	1.039	1.150	0.867	1.04	0.976	0.724	0.973	1.018	0.71
5	1.147	1.044	1.146	0.870	1.04	0.972	0.732	0.961	1.028	0.71
10	1.149	1.047	1.141	0.872	1.03	0.971	0.737	0.949	1.037	0.71
15	1.150	1.048	1.137	0.874	1.03	0.971	0.739	0.939	1.044	0.71
20	1.150	1.049	1.134	0.876	1.04	0.970	0.741	0.930	1.050	0.70
30	1.150	1.050	1.126	0.878	1.03	0.969	0.743	0.914	1.061	0.70
40	1.150	1.051	1.120	0.882	1.03	0.968	0.744	0.901	1.070	0.70
50	1.150	1.052	1.116	0.883	1.03	0.968	0.746	0.890	1.077	0.70

TABLE 6.1—*Continued*

	Polystyrene/Water					A-150 Plastic/Water				
Energy MeV	$\frac{S_{col,m}}{S_{col,w}}$	$\frac{S_{rad,m}}{S_{rad,w}}$	$\frac{S_{tot,m}}{S_{tot,w}}$	$\frac{(r_0/\rho)_m}{(r_0/\rho)_w}$[b]	$\frac{T_m}{T_w}$	$\frac{S_{col,m}}{S_{col,w}}$	$\frac{S_{rad,m}}{S_{rad,w}}$	$\frac{S_{tot,m}}{S_{tot,w}}$	$\frac{(r_0/\rho)_m}{(r_0/\rho)_w}$[b]	$\frac{T_m}{T_w}$
0.1	1.039	0.813	1.039	0.961	0.85	1.137	0.924	1.136	0.879	0.95
0.2	1.038	0.819	1.038	0.963	0.84	1.135	0.929	1.134	0.880	0.94
0.5	1.037	0.830	1.035	0.964	0.84	1.130	0.937	1.130	0.882	0.94
1.0	1.031	0.837	1.031	0.967	0.84	1.121	0.943	1.122	0.886	0.94
2	1.027	0.844	1.025	0.970	0.84	1.114	0.948	1.115	0.891	0.94
5	1.026	0.851	1.020	0.974	0.84	1.112	0.953	1.106	0.897	0.94
10	1.028	0.855	1.012	0.978	0.83	1.113	0.957	1.098	0.902	0.94
15	1.029	0.857	1.004	0.983	0.83	1.112	0.958	1.091	0.906	0.94
20	1.028	0.859	0.998	0.987	0.83	1.112	0.959	1.085	0.909	0.94
30	1.027	0.861	0.987	0.993	0.83	1.111	0.961	1.075	0.914	0.93
40	1.027	0.862	0.977	0.999	0.83	1.111	0.962	1.066	0.919	0.93
50	1.026	0.863	0.969	1.003	0.83	1.110	0.963	1.059	0.922	0.93

TABLE 6.1—*Continued*

	Muscle (skeletal)/Water					Adipose tissue/Water				
Energy MeV	$\frac{S_{col,m}}{S_{col,w}}$	$\frac{S_{rad,m}}{S_{rad,w}}$	$\frac{S_{tot,m}}{S_{tot,w}}$	$\frac{(r_0/\rho)_m}{(r_0/\rho)_w}$[b]	$\frac{T_m}{T_w}$	$\frac{S_{col,m}}{S_{col,w}}$	$\frac{S_{rad,m}}{S_{rad,w}}$	$\frac{S_{tot,m}}{S_{tot,w}}$	$\frac{(r_0/\rho)_m}{(r_0/\rho)_w}$[b]	$\frac{T_m}{T_w}$
0.1	1.029	1.025	1.029	0.972	1.03	0.947	0.751	0.947	1.054	0.77
0.2	1.029	1.025	1.029	0.972	1.03	0.946	0.756	0.945	1.056	0.77
0.5	1.032	1.026	1.029	0.972	1.03	0.944	0.763	0.942	1.059	0.77
1.0	1.030	1.025	1.029	0.972	1.02	0.938	0.769	0.937	1.063	0.77
2	1.026	1.026	1.028	0.972	1.03	0.934	0.774	0.931	1.067	0.77
5	1.024	1.026	1.028	0.973	1.03	0.930	0.779	0.924	1.074	0.76
10	1.024	1.026	1.028	0.973	1.03	0.930	0.782	0.917	1.080	0.76
15	1.026	1.026	1.028	0.973	1.02	0.930	0.784	0.911	1.085	0.76
20	1.026	1.026	1.027	0.973	1.02	0.930	0.785	0.905	1.089	0.76
30	1.027	1.026	1.028	0.973	1.02	0.929	0.786	0.895	1.095	0.76
40	1.027	1.026	1.027	0.973	1.03	0.929	0.787	0.886	1.101	0.76
50	1.027	1.026	1.028	0.973	1.02	0.929	0.788	0.880	1.107	0.76

[a] The elemental composition and densities of these materials are given in Table 2.1b.

[b] r_0 is the range expressed in units of mass per unit area; see Table 2.5.

TABLE 6.2—*The reference depth in a water phantom*

Energy	Depth of Reference Plane
$1 \leq \overline{E}_0 < 5$ MeV	R_{100}
$5 \leq \overline{E}_0 < 10$ MeV	R_{100} or 10 mm[a]
$10 \leq \overline{E}_0 < 20$ MeV	R_{100} or 20 mm[a]
$20 \leq \overline{E}_0 < 50$ MeV	R_{100} or 30 mm[a]

[a] The larger depth should always be chosen.

usually small depth for the energy concerned. In such cases, the depth of the reference plane should be taken as the value given in Table 6.2. The same reference depth should be used for all field sizes for a given energy.

6.3 Absorbed Dose at the Reference Point

6.3.1 General

The absorbed dose per dose monitor scale division at a point of interest in a water phantom is often determined in a two-step procedure when a medical accelerator beam is "calibrated". First, after the reference point has been determined, the absorbed dose per monitor scale division at the reference point is measured for the field sizes to be used in radiotherapy. In the second step, absorbed-dose distributions, which include the reference point, are measured (sometimes with a different dosimeter system which only gives relative absorbed dose values). Of special interest is the absorbed dose maximum along the reference axis in a water phantom (see Section 6.4.1) because the accelerator dose monitor generally should be calibrated to give the absorbed dose to water at this point. If the reference depth and the depth of maximum absorbed dose differ, then the ratio of the dose at the maximum to that at the reference point must be determined.

The choice of the dosimeter system to be used in the determination of absorbed dose to water at the reference point is often based on local convenience. However, in all procedures it is recommended that the calibration factor of at least one of the dosimeter instruments in use, generally an ionization chamber, should be traceable to a calibration at a national standards laboratory. It is also recommended that at least the initial calibration of a medical accelerator be performed with two independent dosimeter systems because stray radiation, microwave fields and other factors may cause large unexpected errors. One of the dosimeters should be of the integrating type, such as the ferrous sulphate dosimeter which is unaffected by electromagnetic fields.

6.3.2 Determination of Absorbed Dose

Ionization chambers are most often used for the absorbed dose measurements at the reference point. The ionization chamber is the only device which is calibrated by all national standards laboratories. In spite of its widespread use for many years, there may be large uncertainties in the absorbed dose measurements unless all of the different steps in the measurement procedures are carried out with great care. The numerical data and the theoretical background necessary for the measurements are discussed at several places in this report (in Sections 2, 3, 4, and 5); a summary is given here. However, other types of dosimeters may be used in measurements at the reference point, often as a check (see Section 6.3.1), and the main part of the procedure described here for the ionization chamber could also be followed with these other dosimeters.

6.3.2.1 Electron Energy. Certain input parameters are needed in order to choose the $s_{w,air}$ and $p_{w,air}$ values to be used in absorbed dose calculations. Suitable parameters are either (a) the mean energy at the phantom surface, together with the depth of the reference point in water, or (b) the mean energy of the electrons at the reference point in water.

Mean Energy at the Phantom Surface. $\overline{E}_0$ can be determined from Eq. 3.22, i.e., from measurements of

R_{50}. R_{50} must be determined from relative depth vs. absorbed-dose curves for large field sizes and an infinite SSD. If R_{50} is determined from a relative "depth ionization curve" with SSD = 1 meter, then $\overline{E}_0$ would be underestimated by approximately 0.5 MeV at $\overline{E}_0$ = 20 MeV and by 3 MeV at $\overline{E}_0$ = 35 MeV (NACP, 1980). This method could be used for beams from most therapy accelerators, but will, generally, underestimate $s_{w,air}$ at the reference depth for beams having a large energy spread—in extreme cases up to 2 or 3% (Johansson and Svensson, 1982). Such beams are produced by accelerators having a flattening system and collimating system of poor design. A simple test to analyze the beam in this respect is to determine the dose gradient (see Section 6.4.3.1). At large depth, for such beams, $s_{w,air}$ may, instead, be overestimated (see Section 6.4.2).

$\overline{E}_0$ can also be estimated from a measurement of R_p. Equation 3.19 gives the relationship between the most probable energy at the phantom surface, $E_{p,0}$ and R_p. Using Eqs. 3.11 and 3.12, $\overline{E}_0$ is obtained from $\overline{E}_0 \approx E_{p,0} - \Sigma\Delta E_{rad}$ where $\Sigma\Delta E_{rad}$ is the total radiation loss in materials in the electron beam such as the accelerator tube window, scattering foils, transmission chambers and air. The equation holds if $E_{p,i} \approx \overline{E}_i$ which is an adequate approximation when the energy spread is small and $\overline{E}_0$ is to be determined for use in dosimetry (see Fig. 3.13).

ΔE_{rad} for each material in the beam can be approximated for low energy electrons by the product of the thickness of the material and its radiative stopping power (Table 2.4). $\Sigma\Delta E_{rad}$ is generally only a fraction of one MeV at 10 MeV, but increases to several MeV at 40 MeV when scattering foils of larger thicknesses are in use.

E_0 may also be determined from nuclear reaction or Cerenkov threshold measurements (see Sections 3.3.2.1 and 3.3.2.2, respectively). The energy parameter obtained generally differs from $\overline{E}_0$, but it should be possible to calculate $\overline{E}_0$ if the beam geometry, including thicknesses of scattering foils, sources of generation of bremsstrahlung that give rise to photonuclear reactions, etc., is well known.

Depth of Reference Point in Water. The depth of the reference point should be determined from central-axis depth-dose curves measured for a field size of 10 cm × 10 cm in a water phantom.

Mean Energy of the Electrons at the Reference Point in Water. $\overline{E}_z$ can be calculated from Eq. 2.28. Equations 2.25 or 2.26 may also be used because $\overline{E}_z \approx E_{p,z}$ at the reference depth (see Fig. 2.4), thus providing an adequate estimate for use in dosimetry.

6.3.2.2 Irradiation Geometry. The set-up used for the absorbed-dose determination at the reference point using an ionization chamber is shown in Fig. 6.1. When horizontal beams are used, the entrance wall of the water phantom should be made of low atomic number materials like PMMA or polystyrene. Its thickness is not critical, but it is convenient to use about 0.5 mm, which is thin enough so that the difference from water can be disregarded (see Section 6.2.2), and yet has sufficient mechanical strength. The ionization chamber should be protected during the measurements with a waterproof sleeve or be placed in a PMMA tube with walls of 1 mm or less.

A solid medium has some practical advantages, especially at low electron energies, when the reference point is situated at a depth equal to or smaller than 1 cm. A plastic block may be used for calibration if a recalculation, giving absorbed dose to water, is carried out according to the method described in 6.2.2. The block should be sufficiently large so that the reference point receives a full contribution from scattered radiation.

6.3.2.3 Ionization Chamber Measurements. The chamber should have properties which ensure that there is only a small uncertainty in the determination of the conversion factor, N_D, in a photon beam (see Eq. 5.15) and that it is suitable for measurements in an electron beam.

Suitable properties for chambers to be calibrated in a cobalt-60 gamma-ray beam are discussed in Section 5.4.3 and the various ways of deriving the factor N_D from a known exposure rate in free air, kerma rate in free air, or absorbed dose rate in water are discussed in Section 5.4.5. Numerical values for the correction factor k_m are given in Table 5.7 for chambers made of air-equivalent material, graphite and tissue-equivalent material calibrated with build-up caps of the same material.

The effective point of measurement, P_{eff}, of the chamber should be placed at the reference point when measurements are to be carried out in the electron beam. The effective point of measurement can be taken as $0.5\,r$ (r is the radius of the air cavity) in front of the chamber center with cylindrical chambers, and as the front surface of the air cavity in a plane-parallel chamber (Section 4.2.1.1).

The absorbed dose to water, $D_w(P_{eff})$, at the effective point of measurement in a homogeneous water phantom, can be determined using a calibrated field instrument and applying Eqs. 4.2 and 5.17, i.e.,

$$D_w(P_{eff}) = N_D M_E s_{w,air} p_{w,air} \qquad (6.2)$$

where $s_{w,air}$ is the water to air stopping-power ratio. It is shown in Section 4.3 that, for practical purposes, the same value can be used for chamber walls of water-equivalent material, thin graphite or air-equivalent material, or thin plastic with an inner lining of graphite or air-equivalent material. Table 6.3 gives the recommended values for different depths in water for monoenergetic broad beams perpendicularly incident on a water phantom. In a practical case, the mean energy at the phantom surface, $\overline{E}_0$, and depth in phantom, z_w, are the best input data. If, instead, $\overline{E}_z$ has been calculated, then $s_{w,air}$ can be calculated from $[S(\overline{E}_z)/\rho]_w/[S(\overline{E}_z)/\rho]_{air}$; see the discussion in Section 4.3.2. The mass collision stopping powers are given in Table 2.2.

The perturbation correction factor, $p_{w,air}$, is discussed in Section 4.2.1 and experimental data for cylindrical chambers, valid at the reference depth in 5- to 25-MeV electron beams, are given in Table 6.4.

A plane-parallel chamber ought to be used below about $\overline{E}_z = 10$ MeV as these can be constructed to give negligible perturbation corrections. The reading, M, to be used, should be the mean value obtained with positive and negative polarity. The plane-parallel chamber may, for convenience, be used in a solid "water-equivalent" phantom (see above). Above about 10 MeV, it is convenient to use a cylindrical chamber because it is simple, robust and may be used with a water-tight sleeve in a water phantom. Its polarity effect should be negligible, but the perturbation correction-factor may be several percent for $\overline{E}_z \geq 10$ MeV.

6.4 Absorbed Dose on the Reference Axis

6.4.1 General

The reference axis (or the beam axis) is defined as the line passing through the center of the effective radiation source or the virtual point source and the center of the radiation field (for circular or rectangular fields). Standardized, reference-axis depth vs. absorbed-dose data for a given energy, or even for a given accelerator type, can generally not be used (see Section 6.1). It is, however, often of interest to compare dose distributions for various accelerators. Such comparisons require careful absorbed dose measurements (see Section 6.4.2), the quality parameters of the beam must be specified and used in a consistent way (see Section 3.3.1.3), and, finally, certain characteristics of the absorbed dose distribution of special importance for therapy must be specified and compared (see Section 6.4.3).

6.4.2 Absorbed Dose Determination

Depth vs. absorbed-dose data should refer to the distribution in a large water phantom (Section 6.2.1). The measurement procedure is very much a matter of choice, convenience and available techniques; dosimeters which may be used are described in Section 5, e.g., ionization chambers, ferrous sulphate dosimeters, liquid ionization chambers, and solid state dosimeters. However, the use of uncorrected relative "depth-ionization curves" or "depth-film density curves" instead of true depth vs. absorbed-dose curves is discouraged.

If an ionization chamber is used for the measurements, it is necessary to correct for the variation of the stopping-power ratio, $s_{w,air}$, with depth. The ionization chamber must be placed with its effective point of measurement at the depth of interest. Values of $s_{w,air}$ can be found in Table 6.3; $\overline{E}_0$ may serve as input data (see Section 6.3.2). Because Table 6.3 was computed for monoenergetic beams, this procedure may give a large uncertainty for a beam of large energy spread, particularly at depths larger than R_{50}, as some of the incident electrons will have a practical range considerably larger

TABLE 6.3—Recommended values (Berger, 1980) of the water/air mass stopping power ratio, $s^{SA}_{w,air}$, for Δ = 10 keV, I(water) = 75.0 eV, I(air) = 85.7 eV, and density effect corrections by Sternheimer and Peierls (1971) (see discussion in section 2.2.2) for monoenergetic electrons[a]
[The practical range in water, R_p, obtained from Eq. 3.18 is also included]

	E_0/MeV = 60.0	50.0	40.0	30.0	25.0	20.0	18.0	16.0	14.0	12.0
	R_p/cm = 29.1	24.6	19.6	14.8	12.3	9.87	8.88	7.89	6.90	5.91
Depth z/cm										
0.0	0.903	0.907	0.916	0.933	0.945	0.961	0.968	0.976	0.986	0.996
0.2	0.904	0.908	0.918	0.935	0.948	0.963	0.971	0.979	0.988	0.998
0.4	0.906	0.910	0.920	0.937	0.950	0.966	0.973	0.981	0.990	1.001
0.6	0.907	0.912	0.922	0.940	0.952	0.968	0.976	0.984	0.993	1.003
0.8	0.909	0.914	0.924	0.942	0.955	0.970	0.978	0.985	0.996	1.007
1.0	0.910	0.915	0.926	0.944	0.957	0.973	0.980	0.989	0.998	1.010
1.2	0.911	0.917	0.927	0.946	0.959	0.975	0.983	0.991	1.001	1.013
1.4	0.913	0.918	0.929	0.948	0.961	0.977	0.985	0.994	1.004	1.017
1.6	0.914	0.920	0.931	0.950	0.963	0.980	0.988	0.997	1.008	1.021
1.8	0.915	0.921	0.933	0.952	0.965	0.982	0.990	1.000	1.011	1.025
2.0	0.916	0.923	0.934	0.953	0.967	0.984	0.993	1.002	1.014	1.030
2.5	0.919	0.926	0.938	0.958	0.972	0.990	0.999	1.010	1.024	1.041
3.0	0.922	0.929	0.942	0.962	0.977	0.996	1.006	1.019	1.034	1.054
3.5	0.925	0.933	0.946	0.967	0.982	1.003	1.014	1.028	1.045	1.068
4.0	0.928	0.936	0.949	0.971	0.987	1.010	1.023	1.038	1.058	1.082
4.5	0.930	0.939	0.953	0.976	0.993	1.018	1.032	1.049	1.071	1.096
5.0	0.933	0.942	0.956	0.980	0.999	1.026	1.042	1.061	1.084	1.109
5.5	0.935	0.945	0.960	0.986	1.005	1.036	1.053	1.073	1.097	1.119
6.0	0.938	0.947	0.964	0.991	1.012	1.045	1.064	1.085	1.108	1.124
7.0	0.942	0.953	0.971	1.002	1.028	1.066	1.086	1.106	1.122	1.126
8.0	0.947	0.959	0.980	1.015	1.044	1.087	1.105	1.119	1.125	
9.0	0.952	0.966	0.989	1.029	1.062	1.104	1.117	1.124		
10.0	0.957	0.973	0.998	1.043	1.080	1.115	1.121			
12.0	0.968	0.987	1.019	1.074	1.107					
14.0	0.980	1.004	1.041	1.101	1.112					
16.0	0.994	1.022	1.066	1.108						
18.0	1.009	1.041	1.090							
20.0	1.025	1.061	1.101							
22.0	1.042	1.079	1.096							
24.0	1.058	1.090								
26.0	1.071	1.092								
28.0	1.080	1.085								
30.0	1.083									
35.0	1.078									

[a] The values may also be used for electrons which have an energy spread at the phantom surface. In this case, the mean energy at the phantom surface, $\bar{E}_0$, and the depth of the effective point of measurement are the best input data. However, for a beam with a very large energy spread this procedure gives a large uncertainty at depths larger than about R_{50} and a particular procedure, described in Section 6.4.2, can be used.

than for a monoenergetic beam with the same $\bar{E}_0$. In this case, the practical range, R_p, determined for a large field size as described in Section 3.3.2.3, may be used as input data to Table 6.3. Only approximate depth-dose data can be determined in this way. Alternatively, $s_{w,air}$ may be evaluated from the ratio of mass collision stopping-powers (Table 2.2) at the mean energy of the electrons at the depth of interest (Eq. 4.11). The mean energy may be approximated from Eq. 2.25 taking $\bar{E}(z) \approx E_p(z)$. Somewhat low $s_{w,air}$ values are obtained using this method for large $\bar{E}_0$ and large phantom depths, e.g., about 2% at 8-cm depth for $\bar{E}_0$ = 30 MeV (see Fig. 4.11). This should be sufficiently accurate in most cases because a larger uncertainty is acceptable in most applications for absorbed dose levels smaller than 50%. After further correction for perturbation ($p_{w,air}$) and recombination losses, which also vary with the depth and mean energy, relative absorbed-dose curves can be determined.

A less accurate dosimeter system may also be used for central-axis depth vs. absorbed-dose measurements, e.g., film in a solid phantom. However, such curves should be checked at selected energies and field sizes against a more accurate system in order to evaluate the relative absorbed dose vs. depth curve in a large water phantom. A number of parameters may influence the sensitivity of such an alternative detector system implying that a variety of beam qualities should be used in testing the procedure. Examples of such parameters are:

TABLE 6.3—*Continued*

E_0/MeV =	10.0	9.0	8.0	7.0	6.0	5.0	4.0	3.0	2.0	1.0
R_p/cm =	5.02	4.52	4.02	3.52	3.02	2.52	2.02	1.51	1.01	0.505
Depth z/cm										
0.0	1.008	1.015	1.023	1.032	1.042	1.053	1.066	1.083	1.101	1.122
0.1	1.009	1.016	1.024	1.032	1.042	1.054	1.068	1.088	1.107	1.128
0.2	1.010	1.017	1.025	1.034	1.044	1.056	1.071	1.090	1.112	1.133
0.3	1.012	1.019	1.026	1.035	1.046	1.058	1.074	1.094	1.116	1.136
0.4	1.013	1.020	1.028	1.037	1.048	1.062	1.079	1.099	1.119	1.137
0.5	1.014	1.022	1.030	1.040	1.051	1.065	1.083	1.103	1.123	
0.6	1.016	1.024	1.032	1.042	1.054	1.069	1.087	1.107	1.127	
0.8	1.020	1.028	1.037	1.048	1.062	1.078	1.096	1.115	1.137	
1.0	1.024	1.033	1.043	1.055	1.070	1.086	1.105	1.124	1.153	
1.2	1.029	1.038	1.049	1.062	1.078	1.095	1.114	1.127		
1.4	1.033	1.044	1.055	1.070	1.086	1.103	1.122	1.130		
1.6	1.038	1.049	1.062	1.077	1.094	1.111	1.127	1.147		
1.8	1.044	1.056	1.069	1.084	1.101	1.119	1.130			
2.0	1.049	1.062	1.076	1.092	1.109	1.125	1.134			
2.5	1.064	1.078	1.093	1.109	1.125	1.133				
3.0	1.080	1.094	1.109	1.124	1.133					
3.5	1.095	1.109	1.124	1.132						
4.0	1.109	1.127	1.130	1.130						
4.5	1.121	1.129	1.129							
5.0	1.127	1.129								
5.5	1.128									

TABLE 6.4—*Perturbation correction factors, $p_{w,air}$[a], for thimble ionization chambers of inner radius r and a cavity length of 15 mm for different mean energies, $\bar{E}_z$, at the reference points inside a water phantom*
[The chambers are irradiated with a beam that is perpendicular to the chamber axis]

,/MeV	r = 1.5 mm	r = 2.5 mm	r = 3.5 mm
4	0.981	0.967	0.955
6	0.984	0.974	0.963
8	0.988	0.980	0.971
10	0.991	0.984	0.978
12	0.993	0.988	0.984
15	0.995	0.992	0.989
20	0.997	0.995	0.994

[a] The values were extracted from experimental determinations by Johansson *et al.* (1978). The difference from unity increases linearly with the radius; values for any other radii between 1.5 and 3.5 mm may thus also be determined from the table. The experimental values were obtained in PMMA rather than water but, as indicated in Section 4.2.1.2, they may be used also for water.

(i) energy distribution of the electron beam
(ii) angular distribution of the electron beam
(iii) absorbed dose rate
(iv) charge deposition distribution.

6.4.3 Characteristics of the Depth-Dose Curve

Some parameters which are useful in describing the beam axis depth vs. absorbed-dose curves are shown in Fig. 6.2: R'_t, the depth at which the extension of the therapeutic interval intersects the depth-dose curve at the dose level selected as the therapeutic-dose value near the skin entrance; R_{100}, the depth of absorbed dose maximum; R_t, the therapeutic range giving the depth interval that should coincide with the target volume (ICRU, 1978); R_{50}, the half value depth; R_p, the practical range (R_{50} and R_p are defined in Section 3.3.2.3); D_s, the entrance or surface absorbed dose; D_x, the photon background absorbed dose; and G, the dose gradient, a measure of the absorbed dose fall-off (see below)

The absorbed-dose level related to the therapeutic range has been a matter of discussion (DIN, 1976; ICRU, 1976; ICRU, 1978). The general opinion is that the absorbed-dose variation inside the target volume should be as small as possible. This goal may conflict with the desire to achieve a rapid dose fall-off beyond the target volume; an increase in energy will usually give a more extended region of relatively constant absorbed

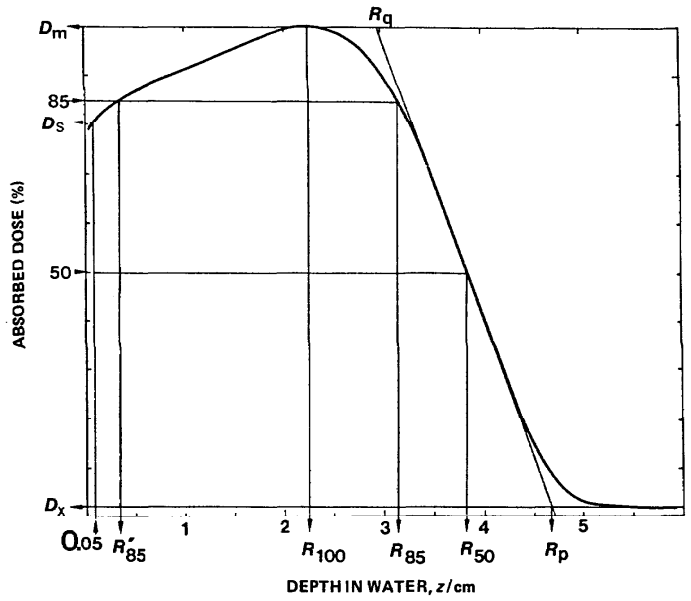

Fig. 6.2. Depth vs. absorbed-dose distribution with definitions of all the parameters used in the text: D_m is the maximum absorbed dose, D_s the surface dose measured at 0.5 mm depth, D_x the absorbed dose attributed to the photon background, R'_t the depth at which the extension of the therapeutic interval intersects the depth-dose curve near the skin entrance (the therapeutic dose level has been taken as 85 percent, i.e., R'_{85}), R_{100} the depth of dose maximum, R_t the therapeutic range (in the figure R_{85}), R_{50} the half-value depth, R_p the practical range, R_q the depth where the tangent at the steepest point intersects the dose level D_m.

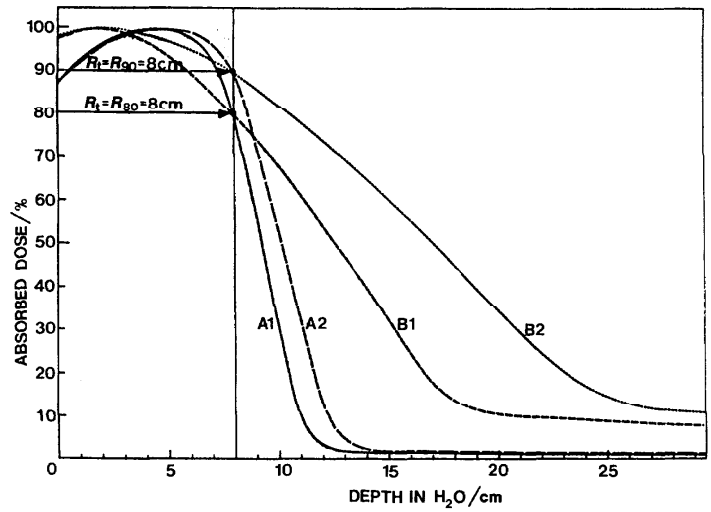

Fig. 6.3. The influence of the dose level chosen for the therapeutic range on the depth-dose curves for electron beams with different dose gradients. Curve A1: $E_{p,0}$ = 23 MeV, G = 2.7; Curve A2: $E_{p,0}$ = 25 MeV, G = 2.7; Curve B1: $E_{p,0}$ = 36 MeV, G = 1.5; Curve B2: $E_{p,0}$ = 50 MeV, G = 1.5.

dose, but will also increase the absorbed dose beyond the target volume. The choice of relative-dose level, t, by various departments may differ because this choice should be influenced by the shape of dose distributions from the particular accelerator(s) in use. Thus, with beams having a large dose gradient (definition below), a very uniform dose distribution may be achievable, i.e., it may be possible to use a high dose level for R_t without substantial irradiation of regions beyond the therapeutic range, as illustrated in Fig. 6.3. It can be seen that with a dose gradient of G = 2.7, an increase in energy, $E_{p,0}$, from 23 MeV (curve A1) to only 25 MeV (curve A2) is sufficient to increase the relative dose from 80% to 90% for a therapeutic range of 8 cm. The corresponding increase with G = 1.5 would be from 36 MeV (curve B1) to nearly 50 MeV (curve B2). Evidently, a higher therapeutic dose level may be chosen with a beam of high dose gradient, resulting in better dose uniformity over the target volume. However, it is generally agreed that the absorbed dose level of the therapeutic range should be between 80 and 90%, so 85% ($R_t = R_{85}$) has been chosen as a typical value to be used in Figs. 6.2, 6.4, and 6.5. The skin absorbed dose is often lower than 85%, but the depth of R'_{85} is never more R'_{85} than 1 cm in clinical

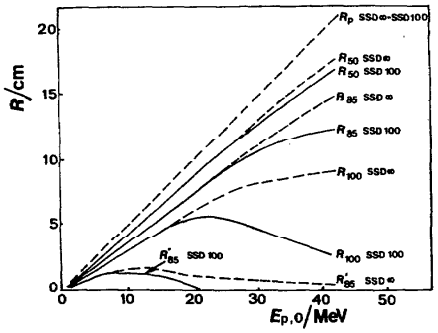

Fig. 6.4. Variation of different range parameters with beam energy for monoenergetic and monodirectional electron beams (Berger and Seltzer, 1969a). The solid lines for SSD 100 cm are obtained after application of an inverse square law correction to the absorbed dose distributions for infinite SSD.

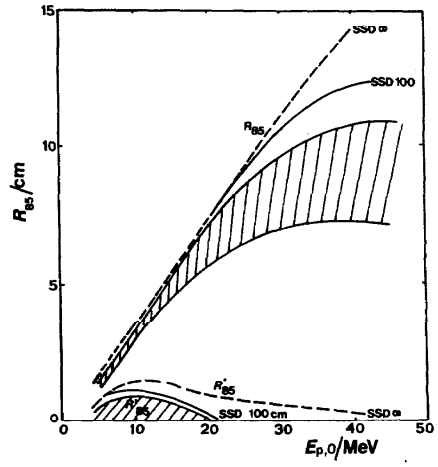

Fig. 6.5. Therapeutic range, R_{85}, and the surface extension of the therapeutic interval, R'_{85} for large field sizes, as a function of the most probable energy at the phantom surface $E_{p,0}$. The upper two curves for R_{85} and for R'_{85} are theoretical data from Berger and Seltzer (1969a); the SSD 100-cm curve is derived using inverse square law corrections. The cross-hatched area encloses measurements performed on various accelerators, linacs as well as betatrons (adapted from Brahme and Svensson, 1976a and 1980).

electron beams.

The absorbed dose at small depths is of interest because of the radiation sensitivity of the layers of tissue just below the epidermis. The entrance dose, defined as the absorbed dose determined by extrapolation to zero phantom thickness, is sometimes stated. Forward-projected, low-energy secondary electrons below about 0.1 MeV generated in the surface layer of the phantom are the main reason for the rapid absorbed dose build-up very close to the surface. The extrapolation will be uncertain, because the range of these electrons in water is less than 0.2 mm, i.e., less than the thickness of most detectors, and as interface problems between the phantom and detector are particularly difficult to handle for depths smaller than this range (see Section 4.3.2). Therefore, the relative entrance or skin absorbed dose is defined as the ratio of absorbed dose at 0.5 mm to the maximum absorbed dose along the reference axis ($= D_s/D_m$). Accurate measurements of absorbed dose are fairly readily obtained at a depth of 0.5 mm and the values so obtained are, for present purposes, an adequate approximation to the absorbed dose just below the epidermis (Svensson and Hettinger, 1967; Hultén and Svensson, 1975; Bertilsson, 1975).

The relative photon background, is D_x/D_m where D_x is the absorbed dose value of background and D_m is the absorbed dose maximum. The photons are either present as a contamination of the incident electron beam or generated in the irradiated medium itself.

The rapid fall-off of the depth vs. absorbed-dose distribution beyond the therapeutic range means that the absorbed dose to the organs behind the target volume may receive considerably less radiation than the target volume.

A normalized absorbed dose gradient

$$G = \left|\frac{dD}{dz}\right|_{max} \frac{R_p}{D_m - D_x} \qquad (6.3)$$

is recommended as a measure of the fall-off (Brahme and Svensson, 1976a, 1979). It can be determined from $G = R_p/(R_p - R_q)$, where R_p is the practical range and R_q is the depth where the tangent at the steepest point (the inflection point) intersects the dose level D_m (Fig. 6.2). Alternatively, the ratio R_{80}/R_p may be used as a measure of fall-off (see Benedetti, 1973). The dose gradient has a very small energy dependence for broad, monoenergetic, plane-parallel beams and is, therefore, a useful quantitative indicator for comparison of the shape of the depth-dose curves from different treatment units.

6.4.3.1 Dependence on Energy and Angular Spread. As an illustration of the general trend, the depths R_{100}, R_{85}, R_{50}, and R_p as a function of energy, determined from Monte Carlo calculations of depth versus absorbed-dose distributions for broad monoenergetic beams perpendicularly incident on a water phantom (Berger and Seltzer, 1969a), are given in Fig. 6.4. These ranges are also recalculated, with the inverse square correction, to a source-to-skin distance (SSD) of 1 m, in order to make comparisons with therapy beams possible are also shown. At this SSD, the R_{100} increases in proportion with energy up to an energy of about 20 MeV, has a broad maximum at about 25 MeV, and then decreases at higher energies, while R_{85} has a

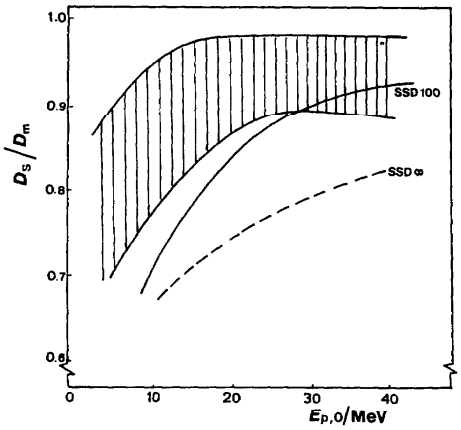

Fig. 6.6 Variation of the surface dose, D_s, expressed as a fraction of the maximum dose, D_m, with the most probable electron energy. The lower two curves are theoretical data and the cross-hatched area encloses the various measured data (adapted from Brahme and Svensson, 1976a and 1980).

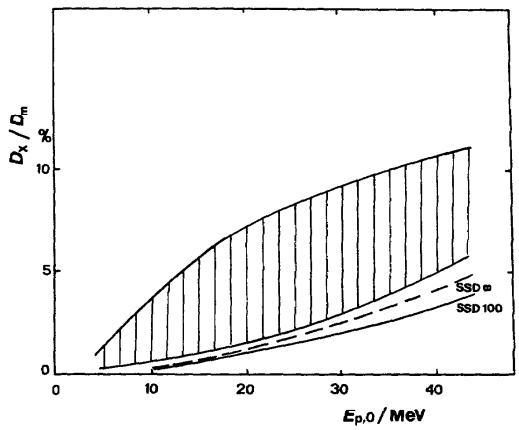

Fig. 6.7. Dependence of relative photon background on the most probable energy, $E_{p,0}$. The fraction of D_x which is produced in the phantom may be estimated from the lowest curve at an SSD of 100 cm. The difference from the measured value is due to photons generated in the treatment head or in the collimating device. The cross-hatched area shows the large variation in the photon background between various accelerators (adapted form Brahme and Svensson, 1976a and 1980).

proportional increase to about 25 MeV and a maximum value above 40 MeV.

Figure 6.5 shows the range of R_{85} and R'_{85} determined experimentally from operating accelerators, compared to the theoretical values given in Fig. 6.4. The theoretical and experimental curves differ principally because of the spread in energy and direction of the electron beams incident on the phantom surface (see Section 3). The most probable energy $E_{p,0}$ associated with the maximum value of the experimentally determined R_{85} can be regarded as the maximum useful electron energy if it is assumed that the treatment is carried out with a single fixed electron beam directed at the target volume (Brahme and Svensson, 1979). The maximum useful energy varies in the range 25–45 MeV for different accelerator facilities. Flattening systems using dual scattering foils made of high atomic number materials, or a scanned beam in combination with a well-designed collimating system, will increase the maximum useful energy (Section 3.2)—they correspond to the upper part of the cross hatched area in Fig. 6.5. Thick scattering foils and poor collimation may lead to a decrease in R_{85} of several centimeters.

The absorbed dose build-up and, therefore, also the relative entrance absorbed dose, D_s/D_m, depend mainly on two different processes, namely, the build-up of the fluence of secondary electrons and the increased obliquity of primary electrons with penetration depth. The former process is almost energy independent (Berger and Seltzer, 1969a), while the latter decreases with energy (see Eq. 2.42). As a consequence, D_s/D_m increases with energy for a broad monoenergetic and monodirectional beam (see Fig. 6.6). The D_s/D_m values for most broad therapy beams are higher than the computed values because the secondary electron build-up takes place to some extent in materials in front of the phantom surface (air, transmission monitors, etc.) and because the primary electrons may already have a distribution in angle and energy at the phantom surface, giving a smaller increase of primary electron fluence with depth (Section 2.8). Collimators of low atomic number materials are often responsible for a large spread in both energy and angle of electrons at the phantom surface (see Section 3.2.3). In most therapy beams, the contaminating x rays from the accelerator have a very small influence on the absorbed dose build-up except at high energies when a thick scattering foil is used. When this is the case, the surface dose may be lower than that theoretically expected (see Fig. 6.6).

The relative absorbed dose from photon background, D_x/D_m, for monoenergetic electrons incident on a water phantom increases with energy and is about 0.06 at 50 MeV (Figs. 6.7 and 2.21; Seltzer *et al.*, 1978). The absorbed dose from contaminating x rays generated in foils and other materials in the beam will also increase with energy and, in some therapy accelerator facilities, may be of the same order or larger than the contribution from the phantom. The contamination in some machines may be dependent on the operating conditions of the accelerator and must, therefore, be measured under various operating conditions (Spira *et al.*, 1962).

The normalized dose gradient, G, is almost constant for monoenergetic broad beams with SSD = 1 m and $\overline{E}_0$

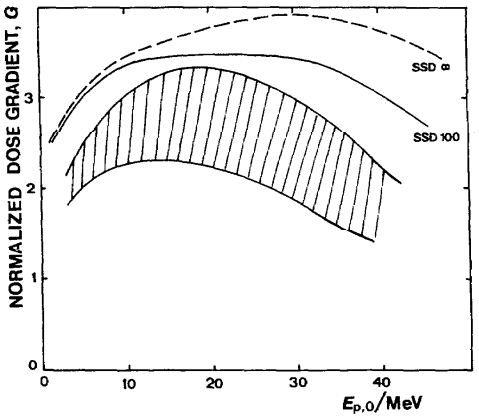

Fig. 6.8. Variation of normalized dose gradient, G, with the most probable energy. The upper two curves are theoretical data and the cross-hatched area encloses measured data on various accelerators. (Adapted from Brahme and Svensson, 1976a and 1980.) Some of the measured data for low or medium energy show small differences from theoretical data whereas the measured data for high energy are much lower than the theoretical ones. (Compare also Benedetti, 1973.)

between 10 and 30 MeV, and decreases somewhat for lower and higher energies (Fig. 6.8). The gradient decreases with the energy spread at the phantom surface (Γ_0) and the spread in angle ($\overline{\theta_c^2}$) of the electrons incident on the phantom. In fact, for broad electron beams, it can be shown that

$$G = G_0 \left(1 + e\frac{\kappa \Gamma_0}{E_p} + (1 - e)\frac{\overline{\theta_c^2}}{T_0 R_p}\right)^{-1}, \quad (6.4)$$

where e is a dimensionless factor ($e \approx 0.45$) and G_0 is the dose gradient for the monoenergetic monodirectional beam (Brahme and Svensson, 1979, see also Figs. 3.12, 3.14, and 6.8). A dose gradient, G, below about 2.3 for large beams in the energy range ($\overline{E}_0$) 5 to 30 MeV indicates that the flattening system and collimating system are of poor design and that unnecessarily large volumes of normal tissue are irradiated in single beam techniques. If a scattering foil system is used to obtain large uniform beams, then a value below about 2.3 has to be accepted above 30 MeV.

A comparison of the parameters measured on the user's beam with the published data (Figs. 6.3 to 6.8) could be used to indicate whether the user's beam is comparable to those in current use. The spread of measured data and the deviation from theoretical values provides a measure of possible improvement. A summary of the various beam parameters, as defined in Section 5, and related absorbed dose distribution characteristics is given in Table 6.5

6.4.3.2 Dependence on Field Size. When a phantom is irradiated with a narrow beam of electrons, most of the electrons are scattered out of the narrow beam and the dose decreases rapidly with depth (see Fig. 2.19). When the field size is increased, this loss of electrons on the central axis is compensated for by electrons scattered from the edges of the irradiated volume towards the central axis, and the depth dose increases gradually with field size as long as the distance between the point of measurement and the edge of the field is shorter than the maximum range of the electrons. For larger field sizes, the central axis depth dose is independent of field size.

Lax and Brahme (1980) have proposed that the difusion depth, z_1, defined as the depth where the root mean square scattering angle is one radian, be used as a measure of the maximum lateral excursion of the

TABLE 6.5—*Related electron beam characteristics and absorbed-dose distribution characteristics*

Electron Beam Characteristics			Dose Distribution Characteristics	
Energy distribution	Maximum energy	E_{max}	Maximum range	R_{max}
	Most probable energy	E_p	Practical range	R_p
	Mean energy	$\overline{E}$	Mean range	R_{50}
	Energy spread	Γ	Dose gradient	G
Angular distribution	Central angular spread	$\overline{\theta_c^2}$	Therapeutic range	R_t
			Surface dose	D_s
	Total angular spread	$\overline{\theta_0^2}$	Uniformity index	$U_{90/50}$
Spatial distribution	Total radial spread	$\overline{r_0^2}$		
	Effective source size	$\overline{r_{eff}^2}$	Penumbra	$P_{80/20}$
	Effective source surface distance	s_{eff}	Therapeutic range	R_t
	Virtual source surface distance	s_{vir}		
	Field diameter	d	Dose gradient	G
Photon contamination	Radiation energy loss in the machine and materials in the beam (e.g., foils)	ΔE_{rad}	Photon background	D_x

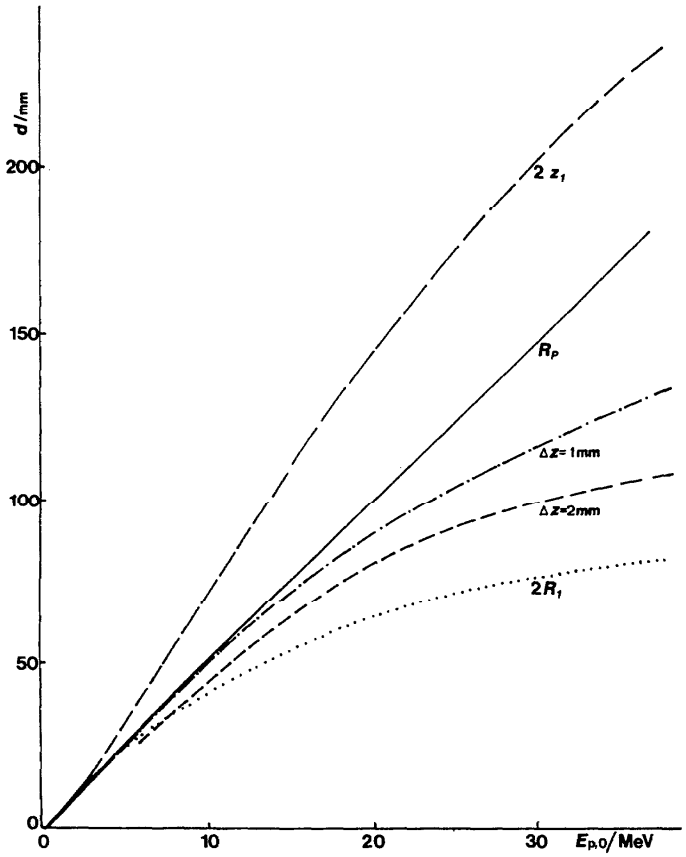

Fig. 6.9. The minimum beam diameter, d, at the surface, for which the depth versus absorbed-dose curve can be considered to be relatively independent of beam diameter, as a function of $E_{p,0}$. The upper curve shows the variation of $2z_1$, where z_1 is a measure of the maximum lateral excursions of electrons (Lax and Brahme, 1980). The solid curve shows the variation of the practical range, R_p, which has been proposed as a practical value of d (ICRU, 1972). The dash and dot-dash curves (labeled Δz) show experimental data corresponding to d values above which the maximum shift of the depth-dose curve is less than 1 and 2 mm of water, respectively. The lowest curve gives $2R_1$, the diameter at which the dose maximum on the central axis has decreased by 1% of its value for a broad beam; scattering in the air and the collimator is disregarded.

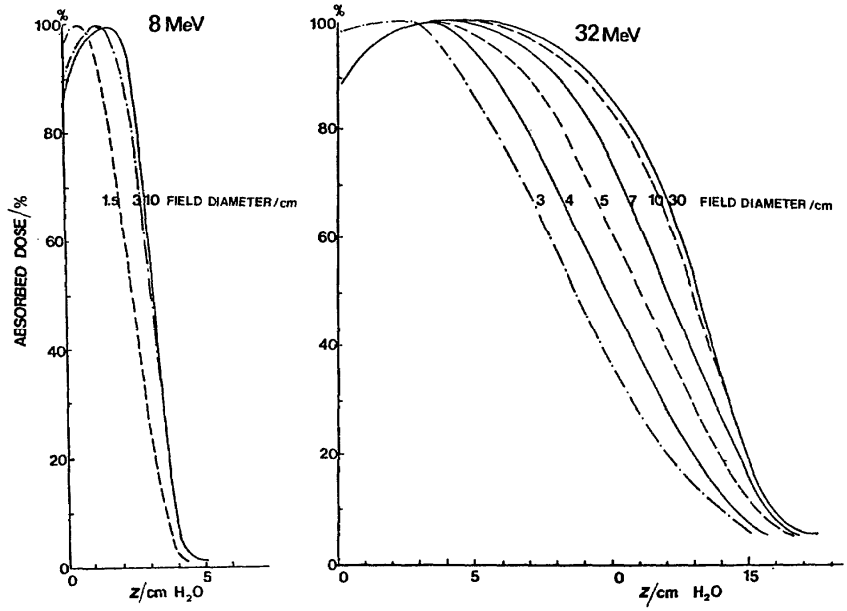

Fig. 6.10. Variation of depth versus absorbed-dose curves with field diameter for 8 and 32 MeV electron beams, normalized to the dose maximum for the broad beam (Briot and Dutreix, 1976; Briot, 1982).

electrons. They also give an expression for the beam radius, R_1, at which the maximum absorbed dose on the central axis has decreased, due to a decrease of lateral scattering in the phantom, by 1% from its maximum value in an infinitely broad beam. Figure 6.9 shows the variation of $2z_1$ and $2R_1$ with the most probable energy $E_{p,0}$ at the phantom surface; $2z_1$ is the diameter of the field size above which the depth dose on the axis is independent of further increase of diameter. ICRU Report 21 (ICRU, 1972) proposed R_p as the lower limit above which the field size dependence of the depth dose is negligible. The field size dimension above which the depth-dose variation leads to an error in depth less than a stated error may be found by experiment. Figure 6.9 shows such curves measured on a linear accelerator for errors equal to 1 mm or 2 mm. The experimental data for the field size limits are intermediate between the practical range and the theoretical diameter, $2R_1$, at high energies. A large angular spread of the electrons at the phantom surface may further decrease the influence of field size on the depth-dose curve

When the beam diameter is decreased below the minimum value which provides a central-axis depth dose which is independent of field size, it is observed that:

(i) the maximum decreases and moves towards the entry surface and the relative surface dose, D_s, is increased;
(ii) the dose gradient G is reduced;
(iii) the practical range becomes difficult to specify because the descending part of the depth-dose curve no longer shows an extended linear portion. Furthermore, the practical range decreases, especially for very small field diameters (see Fig. 6.10, data from Briot and Dutreix, 1976; Briot, 1982).

The variation of the depth-dose curve with field si: is more difficult to predict when there is much scatte. ing by the collimator and measurements have to be performed for each set of working conditions.

6.4.3.3 Dependence on Source-Surface Distance. The change in shape of the depth-dose curve with source-surface distance is determined mainly by the geometrical divergence of the beam. Application of the inverse square law, using the effective source-surface distance (see Sections 3.2.4.1 and 3.2.4.6) brings the depth vs. absorbed-dose curves obtained at different SSD into close agreement (Pohlit, 1965; Briot and Dutreix, 1976). The variation of the relative depth vs. absorbed dose with SSD may be disregarded for low energies due to the high dose gradient and small penetration, but corrections have to be carried out for energies higher than 15 MeV. If the contribution by electrons scattered from the collimator walls is large, a decrease in relative surface dose and an increase in the depth of the maximum are observed when the distance from the surface to the collimator is increased. When the variation in SSD is very large, the increase of air absorption and air scattering cannot be neglected and larger variations in relative depth absorbed dose are obtained, particularly at low energies. In order to increase the field size at low electron energies for the treatment of mycosis fungoides, source distances as large as 4 meters are sometimes used. The working conditions are then very different from normal and careful measurements must be performed (see Section 7.5 and Karzmark *et al.*, 1960; Edelstein *et al.*, 1973; Kahn *et al.*, 1977; Tetenes and Goodwin, 1977; Bjärngard *et al.*, 1977; Meyler *et al.*, 1978; Kase and Bjärngard, 1979).

6.5 Absorbed Dose in Planes Perpendicular to or Parallel to the Beam Axis

6.5.1 General

As pointed out in Section 6.4, the absorbed dose distributions from electron beams are more critically dependent on constructional details of the particular accelerator than is the case for photon beams. With electron beams, it is, therefore, recommended that dose distributions be measured for each accelerator and it is not advisable to use curves from the manufacturer or from other departments (cf. ICRU Report 24—ICRU, 1976—Section 2.3.1 for photon beams). It is recommended that the absorbed dose distribution be measured both in a plane perpendicular to the beam axis and in a plane parallel to that axis. The first type of distribution should be used to investigate the uniformity and the physical penumbra of the beam, while the other distribution, the isodose chart, is mainly used in planning radiation treatments (Fig. 6.11).

6.5.2 Measurements

Investigations of uniformity in the plane perpendicular to the beam axis can be conveniently carried out with film dosimetry because irregularities in the distribution at any point in the plane are then revealed. Automatic isodose scanners using solid-state or ionization-chamber detectors may also be used, but some care is needed not to miss hot or cold spots; note region a in Fig. 6.11 where the absorbed dose is greater than D_m. It is often sufficient to measure uniformity in relative values of film blackening, ionization chamber signal, etc., because the beam quality changes fairly slowly at a given depth.

The isodose charts can be determined either by integrating dosimeters such as film, TLD or condenser ionization chambers, or by dose-rate measuring equiment such as diodes or ionization chambers.The choice may depend on the accelerator characteristics, e.g., short-time stability, scanning beam or scattering foil

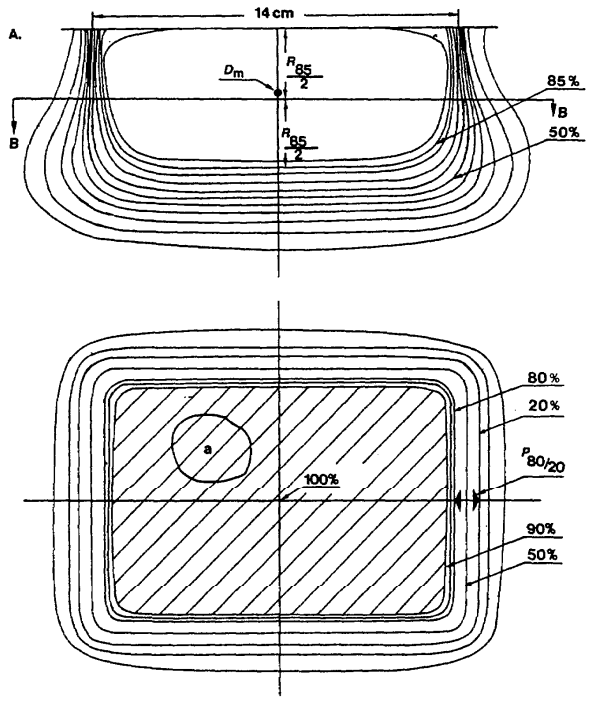

Fig. 6.11. Absorbed-dose distributions in two planes. The upper drawing shows the distribution in the plane parallel to the incident beam and through the reference point. The isodose levels of 90, 85, 80, 70, 60, 50, 40, 30, 20, 10, and 5% are shown (D_m = 100%). The lower drawing shows the absorbed-dose distribution in a section B-B that is perpendicular to the beam axis at a depth of $R_{85}/2$. The uniformity index, $U_{90/50}$, is defined in this plane as the ratio of the dashed area inside the 90 percent isodose curve to the area inside the 50 percent isodose curve. The normalization to 100 percent is made at the reference axis of this plane. The absorbed dose at this point is usually close to the dose maximum (D_m) on the beam axis. The peak absorbed dose may, in some beams, be situated outside the cross point—for instance at a. It is recommended that the physical penumbra be determined in section B-B. The physical penumbra is the average distance between two specified dose levels, generally the 80 and 20% levels, and is written $P_{80/20}$.

system, and monitor design. It may be convenient to include several types of detector systems in the complete evaluation of the absorbed dose distributions. Whatever system is used, the aim should be to determine distributions of absorbed dose in water, and not relative signal distributions from ionization chamber measurements (sometimes named "ionization distribution"), optical density distributions from films in various plastic materials, etc. A common procedure is to base measurements on a rapid, but, from the physical point of view, less accurate method, which is then calibrated to give absorbed dose distributions in water, e.g., film measurements using a polystyrene phantom evaluated after comparisons with absorbed dose measurements with ferrous sulphate dosimeters in water to give absorbed dose distribution in water (see e.g., Loevinger *et al.*, 1961; and Hettinger and Svensson, 1967). The dosimeter system should be checked for the type of use, as pointed out in Section 6.4.2.

6.5.3 Uniformity

A characteristic of the uniformity of absorbed dose in a plane perpendicular to the reference axis within the geometrical field borders was defined and measured by Svensson and Hettinger (1971). As a figure of merit, they used the ratio of the area inside the 90% isodensity line in the plane through the dose maximum—using 100% as the peak value in this plane—to the area of the geometrical field on the phantom surface. For eleven different accelerators, they found that the ratio varied between 0.26 and 0.82 for field sizes commonly used in radiation treatments. This fact means that a rather large absorbed dose variation had to be accepted with these beams.

Some accelerators produce electron beams which give a fairly uniform dose distribution at small depths, but not at larger ones. Lax and Brahme (1980) showed that some electrons which, ideally, should be stopped in the collimator are, instead, scattered back into the beam through the edge of the collimator and have then approximately 40% of the mean electron energy in the beam. These electrons may improve the uniformity at depths down to a few centimeters, but cause a rapid decrease near the field borders at larger depths.

A uniformity index similar to that of Svensson and Hettinger (1971) was defined by NACP (1972 and 1980) as a figure of merit of the uniformity at the reference depth. In order to exclude any significant influence of low energy electrons which may increase the uniformity at small depths, the index specified below refers to a depth of half the therapeutic range (Fig. 6.11). This index is equal to the ratio of the area inside the 90% isodose line to the area inside the 50% isodose line; the normalization is made to 100% at the beam axis in this plane. A value of the index ($U_{90/50}$) larger than 0.70 is readily achievable for field sizes larger than 100 cm^2; e.g., $U_{90/50}$ is equal to 0.77 in Fig. 6.11.

In order to exclude adverse local effects, "hot spots" must be avoided. A peak value less than 103% and covering an area of less than 2 cm in diameter is generally acceptable (cf., NACP, 1980, and ICRU, 1978).

It has been shown that a uniform distribution can be obtained using a proper design of the beam-flattening system and of the collimators (see e.g., Svensson, 1971; Brahme and Svensson, 1979). It must be realized, however, that an improvement of the uniformity is sometimes gained at the cost of a deterioration in depth vs. absorbed-dose distribution. Dual scattering-foil systems (see Section 3.2.2) or a scanning beam system (Aucouturier *et al.*, 1970), in combination with a well-

designed collimator, may give a large value of the uniformity index, and therapeutic range, and the dose gradient.

6.5.4 Penumbra

The physical penumbra of an electron beam may be defined by the distance between two specified isodose curves at a specified depth (ICRU, 1976). A penumbra defined in this way is a rapidly varying function of depth. From a clinical point of view, the center of the target volume is the most relevant and, therefore, half the therapeutic range is recommended as the depth of measurement. Definition of the penumbra using the average distance separating the 80 and 20% isodose levels ($P_{80/20}$) is recommended because these levels are generally located on the linear part of the absorbed dose decrease and thus place less strict conditions on the detector dimensions.

The physical penumbra, due solely to multiple electron scattering in the phantom or body, can be estimated by using the multiple scattering formulas from Section 2.6. For broad beams, the lateral distance on the major axes between the 80 and 20% isodose lines is obtained from Eq. 2.38 and tabulated values of the error function. Assuming that the collimator is in direct contact with the phantom, and that the electrons are perpendicularly incident on the phantom, the $P_{80/20}$ values are as given in Table 6.6. These can serve as the theoretical lower limit for the physical penumbra. The width of the penumbra region $P_{80/20}$ at a depth of $R_{85}/2$ increases fairly rapidly with energy up to about 20 MeV, and then stays roughly constant at higher energies. As in the case of photon radiation, several beam geometry factors will also influence the physical penumbra for electrons, namely: the effective source-surface distance, the scattering in the collimator, and the collimator to phantom distance (see Section 3.2.4). The effective angular spread at the phantom surface due to scattering in different materials in the beam (air, foils, etc.), and the width of the effective electron source, will decrease the penumbra (Section 3.2.4.2). With a well-designed beam geometry, the physical penumbra at $R_{85}/2$ should, in spite of all of these factors, be less than twice the value given in Table 6.6, as shown in an experimental determination at a number of accelerators by Almond (1979).

TABLE 6.6–*The physical penumbra, $P_{80/20}$, at the depth of $R_{85}/2$ calculated for a beam of electrons perpendicularly incident on a water phantom*

E_0/MeV	$\frac{R_{85}}{a}$/cm	$P_{80/20}$/mm
10	1.5	4
20	3.5	6.5
30	5	7.5
40	6	8

6.5.5 Leakage Radiation

Outside the collimated electron beam, stray electrons and bremsstrahlung photons may be present. From a radiation protection point of view, it is important to know the extent of this background. Such a background could either be caused by electrons scattered through the collimator walls or in the air, or by bremsstrahlung generated in scattering foils or beam limiting diaphragms and collimator walls. In making dose measurements, it may be necessary to make a correction to the response of the instrument because of the exposure of cables and electronic devices to this background radiation.

7. Determination of Absorbed Dose Distribution in a Patient

7.1 General

Standard central-axis depth vs. absorbed dose and isodose distributions discussed in Section 6 refer to a cuboid water phantom. However, the dose distribution in a patient may differ appreciably from the standard dose distributions when the elemental composition, density, and shape of the irradiated tissues differ from that of the water phantom. Furthermore, the irradiated tissue may change in these respects during the course of the treatment.

7.2 Conversion of Phantom Data to Tissue Data

Methods for the transfer of relative dose distributions from one material to another are discussed in Sections 6.2.2 and 7.4. However, even if the relative distribution measured in water can be used for a fairly accurate evaluation of the relative distributions in various soft tissues (muscle, fat, brain, liver etc.), there may still be differences in the absolute absorbed-dose values when the materials are irradiated in a given beam. The reasons are that the scattering properties of the materials may differ (which could result in different fluences at dose maximum in the various materials) as may the mass collision stopping-powers. An estimation of the difference in absorbed dose values can be obtained from the scaling law of Section 2.8.3.

The result of measurements in five different uniform phantom materials of different compositions indicate that the scatter properties should not cause a difference in the electron fluence of more than 1 or 2% at the depth of the dose maximum of various low atomic number materials, such as soft tissues (Mattsson *et al.*, 1981). From Table 2.2, it is seen that the differences in mass collision stopping powers between water and the various tissues, for the energy region used in radiation treatment, are a few per cent. It is, however, current practice to state the absorbed dose to water even if these differences are obvious.

The recent development in radiodiagnostics of computerized tomography has improved the accuracy of the determination of the densities of various tissues in vivo; their atomic composition may also be estimated by using different x-ray qualities. Previously, in the case where inhomogeneity corrections were made, only four types of inhomogeneities were taken into account, namely, air cavities, lung, bone and fat. It is evident that the composition, and often the density, of every tissue or organ is different and different from water. However, it must be pointed out that the major part of radiotherapy experience now available was gained without considering possible corrections for tissue composition. If such corrections are now taken into account, the old information should be reviewed in the same light in order to produce a new data base.

7.3 Correction for Oblique Incidence

Standard absorbed-dose distributions are measured with the beam at right angles to the surface of the phantom (Fig. 6.1). During treatment, the beam may be inclined to the body surface or the surface may be curved. Correction must be made for this difference.

The dose along a line parallel to the body surface at depth z varies, as a first approximation, with source-skin distance as measured along the ray passing through the point under consideration. The dose at a depth z along each ray, $D'(z)$, can thus be calculated by correcting the dose values $D(z)$ for a beam of perpendicular incidence using the inverse square law

$$D'(z) = \left(\frac{s_{vir} + z}{s_{vir} + d + z}\right)^2 D(z) \qquad (7.1)$$

where d is the distance between the plane perpendicular to the axis at the normal virtual source distance, s_{vir}, and the skin surface along the ray under consideration; d can be positive or negative [Fig. 7.1(a)]. For a 20 cm × 20 cm field treated with an angle of 30° between the reference plane and the skin and an s_{vir} of 100 cm, the above inverse square law factor is equal to about 0.8 for the point corresponding to the largest distance, d, at $z = R_{100}$. However, modifications in the absorbed dose in the build-up region and at the depth of the maximum absorbed dose, for oblique incidence, depend strongly upon the fraction of electrons scattered by the collimator walls back into the beam (see Section 3.2.3). When the contribution of collimator-scattered electrons is important, large deviations from the values for skin dose, D_s, and depth, R_{100}, of maximum dose derived from Eq. 7.1 are observed. In such cases, measurements should be made for each type of accelerator and collimator in order to estimate the correction to be applied.

For low energy electron beams (<15 MeV), where the dose gradient is high, and for small obliquities (<15°), the isodose curves for most practical situations may be considered as running parallel to the surface. For higher energies and large depths, inverse square law corrections must always be applied, as illustrated in Fig. 7.1(b). These corrections can be employed for the moderate inclination of the skin surface to the plane perpendicular to the beam axis. They are also valid for smooth surface irregularities, i.e., when the radius of curvature is large compared to the beam diameter.

In addition to the changes in the dose distribution of the useful beam, large variations in the dose distribution

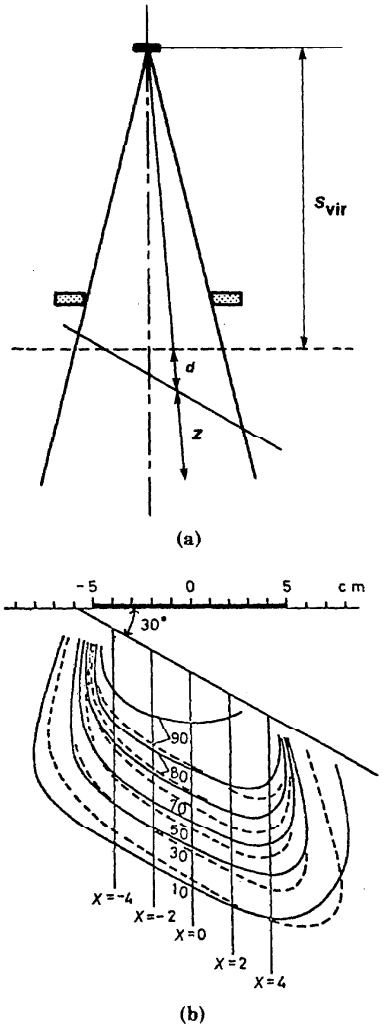

Fig. 7.1 (a) Definition of the electron beam geometry for oblique incidence. (b) Isodose curves for a 30° angle of incidence with a 22-MeV beam and a 10 cm × 10 cm field measured at the normal plane. Solid curves are from measurements, and broken curves are from the standard isodose curves modified according to Eq. 7.1 (Okumura, 1972). In both (a) and (b), the skin surface is indicated by the solid line inclined 30° to the normal plane.

appear in the penumbra region. Due to air scattering, the penumbra width varies rapidly with the distance from the skin to the collimator edge (see Sections 2.6 and 6.5.2), especially at low electron energies. Consequently, the penumbra width is different on the two sides of the field for oblique incidence; the longer the distance to the collimator, the larger the penumbra. If ignored, such variations may lead to severe underdosage of a part of the target volume [Fig. 7.1(b)].

More marked surface irregularities produce a more complex situation. The electrons are predominantly scattered outward by projections and inward by depressions. The deformation of the isodose curves is usually extensive near the surface irregularity, but at large depths, scattering tends to reduce the effects of the irregularity. Electrons striking a surface at large inclinations to the normal may give rise to localized over- and under-dosage ("hot spots" and "cold spots") in the underlying medium (Regourd, 1962; Breitling and Seeger, 1963; Netteland, 1965).

7.4 Corrections for Inhomogeneities

When a portion of the irradiated volume of tissue contains material with different penetrability or scattering properties than those of water, a correction to the isodose data in water may be needed. The coefficient of equivalent thickness, C_{ET}, may be used for this purpose if the inhomogeneity is relatively large and of somewhat uniform thickness (Laughlin, 1965; Laughlin *et al.*, 1965; Boone *et al.*, 1965, 1967; Almond *et al.*, 1967b; Dahler *et al.*, 1969; Harder and Abou-Mandour, 1976). C_{ET} is defined for a parallel beam of incident radiation and is the ratio of the thickness of water to that of the inhomogeneity that will produce the same transmission of absorbed dose rate (see Eq. 7.3). For parallel rays it is possible to choose a depth, z, in water for which the absorbed dose, $D_w(z')$, is the same as the absorbed dose, $D_i(z)$, obtained after such rays pass through a thickness, $z - h$ of water and a thickness, h, of an "in homogeneity". Those distances are related by:

$$z = z' - h(C_{ET} - 1)$$

For an incident, diverging beam of electrons, an inverse square correction may also be required. For such a diverging beam, the absorbed dose $D_i(z)$ at a depth z behind the inhomogeneity is

$$D_i(z) = D_w(z') \frac{(S_{vir} + z')^2}{(S_{vir} + z)^2} \tag{7.2}$$

Corrections are made along each ray through the inhomogeneity.

The usefulness of the C_{ET} concept depends on the type of inhomogeneity:

(1) for tissues like brain, liver, kidneys, fat, etc.—$\overline{Z}$ and ρ are not very different from water,
(2) for lung—$\overline{Z}$ is not very different from water, but ρ is different from water,
(3) for bone—$\overline{Z}$ and ρ are different from water.

When $\overline{Z}$ and ρ are not very different from water, the C_{ET} may be estimated from

$$C_{ET} = S_{tot,i}/S_{tot,w} \tag{7.3}$$

where $S_{tot,i}/S_{tot,w}$ is the ratio of the total linear stopping-power of organ i to water *at the mean electron energy considered* (Table 6.1). As a first approximation, when $S_{tot,i}$ is not known, the C_{ET} value can be estimated from the ratios of the electron densities, N_e, of organ i

TABLE 7.1—*Densities, ρ, and electron densities, N_e, calculated from published compositions of water and tissues.*

Tissue or material	ρ/g cm^{-3}	$N_e/10^{23}$ g^{-1}	Reference for value of ρ	Reference for composition
Water[2]	1.00	3.349		
Muscle	1.06	3.25–3.32	Jayachandran, 1971	ICRU, 1972
			Rao, 1975	Kim, 1974
Bone	1.09–1.65	3.10–3.25	ICRU, 1963	ICRU, 1972
			Jayachandran, 1971	Woodard, 1962
			Lindskoug and Hultborn 1976	Kim, 1974
Lung	0.26–1.05	3.25–3.33	ICRU, 1972	Kim, 1974
Fat	0.92–0.94	3.38	Rao, 1975	White, 1974
			White, 1974	
Brain	1.03–1.05	3.31–3.33	Cho *et al*, 1975	Kim, 1974
			Rao, 1975	
Liver	1.05–1.07	3.32–3.34	Rao, 1975	Kim, 1974
Other tissues			Rao, 1975	Kim, 1974

[a] Composition: H (11.19), O (88.81) percentage by weight.

and water (Table 7.1). This correction may be applied for any large organ except for lung and bone. Almond *et al.* (1967) and Boone *et al.* (1967) have proposed values of C_{ET}, experimentally verified for cork $\rho = 0.39$ g cm^{-3}, using large fields and electron energies between 6 and 18 MeV.

Large, parallel slabs of bone are uncommon in the skeleton apart from the skull. The maxilla or sternum may be considered as "large" when the entire cross-section of the beam is intersected by these bones. The mean scattering angle of electrons is increased by bone and, consequently, the dose is increased within bone and in soft tissue immediately beyond. However, measurements with fresh specimens of sternum or ribs have shown that the maximum dose increase beyond large slabs of these bones was less than 2% and could be neglected (Almond, 1967; Lindskoug and Hultborn, 1976). At depths larger than a few centimeters beyond bone, the electron fluence and absorbed dose decrease. Therefore, a constant C_{ET} cannot be used for bone and a more sophisticated method is necessary (Dutreix, 1968).

Only when the field size is large enough to assure broad-beam conditions on the central axis in the material in question, can depth-dose curves in low density materials, like the lung, be calculated from depth-dose curves in water using the C_{ET} concept. For smaller field sizes, as a rough first approximation, the depth dose in a material of density ρ_i (and $\bar{Z}$ similar to water) for a field size $x_i \times x_i$ can be considered to be comparable to the depth dose in water for a field size

$$\frac{x_i\rho_i}{\rho_w} \times \frac{x_i\rho_i}{\rho_w},$$

if the depths are expressed in g cm^{-2}. When a divergent beam is used, an inverse square correction may also be required.

For inhomogeneities of small dimensions, such as bones, air cavities or lungs, when they are present only in a limited part of the beam, a correction method has been suggested by Harder and Abou-Mandour (1976) and Abou-Mandour and Harder (1978a). The dose distribution in a broad beam is assumed to be given by the addition of a large number of adjacent small beams or, more simply, to be the addition of two beams; one small beam with a field size equal to the cross-section of the inhomogeneity and a second "hollow" beam irradiating the homogeneous medium. The dose $D_i(z)$ at a point in the inhomogeneous medium is obtained from the dose $D_w(z)$ at the same point in water by subtracting the dose $D'_w(z)$ which would be delivered by the small beam (A_H) [Fig. 7.2(a)] in water and adding the dose $D'_i(z)$ delivered by the small beam (A_I) through the inhomogeneity

$$D_i(z) = D_w(z) - D'_w(z) + D'_i(z)$$

and using Eq. 7.2 for $D'_i(z)$, then

$$D_i(z) = D_w(z) - D'_w(z) + D'_w[z - h(1 - C_{ET})] \times \left[\frac{s_{vir} + z - h(1 - C_{ET})}{(s_{vir} + z)^2}\right]^2 \quad (7.4)$$

This method of calculation should yield accurate values of the dose distribution within or beyond an inhomogeneity. Unfortunately, data on small beams are not always available—more data on C_{ET} values for bone and lung in small beams are needed. Experimentally determined correction factors for small air cavities have been published by Nüsslin (1975) and Skoropad (1975).

Significant overdosages (hot spots) or underdosages (cold spots) may occur in rather limited regions due to the unbalanced electron fluence at the edges of an inhomogeneity (Breitling and Vogel, 1965). Such effects are very similar to those observed for surface irregularities (see Section 7.3) and are specially important

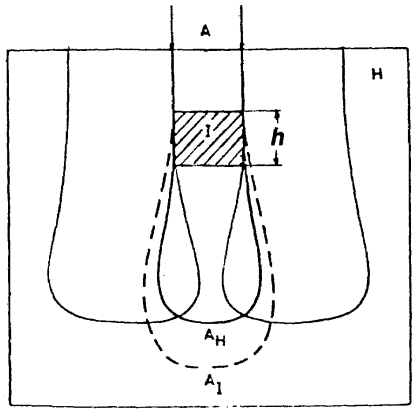

a

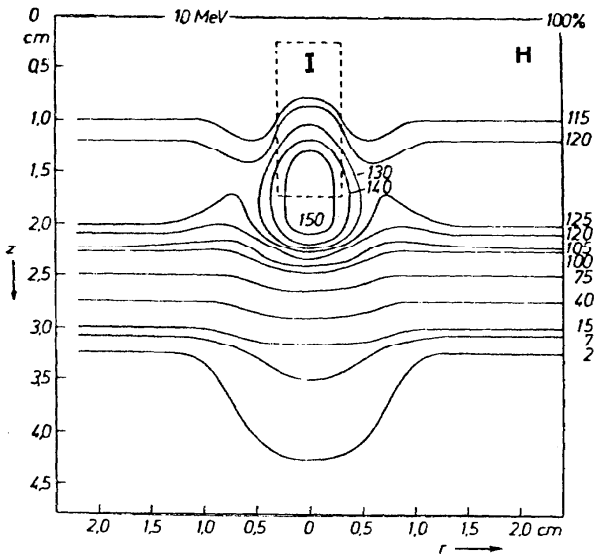

b

Fig. 7.2. (a) Schematic representation of the radiation beam geometry used when correcting for a small inhomogeneity using method of Harder and Abou-Mandour (1976): H indicates the homogeneous material. The inhomogeneity, I, is indicated by the rectangle, of thickness, h. The density of I is lower than that of H. The isodose of the partial beam A is for the inhomogeneous case (A_I) shifted here to below the isodose for the homogeneous case (A_H). (b) Isodose diagram showing the effect of an air cavity in a uniform beam (Abou-Mandour and Harder, 1978b).

when the edges of the inhomogeneity are tangential to the beam direction [see Fig. 7.2(b)].

Because of the decrease of electron backscatter by lung, the dose to the soft tissues in front of the lung interface is slightly decreased (Almond, 1967). Similarly, a slight overdosage (3–7%) is expected in front of bone due to the increased backscatter of the electrons from bone (Dutreix, 1968). The modifications in the electron

TABLE 7.2—*The ratio of the mass ionization in a thin air layer at a PMMA-metal interface relative to that at a PMMA-PMMA interface (i.e., in pure material) at the dose maximum for electron beams*

[The numbers in parentheses are the depths of maximum mass ionization in g cm^{-2}] (from Dutreix and Bernard, 1968)

Material	Electron Energy		
	10 MeV	15 MeV	20 MeV
PMMA	1.00 (2.2)	1.00 (2.5)	1.00 (2.3)
Al	1.075 (1.7)	1.04 (2.4)	1.05 (3)
Cu	1.10 (1.2)	1.08 (2)	1.085 (2.5)
Sn	1.13 (0.9)	1.12 (1.4)	1.13 (2.3)
Pb	1.15 (0.7)	1.16 (1.1)	1.16 (1.8)

fluence and, hence, the dose distributions in soft tissue are much greater when a high-Z material is behind, but in contact with, soft tissues (Dutreix, 1968). In the shallow layers of tissue, the absorbed dose in soft tissue in contact with a high-Z material layer is increased by a factor depending upon the beam energy, the layer thickness and the Z of the material. Table 7.2 gives the ratio of maximum mass ionization in a thin air layer at the interface between a high-Z material and PMMA, relative to the maximum mass ionization in air in homogeneous PMMA. The data were obtained for a 10 cm × 10 cm field size. The cross sectional areas of the PMMA phantom and the high-Z material were larger than the field size. The thickness of the high-Z material was large enough to give maximum backscatter. The figures in parentheses are the mass thickness of the material where maximum ionization is achieved.

7.5 Decelerators, Bolus and Wedges

7.5.1 Decelerators

On most treatment units used for electron therapy, the lowest electron energy is 5 MeV or more. This energy is generally too high for the treatment of very superficial target volumes, such as for mycosis fungoides. For this purpose, very low atomic number absorbers (e.g., beryllium, carbon or polystyrene) may be used to reduce the electron beam energy without excessive bremsstrahlung production. Special attention must be given to the contaminating bremsstrahlung background in the treatment of the whole skin surface (Karzmark *et al.*, 1960; Edelstein *et al.*, 1973; Sewchand *et al.*, 1979; Kase and Bjärngard, 1979) because it may constitute a considerable contribution to the whole body dose. The decelerator should, ideally, be placed close to the irradiated area to minimize the dose from the contaminating bremsstrahlung.

However, when using decelerators for normal beam sizes and higher initial beam energies, the best location is close to the primary scattering foil (see Fig. 3.1), be-

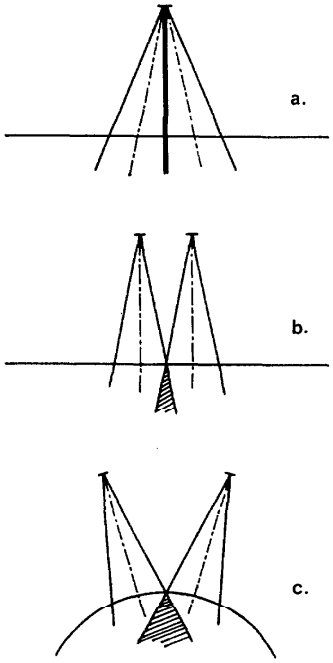

Fig. 7.3. Three possible beam configurations of adjacent radiation beams placed in order of increasing overlap problems.

cause this will not cause deterioration of the shape of the depth-dose curve (Brahme, 1975; see also, Fig. 3.11).

7.5.2 Bolus

The simplest way to locally vary the depth of penetration of a high energy electron beam is to place an approximately tissue-equivalent layer of varying thickness on the body surface (bolus). However, this method will remove the dose build-up in the surface region which may be disadvantageous for some treatments. For such cases, better dose distributions with good skin sparing are generally obtained by using adjacent beams of different energies (see Section 7.6.2.1 and Fig. 7.3).

For superficial target volumes, a bolus can also be used to increase the dose uniformity in the surface region. This will be obtained at the cost of a less steep dose fall-off behind the target volume, because a higher electron beam energy must be used. To eliminate this effect, a depth-dose flattening filter may instead be used to increase the surface dose without the accompanying decrease in dose fall-off gradient (Brahme and Svensson, 1976b).

7.5.3 Wedges

Wedge filters are standard devices for use with high energy photon beams due to the special shape of the photon depth-dose curve with a long gradual dose decrease. For electron beams, the dose fall-off section of the depth-dose curve is generally very short and steep, with a limited range and, therefore, wedge filters are rarely used for electron beam therapy.

Wedge-shaped isodose distributions were produced by Okumura *et al.* (1969) using split scattering foils to treat regionally invasive tumors in the head and neck region. A similar technique may be achieved on some accelerator types, by simply offsetting the beam symmetry control.

Wedge shaped degraders are sometimes used to produce a gradual variation of the therapeutic range, R_{85} (Kuttig and Ziegler, 1975). However, this is not strictly a wedge, but rather a wedge-shaped type of bolus or decelerator. When the wedge-shaped filter is placed at some distance from the irradiated area, the isodose distributions are disturbed due to the scattering action of such a filter (Dutreix *et al.*, 1968). The most common use of small wedge filters is probably to broaden the penumbra and simplify the alignment problems of adjacent electron beams.

7.6 Electron Beam Treatment Planning

7.6.1 General

The principal advantage of high-energy electron beams in radiation therapy is their ability to deliver a high dose to superficial and moderately deep target volumes without damaging deeper-situated healthy tissues.

Determination of dose distributions in a patient undergoing treatment with single, multiple or moving electron beams is based on detailed information about each individual patient and about all the available electron beam qualities.

The geometrical information on the patient usually consists of one or more cross-sectional drawings covering the region of interest. One of these drawings is in the plane of the reference axis of the beam. The drawings should be full scale and contain contours of the body surface and all internal structures relevant for the treatment, such as target volume, body inhomogeneities and organs at risk. In addition to the geometrical information, the physical properties of the involved tissues are needed. The CT-scanner is the ideal instrument for obtaining this information, but it is generally necessary to convert its CT-numbers to the data needed for electron beam treatment planning (Purdy, 1977; Datta *et al.*, 1979; Hogstrom *et al.*, 1981). The technique of patient data acquisition is, apart from the above problem, independent of radiation modality and is described in detail in ICRU Report 24 (ICRU, 1976).

7.6.2 Multiple Beams

In some situations, a combination of two or more electron beams may be required to achieve the best distribution of absorbed dose in the target volume and the surrounding tissues. In order to obtain the isodose distribution of multiple, fixed electron beams, the isodose distribution of each individual beam must be normalized and added. The relative absorbed dose of each beam is determined at each point of interest including weighting factors and other necessary corrections. The total absorbed dose at each point is then obtained by adding the dose contributions of all the beams

$$D(\mathrm{P}) = \sum_{i=1}^{n} w_i \cdot D_i(\mathrm{P}) \qquad (7.5)$$

where

$D(\mathrm{P})$: absorbed dose at the point P
i: beam number
w_i: weighting factor of beam i
$D_i(\mathrm{P})$: absorbed dose from beam i at the point P
n: number of beams.

A sufficiently large number of dose values in the region of interest are calculated according to Eq. 7.5. The values are then normalized to the dose at the reference point as discussed in ICRU Report 24 (ICRU, 1976).

The isodose contours are now obtained by connecting all points (or interpolated points) of equal relative dose.

7.6.2.1 Adjacent Beams. Two or more electron beams may be used side by side in order to increase the irradiated area outside the maximum field size of a single beam or to treat a target volume of varying depth below the patient surface. If the collimator were perfect, with a negligible amount of scattered electrons (see Section 3.2.3), the field size could be increased without any border problems between adjacent beams simply by placing the adjacent beam edges in perfect alignment [see Fig. 7.3(a)]. This is due to the fact that the dose reduction at the beam edge by electrons scattered out of one beam is fully compensated by the scatter from the adjacent beam when the beam energies and directions coincide. However, most electron collimators are far from ideal because a considerable number of electrons are scattered from the edges of the collimator (Briot *et al.*, 1973; Lax and Brahme, 1980).

Furthermore, the beam edges are normally inclined to one another due to divergence of each beam and to the curvature of the body contour [Fig. 7.3(b) and (c)]. The isodose contours in the common plane of two electron beams with $(E_p)_0 = 20$ and 10 MeV are shown in Fig. 7.4(a) (Svensson, 1978). The collimator used was of high quality and the adjacent beam edges coincided. The slight overdosage in this case is only due to the higher electron scattering out from the low-energy beam. In Fig. 7.4(b) (Almond, 1975), the effect of nonaligned electron beam edges and nonideal collimation is seen. The considerable overdosage obtained in this case could be reduced at the expense of an underdosage by increasing the field separation. A somewhat better dose distribution could be obtained by using small polystyrene or aluminum wedges at the edge of one or both the beams, although at the cost of a more complicated set-up (Laughlin, 1967). However, an almost perfect dose distribution can be obtained, as mentioned above, by placing the neighboring beam edges in coincidence through a rotation of the reference axis of the radiation beams [see Fig. 7.3(a) and Bagne, 1978].

7.6.2.2 Parallel Opposed Beams. Single electron beams are not very suitable for treatment of large deep-seated target volumes due to the high doses given to superficial tissues. However, the steep dose fall-off in electron beams may still be used at high beam energies with deep target volumes when two parallel, opposed beams are applied. This situation is illustrated in Fig. 7.5 by the reference axis absorbed dose distributions for three different phantom depths (16, 20, and 24 cm) and electron beam energies between 20 and 60 MeV. It is clearly seen that for the correct choice of electron beam energy, the absorbed dose in superficial regions is considerably reduced compared to that using photon beams in the same configuration (Ovadia and Uhlmann, 1960; Zatz *et al.*, 1961).

The use of opposed electron beams is very difficult when low energies and small body cross-sections are involved because the very rapid dose fall-off in low energy beams may lead to substantial under- or overdosage as a result of inhomogeneities and curved body surfaces. However, at high energies, this problem is considerably reduced. Furthermore, the reduced electron scattering at high electron energies results in an acceptably narrow penumbra even for very deep-seated target volumes, as seen in Fig. 7.6 (Brahme *et al.*, 1980a).

7.6.3 Moving Beams

In moving beam electron therapy, the position of the electron source and the electron beam direction are changed continuously relative to the patient. The absorbed dose rate, $\dot{D}(\mathrm{P},\alpha)$ at the point of interest P will vary depending on the angle, α, of the beam. Hence, the absorbed dose at each point in the patient cross-section is given by

$$D(\mathrm{P}) = \int_{\alpha_{start}}^{\alpha_{stop}} \frac{\dot{D}(\mathrm{P},\alpha)\,d\alpha}{\omega(\alpha)} \qquad (7.6)$$

where α_{start} and α_{stop} are the start and stop angle of the

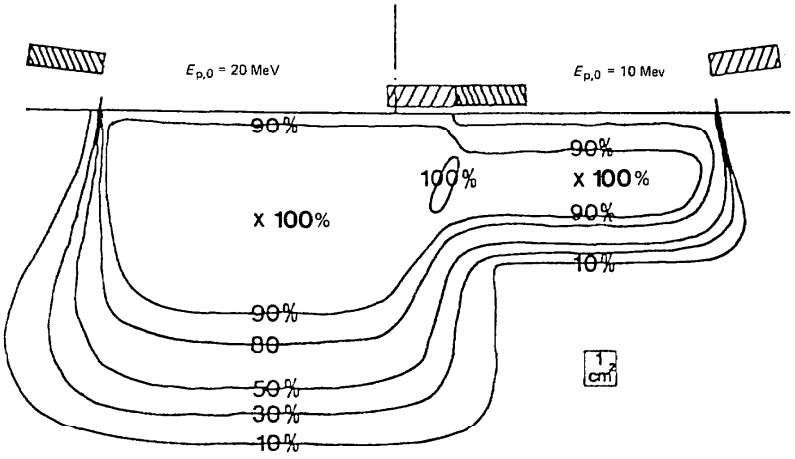

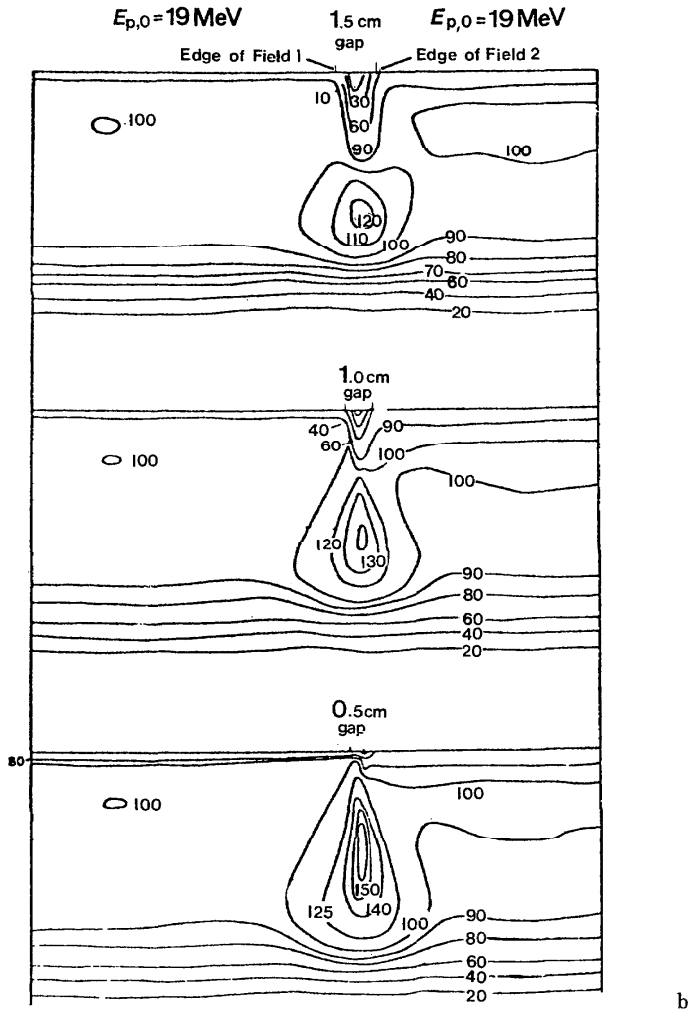

b

Fig. 7.4a and b. Isodose contours of adjacent high energy electron beams. Figures a (Svensson, 1978) and b (Almond, 1975) pertain to different beam configurations according to Fig. 7.3 a and b, respectively. The sets of isodose data in b are for different gaps between the entrance fields.

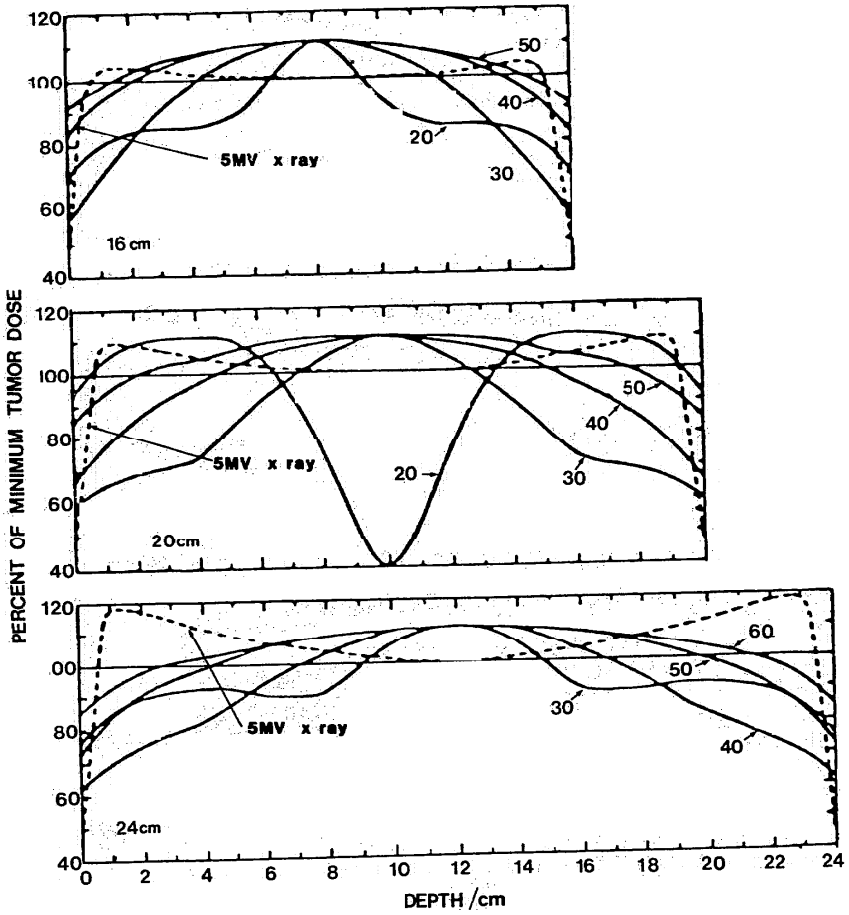

Fig. 7.5 Central-axis depth-dose curves for opposing parallel electron fields (solid curves) for three different phantom thicknesses. The minimum tumor dose was taken as 90% (labeled 100 on the ordinate) of the maximum dose for each energy (MeV). The most probable energies at the phantom surface are indicated. Corresponding curves (dashed lines) for 5-MV x-rays are included for comparison (Zatz *et al.*, 1961), normalized to 100% at the center of the phantom.

beam rotation and $\omega(\alpha)$ is the angular velocity of the beam.

Direct evaluation of Eq. 7.6 is simple in the case of an homogeneous medium of circular cross-section. In other cases, an approximate evaluation of Eq. 7.6 is achieved by numerical integration for a limited number of fixed beams.

Both for superficial and deeper therapy with electron beams, a constant dose (in free air) per unit angle of rotation of the moving gantry at the isocenter of the treatment facility is essential. This can be achieved by a constant dose rate at the isocenter and constant angular velocity, but may also be achieved by varying the angular velocity in proportion to the instantaneous dose rate or vice versa. The integrand in Eq. 7.6 is, therefore, generally a constant independent of α when P is located at a constant depth and distance from the source.

7.7 Computerized Treatment Planning

The uses of computers in electron-beam treatment planning is becoming increasingly important because it allows the rapid addition of isodose data for two or more fields. Furthermore, more sophisticated corrections for patient contour, inhomogeneities, etc. may be introduced. Computer programs for electron-dose planning are undergoing rapid development at the present time. The following is a brief summary of the different lines of approach.

7.7.1 Empirical Methods

Empirical methods use isodose distributions reconstructed from a very large amount of measured data and are often referred to as matrix methods (Leetz, 1976,

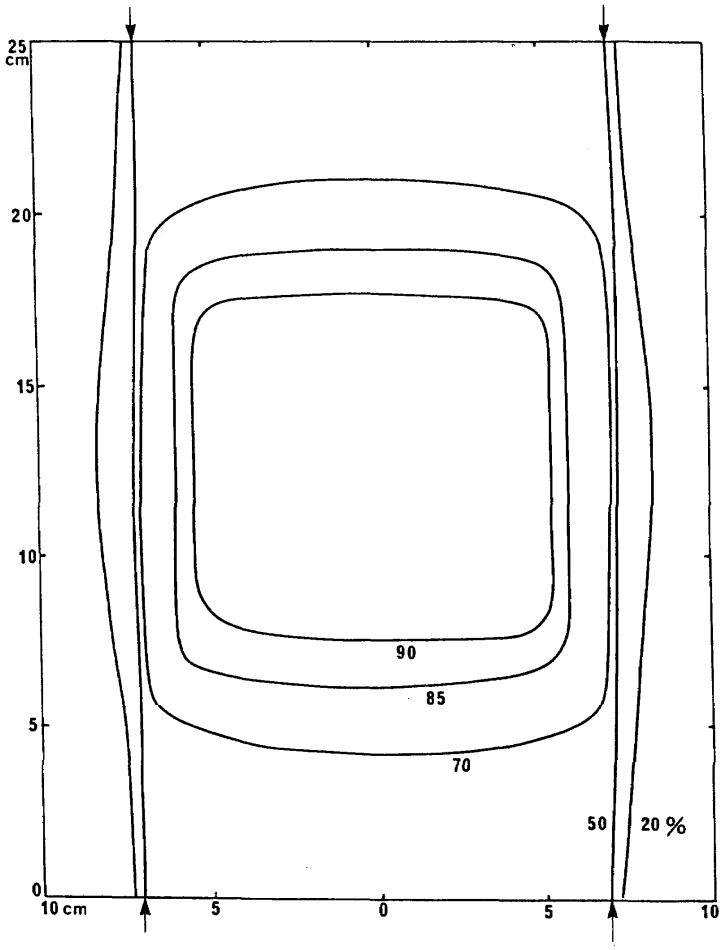

Fig. 7.6. Isodose contours of parallel opposed 50-MeV electron beams at a field size of 14 × 14 cm² and a patient thickness of 25 cm. Due to the high electron energy, the penumbra is fairly narrow and the influence of inhomogeneities is small.

1979). Such methods are most suitable for reconstructing irregular dose distributions from different types of accelerators with high accuracy. The number of measured data points to be stored is high. A significant reduction of data is achieved if broad beams are constructed from pencil beam distributions (Boag and Lillicrap, 1972; Benedetti, 1973; Lillicrap *et al.*, 1975; Brahme *et al.*, 1981).

7.7.2 Analytical Methods

A method based on a general solution of the diffusion equation has been applied to generate isodose data for beams from different types of electron accelerators (Kawachi, 1975; Brahme, 1975; Osman, 1976; Steben *et al*, 1976, 1979; Iversen *et al.*, 1976; Nüsslin, 1978; Abou-Mandour and Harder, 1978a; Millan *et al.*, 1979; Hogstram *et al.*, 1981; Schröder-Babo and Harder, 1981; Perry and Holl, 1980; Brahme *et al.*, 1981). The three-dimensional solution of the transport equation contains the depth-dose distribution and the lateral beam profile separated. For a beam size of 2a × 2b (see Section 2.6.3), the absorbed dose distribution, normalized to the broad beam depth dose $D(z)$, may be written,

$$D(x,y,z) = \Phi^{p}(x,y,z) \cdot D(z) / \Phi^{p}(0,0,0) \qquad (7.7)$$

where z is the depth in the phantom, x and y the lateral coordinates (see Fig. 2.9), $\Phi^{p}(x,y,z)$ is the lateral distribution function (already given by Eq. 2.41). Kawachi (1975) has given a solution for $D(z)$ in Eq. 7.7. However, this solution is only useful for electron beams where there is negligible dose build-up, e.g., due to contamination by low energy electrons, because it does not take into account the dose build-up of electron fluence due to multiple electron scattering or the production of secondary electrons. A more accurate fit to experimentally-measured dose distributions is, therefore, obtained by putting $D(z)$ equal to the real measured distribution. This could be done by storing the discrete values and interpolating or by fitting the experimental data to analytic functions (see the above references and those of Section 2.8.1).

The lateral distribution of electrons, Φ, can be described by one single parameter when the influence of secondary electrons is disregarded. This depth-dependent parameter is related to the broadening of a narrow electron beam and is denoted by r_{rms} in Eq. 2.41. This parameter is related to the mean square radius of a narrow beam [$\overline{r^2}(z)$, Eq. 2.37] and to the age diffusion parameter often used in this context ($\kappa\tau$, cf Kawachi, 1975) by

$$r_{rms}^2 = \overline{r^2}(z) = 4\kappa\tau \tag{7.8}$$

Several different approximations to this parameter have been given by the authors cited above, often based on a fitting of available experimental data. The results are in quite good agreement with the theoretically expected expression given in Eq. 2.37 and Table 3.1.

7.7.3 Monte Carlo Methods

The usefulness of statistical methods for calculating electron beam dose distributions is limited because very time-consuming computations, such as the Monte Carlo method, cannot be part of routine treatment planning. Nevertheless, Monte Carlo results, e.g., for the pencil beam, can be of use as source data on which repetitive routine calculations can be based. Moreover, theoretical methods are expedient for the analysis of basic questions such as the origin of the maximum of the depth-dose curve. Very widespread use has been made of the semi-empirical approach in which all integrations over the pencil beam are performed by analytical calculus, whereas the dose distribution for the pencil beam is empirically determined.

7.7.4 Conclusions

A number of published algorithms are available for implementation in computerized electron beam treatment planning systems. Users of such algorithms must be prepared to make extensive direct measurements on their treatment units to verify the suitability of the algorithm selected for their particular electron beam qualities.

8. Electron Beam Monitors

8.1 Introduction

In the present context, a monitor is an instrument which gives an indication proportional to certain parameters of the radiation beam such as electron fluence rate or absorbed dose rate in air at a position in the beam, or absorbed dose rate at some point in the irradiated object. However, many other parameters can be monitored, such as beam uniformity or electron energy. The response of the monitor should, as far as possible, be directly proportional to the parameter of interest in a particular irradiation and the constant of proportionality should be independent of other parameters of the beam. A monitor will not, however, give an absolute value of any parameter of the beam unless the relationship of its response to this parameter has been experimentally established. A further essential property of a monitor is that the necessary information can be obtained from the beam without causing appreciable perturbation of the beam.

A number of different instruments and methods have been used for monitoring electron beams: transmission ionization chambers, secondary electron emission detectors, electromagnetic induction detectors, and sampling, either by ionization chambers, or collection of electrons.

Except in the case of sampling, the instruments are placed where the electron beam emerges from the accelerator. This has the advantage of leaving the radiation field free for the disposition of experimental apparatus, samples to be irradiated, or patients.

The sampling method involves placing one of these monitors close to the position where the material being irradiated is located. This has the advantage of monitoring at a position close to that part of the beam which is actually being used, instead of the total beam as it emerges from the accelerator. In some circumstances, the response of a monitor used in this way is the best indication of the reproducibility of irradiation conditions at the point of measurement. However, the sampling method must be used together with another method; it gives an indication of only a part of the beam, and important changes occurring in another part of the beam may not be noticed.

Only *transmission ionization chambers*, which are used in most of the modern high-energy electron generators, will be described here. For the description of other types of electron beam monitors, the reader is referred to the literature, e.g., secondary emission monitors (Tautfest and Fechter, 1955; Taimuty and Deaver, 1961; Vanhuyse *et al.*, 1962; Isabelle and Roy, 1963; Frerejacque and Benaksas, 1964; Karzmark, 1964), induction monitors (Bess and Hanson, 1948; Bess *et al.*, 1959; Grishaev *et al.*, 1960; Bergere *et al.*, 1962; and Isabelle, 1962) and partial beam monitoring by collection of electrons (Bewley, 1971).

8.2 Transmission Ionization Chambers

Transmission ionization chambers have been the most common type of instrument used during the early period of work with electron beams owing to their high sensitivity and because of the familiarity of radiological physicists with ionization chamber techniques. The relationship between monitor reading and absorbed-dose rate at the dose maximum in water is a complicated function of beam energy, collimator type and field size. Thus, the monitor must be separately calibrated for each different beam quality used. It is, however, desirable, that the monitor response be as independent of the above-mentioned factors as possible (see Table 8.1 for responses obtained with two machines—Svensson, 1981).

If the ionization chamber is not sealed, its response will change with the temperature and pressure of the air. This is a considerable disadvantage when the monitor is situated near accelerator parts whose temperature changes during operation. On the other hand, sealed monitors need to be constructed more solidly and may, therefore, introduce unwanted scattering materials in the beam.

Another problem with the transmission monitor is the effect of ionic recombination in the chamber when high beam currents are used. The theory and practical consequences of ionic recombination have been discussed by Mie (1904), Boag and Wilson (1952), Chodorow (1955), Burlin and Husain (1964), Greening (1964), Armstrong and Tate (1965), and Boag (1966). An upper limit to the electron beam current that can be adequately determined is obtained from the following computation. The minimum practical electrode spacing is about 0.5 mm and the maximum potential difference 500 volts. With these parameters, under continuous irradiation, a collection efficiency of 99% is obtained when an ion charge of one sign per unit volume is produced at the rate of $6.2 \cdot 10^{-4}$ C cm^{-3} s^{-1}. The response of the chamber for electrons of a few MeV (i.e., the number of ion pairs produced per electron passing through) is directly proportional to the plate separation, l. There are about 3.5 ion pairs formed for $l = 0.5$ mm and normal air pressure and temperature. This gives an upper limit for the beam current density of 10^{-5} A·cm^{-2}. The collection efficiency should not be allowed to fall much below 99%. Below this efficiency level, the efficiency falls rapidly with increasing ion current.

The theory of recombination in an ionization chamber exposed to pulsed radiation has been given by Boag

TABLE 8.1—*Absorbed dose (in grays) to the patient[a] for 1.00 monitor unit*

Field Size	Energy			
	Machine A		Machine B	
	11 MeV	20 MeV	11 MeV	20 MeV
12 cm × 14 cm	1.07	1.02	0.99	0.99
8 cm × 10 cm	0.98	1.00	0.98	0.99
4 cm × 8 cm	0.77	0.93	0.97	0.99
Circular 8 cm in diameter	0.92	0.98	0.98	0.99
Circular 4 cm in diameter	0.51	0.76	0.96	1.00

[a] Absorbed doses are specified at the location of the maximum on the beam axis, R_{100}. Data from Svensson, 1981.

(1950, 1966) and Boag and Currant (1980), on the assumption that the pulse is short compared with the transit time of ions across the chamber. This is nearly always true for conventional dosimetric ionization chambers; the transit time is over 100 μs while the pulse length from an accelerator is generally no greater than 4 μs (see Section 3.4). However, in a monitor chamber, one may have 500 volts across an 0.5-mm airgap, in which case the transit time will be only about 4 μs, and neither the theory for pulsed radiation nor that for continuous radiation is strictly valid. However, if one treats the pulse as instantaneous, the calculated collection efficiency will be lower than the actual value and this is, therefore, a safe guide when designing a monitor chamber.

Theoretically derived transit times do not correct for the possibility of electron collection rather than ion collection. With the shorter time for electron collection, and, therefore, the shorter time for possible recombination, the efficiency of collection may be higher than that given by present theory.

The theory assumes a uniform ion density throughout the ion production gap. Actually, the ion density in the monitor chamber will be highest at the center and lowest near the edge. Thus, reliance should not be placed solely upon a calculated value for collection efficiency; experimental checks should be made, but these also require careful consideration.

For a collection potential of U, the method of plotting the collected current (I) either against I/U (in accordance with pulsed theory) or against I/U^2 (for continuous irradiation), and then extrapolating to $I/U = 0$ (i.e., $U \rightarrow \infty$), becomes a purely empirical approach when the theory on which these methods are based is not exact. If a good straight line is obtained by either method over a wide range of U, the method has an empirical justification. For a rapid check of collection efficiency the two-voltage technique described in Section 5.4.3 may be useful.

Boag (1966) has pointed out that under pulsed conditions, collection efficiency begins to fall when the space charge due to positive ions reduces the electric field at the anode to zero. It is possible to improve the performance of these chambers by using a gas such as argon, which does not attach electrons to form negative ions. The maximum beam current can thus be increased by a factor of about 26 compared with air at 99% collection efficiency. A disadvantage with gases other than air is the risk of leakage of air into, or gas out of, the chamber.

In a practical transmission chamber, the amount of material in the beam is minimized in order to limit the amount of electron scattering and bremsstrahlung production by the chamber. Consequently, the chamber is usually made from thin foils of aluminum or aluminized plastic (Melinex, Mylar, Kapton, Hostaphan). On the other hand, when scattering foils are used in order to obtain broad, uniform electron beams, the plates of the transmission chamber may also serve as a useful part of the scattering system if the chamber is suitably designed and positioned (see Section 3.2.4.2). This means that the thickness of the scattering foil can be reduced. The practical use and construction of transmission chambers is discussed by Laughlin *et al.* (1953), Karzmark *et al.* (1960), Ovadia and Uhlmann (1960), Sempert (1960), Moore (1961), Veraguth (1961), Beattie *et al.* (1962), Kretschko *et al.* (1962), Pohlit (1965), and Harder (1965c).

8.3 Choice of Monitor Systems—Practical Implications and Safety Considerations

Two completely independent monitor systems are strongly recommended; each of them being able to stop the irradiation when the pre-set dose has been delivered.

In modern high-energy electron accelerators, two independent transmission ionization chambers are generally used. A further refinement in safety is achieved by a continuous *automatic comparison* of the signals of the two monitor systems, the irradiation being stopped when the ratio of the signals varies outside pre-set limits. This prevents irradiation when one of the monitors is out of order.

A timer may be used as an additional safety device as in most modern accelerators the dose rate is accurately controlled. A pre-set timer can prevent serious overdosage.

The response of the dose monitors should be as independent as possible of the following operating conditions:

(a) *Dose Rate:* The response of the dose monitor should be independent of the dose rate over the useful range. This requirement can generally be met for the transmission ionization chamber monitors by correct design and selection of applied voltage (see Section 8.2). However, the problem is enhanced by the fact that one is dealing with pulsed radiation

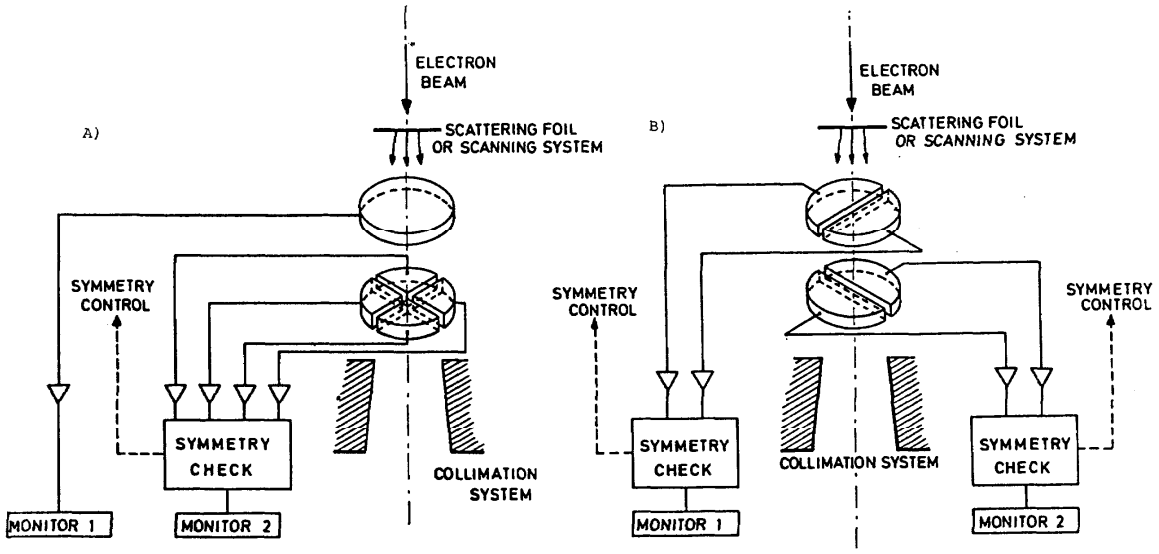

Fig. 8.1. Transmission monitors for the monitoring of absorbed dose to the patient and symmetry of the beams.

which leads to an instantaneous dose rate much higher than the measured mean dose rate; the dose per pulse is, in general, the critical parameter (see ICRU, 1982). The constancy of the monitor response as a function of the dose rate has to be checked for all dose rates to be used. If a small variation is noticed, appropriate correction factors should be applied.

(b) *Temperature:* As the temperature may vary during machine operation, the response of the monitors should, ideally, be independent of the temperature. This requirement is not met by unsealed ionization chambers and the drift during operation of the machine has to be checked. For sealed chambers, temperature corrections should, in principle, not be necessary, although the chamber has to be checked for possible gas leakage. The worst situation to deal with is when the chambers are intermittently sealed.

(c) *Other Operating Conditions:* The quotient of the monitor signals to either the dose rate or absorbed dose at a specified point in the patient should be known within given limits. Therefore, the monitors are generally located downstream with respect to the scattering foil(s) in the irradiation head. For practical reasons, they are generally located between the scattering foil(s) and the collimator system. It is impossible, for technical reasons, to make the monitor signal independent of factors such as energy, scattering foil, field size (different scattering foils can be chosen as a function of energy and/or field size). Even if the chamber response itself is only weakly dependent on the energy of the electrons, changes in their energy may modify the downstream scattering conditions. The field size also influences the scattering conditions, depending on the construction of the irradiation head.

The response of the monitors should not, in principle, be influenced too much by a slight variation of the beam position. For this reason, a transmission ionization chamber traversed by the total electron beam is better than a detector located near the beam edge.

It may be useful to have a continuous record of the position and/or symmetry of the beam; in order to achieve this, one possibility is to divide one of the transmission ionization chambers into four quadrants. The charge collected on each of the quadrants is compared to provide an indication of the beam position and/or symmetry. These charges can then be added in order to give the signal from that monitor (see A in Fig. 8.1). As an alternative solution, each transmission ionization chamber can be divided into two equal parts, for instance along the two main axes (see B in Fig. 8.1). The collected charges on each of these "half chambers" can be compared in order to study the position and/or the symmetry of the beam along the two main axes. In some accelerators, the comparison of the charges collected on each quadrant, or on the halves of the ionization chambers, automatically controls the position of the beam by means of a feedback system.

The dose to the patient as a function of the operating conditions for a given number of "monitor units" may vary considerably from one type of machine to another. As an example, Table 8.1 gives data for two types of high-energy electron accelerators, A and B. In both cases, the SSD was kept constant in all irradiations.

9. Tests of Constancy of Performance Parameters and Schedules for Such Testing

9.1 Introduction

Modern radiotherapy equipment is complicated and the delivery of the correct dose to the patient requires that the various electrical and mechanical components are performing correctly. Tests should, therefore, be carried out on a routine basis to check these components. All technical checking procedures prescribed by the manufacturer should be followed and, in addition, it may be necessary to establish other routine tests. A log book for recording these measurements should be kept. It is also advisable and helpful to perform direct measurements of absorbed dose on the patients, at least on a sample basis.

9.2 What Should Be Checked and When

9.2.1 Light Beam, Radiation Beam Alignment, Distance Indicators and Mechanical Alignments

A simple check on the light beam should be carried out daily. A white card, on which a square field is drawn, is placed at the normal treatment distance. With use of the numerical field size indicator, a corresponding field size is set up and the light field is compared with the drawing. Without moving the card, this comparison is again performed after the radiation head has been rotated through 180°. It should be checked that the cross-hair light image and the front pointer indicate the center of the light field and that the cross-hair is projected into the back pointer tip.

Checks of agreement between the light beam and the radiation beam should be performed each week and whenever the light-beam bulb is changed. It is often convenient to combine this check with the radiation beam uniformity check.

Mechanical and optical distance pointers should initially be checked daily. If they are found to be stable, they may be checked at longer intervals (weekly) and, again, whenever a projector lamp is replaced.

A thorough alignment test should be performed once a year. Detailed information on relevant procedures is available (HPA, 1970; NACP, 1980; and AAPM, 1975).

9.2.2 Monitor Check

The monitor linearity must be checked as outlined in Section 8 on monitors. In particular, care should be taken that the linearity relationship extends over the whole monitor range to be used. For example, some calibration chambers only measure a total dose that is a fraction of the normal clinical dose, whereas the iron sulfate dosimeter can only measure doses that are factors of 10 or more higher than the clinical doses. Because the chemical dosimeter must be exposed for a long time, there is the possibility of a temperature change in the monitor during the irradiation. The monitoring system should also be checked for leakage, and temperature and pressure effects. This should be done for the periods of time that the monitor is to be used for both calibration and clinical applications.

9.2.3 Absorbed Dose Checks

The initial dose calibration of the accelerator dose monitor, carried out in the standard geometry shown in Fig. 6.1, must be checked regularly. A simplified set-up may be used for these dose checks; for instance, the polystyrene phantom[15] known as the SCRAD phantom shown in Fig. 9.1 (AAPM, 1966) may be used. Measurements should be made at approximately those depths given in Table 6.2. The geometry and the procedure for carrying out checks should be carefully investigated during the initial calibration of a new accelerator. The accelerator should not be used for treatments until such a check program has been put into service. The frequency of the routine dose calibration checks depends on the stability of the machine. It is recommended that the machine be checked once a week at all energies, but if it is found that a variation of more than 3% in the quotient of the absorbed dose at the reference point to that of the monitor reading occurs between measurements, then it should be done more frequently.

The routine calibration should be carried out for the standard field size at each of the electron beam energies. The calibration for other field sizes should be checked by measuring the ratios of the output for the standard field and one or more other field sizes. If differences from the initial calibration are found, the scattering foils, if used, should be checked to make sure that they are in the correct position. In fact, this should be done routinely because misalignment of the scattering foils can affect the dose uniformity and energy as well as the calibration.

[15] Very recent investigations (Galbraith *et al*, 1984; Mattsson and Svensson, 1984) have shown that large errors may be introduced due to charge build-up in insulating phantom material irradiated with electron beams. Thus, a very high electrical field may result between the chamber wall and the internal phantom (see Sec. 2.7.3.3). This electrical field is sufficient to change the direction of some electrons. After irradiation of a polystyrene or PMMA phantom with 50 Gy the error may be several per cent. Therefore, a conductive phantom (e.g., A-150) would be preferable.

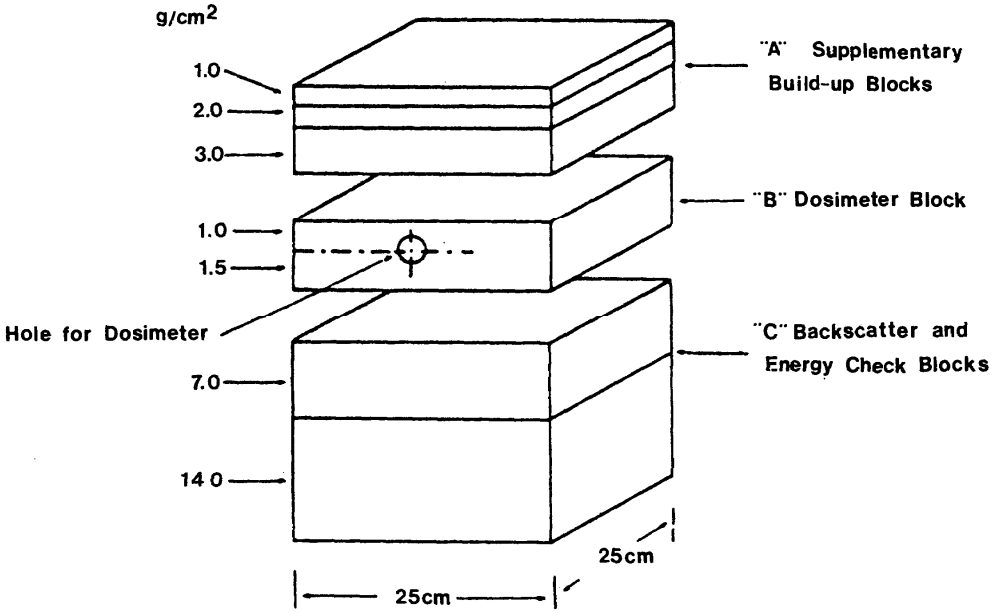

Fig. 9.1. SCRAD calibration phantom (AAPM, 1966)[15].

9.2.4 Energy Check

The method described in the Section 3.3.2.3, for determining the electron beam energy by the range-energy relationship should be used, because it is also necessary to make these measurements to obtain the central axis depth-dose curves. It is also advisable to check the energy on a routine basis (i.e., monthly or when there is an indication of energy shift), but it is not necessary to use the fairly lengthy method described in that section. Several rapid methods have been described (Pohlit, 1965; Almond, 1967; Feldman *et al.*, 1974) which are all based upon the range method. Figure 9.2 illustrates results of a technique using film dosimetry. If an automatic film developer is available, the film technique is probably the most convenient since it takes a minimum of machine time.

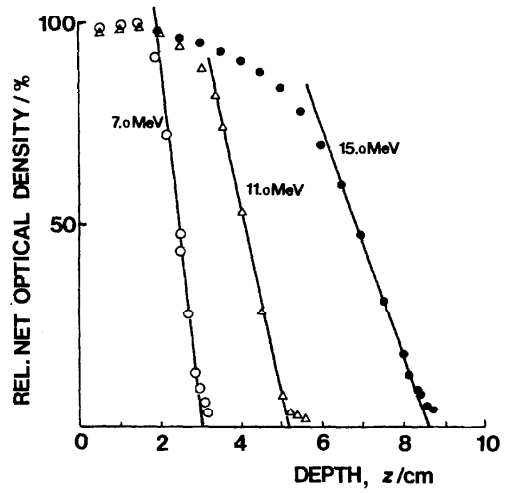

Fig. 9.2. Typical results of central-axis optical density measurements (Feldman *et al.*, 1974) showing how R_{ex} may be determined in order to check the energy (see Fig. 3.18).

9.2.5 Radiation Beam Uniformity Checks

The uniformity should be checked by means of a photographic film method at the reference depth (see Section 6.5.2) as outlined earlier. In each check, at least the maximum optical density of the film and the optical density along the major axes and diagonals of the field should be determined. A full evaluation of the optical density is of great value because the uniformity index may then be determined (see Section 6.5.3 and Fig. 6.11). The check should be made weekly with a cyclic permutation of some relevant irradiation conditions (e.g., beam energy and direction, field size, etc.) so that each combination is checked at least every month.

9.2.6 Contamination and Leakage Measurements

9.2.6.1 X-ray Contamination. The x-ray contamination in the electron beam can be determined by extending the beam axis depth-dose curves beyond the

TABLE 9.1—*Suggested frequency for routine checks on electron accelerators*

Items to be checked	Frequency				
	Daily	Weekly	Monthly	Quarterly	Yearly
Light Beam	X	X (if system is found stable)			
Radiation Beam Alignment		X			
Distance Indicators	X	X (if system is found stable)			
Mechanical Alignments					X
Monitor[a]				X	
Absorbed Dose	X	X (if system is found stable)			
Energy			X		
Beam Uniformity		X			
X-ray Contamination				X	
Leakage					X

[a] This check is to identify small systematic changes in the monitor response (which may not be discovered in the daily absorbed-dose checks) as a function of various parameters, e.g., room temperature, dose rate, and irradiation direction.

practical range of the electrons, where the curve flattens out. This magnitude of absorbed dose, minus the background absorbed dose (with no electron acceleration), gives the absorbed dose due to bremsstrahlung.

9.2.6.2 Neutron Contamination. For electron beam energies above those of the photonuclear reaction threshold (about 10 MeV), neutrons are present (see Section 2.9.4). Since the probability for the electron-induced reactions is approximately one-hundredth of that for the photons, the neutron contamination around an accelerator in the electron mode is much less than in the photon mode (see Section 2.9.5). The neutron contribution to the absorbed dose has been measured at 35 MeV as less than 0.035% of the maximum electron absorbed dose (Pohlit, 1960; Brenner, 1965; Frost and Michel, 1965). Measurements can be made with foil activation techniques or by using dosimeter instruments which have a specifically high and low response for neutrons (ICRU, 1977; NBS, 1979).

Neutrons are also produced in the irradiated tissues, chiefly through (γ,n) reactions due to the bremsstrahlung because the cross-sections for electronuclear reactions are much smaller. These reactions also produce radioactive nuclides (^{15}O, ^{11}C, ^{13}N) which contribute less than 10^{-5} of the maximum electron absorbed dose (Frost and Michel, 1965; Swansson, 1979).

9.2.6.3 Radiation Leakage. Leakage measurements fall into two categories: those to check for anomalous leaks that may require extra shielding and those to determine the absolute leakage. The anomalous leakage can be checked by blocking the primary beam with the collimator or supplemental lead blocks and enclosing the treatment head in film. Any faults in the shielding should appear upon developing the film. For absolute determination of the leakage, ionization chambers, provided with sufficient build-up material for the contaminating x rays, should be used for measurements at 1 meter from the accelerator window.

In general, leakage is not a problem with the electron beam because the accelerator current is reduced considerably below that used in the x-ray mode of operation. If the electron beam becomes misaligned and strikes part of the accelerator internally, it may produce excessive x-ray leakage which must be reduced.

9.2.7 Summary

In order to make sure that treatment machines are operating correctly, the above tests should be performed frequently. The recommended frequency of such tests varies (HPA 1970; AAPM 1975; NACP 1980). The frequency will depend upon the likelihood of a fault developing and also on whether the fault will result in a significant change in the patient dose. It is advisable to start by making the routine checks more frequently than might be considered necessary. If the parameters are found to be stable with time, the frequency can be decreased. If, however, the parameters vary considerably between checks, the frequency should be increased. Table 9.1 summarizes the tests and gives suggested times between measurements.

9.3 Dosimetric Measurements on the Patient

In order to ensure that the patient is receiving the correct absorbed dose, direct measurements on the patient can be made. To detect systematic errors in the irradiation procedure, the measurements should be made at the initial treatment and whenever a treatment parameter is changed. To detect operator and equipment errors, measurements should be made at every treatment. Möller *et al.* (1976) have given a thorough discussion of the possible errors and control of the absorbed dose to the patient for specified therapy procedures. Routine patient dosimetry systems should be reasonably precise and simple to handle. Small condenser ionization chambers (Sievert chambers), thermoluminescent dosimeters (TLD) and small semiconductor detectors with suitable build-up caps can fulfill these requirements.

10. Radiobiological Aspects

10.1 Introduction

At the time of the introduction of high-energy electrons into radiotherapy, there were controversies amongst radiobiologists and radiotherapists about the following problems:

(1) The RBE of high-energy electron beams with respect to conventional or high-energy x-ray beams
(2) the existence of a possible "therapeutic differential effect" (i.e., that the ratio of tumor response to normal tissue response may be different for electron and photon beams)
(3) the practical consequences of the above in radiotherapy, concerning, in particular, when one should use electron beam therapy in preference to photons, and the choice of the type and of the energy of the electron beam accelerators.

It is now generally accepted that these controversies were due, at least partly, to dosimetric difficulties which were not fully understood at that time, as indicated by Sinclair and Kohn (1964).

The situation has been progressively clarified, although it will always remain difficult, when assessing clinical effects, to distinguish what is to be related to the purely "physical" dose distribution and what could be related, specifically, to the radiobiological properties of the electron beams.

The problem of the time-dose distribution (pulsed irradiation, see Section 3.4) in electron therapy has also been raised. At the present time, it can be assumed that biological effects are not significantly modified by the pulsed characteristics of high-energy electron beams for the conditions currently encountered in radiotherapy (Hall, 1978). However, modifications in the biological effects have been observed when large doses were delivered in very short pulses (Hornsey and Alper, 1966; Epp *et al.*, 1968; Hornsey, 1970; Nias *et al.*, 1973; Mill, 1979).

10.2 Survey of the Radiobiological Data

Many experiments have been performed to determine the RBE of high-energy electrons for different types of accelerators, different beam energies, and different biological systems and biological effects under differing experimental conditions such as various absorbed-dose levels, various levels of oxygenation, etc. The results have been reviewed and discussed by several authors (Sinclair and Kohn, 1964; Wambersie, 1967, 1971; Linden, 1972; Dutreix and Wambersie, 1981).

Almost all of the radiobiological experiments carried out after 1960 on biological effects relevant in radiotherapy put the RBE of high-energy electrons in the narrow range of 0.8–0.9 with respect to conventional x rays (≈150–250 kV). Data obtained for the inactivation of microorganisms or mammalian cells, and for survival in mammals, are presented in Table 10.1.

However, it should be pointed out that for some biological effects other than cellular lethality (e.g., chromosome aberrations and tumor induction) and especially for small doses, lower RBE's have been observed for high-energy electrons (as well as high-energy photons) with respect to conventional x rays (Schmid *et al.*, 1974; Lloyd *et al.*, 1975; Barendsen, 1978). These are consistent with radiobiological expectations at small doses (NCRP, 1980) and are not applicable to radiotherapeutic situations.

Although it has been the custom to use conventional x rays as the reference radiation for RBE (ICRP-ICRU, 1962), a reference based upon high-energy photons would be more sensible in modern radiotherapy. Relatively few direct comparisons have been made, but all indicate an RBE value close to unity for high-energy electrons with respect to cobalt-60 gamma rays or high-energy x rays (Table 10.2).

The experiments mentioned above were made in the plateau region of the depth-dose curve, where the dose is constant over the volume in which the biological system is positioned. However, the electron spectrum varies as a function of depth and the possibility that this variation could modify the biological effects has been examined. Meaningful experiments are particularly difficult to perform due to the steep dose gradient and, thus, only biological systems which can be irradiated in thin layers can be used. Furthermore, the variation with depth of the response of some detectors (e.g., gas-filled ionization chambers) presents additional difficulties.

The variation of RBE as a function of depth in the irradiated medium has been investigated for electron beams of different initial energy (Table 10.3). Only data obtained with $FeSO_4$ as the reference dosimeter have been included. It can be assumed that the response of the $FeSO_4$ does not vary as a function of depth and that the dosimeter solution can occupy the same volume as the biological samples.

The more recent experimental results do not indicate any significant variation of RBE with depth (Table 10.3). Furthermore, experiments on chromosome aberrations in Allium cepa (which was proven to be a system very sensitive to a change in radiation quality) did not show any significant RBE variation in the first millimeters of the irradiated medium, i.e., between the "surface" and the maximum of the depth-dose curve, for a 15-MeV electron beam. Observation of skin reactions in patients lead to the same conclusion (Wambersie *et al.*, 1974).

It can be concluded from the available radiobiological data:

TABLE 10.1—*RBE of high energy electrons compared to conventional x rays*

Biological System and Effect	Initial Electron Energy/ MeV	Reference Radiation Quality	RBE	References
Bacteria inactivation	20	180 kV x rays (HVL = 0.8 mm Cu)	0.82 ± 0.01	Leskowitz *et al.* (1960)
Chick embryo survival	20	250 kV x rays (HVL = 2 mm Cu)	0.82 ± 0.04	Copper *et al.* (1962)
Yeast inactivation	20	180 or 250 kV x rays	0.82 or 1[a]	Mookerjee *et al.* (1964)
$LD_{50/30}$ in mice	35	230 kV x rays (HVL = 2 mm Cu)	0.79	Schulz *et al.* (1963)
$LD_{50/30}$ in mice	15	250 kV x rays	0.86	Ward (1964)
HeLa cell survival	15	200 kV x rays	0.61 – 0.85[b]	Marquardt and Markus (1965)
Yeast inactivation	30	200 kV x rays (HVL = 1.2 mm Cu)	0.88 ± 0.03	Hettinger *et al.* (1965)
Bacteria inactivation	20	260 kVp x rays (HVL = 0.9 mm Cu)	0.89 ± 0.03	Wambersie (1967); Wambersie and Dutreix, (1971)—revised value.
Survival of human bladder cells	35	300 kVp x rays HVL = 2 mm Cu	0.87	Robinson and Erwin (1969)

[a] Depending on experimental conditions.
[b] Depending on absorbed dose level.

TABLE 10.2—*RBE of high-energy electrons compared to high-energy photons*

Biological System and Effect	Initial Electron Energy/ MeV	Reference Radiation Quality	RBE	References
Yeast inactivation	30	Cobalt 60	1.04 ± 0.03	Hettinger *et al.* (1965)
Bacteria inactivation	20	Cobalt 60	1.06 ± 0.02	Wambersie (1967); Wambersie and Dutreix (1971) —revised values
Yeast inactivation	20	Cobalt 60	1.02 ± 0.08	Wambersie (1967); Wambersie and Dutreix (1971) —revised values
$LD_{50/30}$ in mice	20	21 MV x rays	0.98 ± 0.03	Wambersie (1967); Wambersie and Dutreix (1971) —revised values
Colony forming units in mice	20	21 MV x rays	1.01 ± 0.05	Wambersie (1967); Wambersie and Dutreix (1971) —revised values
$LD_{50/4}$ in mice	20	21 MV x rays	1.04 ± 0.05	Wambersie (1967); Wambersie and Dutreix (1971) —revised values
$LD_{50/4.5}$ in mice	35	Cobalt 60	1.01 ± 0.05	Wambersie *et al.* (1971)
Tail necrosis in mice	10	Cobalt 60	0.96 ± 0.05	Williams and Hendry (1978)
	3	4 MV x rays	1.02 ± 0.06	

(1) that there is no clinically significant difference in RBE between high-energy electrons, cobalt-60 gamma rays and high-energy x rays (for the energies at present used in radiotherapy). An RBE of 0.85 can be assumed for high-energy electrons with respect to conventional x rays (180–300 kV) for the biological systems and biological effects relevant in radiotherapy.

(2) that no therapeutic differential effect is expected between these radiation qualities.

(3) that there is no clinically significant variation of RBE as a function of depth in an electron beam.

Systematic clinical studies (Haas *et al.*, 1954; Ward, 1964; Flamant *et al.*, 1967; Dutreix, 1968; Eschwege and Dutreix, 1969; Wambersie *et al.*, 1974), as well as the general clinical impression (Tapley, 1973; Fletcher,

TABLE 10.3—*Variation of RBE for electron beams as a function of depth in the irradiated medium: reference dosimeter; $FeSO_4$*

Biological System and Effect	Initial Electron Energy/ MeV	Isodose	RBE	References
Bacteria	20	100 %	1.00 (reference)	Wambersie (1967)
inactivation		95 %	1.02 ± 0.03	Wambersie and
		83 %	1.01 ± 0.03	Dutreix (1971)
		37 %	0.99 ± 0.02	
		24 %	0.98 ± 0.02	
Yeast inactivation	20	100 %	1.00 (reference)	
		80 %	1.00 ± 0.05	
		37 %	0.97 ± 0.11	
HeLa cell	14	100 %	No significant	Fehrentz (1968)
survival		20 %	difference	
	5	100 %		
		45 %		
Survival of	35	100 %	1.00 (reference)	Robinson and Erwin (1969)
human bladder cells		41 %	1.01	
		23 %	0.99	
		9 %	1.00	
HeLa cell survival	20	100 %	No significant	Kim *et al.* (1969)
		25 %	difference[a]	
Chromosome aberrations	15	100 %	No significant	Wambersie *et al.* (1972)
in Allium cepa		33 %	difference[b]	
	15	100 %	1.00 (reference)	Wambersie *et al.* (1973)
		(10.5 mm in depth)		
		"Surface"	0.97 ± 0.08	
		(1.mm in depth)		

[a] No significant RBE difference for survival level, early recovery capacity, or clone size distribution.

[b] No significant RBE difference was found in any of the experimental conditions or endpoints:—incubation time after irradiation: 3, 6, or 9 hours—cells scored in anaphase or telophase—endpoint: average number of aberrations per cell or percentage of intact cells. Confidence interval (P = 0.05) estimated 10–15%.

1976; Ho *et al.*, 1976; Dutreix and Wambersie, 1981), support these radiobiological conclusions.

10.3 Theoretical Considerations

The experimental measurements of Schulz and Harder (1969) and the computations of Berger and Seltzer (1969a) and Nahum (1976) have shown that below about 0.1 MeV, the electron fluence spectrum per unit absorbed dose varies only extremely slowly with initial electron beam energy and depth. Figure 10.1 indicates that cobalt-60 gamma rays and high-energy x rays have low-energy electron spectra that are very similar to those for electron beams, whereas the number of low-energy electrons is somewhat higher for conventional x rays. It would thus appear that the differences in the biological effects of these radiations may be predicted from differences in the electron spectra at the lowest energies. However, recent slowing-down calculations by Hamm *et al.* (1978) may cast doubt on this conclusion (see Section 2.4.4).

Microdosimetric measurements have provided a further confirmation of the radiobiological and clinical data. In particular, no significant RBE differences

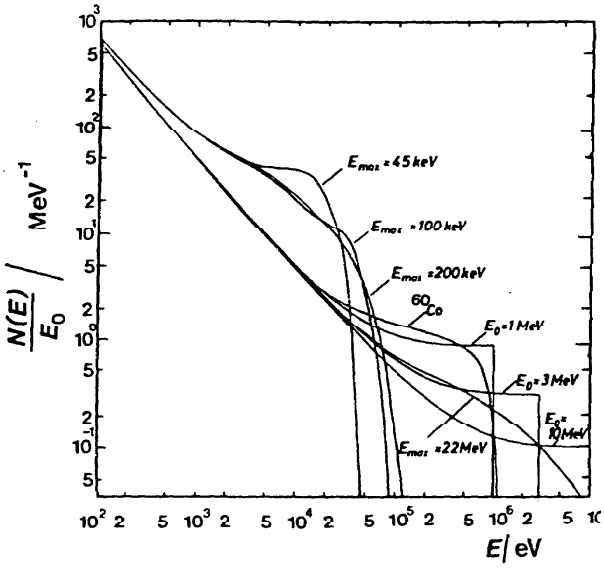

Fig. 10.1. Calculated slowing down spectra in water. $N(E)/E_0$ is the number of electrons passing the energy E in the course of slowing down, for an incident electron of energy E_0, or a photon-generated electron spectrum of maximum energy E_{max} and total energy E_0 (from Harder, 1970a).

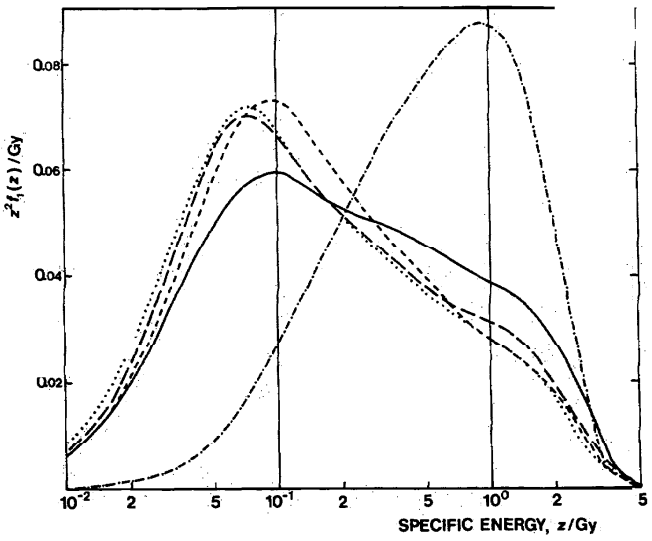

Fig. 10.2. Single-event specific-energy distributions measured in five different beams, at the maximum of the depth-dose curves: cobalt-60 gamma rays (—), 180 kV x rays with HVL = 0.9 mm Cu (· — · — ·), 39 MeV e^- (- - - -), 8 MeV e^- (·····), 42 MV x rays (– – – –). The distributions are normalized per logarithmic interval and thus equal areas under the curve will contribute equally to the specific energy (from Lindborg, 1976 and Lindborg, private communication, 1980).

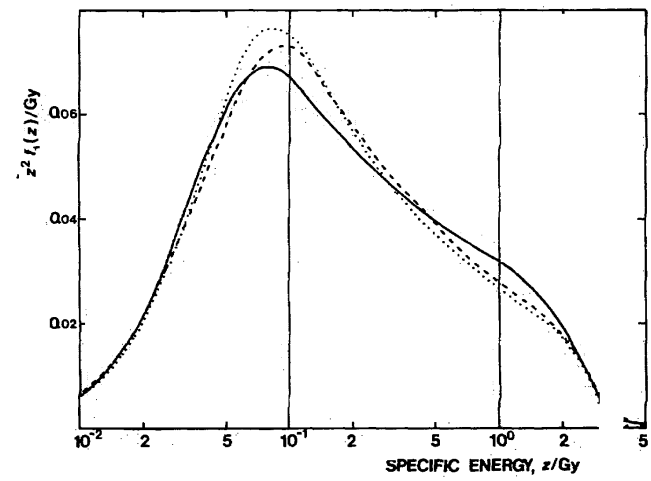

Fig. 10.3. Single-event specific-energy distributions measured in an electron beam with most probable energy at the phantom surface $E_{p,0}$ = 15 MeV at different depths in the irradiated phantom: 0.5 g cm^{-2}, percentage depth-dose level 97% (·····); 2.4 g cm^{-2}, percentage depth-dose level 100% (- - - -); 5.7 g cm^{-2}, percentage depth-dose level 66% (—). The normalizations are the same as in Fig. 10.2 (from Lindborg, 1976).

should be expected between beam qualities having similar microdosimetric characteristics.

Figure 10.2 compares the single-event specific-energy[16] distributions in small spherical volumes (diameter 1 μm) irradiated with high-energy electrons, high-energy and conventional x rays and cobalt-60 gamma rays (from Lindborg, 1976). The spectra are very similar for electrons, high-energy x rays and co-

[16] The specific energy (imparted) is defined in ICRU Report 33 (ICRU, 1980) as the quotient of energy imparted by ionizing radiation to matter by the mass of that matter.

TABLE 10.4—*Comparison of data pairs* ($\bar{y}_F$, $\bar{y}_D$) *for 1 μm diameter spherical site of unit density material (from Booz, 1978)*

Radiation Quality	$\bar{y}_F$/keV μm^{-1}	$\bar{y}_D$/keV μm^{-1}
200 kV x rays (5 mm Al + 1 mm Cu)	1.52	4.20
250 kV x rays (1.77 mm Al)	1.22	3.79
^{137}Cs	0.37	1.85
^{60}Co	0.28	1.59
42 MV x rays	0.30	2.08
Electrons $\bar{E}_0$ = 39 MeV	0.30	1.81
$\bar{E}_0$ = 15 MeV	0.30	1.95
$\bar{E}_0$ = 8 MeV	0.26	1.86

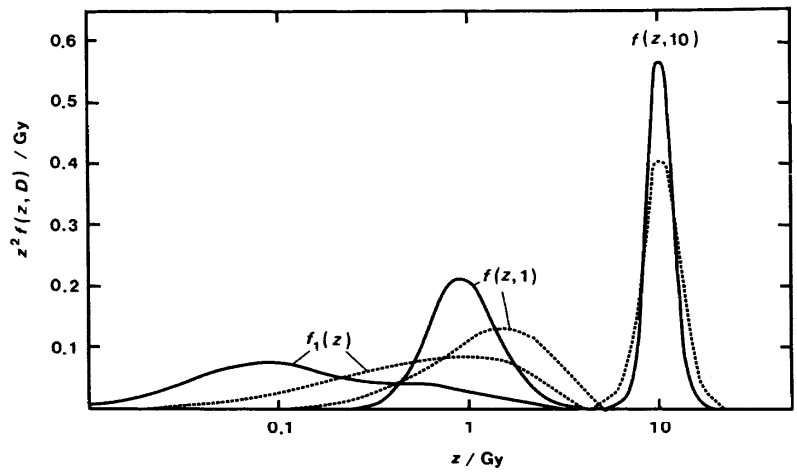

Fig. 10.4. Single-event spectra, $f_1(z)$, and multiple-event specific-energy distributions for 1 and 10 Gy, calculated from experimentally-determined single-event distributions (see Fig. 10.2). The solid lines pertain to 8-MeV electrons, for which the mean number of events is 15 and 148 at 1 and 10 Gy, respectively. The dotted lines pertain to 180-kV x rays with HVL = 0.9 mm Cu. In this case, the mean number of events are 4 and 44, respectively. The normalization of the single-event distributions is the same as in Fig. 10.2. The dose-dependent distributions are normalized to the same area as that of the single-event distributions.

balt-60 gamma rays, whereas the spectrum for conventional x rays is shifted towards higher specific energies.

The specific-energy distributions obtained at various depths in an electron beam with initial energy of 15 MeV are compared in Fig. 10.3. Again, the spectra are very similar and, consequently, no significant RBE difference with depth should be expected in high-energy electron beams.

Table 10.4 presents the track mean lineal energy, $\bar{y}_F$, and the dose mean lineal energy, $\bar{y}_D$, for the radiation qualities that have been considered. As can be expected from the spectra (Figs. 10.2 and 10.3), the values of $\bar{y}_F$ and $\bar{y}_D$ are each very nearly constant for high-energy photons and electrons. They differ significantly from those for 200–250 kV x rays. It should be noted, however, that such differences in energy deposition occur for single events only. At absorbed doses of the order of those employed in radiotherapy, a multiplicity of electrons traverse the cell (or sub-cellular structures) and differences in energy concentrations are, therefore, much less. Consequently, the RBE of high-energy electrons or photons is smaller than (about 0.85) rather than equal to, the ratio of the applicable single-event $\bar{y}_D$ values (about 0.5). At very low doses the 0.5 value seems appropriately applicable.

This effect is illustrated further in Fig. 10.4 by the specific-energy distribution for electrons and conventional x rays in a 1-μm diameter volume at absorbed doses of 0.01, 1.0, and 10 Gy. At 0.01 Gy the single event spectra are obtained, whereas at 1 and 10 Gy, the higher multiplicity of events reduces the differences between the curves. Furthermore, as the differences are small at this diameter, they will differ even less for larger volumes.

10.4 Conclusions: Implications in Radiotherapy

All the radiobiological, clinical and dosimetric data presently available indicate that there is no clinically significant RBE difference between high-energy electrons, high-energy x rays (for the energy range at present used in therapy) and cobalt-60 gamma rays. This implies that the relative advantage of high-energy electrons, compared to high-energy x rays or cobalt-60 gamma rays, is due only to their respective absorbed dose distributions. At equal absorbed dose levels, the biological effects are similar, and no therapeutic differential effect can be expected.

In practical radiotherapy, as recommended in ICRU Report 29 (ICRU, 1978b), no conversion factor is needed when adding absorbed doses from high-energy photon and electron beams. However, one does have to take into account the RBE differences between high-energy electrons (or high-energy x rays and cobalt-60 gamma rays) and conventional x rays. In order to do this, absorbed dose values of conventional x rays should be multiplied by 1.18 (= 1/0.85) when their radiotherapeutic effects are compared with those of high-energy electrons or photons (ICRU, 1978).

References

AAPM (1966). American Association of Physicists in Medicine, "Protocol for the dosimetry of high energy electrons," Phys. Med. Biol. **11,** 505.

AAPM (1975). American Association of Physicists in Medicine, "Code of practice for x-ray therapy linear accelerators," Med. Phys. **2,** 110.

ABOU-MANDOUR, M. (1978). *Analyse des Durchgangs Energiereiche Elektronen Durch Räumlich Begrenzte und Inhomogene Medien Mit Hilfe der Monte-Carlo-Methode*, Thesis, University of Würzburg, Germany.

ABOU-MANDOUR, M. and HARDER, D. (1975). "Scheinbare Reflexion schneller Elektronen bei streifendem Einfall," Z. Naturforsch. **30a,** 265.

ABOU-MANDOUR, M. and HARDER, D. (1978a). "Systematic optimization of the double-scatterer system for electron beam field-flattening," Strahlentherapie **154,** 328.

ABOU-MANDOUR, M. and HARDER, D. (1978b). "Berechnung der Dosisverteilung schneller Elektronen in und hinter Gewebeinhomogenitäten beliebiger Breite II," Strahlentherapie **154,** 546.

ADAWI, I. (1957). "Penetration of electron beams into water below the critical energy," Phys. Rev. **107,** 1476.

ALBURGER, D. E. (1972). "Half life of ^{14}O," Phys. Rev. **C5,** 274.

ALMOND, P. R. (1967). "The physical measurements of electron beams from 6 to 8 MeV: Absorbed dose and energy calibration," Phys. Med. Biol. **12,** 13.

ALMOND, P. R. (1970). "The use of ionization chambers for the absorbed dose calibration of high energy electron beam therapy units," Int. J. Appl. Radiat. Isot. **21,** 1.

ALMOND, P. R. (1976). "Dosimetry considerations of electron beams," p. 131 in *High-energy Photons and Electrons: Clinical Applications in Cancer Management*, Kramer, S., Suntharalingam, N. and Zinninger, G., Eds. (John Wiley and Sons, Inc., New York).

ALMOND, P. R. (1981). "Characteristics of current medical electron accelerator beams," p. 43 in *Proceedings of the Symposium on Electron Beam Therapy*, Chu, F. C. H. and Laughlin, J. S. Eds. (Memorial Sloan Kettering, New York).

ALMOND, P. R. and SVENSSON, H. (1977). "Ionization chamber dosimetry for photon and electron beams," Acta Radiol. Ther. Phys. Biol. **16,** 177.

ALMOND, P. R., WRIGHT, B. S. and BOONE, M. L. M. (1967a). "High-energy electron dose perturbations in regions of tissue heterogeneity," Radiology **88,** 1146.

ALMOND, P. R., WRIGHT, A. and LONTZ, J. F. (1967b). "The use of lithium fluoride thermoluminescent dosimeters to measure the dose distribution of a 15 MeV electron beam," Phys. Med. Biol. **12,** 389.

ALMOND, P. R., MENDEZ, A. and BEHMARD, M. (1978). "Ionization-chamber-dependent factors for calibration of megavoltage x-ray and electron beam therapy machines," p. 271 in *National and International Standardization of Radiation Dosimetry Vol. II*, IAEA Publication STI/PUB/471 (International Atomic Energy Agency, Vienna).

ANDERSON A. R. (1962). "A calorimetric determination of the oxidation yield of the Fricke dosimeter at high dose rates of electrons," J. Phys. Chem. **66,** 180.

ANDREO, P. (1980). "Monte-Carlo simulation of electron transport in water," FANZ 80-3 (Dept. of Nuc. Phys., Univ., Zaragoza, Spain).

ANDREO, P. and BRAHME, A. (1981). "The mean energy in electron beams," Med. Phys. **8,** 682.

ARMSTRONG, W. and TATE, P. A. (1965). "Accuracy of approximate solutions for currents in a plane parallel ion chamber," Phys. Med. Biol. **10,** 229.

ASHLEY, J. C. (1982). "Density effect in liquid water," Radiat. Res. **89,** 32.

ATTIX, F. H., DE LA VERGNE, L. and RITZ, V. H. (1958). "Cavity ionization as a function of wall material," J. Res. Nat. Bur. Std. **60,** 235.

AUCOUTURIER, J., HUBER, H. and JAOUEN, J. (1970). "Système de transport du faisceau d'électrons dans le sagittaire," Rev. Tech. Thomson—C.S.F. **2,** 655.

BADWAR, G. D. (1973). "Calculation of the Vavilov distribution allowing for electron escape from the absorber," Nucl. Instrum. Methods **109,** 119.

BAGNE, F. (1978). "Adjacent fields of high-energy x-rays and electrons: flat surface," Phys. Med. Biol. **23,** 1186.

BANFORD, A. P. (1966). *The Transport of Charged Particle Beams*, (Spon, London).

BANKVALL, G. and LIDÉN, K. (1977). "Interface effects and cavity theory at TLD-measurements," p. 201 in *Book of Abstracts of XIII International Congress of Radiology.*

BARBER, W. C. (1955). "Specific ionization by high-energy electrons." Phys. Rev. **97,** 1071.

BARBER, W. C. and GEORGE, W. D. (1959). "Neutron yields from targets bombarded by electrons," Phys. Rev. **116,** 1551.

BARENDSEN, G. W. (1978). "RBE-LET relations for induction of reproductive death and chromosome aberrations in mammalian cells," p. 55 in *Sixth Symposium on Microdosimetry, Brussels*, Vol. I, Booz, J. and Ebert, H. G., Eds., (Harwood Academic Publishers Ltd., London).

BARKAS, W. H., BARRETT, P. H., CUER, P., HECKMAN, H., SMITH, F. M. and TICHE, H. K. (1958). "The range-energy relation in emulsion," Nuovo

Cimento 8, 186.

BARNARD, G. P., AXTON, E. J. and MARSH, A. R. S. (1962). "On the use of roentgen-calibrated cavity-ionization chambers in tissue-like phantoms to determine absorbed dose," Phys. Med. Biol. **7**, 229.

BARTINE, D. E., ALSMILLER, R. G., MYNATT, F. R., ENGEL, W. W. and BARISH, J. (1972). "Low energy electron transport by the method of discrete ordinates," Nucl. Sci. Eng. **48**, 159.

BEATTIE, J. W., TSIEN, K. C., OVADIA, J. and LAUGHLIN, J. S. (1962). "Production and properties of high energy electrons for therapy," Am. J. Roentgenol. **88**, 235.

BECKURTS, K. H. and WIRTZ, K. (1964). *Neutron Physics* (Springer Verlag, Berlin).

BENDEL, W. L., MCELHINNEY, J. and TOBIN, R. A. (1958). "Photoneutron reactions in N, O, F, Cu, Ag, and In," Phys. Rev. **111**, 1297.

BENEDETTI, G. R. (1973). *Die modifizierenden Parameter der Dosisverteilung schneller Elektronen bei hohen Anfangsenergien.* Thesis, University of Würzburg, Germany.

BERGER, M. J. (1963). "Monte-Carlo-calculations of the penetration and diffusion of fast charged particles, II," p. 135 in *Methods in Computational Physics*, Aloer, B., Fernbach, S. and Rotenberg, M., Eds. (Academic Press, Inc., New York).

BERGER, M. J. (1969). *ETRAN Monte Carlo Code System for Electron and Photon Transport Through Extended Media*, CCC-107, Oak Ridge Nat. Lab., Oak Ridge, Tenn.

BERGER, M. J. (1979). Private communication.

BERGER, M. J. (1980). Work commissioned by ICRU Electron Report Group.

BERGER, H. and PAUL, W. (1949). "Verteilung der Ionisationsdichte in einem mit schnellen Elektronen bestrahlten KCl-Kristall," Z. Phys. **126**, 422.

BERGER, M. J. and SELTZER, S. M. (1964). *Tables of Energy Losses and Ranges of Electrons and Positrons*, NASA SP-3012 (National Aeronautics and Space Administration, Washington, D.C.).

BERGER, M. J. and SELTZER, S. M. (1966). *Additional Stopping Power and Range Tables for Protons, Mesons, and Electrons*, NASA SP-3036 (National Aeronautics and Space Administration, Washington, D.C.).

BERGER, M. J. and SELTZER, S. M. (1969a). "Quality of radiation in a water medium irradiated with high-energy electron beams," p. 127 in *Book of Abstracts of XII International Congress of Radiology.*

BERGER, M. J. and SELTZER, S. M. (1969b). "Calculation of energy and charge deposition and of the electron flux in a water medium bombarded with 20 MeV electrons," Ann. N.Y. Acad. Sci. **161**, 8.

BERGER, M. J. and SELTZER, S. M. (1970). "Bremsstrahlung and photo neutrons from thick tungsten and tantalum targets," Phys. Rev. **C2**, 621.

BERGER, M. J. and SELTZER, S. M. (1978). *The Influence of Scattering Foils on Absorbed Dose Distributions from Electron Beams*, NBSIR 78-1552 (National Bureau of Standards, Washington, D.C.).

BERGER, M. J. and SELTZER, S. M. (1982). *Stopping Power and Ranges of Electrons and Positrons*, NBSIR 82-2550 (National Bureau of Standards, Washington, D.C.).

BERGER, M. J., SELTZER, S. M., DOMEN, S. R. and LAMPERTI, P. J. (1975). "Stopping power ratios for electron dosimetry with ionization chambers," p. 589 in *Biomedical Dosimetry*, IAEA Publication STI/PUB/401 (International Atomic Energy Agency, Vienna).

BERGERE, R., DELEZENNE, E. and VEYSSIERE, A. (1962). "Etude de moniteurs de courant pour un accelerateur lineaire," Nucl. Instrum. Methods **15**, 327.

BERMAN, B. L. (1976). *Atlas of Photoneutron Cross Section Obtained by Monoenergetic Photons*, UCRL-78482 (University of California, Livermore).

BERRY, R. J. and ORTON, C. G. (1966). "Reference perspex radiation dosemeter," Phys. Med. Biol. **11**, 475.

BERRY, R. J. and MARSHALL, C. H. (1969). "Clear perspex H. X. as a reference dosemeter for electron and gamma radiation," Phys. Med. Biol. **14**, 585.

BERTILSSON, G. (1975). *Electron Scattering Effects on Absorbed Dose Measurements with LiF-Dosimeters*, Thesis, University of Lund, Sweden.

BESS, L. and HANSON, A. O. (1948). "Measurement of the electron current in a 22 MeV betatron," Rev. Sci. Instrum. **19**, 108.

BESS, L., OVADIA, J. and VALASSIA, F. (1959). "External beam current monitor for linear accelerators," Rev. Sci. Instrum. **30**, 985.

BETHE, H. (1933). "Quantenmechanik der Ein- und Zweielektronenprobleme," p. 273 of *Handbuch der Physik 24/1, Quantentheorie*, Geiger, H. and Scheel, K., Eds. (Springer-Verlag, Berlin).

BETHE, H. A. and HEITLER, W. (1934). "Stopping of fast particles and creation of electron pairs," Proc. R. Soc. London Ser. A. **146**, 83.

BETHE, H. A., ROSE, M. E. and SMITH, L. P. (1938). "The multiple scattering of electrons," Proc. Am. Philos. Soc. **78**, 573.

BEWLEY, D. K. (1971). "Collector monitors for electron beams," Phys. Med. Biol. **16**, 131.

BEWLEY, D. K., MCCULLOUGH, E. C., PAGE, B. C. and SAKATA, S. (1972). "Heat defect in tissue-equivalent radiation calorimeters," Phys. Med. Biol. **17**, 95.

BIRKHOFF, R. D. (1958). "The passage of fast electrons

through matter," p. 53 in *Encyclopedia of Physics*, Vol. 34, Flügge, S., Ed. (Springer-Verlag, Berlin).

BJÄRNGARD, B. E. and JONES, D. (1968). "Experience with a new thermoluminescence method for finger and hand dosimetry employing lithium fluoride teflon dosimeters," p. 473 in *Proceedings of the First International Congress of Radiation Protection*, Snyder, W. S., Abee, H. H., Burton, L. K., Marshart, R., Benco, A., Duhamel, F. and Wheatley, B. M., Eds. (Pergamon Press, Oxford).

BJÄRNGARD, B. E., PIONTEK, R. W. and SVENSSON, G. K. (1976). "Electron scattering and collimation system for a 12-MeV linear accelerator," Med. Phys. **3,** 153.

BJÄRNGARD, B. E., CHEN, G. T. Y., PIONTEK, R. W. and SVENSSON, G. K. (1977). "Analysis of dose distribution in whole body superficial electron therapy," Int. J. Radiat. Oncol. Biol. Phys. **2,** 319.

BLANC, D., MATHIEU, J., VERMANDE, P. and TORRES, L. (1965). "Sur la Possibilité de Mesurer le Facteur de Qualité des Rayonnements Nucléaires au Moyen de Chambres d'Ionisation Remplies d'un Liquide Dielectrique," Health Physics **11,** 63.

BLUNCK, O. and LEISEGANG, S. (1950). "Zum Energieverlust schneller Elektronen in dünnen Schichten," Z. Phys. **128,** 500.

BLUNCK, O. and WESTPHAL, K. (1951). "Zum Energieverlust energiereicher Elektronen in dünnen Schichten," Z. Phys. **130,** 641.

BOAG, J. W. (1950). "Ionization measurements at very high intensities. I. Pulsed radiation beams," Br. J. Radiol. **23,** 601.

BOAG, J. W. (1956). "Ionization Chambers," p. 153 in *Radiation Dosimetry*, Hine, J. H. and Brownell L. B., Eds. (Academic Press, Inc., New York).

BOAG, J. W. (1964). "Distortion of the electric field in an ionization chamber due to a difference in potential between guard ring and collector," Phys. Med. Biol. **9,** 25.

BOAG, J. W. (1966). "Ionization chambers," p. 1 of *Radiation Dosimetry*, Vol. II, Attix, F. H., Roesch, W. C. and Tochilin, E., Eds. (Academic Press, Inc., New York).

BOAG, J. W. and LILLICRAP, S. C. (1972). "Dose distribution in high energy electron beams," in *Digest of the Third International Conference on Medical Physics, Including Medical Engineering* (Chalmers, University of Technology, Göteborg, Sweden).

BOAG, J. W. and CURRANT, J. (1980). "Current collection and ionic recombination in small cylindrical ionization chambers exposed to pulsed radiation," Br. J. Radiol. **53,** 471.

BOAG, J. W. and WILSON, T. (1952). "The saturation curve at high ionization intensity," Br. J. Appl. Phys. **3,** 222.

BOAG, J. W., DOLPHIN, G. W. and ROTBLAT, J. (1958). "Radiation dosimetry by transparent plastics," Radiat. Res. **9,** 589.

BOONE, M. L. M., CROSBY, H. E. and SHALEK, R. J. (1965). "Skin reactions and tissue heterogeneity in electron beam therapy Part II: In vivo dosimetry," Radiology **84,** 817.

BOONE, M. L. M., JARDINE, J. H., WRIGHT, A. E. and TAPLEY, N. (1967). "High energy electron dose perturbation in regions of tissue heterogeneity Part I: In vivo dosimetry," Radiology **88,** 1136.

BOOZ, J. (1978). "Mapping of fast neutron radiation quality," p. 499 in *Proceedings Third Symposium on Neutron Dosimetry in Biology and Medicine*, Burger, G. and Ebert, H. G., Eds. (Commission of the European Communities, Luxembourg).

BOUTILLON, M. (1977). "Some remarks concerning the measurement of kerma with a cavity ionization chamber," Bureau International des Poids et Mesures, Document CCEMRI(I)/77-114.

BOUTILLON, M. and NIATEL, M. T. (1973). "A study of a graphite cavity chamber for absolute exposure measurements of ^{60}Co gamma rays," Metrologia **9,** 139.

BRADSHAW, A. L. (1965). "Calorimetric measurement of absorbed dose with 15 MeV electrons," Phys. Med. Biol. **10,** 355.

BRADSHAW, A. L. and MAYSENT, A. M. (1964). "Physical aspects of electron therapy using a 15 MeV linear accelerator," Br. J. Radiol. **37,** 219.

BRAGG, W. H. (1912) p. 94 in *Studies in Radioactivity* (Macmillan, New York).

BRAHME, A. (1971). *Multiple Scattering of Relativistic Electrons in Air*, TRITA-EPP 71-22 (Royal Inst. Technology, Stockholm, Sweden).

BRAHME, A. (1972). *On the Optimal Choice of Scattering Foils for Electron Therapy*, TRITA-EPP 72-17 (Royal Inst. of Technology, Stockholm, Sweden).

BRAHME, A. (1975). *Simple Relations for the Penetration of High Energy Electron Beams in Matter*, SSI: 1975-011, Dep. Radiation Physics, Karolinska Institutet, Stockholm, Sweden.

BRAHME, A. (1977). "Electron transport phenomena and absorbed dose distributions in therapeutic electron beams," p. 198 in *Book of Abstracts of XIV International Congress of Radiology.*

BRAHME, A. (1978). "Physical aspects of equipment for external beam radiation therapy," p. 20 in *Symposium on Precision Demands in External Radiotherapy*, Svensk, förening för radiofysik Ed. (available from Radiation Physics Department, University of Umeå, Umeå, Sweden)

BRAHME, A. (1981). "Correction of a measured distribution for the finite extension of the detector," Strahlentherapie **157,** 258.

BRAHME, A. and SVENSSON, H. (1976a). "Specification

of electron beam quality from the central-axis depth absorbed-dose distribution," Med. Phys. **3,** 95.

BRAHME, A. and SVENSSON, H. (1976b); "Methods of improving dose uniformity in high energy photon and electron beams," Digest 4th ICMP, Phys. Canada **32,** 28.3.

BRAHME, A. and SVENSSON, H. (1979). "Radiation beam characteristics of a 22 MeV microtron," Acta Radiol. Oncol. **18,** 244.

BRAHME, A. and SVENSSON, H. (1980). "Electron beam quality parameters and absorbed dose distributions from therapy accelerators," p. 12 in *High Energy Electrons in Radiation Therapy*, Zuppinger, A., Bataini, J. P., Irigaray, J. M. and Chu, F., Eds. (Springer-Verlag, Berlin).

BRAHME, A., HULTÉN, G. and SVENSSON, H. (1975). "Electron depth dose distribution for a 10 MeV clinical microtron," Phys. Med. Biol. **20,** 39.

BRAHME, A., KRAEPELIEN, T. and SVENSSON, H. (1980a). "Electron and photon beams from a 50 MeV racetrack microtron," Acta Radiol. Oncol. **19,** 305.

BRAHME, A., MONTELIUS, A., NORDELL, B., REUTHAL, M. and SVENSSON, H. (1980b). "Investigation of the possibility of using photoneutron beams for radiation therapy," Phys. Med. Biol. **25,** 1111.

BRAHME, A., LAX, J. and ANDREO, P. (1981). "Electron beam dose planning using discrete gaussian beams: Mathematical background," Acta Radiol. Oncol. **21,** 147.

BREITLING, G. and SEEGER, W. (1963). "Zur Filmdosimetrie schneller Elektronen," Strahlentherapie **122,** 483.

BREITLING, G. and VOGEL, K. H. (1965). "Über der Einfluss der Streuung auf den Dosisverlauf schneller Elektronen," p. 20 in *Symposium on High-Energy Electrons*, Zuppinger, A. and Poretti, G., Eds. (Springer-Verlag, Berlin).

BRENNER, M. (1965). "Neutron contamination of electron beams," p. 153 in *Symposium on High-Energy Electrons*, Zuppinger, A. and Poretti, G., Eds., (Springer-Verlag, Berlin).

BREUER, H. (1964). "Energieverlust von Elektronen in Aluminium in Energiebereich 20 bis 60 MeV," Z. Phys. **180,** 209.

BREUER, H. and POHLIT, W. (1962). "Der (γ, 2n)-Prozess in ^{16}O von 28.9 bis 32.5 MeV," Nucl. Phys. **30,** 417.

BREUER, H., HARDER, D. and POHLIT, W. (1958). "Zur Energie-Reichweite-Beziehung für monoenergetische schnelle Elektronen," Z. Naturforsch. **13a,** 567.

BRIOT, E. (1982) *Etude Dosimétrique et Comparaison des Faisceaux d'Électrons de 4 à 32 MeV issus de 2 Types d'Accélérateurs Lineaires avec Balayage et Diffusion Multiple.* Thesis, University of Toulouse, France.

BRIOT, E. and DUTREIX, A. (1976). "Dosimetrie des faisceaux d'électrons de haute energie d'un accélérateur linéaire," J. Radiol. Electrol. **57,** 447.

BRIOT, E., DUTREIX, A., DUTREIX, J. and PENET, A. (1973). "Etude experimental de la collimation des faisceaux d'électrons par un diàphragme de plomb réglable," J. Radiol. Electrol. **54,** 39.

BROSZKIEWICZ, R. K. and BULHAK, Z. (1970). "Errors in ferrous sulphate dosimetry," Phys. Med. Biol. **15,** 549.

BROWN, K. L. (1956). "Achromatic Beam Translation System for Linear Accelerators," Rev. Sci. Instrum. **27,** 959.

BRUCE, W. R., PEARSON, M. L. and FREEDHOFF, H. S. (1963). "The linear energy transfer distributions resulting from primary and scattered x-rays and gamma rays with primary HVL's from 1.25 mm Cu to 11 mm Pb," Radiat. Res. **19,** 606.

BRUKE, R. W. and MAURODINEANU, R. (1977). *Standard Reference Materials: Certification and Use of Acidic Potassium Dichromate Solutions as an Ultraviolet Absorbance Standard*, SRM 935, NBS Special Publication 260-54 (National Bureau of Standards, Washington D.C.).

BRYANT, T. H. E. and RIDLER, T. P. (1968). "Factors affecting the measurements of the extinction coefficient of Fe^{3+} ions in a Fricke dosimeter solution," Health Phys. **15,** 263.

BRYNJOLFSSON, A. and MARTIN, T. G. (1971). "Bremsstrahlung production and shielding of electron accelerators below 50 MeV," Int. J. Appl. Radiat. Isot. **22,** 29.

BUMILLER, F. A., BUSKIRK, F. R., DYER, J. N. and MILLER, R. D. (1969). "The measured energy loss of high-energy electrons in aluminium," Z. Phys. **223,** 415.

BURCH, P. R. J. (1957). "Comment on recent cavity ionization theories," Radiat. Res. **6,** 79.

BURLIN, T. E. (1959). "The measurement of exposure dose for high energy radiation with cavity ionization chambers," Phys. Med. Biol. **3,** 197.

BURLIN, T. E. (1968). "Cavity-chamber theory," p. 331 of *Radiation Dosimetry*, Vol. I, Attix, F. H. and Roesch W. C., Eds. (Academic Press, Inc., New York).

BURLIN, T. E. and HUSAIN, S. R. (1964). "Saturation characteristics of a spherical ionization chamber and a determination of Boag's constant for air," Nature **204,** 670.

BÜLOW, B. and FORKMAN, B. (1974). "Photonuclear cross sections," p. 495 in *Handbook on Nuclear Activation Cross-Sections*, International Atomic Energy Agency, Tech. Rep. Series No. 156. (International Atomic Energy Agency, Vienna).

CAMERON, J. R., DEWERD, T., WAGNER, J., WILSON, C., DOPPKE, K. and ZIMMERMAN, D. (1967). "Nonlinearity of thermoluminescence as a function of dose for LiF (TLD-100)," p. 99 in *Solid State and Chem-*

ical Radiation Dosimetry in Medicine and Biology (International Atomic Energy Agency, Vienna).

CAMERON, J. R., SUNTHARALINGAM, N. and KENNEY, G. N. (1968). *Thermoluminescent dosimetry* (University of Wisconsin Press, Madison, Wisconsin).

CARLSSON, C. A. (1979). "Relationships between energy fluence and energy incident on, emitted by or imparted to a body," Phys. Med. Biol. **24,** 1209.

CASANOVAS, J. (1975). *Etude de la Conduction Induite par des rayonnements à transfers lineiques d'énergie très Differentes des Certains Liquides Organiques non Polaires.* Thesis, Université Paul Sabatier.

CASANOVAS, J., PATAU, J. P., MATHIEU, J. and BLANC, D. (1971). "Comparaison entre l'ionisation produite dans le volume sensible d'une chambre d'ionisation a diélectrique liquide et l'énergie qui y est déposée, calculée par la méthode de Monte-Carlo, dans le cas d'irradiation par des électrons monocinétiques de 1.5 et 1.9 MeV," p. 571 in *Third Symposium on Microdosimetry*, Report No. EUR 4810, Ebert, H. G., Ed. (Commission of the European Communities, Luxembourg).

CHO, Z. H., TSAI, C.M. and WILSON, G. (1975). "Study of contrast and modulation mechanism in x-ray photon transverse axial transmission tomography," Phys. Med. Biol. **20,** 879.

CHODOROW, M. (1955). "Stanford high-energy linear electron accelerator (Mark III)," Rev. Sci. Instrum. **26,** 134.

COOPER, G. W., VAN DYCKE, J. G., NICKSON, J. J. and LAUGHLIN, J. S. (1962). "The relative biological efficiency of 20 MeV electrons and 250 Kevp x-rays as measured in the 12-day-old chick embryo," Radiat. Res. **16,** 686.

CORDARO, M. C. and ZUCKER, M. S. (1971). "A method for solving time dependent electron transport problems," Nucl. Sci. Eng. **45,** 107.

COTTENS, E. (1979). *Geabsorbeerde Dosis Kalorimetrie bij Hoge Energie Elektronenbundels en Onderzoek van de Ijzersulfaat Dosimeter,"* Thesis, Laboratorium voor Kernfysica, University of Gent, Belgium.

COVA, P. L., BOTTI, G. and TOSI, G. (1967). "Critical considerations on employing scatterers with electron beams accelerated by the betatron," Strahlentherapie **133,** 7.

DAHLER, A. (1965). "Effect of collimator shape on electron depth dose curve," p. 98 in *Symposium on High Energy Electrons*, Zuppinger, A. and Poretti, G., Eds. (Springer-Verlag, Berlin).

DAHLER, A., BAKER, A. S. and LAUGHLIN, J. S. (1969). "Comprehensive electron-beam treatment planning," Ann. N.Y. Acad. Sci. **161,** 198.

DALTON, P. and TURNER, J. E. (1968). "New evaluation of mean excitation energies for use in radiation dosimetry," Health Phys. **15,** 257.

DATTA, R., DATTA, S., MCDAVID, W. D. and WAGGONER, R. G. (1979). "Electron beam depth dose scaling by means of effective atomic number reconstructed from CT-scans," Med. Phys. **6,** 526.

DAVIES, J. V. and LAW, J. (1963). "Practical aspects of ferrous sulphate dosimetry," Phys. Med. Biol. **8,** 91.

DAY, M. J. and LAW, J. (1969). "Ferrous sulphate G-values in 0.8 and 0.1N H_2SO_4," Phys. Med. Biol. **14,** 665.

DECKEN, C. B., BECKER, J. and WEITZERL, G. (1956). "Tubusse für die Feldbegrenzung bei Bestrahlung mit schnellen Elektronen eines Betatrons," Strahlentherapie **101,** 197.

DE ALMEIDA, C. E. and ALMOND, P. R. (1974a). "Comparison of electron beams from the Siemens betatron (6.0–18.0 MeV) and the sagittaire linear accelerator," Radiology **111,** 439.

DE ALMEIDA, C. E. and ALMOND, P. R. (1974b). "Energy calibration of high energy electrons using a Cerenkov detector and a comparison with different methods," Phys. Med. Biol. **19,** 476.

DIN (1972). Deutsches Institut für Normung, *Medizinische Elektronenbeschleunigess-Anlagen*, DIN-6847 (Deutsches Institut für Normung, Berlin).

DIN (1975). Deutsches Institut für Normung, *Dosismesverfahren in der radiologischen Technik; Ionisationsdosimetrie*, DIN6800 (Deutsches Institut für Normung, Berlin).

DIN (1976). Deutsches Institut für Normung, *Klinische Dosimetrie*, DIN 6809 (Deutsches Institut für Normung, Berlin).

DOLPHIN, G. W., GALE, N. H. and BRADSHAW, A. L. (1959). "Investigations of high energy electron beams for use in therapy," Br. J. Radiol. **32,** 373.

DOMEN, S. R. (1981). "Absorbed dose water calorimeter," Med. Phys. **7,** 157.

DOMEN, S. R. and LAMPERTI, P. J. (1974). "A heat-loss-compensated calorimeter: theory, design, and performance," J. Res. Nat. Bur. Stand. **5,** 595.

DOMEN, S. R. and LAMPERTI, P. J. (1976). "Comparisons of calorimetric and ionimetric measurements in graphite irradiated with electrons from 15 to 50 MeV," Med. Phys. **3,** 294.

DUDERSTADT, J. J. and MARTIN, W. R. (1979). *Transport Theory*, (John Wiley and Sons, Inc., New York).

DUTREIX, J. (1958). "Mesure par films de la distribution en profondeur de la dose pour les electrons," p. 160 of *Betatron und Telekobalttherapie*, Becker, J. and Scheer, K. E., Eds. (Springer-Verlag, Heidelberg).

DUTREIX, J. (1968). "The correlation of basic and clinical data," p. 140 in Vol. 2 *Electron Beam Therapy, Frontiers of Radiation Therapy and Oncology*, Vaeth, J. M., Ed. (S. Karger, Basel, New York).

DUTREIX, A. (1979). Private communication.

DUTREIX, J. and BERNARD, M. (1966). "Dosimetry at interfaces for high energy x- and gamma rays," Br. J. Radiol. **39,** 205.

DUTREIX, J. and BERNARD, M. (1968). "Influence d'une lame métallique sur la distribution de la dose dans le plexiglas irradié par des électrons de haute énergie," Biophysik **4,** 302.

DUTREIX, J. and DUTREIX, A. (1966). "Etude comparée d'une série de chambres d'ionisation dans des faisceaux d'électrons de 20 et 10 MeV." Biophysik **3,** 249.

DUTREIX, J. and DUTREIX, A. (1969). "Film dosimetry of high-energy electrons" Ann. N.Y. Acad. Sci. **161,** 33.

DUTREIX, J. and WAMBERSIE, A. (1981). "Clinical radiobiology of high energy electrons," p. 181 in *Proceedings of the Symposium on Electron Beam Therapy*, Chu, F. C. H. and Laughlin, J. S., Eds. (Memorial Sloan-Kettering Cancer Center, New York).

DUTREIX, J., PRIGNOT, M. and DUTREIX, A. (1968). "Influence sur la distribution de la dose d'un écran interposé dans un faisceau d'électrons de haute énergie," Radiobiol. Radiother. **9,** 309.

EDELSTEIN, G. E., CLARK, T. and HOLT, J. G. (1973). "Dosimetry for total-body electron-beam therapy in the treatment of mycosis fungoides," Radiology **108,** 691.

EGGERMONT, G., BUYSSE, J., JANSSENS, A., THIELENS, G. and JACOBS, R. (1978). "Discrepancies in molar extinction coefficients of Fe^{3+} in Fricke dosimetry," p. 317 in *National and International Standardization of Radiation Dosimetry* Vol. II (International Atomic Energy Agency, Vienna).

EHRLICH, M. (1971). "Influence of size of CaF_2: Mn Thermoluminescence Dosimeters on Cobalt-60 gamma-ray dosimetry in extended media," p. 550 in Proceedings 3rd International Conference on Luminescence Dosimetry (Danish AEC, Risø).

EHRLICH, M. and LAMPERTI, P. J. (1969). "Uniformity of high-energy electron-beam calibrations," Phys. Med. Biol. **14,** 305.

ELLIS, S. C. (1974). "The dissemination of absorbed dose standards by chemical dosimetry," Rad. Sci. 30. (Nat. Phys. Lab., Teddington).

ELLIS, R. E. and READ, L. R. (1969). "Recombination in ionization chambers irradiated with pulsed electron beams. I: Plane parallel plate chamber," Phys. Med. Biol. **14,** 293.

ENGE, H. A. (1963). "Achromatic magnetic mirror for ion beams," Rev. Sci. Instrum. **34,** 385.

ENGELKE, B. A. and HOHLFELD, K. C. (1971). "Einfluss von Temperaturgradienten im Absorber bei der kalorimetrischen Bestimmung der Energiedosis," PTB-Mitt. No. 3, 185.

EPP, E. R., WEISS, H. and HESLIN, J. (1965). "The energy spectrum of electron flux inside tissue irradiated with 20 MeV electrons," p. 324 in *XIth International Congress of Radiology*, International Congress Series No. 89 (Excerpta Medica Foundation, Amsterdam) (cited by Laughlin, 1969).

EPP, E. R., WEISS, H. and SANTOMASSO, A. (1968). "The oxygen effect in bacterial cells irradiated with high-intensity pulsed electrons," Radiat. Res. **34,** 320.

ESCHWEGE, F. and DUTREIX, J.(1969). "Réactions cutanées produites par les électrons de haute énergie," Ann. Radiol. **12,** 67.

EVERLING, F., KÖNIG, L. A. and MATTAUCH, J. E. (1960). "Atomic masses of nuclides for $A \leq 70$," Nucl. Phys. **15,** 342.

EYGES, L. (1948). "Multiple scattering with energy loss," Phys. Rev. **74,** 1534.

EYGES, L. (1949). "Straggling of electrons near the critical energy," Phys. Rev. **76,** 264.

EYGES, L. (1950). "Straggling of electrons near the critical energy," Phys. Rev. **77,** 81.

FEHRENTZ, D. (1968). "Untersuchungen Über die Abhängigkeit der biologischen Wirkung schneller Elektronen von der Gewebstiefe," Strahlentherapie **136,** 56.

FEHRENTZ, D., LIEBIG, B. and SCHRÖDER-BABO, P. (1976). "Berücksichtigung grosser Inhomogenitätsbereiche bei der Berechnung von Elektronen-Dosisverteilungen," Strahlentherapie **151,** 423.

FEIST, H. (1963). *Messungen zur Abbremsung schneller Elektronen in dicken Materieschichten.* Thesis, University of Würzburg, Germany.

FEIST, H., HARDER, D. and METZNER, R. (1968). "Ein Plastik-Szintillationsspektrometer für Elektronen im Energiebereich 2 bis 20 MeV," Nucl. Instrum. Methods **58,** 236.

FELDMAN, A., DE ALMEIDA, C. E. and ALMOND, P. R. (1974). "Measurements of electron-beam energy with rapid processed film," Med. Phys. **1,** 74.

FERMI, E. (1940). "The ionization loss of energy in gases and in condensed materials," Phys. Rev. **57,** 485.

FIRK, F. W. K. (1970). "Low-energy photonuclear reactions," Annu. Rev. Nucl. Sci. **20,** 39.

FLAMANT, R., MALAISE, E., DUTREIX, J., HAYEN, M., PIERQUIN, B., TUBIANA, M. and DUTREIX, A. (1967). "Un essai thérapeutique clinique sur l'irradiation des cancers amygdaliens par faisceaux de photons ou d'électrons de 20 MeV," Eur. J. Cancer, **3,** 169.

FLEMING, D. M. and GLASS, W. A. (1969). "Endothermic processes in tissue-equivalent plastic," Radiat. Res. **37,** 316.

FLETCHER, G. H. (1976). "Introduction" p. 1 in *Clinical Applications of the Electron Beam*, Tapley, N. du V., Ed. (J. Wiley and Sons, New York).

FOWLER, J. F. (1963). "Solid-state dosimeters for *in-*

vivo measurements," Nucleonics **21,** No. 10, 60.

FOWLER, J. F. (1966). "The place of thermoluminescence dosimeters and ionization chambers in praetical dosimetry," p. 46, in *Proceedings IV Nordic Meeting on Clinical Physics, Hanko, Finland,* Rytilä, A. and Spring, E., Eds. (Radiotherapy Clinic, University Central Hospital, Helsinki).

FRANK, I. M. and TAMM, I. (1937). "Coherent visible radiation of fast electrons passing through matter," Compt. Rend. Acad. Sci. **3,** 109.

FREEWICK, D. C. and SHAMBON, A. (1970). "Light sensitivity of LiF thermoluminescent dosimeters," Health Phys. **19,** 65.

FREGENE, A. O. (1967). "Calibration of the ferrous sulfate dosimeter by ionometric and calorimetric methods for radiation of a wide range of energy," Radiat. Res. **31,** 256.

FREREJAQUES, D. and BENAKSAS, D. (1964). "A thin foil secondary emission monitor," Nucl. Instrum. Methods **26,** 351.

FREYBERGER, K. (1964). *Örtliche Verteilung der Energiedosis beim Durchgang schneller Elektronen durch dicke Materieschichten.* Thesis, University of Würzburg, Germany.

FRICKE, H. and MORSE, S. (1927). "The action of roentgen rays on dilute ferrosulphate solutions as a measure of dose," Am. J. Roentgenol. **18,** 430.

FRICKE, H. and MORSE, S. (1929). "The action of x rays on ferrous sulphate solutions," Philos. Mag. **7,** 129.

FRICKE, H. and HART, E. J. (1966). "Chemical dosimetry," p. 167 in *Radiation Dosimetry* Vol. II, Attix, F. W., Roesch, W. C. and Tochilin, E., Eds. (Academic Press, New York).

FRIGERIO, N. A. (1962). "Increased sensitivity for ferrous and ceric sulfate dosimetry," Radiat. Res. **16,** 606.

FROST, D. and MICHEL, L. (1965). "Über die Zusatzdosis durch Betatron-Neutronen," p. 156 in *Symposium on High-Energy Electrons,* Zuppinger, A. and Poretti, G., Eds. (Springer-Verlag, Berlin).

GALBRAITH, D. M. RAWLINSON, J. A. and MUNRO, P. (1984). "Dose errors due to charge storage in electron irradiated plastic phantom," Med. Phys. **11,** 253.

GANTCHEW, M. G. and TOUSHLEKOVA, K. (1976). "The influence of the composition of LiF TLD materials on their sensitivity to high energy electrons," Phys. Med. Biol. **21,** 300.

GEISSELSODER, J., KOEPKE, K. and LAUGHLIN, J. S. (1963). "Calorimetric determination of absorbed dose and $G_{Fe^{+++}}$ of the Fricke dosimeter with 10 MeV and 20 MeV electrons," Radiat. Res. **20,** 423.

GELLER, K. N., HALPERN, J. and MUIRHEAD, E. G. (1960). "Photoneutron reactions: ^{12}C, ^{14}N, ^{16}O and ^{19}F near threshold," Phys. Rev. **119,** 716.

GIARRATANO, J. C., DUERKES, R. J. and ALMOND, P. R. (1975). "Lead shielding thickness for dose reduction of 7- to 28-MeV electrons," Med. Phys. **2,** 336.

GLAZUNOV, P. Y. and PIKAEV, A. K. (1960). "An investigation of the radiolytic oxidation of divalent iron with irradiation doses of high power," Dokl. Akad. Nauk SSSR **130,** 1051.

GOEDE, M. R., GOODEN, D. S., ELLIS, R. G. and BRICKNER, T. J. (1977). "A versatile electron collimation system to be used with electron cones supplied with Varian's Clinac 18," Int. J. Radiat. Oncol. Biol. Phys. **2,** 791.

GOLDWASSER, E. L., MILLS, F. E. and HANSON, A. O. (1952). "Ionization loss and straggling of fast electrons," Phys. Rev. **88,** 1137.

GOODMAN, L. J. (1969). "A modified tissue equivalent liquid," Health Phys. **16,** 763.

GRAY, L. H. (1936). "Ionization method for the absolute measurement of gamma-ray energy," Proc. R. Soc. London Ser. A. **156,** 578.

GREENE, D., LAW, J. and MAJOR, D. (1973). "The G-value for the ferrous sulphate dosimeter for the radiation from Californium-252," Phys. Med. Biol. **18,** 800.

GREENING, J. R. (1964). Saturation characteristics of parallel-plate ionization chambers," Phys. Med. Biol. **9,** 143.

GREENING, J. R. (1974). "Dose conversion factors for electrons," Phys. Med. Biol. **19,** 746.

GRISHAEV, I. A., MOCHESNIKOV, N. I. and IVANOV, V. F. (1960). "Izmerenie polozheniya i toka proletayushchevo impulsnogo puchka zapyazhennykh chastitz," Prib. Tekh. Eksp. **4,** 17.

GROSS, B. and WRIGHT, K. A. (1959). "Charge distribution and range effects produced by 3-MeV electrons in plexiglass and aluminium," Phys. Rev. **114,** 725.

GUND, K. and SCHITTENHELM, R. (1953). "Die physikalischen Eigenschaften der 15 MeV-Elektronenschleuder," Strahlentherapie **92,** 506.

GUNN, S. R. (1964). "Radiometric calorimetry," Nucl. Instrum. Methods **29,** 1.

GUNN, S. R. (1970). "Radiometric calorimetry: A review," Nucl. Instrum. Methods **85,** 285.

GUNN, S. R. (1976). "Radiometric calorimetry: A review, 1976 supplement," Nucl. Instrum. Methods **135,** 251.

HAAS, L. L., LAUGHLIN, J. S. and HARVEY, R. A. (1954). "A biological effectiveness of high-speed electron beam in man," Radiology **62,** 845.

HAGEMANN, G. (1967). "Tiefenabhängige Anderungen von RBW, LET und Energiespektrum bei hochenergetischer Elektronenstrahlung. I. Das Energiespektrum der Elektronenflussdichte," Biophysik **3,** 339.

HALL, E. J. (1978). *Radiobiology for the Radiologist,* Second edition (Harper and Row, Hagerstown, Maryland).

HALL, H. E., HANSON, A. O. and JAMNIK, D. (1959). "Most probable energy loss of fast electrons," Phys. Rev. **115,** 633.

HAMM, R. N., WRIGHT, H. A., KATZ, R., TURNER, J. E. and RITCHIE, R. H. (1978). "Calculated yields and slowing-down spectra for electrons in liquid water: Implications for electron and photon RBE," Phys. Med. Biol. **23,** 1149.

HANSON, A. O., LANZL, L. H., LYMAN, E. M. and SCOTT, M. B. (1951). "Measurement of multiple scattering of 15.7 MeV electrons," Phys. Rev. **84,** 634.

HANSON, A. O., GOLDWASSER, E. L. and MILLS, F. E. (1952). "Energy loss of 15 MeV electrons," Phys. Rev. **86,** 617.

HARDER, D. (1965a). "Energiespektren schneller Elektronen in verschiedenen Tiefen," p. 260 in *Symposium on High-Energy Electrons*, Zuppinger, A. and Poretti, G., Eds. (Springer-Verlag, Berlin).

HARDER, D. (1965b). "Berechnung der Energiedosis aus Ionisationsmessungen bei Sekundärelektronen-Gleichgewicht," p. 40 in *Symposium on High-Energy Electrons*, Zuppinger, A., and Poretti, G., Eds. (Springer-Verlag, Berlin).

HARDER, D. (1965c). *Durchgang Schneller Elektronen durch Dicke Materieschichten.* Thesis, University of Würzburg, Germany.

HARDER, D. (1966). "Spectra of primary and secondary electrons in material irradiated by fast electrons," p. 140 in *Biophysical Aspects of Radiation Quality*, IAEA Techn. Rep. Ser. No. 58 (International Atomic Energy Agency, Vienna).

HARDER, D. (1967). "Berechnung der Energiespektren abgebremster Elektronen in verschiedenen Absorbertiefen," Biophysik **4,** 38.

HARDER, D. (1968). "Einfluss der Vielfachstreuung von Elektronen auf die Ionisation in gasgefüllten Hohlräumen," Biophysik **5,** 157.

HARDER, D. (1970a). "Some general results from the transport theory of electron absorption," p. 567 in *Proceedings of the Second Symposium on Microdosimetry*, Report No. 4452, Ebert, H. G., Ed. (Commission of the European Communities, Brussels).

HARDER, D. (1970b). "On electron dosimetry," p. 55 in *Symposium on High-Energy Electrons.* Compiled by Gil y Gil, C. and Gil Gayarre, C. (General Directorate of Health, Madrid).

HARDER, D. (1974). "Fano's theorem and the multiple scattering correction," p. 677 in *Proceedings of the 4th Symposium on Microdosimetry*, Booz, J., Ebert, H. G., Eickel, R. and Walker, A., Eds. (Commission of the European Communities, Luxembourg).

HARDER, D. (1977). "Present status of electron beam dosimetry," p. 199 in *Book of Abstracts of: XIVth International Congress of Radiology*, Rio de Janeiro.

HARDER, D. (1980). Private communication.

HARDER, D. and ABOU-MANDOUR, M. (1976). "Berechnung der Dosisverteilung schneller Elektronen in und hinter Gewebeinhomogenitäten beliebiger Breite," Strahlentherapie **152,** 509.

HARDER, D. and POSCHET, G. (1967). "Transmission und Reichweite schneller Elektronen im Energiebereich 4 bis 30 MeV," Phys. Lett. **24B,** 519.

HARDER, D. and SCHULZ, H. J. (1972). "Some new physical data for electron beam dosimetry," p. 475 in *Amsterdam, 1971 Proceedings of the European Congress of Radiology* (Excerpta Medica, Amsterdam).

HARDER, D., HARIGEL, G. and SCHULTZE, K. (1961). "Bahnspuren schnellen Elektronen," Strahlentherapie **115,** 1.

HARDWICK, T. J. (1953). "The oxidation of ferrous sulfate by gamma-rays. The temperature coefficient of air-saturated solutions," Can. J. Chem. **31,** 881.

HAWKINGS, R. C., EDWARDS, W. J. and MCLEOD, E. M. (1961). *Tables of Gamma Rays from the Decay of Radionuclides*, AECL 1225 (Atomic Energy Commission, Chalk River, Ontario).

HAYNES, H. and DOLPHIN, G. W. (1959). "The calculation of linear energy transfer, with special reference to a 14 MeV electron beam and 10 MeV per nucleon ion beams," Phys. Med. Biol. **4,** 148.

HAYWARD, E. (1965). p. 141 in *Nuclear structure and electromagnetic interactions*, MacDonald, N., Ed. (Plenum, New York).

HEISENBERG, W. (1953). *Vorträge Über Kosmische Strahlung*, 2nd ed. (Springer-Verlag, Berlin).

HENRY, W. H. (1979) "On C_E, C_λ, and the effective wall material in a Baldwin-Farmer chamber," Phys. Med. Biol. **24,** 37.

HETTINGER, G. and SVENSSON, H. (1967). "Photographic film for determination of isodoses from betatron electron radiation," Acta Radiol. **6,** 74.

HETTINGER, G., BERGMAN, S. and ÖSTERBERG, S. (1965). "The relative biological efficiency (RBE) of 30 MeV electrons on haploid yeast," Biophysik **2,** 276.

HETTINGER, G., PETTERSON, C. and SVENSSON, H. (1967). "Displacement effect of thimble chambers exposed to a photon or electron beam from a betatron," Acta Radiol. **6,** 61.

HISDALE, E. (1957). "Bremsstrahlung spectra corrected for multiple scattering within the target," Phys. Rev. **105,** 1821.

HO, J. H. C., LAM, C. M. and LAI, K. C. (1976). "The value of and need for high-energy electrons," p. 51 in *High-Energy Photons and Electrons*, Kramer, S., Suntharalingam, N. and Zinninger, G. F., Eds. (J. Wiley and Sons, New York, London).

HOGSTROM, K. E., MILLS, M. D. and ALMOND, P.

(1981). "Electron beam dose calculations," Med. Phys. Biol. **26,** 445.

HOHLFELD, K. and REICH, H. (1978). "Calibration of dose meters in terms of absorbed dose in water for ^{60}Co gamma rays," p. 81 in *National and International Standardization of Radiation Dosimetry* Vol. II, IAEA Publication STI/PUB/471 (International Atomic Energy Agency, Vienna).

HOLT, J. G., MCDONALD, J. C., BUFFA, A., PERRY, D., MA, J. and LAUGHLIN, J. S. (1978). "Primary dosimetric standards at the Memorial Sloan-Kettering Cancer Center," p. 229 in *National and International Standardization of Radiation Dosimetry* Vol. I, IAEA Publication STI/PUB471 (International Atomic Energy Agency, Vienna).

HOLT, J. G., BUFFA, A., PERRY, D. J., I-CHANG and MCDONALD, J. C. (1979). "Absorbed dose measurements using parallel plate polystyrene ionization chambers in polystyrene phantoms," Int. J. Radiat. Oncol. Biol. Phys. **5,** 2031.

HOLTHUSEN, H. (1919). "Über die Bedingungen der Röntgenstrahlenenergiemessung bei verschiedenen Impulsbreiten auf luftelektrischen Wege," Fortschr. Geb. Röntgenstr. **26,** 211.

HORNSEY, S. (1970). "Differences in survival of jejunal crypt cells after radiation delivered at different dose-rates," Br. J. Radiol. **43,** 802.

HORNSEY, S. and ALPER, T. (1966). "Unexpected dose rate effect in the killing of mice by radiation," Nature **210,** 212.

HPA (1970). Hospital Physicist Association, *A Suggested Procedure for the Mechanical Alignment of Telegamma and Megavoltage X-ray Beam Units*, HPA Report Series No. 3 (The Hospital Physicists' Association, London).

HPA (1971). Hospital Physicists Association, *A Practical Guide to Electron Dosimetry 5-35 MeV*, HPA Report Series No. 4 (The Hospital Physicists' Association, London).

HPA (1975). Hospital Physicists Association, *A Practical Guide to Electron Dosimetry below 5 MeV for Radiotherapy Purposes*, HPA Report Series No. 13, (The Hospital Physicists' Association, London).

HSIEH, C. L. and UHLMANN, E. M. (1956). "Experimental evaluation of the physical characteristics of a 45 MeV medical linear electron accelerator," Radiology **67,** 263.

HUBBELL, J. H. (1969). *Photon Cross Sections, Attenuation Coefficients, and Energy Absorption Coefficients from 10 keV to 100 GeV*, NSRD-NBS 29 (National Bureau of Standards, Washington, D.C.)

HUBBELL, J. H. (1977). "Photon mass attenuation and mass energy-absorption coefficients for H, C, N, O, Ar, and seven mixtures from 0.1 keV to 20 MeV," Radiat. Res. **70,** 58.

HULTÉN, G. and SVENSSON, H. (1975). "Electron depth absorbed doses for small phantom depths," Acta Radiol. Ther. Phys. Biol. **14,** 537.

HUSSMAN, E. K. and MCLAUGHLIN, W. L. (1971). "Dose-distribution measurements of high-intensity pulsed radiation by means of holographic interferometry," Radiat. Res. **47,** 1.

ICRP (1960). International Commission on Radiological Protection, *Protection Against X-rays up to Energies of 3 MeV and Beta- and Gamma-Rays from Sealed Sources*, ICRP Publication 3 (Pergamon Press, New York).

ICRP (1964). International Commission on Radiological Protection, *Protection Against Electro-Magnetic Radiation Above 3 MeV and Electrons, Neutrons and Protons*, ICRP Publication 4 (Pergamon Press, New York).

ICRP (1970). International Commission on Radiological Protection, *Protection Against Ionizing Radiation from External Sources*, ICRP Publication 15 (Pergamon Press, New York).

ICRP (1972). International Commission on Radiological Protection, *Protection Against Ionizing Radiation from External Sources*, ICRP Publication 21 (Pergamon Press, New York).

ICRP (1975). International Commission on Radiological Protection, *Report of the Task Group on Reference Man*, ICRP Publication 23 (Pergamon Press, New York).

ICRP-ICRU (1962). "Report of the RBE committee to the International Commissions on Radiological Protection and on Radiological Units and Measurements," Health Phys. **9,** 357.

ICRU (1963). International Commission on Radiation Units and Measurements, *Clinical Dosimetry*, ICRU Report 10d, published as National Bureau of Standards Handbook 87 (U.S. Government Printing Office, Washington, D.C.).

ICRU (1964). International Commission on Radiation Units and Measurements, *Physical Aspects of Irradiation*, ICRU Report 10b, published as National Bureau of Standards Handbook 85 (U.S. Government Printing Office, Washington, D.C.).

ICRU (1969). International Commission on Radiation Units and Measurements, *Radiation Dosimetry: X Ray and Gamma Rays with Maximum Photon-Energies Between 0.6 and 50 MeV*, ICRU Report 14 (International Commission on Radiation Units and Measurements, Bethesda, Maryland).

ICRU (1970). International Commission on Radiation Units and Measurements, *Radiation Dosimetry: X Rays Generated at Potentials of 5 to 150 kV*, ICRU Report 17 (International Commission on Radiation Units and Measurements, Bethesda, Maryland).

ICRU (1972). International Commission on Radiation Units and Measurements, *Radiation Dosimetry:*

Electrons with Initial Energies Between 1 and 50 MeV, ICRU Report 21 (International Commission on Radiation Units and Measurements, Bethesda, Maryland).

ICRU (1976). International Commission on Radiation Units and Measurements, *Determination of Absorbed Dose in a Patient Irradiated by Beams of X or Gamma Rays in Radiotherapy Procedures*, ICRU Report 24 (International Commission on Radiation Units and Measurements, Bethesda, Maryland).

ICRU (1977). International Commission on Radiation Units and Measurements, *Neutron Dosimetry for Biology and Medicine*, ICRU Report 26 (International Commission on Radiation Units and Measurements, Bethesda, Maryland).

ICRU (1978). International Commission on Radiation Units and Measurements, *Dose Specification for Reporting External Beam Therapy with Photons and Electrons*, ICRU Report 29 (International Commission on Radiation Units and Measurements, Bethesda, Maryland).

ICRU (1979). International Commission on Radiation Units and Measurements, *Average Energy Required to Produce an Ion Pair*, ICRU Report 31 (International Commission on Radiation Units and Measurements, Bethesda, Maryland).

ICRU (1980). International Commission on Radiation Units and Measurements, *Radiation Quantities and Units*, ICRU Report 33 (International Commission on Radiation Units and Measurements, Bethesda, Maryland).

ICRU (1982). International Commission on Radiation Units and Measurements, *The Dosimetry of Pulsed Radiation*, ICRU Report 34 (International Commission on Radiation Units and Measurements, Bethesda, Maryland).

ICRU (1984). International Commission on Radiation Units and Measurements, *Stopping Powers for Electrons and Positrons*, ICRU Report 37 (International Commission on Radiation Units and Measurements, Bethesda, Maryland).

INADA, T., HOSHINO, K, and MATSUZAWA, H. (1969). "Primary and secondary spectra of MeV electrons in water phantoms," p. 461 in *Book of Abstracts of the 12th International Congr. Radiology*. (XII International Congress of Radiology, Tokyo).

INOKUTI, M. and SMITH, D. Y. (1982). "Fermi density effect on the stopping power of metallic aluminum," Phys. Rev. **B25,** 61.

ISABELLE, D. (1962). "La mesure de l'intensité du courant produit par un accélérateur lineaire," L'onde électrique, **48,** 354.

ISABELLE, D. and ROY, P. H. (1963). "Factors influencing the stability of a secondary electron monitor," Nucl. Instrum. Methods **20,** 17.

IVERSEN, N. A. IBBOTT, G. S., CACAK, R. K. and HENDEE, W. R. (1976). "An evaluation of the EMI-Rad 8 electron beam simulation program," presented at the *19th Annual Meeting of the AAPM, Cincinnati, Ohio, August 1976* Paper No. P2.

JAYACHANDRAN, C. A. (1971). "Calculated effective atomic number and kerma values for tissue-equivalent and dosimetry materials," Phys. Med. Biol. **16,** 617.

JOHANSSON, K. A., MATTSSON, O., LINDBORG, L. and SVENSSON, H. (1978). "Absorbed-dose determination with ionization chambers in electron and photon beams having energies between 1 and 50 MeV," p. 243 in *National and International Standardization of Radiation Dosimetry*, Vol. II, IAEA Publication STI/PUB/471 (International Atomic Energy Agency, Vienna).

JOHNS, H. E., ASPIN, N. and BAKER, R. G. (1958). "Currents induced in the dielectrics of ionization chambers through action of high-energy radiation," Radiat. Res. **9,** 573.

JOST, K. and KESSLER, J. (1963). "Die Ortsverteilung mittelschneller Elektronen bei Mehrfachstreuung," Z. Phys. **176,** 126.

KARZMARK, C. J. (1964). "Secondary emission monitor as a linear accelerator electron beam dose monitor," Rev. Sci. Instrum. **35,** 1646.

KARZMARK, C. J. and PERING, N. C. (1973). "Electron linear accelerators for radiation therapy: history, principles and contemporary developments," Phys. Med. Biol. **18,** 321.

KARZMARK, C. J., LOEVINGER, R., STEELE, R. E. and WEISSBLUTH, M. (1960). "A technique for large-field superficial electron therapy," Radiology **74,** 633.

KASE, K. R. and BJÄRNGARD, B. E. (1979). "Bremsstrahlung dose to patients in rotational electron therapy," Radiology **133,** 531.

KATO, H., ONO, R. and KATO, R. (1977). "Absorption of high energy electrons in liquid medium," Nucl. Instrum. Methods **145,** 525.

KATZ, L. and LOKAN, K. H. (1961). "The generation of positrons in a thick target bombarded by fast electrons," Nucl. Instrum. Methods **11,** 7.

KATZ, L. and PENFOLD, A. S (1952). "Range-energy relations for electrons and the determination of beta-ray endpoint energies by absorption," Rev. Mod. Phys. **24,** 28.

KAWACHI, K. (1975). "Calculation of electron dose distribution for radiotherapy treatment planning," Phys. Med. Biol. **20,** 571.

KESSARIS, N. D. (1966). "Penetration of high energy electron beams in water," Phys. Rev. **145,** 164.

KESSARIS, N. D. (1970). "Absorbed dose and cavity ionization for high-energy electron beams," Radiat. Res. **43,** 288.

KHAN, F. M., FULLERTON, G. D., LEE, J. M.-F., MOORE, V. C. and LEVITT, S. H. (1977). "Physical

aspects of electron-beam arc therapy," Radiology **124,** 497.

KHAN, F. M., SEWCHAND, W. and LEVITT, S. H. (1978). "Effect of air space on depth dose in electron beam therapy," Radiology **126,** 249.

KIM, Y. S. (1974). "Human tissue: chemical composition and photon dosimetry data," Radiat. Res. **57,** 38.

KIM, J. H., PINKERTON, A. and LAUGHLIN, J. S. (1969). "Dosimetry and biological parameters in studies of relative biological effectiveness of high-energy electron beams," Ann. N.Y. Acad. Sci. **161,** 310.

KNASEL, T. M. (1970). "Accurate calculation of radiation lengths," Nucl. Instrum. Methods **83,** 217.

KOCH, H. W. and MOTZ, J. W. (1959). "Bremsstrahlung cross-section formulas and related data," Rev. Mod. Phys. **31,** 921.

KOVALIEV, V. P., KHARIN, V. P., GORDEEV, V. I. and ISAEV, V. I. (1972). "Angular distribution of transmitted electrons in the energy range 12–15 MeV," At. Energ. **33,** 932.

KOZLOW, A. P. and SHISHOV, V. A. (1976). "Forming of electron beams from a betatron by foil scatterers," Acta Radiol. Ther. Phys. Biol. **15,** 493.

KRETSCHKO, J. (1960). *Absolutmessungen an schnellen Elektronen mit einem Faraday-Käfig.* Thesis, University of Frankfurt, Germany.

KRETSCHKO, J., HARDER, D. and POHLIT, W. (1962). "Absolutmessung der Teilschenflussdichte schneller Elektronen mit einem Faraday-Käfig," Nucl. Instrum. Methods **16,** 29.

KUTTIG, H. and ZIEGLER, F. (1975). "Elektronentherapie mit Keilfilter," Strahlentherapie **150,** 383.

LANDAU, L. (1944). "On the energy loss of fast particles by ionization," J. Phys. USSR **8,** 201.

LANZL, L. H. (1969). "Magnetic and threshold techniques for energy calibration of high energy radiations," Ann. N.Y. Acad. Sci. **161,** 101.

LAUGHLIN, J. S. (1956). "High-energy electron beams," p. 597 in *Radiation Dosimetry*, Hine, G. and Brownell, G., Eds. (Academic Press, Inc., New York).

LAUGHLIN, J. S. (1965). "High energy electron treatment planning for inhomogeneities," Br. J. Radiol. **38,** 143.

LAUGHLIN, J. S. (1967). "Physical aspects of high energy electron therapy," Am. J. Roentgenol. **99,** 915.

LAUGHLIN, J. S. (1969). "Electron beams," p. 91 in *Radiation Dosimetry*, Vol. III, Attix, F. H. and Tochilin, E., Eds. (Academic Press, Inc., New York).

LAUGHLIN, J. S., OVADIA, J., BEATTIE, J. W., HENDERSON, W. J., HARVEY, R. A. and HAAS, L. L. (1953). "Some physical aspects of electron beam therapy," Radiology **60,** 165.

LAUGHLIN, J. S., LANDY, A., PHILIPS, R., CHU, F. and SATTAR, A. (1965). "Electron beam treatment planning in inhomogeneous tissue," Radiology **85,** 524.

LAW, J. and SVENSSON, H. (1972). "Comparisons of radiation dosimetry," Phys. Med. Biol. **18,** 464.

LAW, J., PRIGNOT, M. and WAMBERSIE, A. (1975). "Comparisons of radiation dosimetry between Louvain (Belgium) and Edinburgh (U.K.)," J. Radiol. Electrol. **56,** 419.

LAX, I. and BRAHME, A. (1980). "On the collimation of high energy electron beams," Acta Radiol. Oncol. **19,** 199.

LEDERER, C. M. and SHIRLEY, V. S. (1978). *Tables of Isotopes* (J. Wiley and Sons, Inc., New York).

LEETZ, H.-K. (1976). "Calculation of dose distribution in 5-42 MeV betatron electron beams for treatment planning," Digest of the 4th ICMP, Phys. in Canada **32,** 23.5.

LEETZ, H.-K. (1979). "Dosisberechnung für schnelle Elektronen nach einem Matrix-Verfahren," Strahlentherapie **155,** 181.

LEISS, J. E., PENNER, S. and ROBINSON, C. S. (1957). "Range straggling of high-energy electrons in carbon," Phys. Rev. **107,** 1544.

LESKOWITZ, I., VAN DYKE, J. G., LAUGHLIN, J. S. and NICKSON, J. J. (1960). "The relative biological efficiency of 20-MeV electrons and 180-Kvp x-rays in Escherichia coli inactivation," Radiat. Res. **13,** 445.

LEVINGER, J. S. (1960). *Nuclear photo disintegration* (Oxford Univ. Press, London).

LEWIS, H. W. (1950). "Multiple scattering in an infinite medium," Phys. Rev. **78,** 526.

LIESEM, H. (1976). "A Cerenkov detector for energy calibration of electron accelerations in clinical use," Phys. Med. Biol. **21,** 360.

LIESEM, H. and POHLIT, W. (1962). "Dosismessung an schnellen Elektronen nach der Eisensulfatmethode," Z. Phys. Chem. **35,** 352.

LIESEM, H. and POHLIT, W. (1978). "A simple method of energy determination for electron accelerators used in medicine," p. 291 in *National and International Standardization of Radiation Dosimetry*, Vol. II, IAEA Publication STI/PUB/471 (International Atomic Energy Agency, Vienna).

LIESEM, H., POHLIT, W. and HELLER, R. (1974). "Einfaches Verfahren zur Energiebestimmung bei medizinisch genutzten Elektronenbeschleunigern," Strahlentherapie **148,** 1.

LILLICRAP, S. C. and ROSENBLOOM, M. (1972). "Theoretical and experimental depth-dose curves for electrons in the energy ranges 3–10 MeV," Br. J. Radiol. **45,** 229.

LILLICRAP, S. C., WILSON, P. and BOAG, J. W. (1975). "Dose distributions in high energy electron beams: Production of broad beam distributions from narrow beam data," Phys. Med. Biol. **20,** 30.

LINDBORG, L. (1976). "Microdosimetry measurements

in beams of high energy photons and electrons: Technique and results," p. 347 in *Proceedings of the Fifth Symposium on Microdosimetry*, Report No. EUR 5452, Booz, J., Ebert, H. G. and Smith, B. G. R., Eds. (Commission of the European Communities, Luxembourg).

LINDEN, W. A. (1972). "Die relative biologische Wirksamkeit der Hochvoltstrahlen in der Strahlentherapie," Strahlentherapie **144,** 679.

LINDSKOUG, B. (1974). *Development and use of a Radiothermoluminescence Dosimetry System—Automation of Equipment and Procedures.* Thesis, University of Göteborg, Sweden.

LINDSKOUG, B. and HULTBORN, A. (1976). "Tissue heterogeneity in the anterior chest wall and its influence on radiation therapy of the internal mammary lymph nodes," Acta Radiol. Ther. Phys. Biol. **15,** 97.

LIPPERT, J. and MEJDAHL, V. (1967). "Thermoluminescent readout instrument for measurement of small doses," p. 204 in *Luminescence Dosimetry*, CONF-650637, USAEC Symp. Ser. No. 8, Attix, F. H., Ed. (National Technical Information Service, Springfield, Virginia).

LLOYD, D. C., PURROTT, R. J., DOLPHIN, G. W., BOLTON, D., EDWARDS, A. A. and CORP, M. J. (1975). "The relationship between chromosome aberrations and low LET radiation dose to human lymphocytes," Int. J. Radiat. Biol. **28,** 75.

LOCKWOOD, G. J., MILLER, G. H. and HALBLIEB, J. A. (1976). "Electron energy deposition in multilayer geometries," IEEE Trans. Nucl. Sci. **23,** 1862.

LOEVINGER, R. (1980). "Calculation of absorbed dose in high-energy photon and electron beams using a calibrated ionization chamber," p. 283 in *Biomedical Dosimetry: Physical Aspects, Instrumentation, Calibration*, IAEA Publication STI/PUB/567 (International Atomic Energy Agency, Vienna).

LOEVINGER, R. (1981). "A formalism for calculation of absorbed dose to a medium from photon and electron beams," Med. Phys. **8,** 1.

LOEVINGER, R., KARZMARK, C. J. and WEISSBLUTH, M. (1961). "Radiation therapy with high-energy electrons," Radiol. **77,** 906.

LOFTUS, T. P. and WEAVER, J. T. (1974). "Standardization of ^{60}Co and ^{137}Cs gamma-ray beams in terms of exposure," J. Res. Nat. Bur. of Stand. **78A,** 465.

LONERGAN, J. A., JUPITER, C. P. and MERKEL, G. (1970). "Electron energy straggling measurements for thick targets of beryllium, aluminium, and gold at 4.0 and 8.0 MeV," J. Appl. Phys. **41,** 678.

LYMAN, E. M., HANSON, A. O. and SCOTT, M. B. (1951). "Scattering of 15.7 MeV electrons by nuclei," Phys. Rev. **84,** 626.

MARBACH, J. R. and ALMOND, P. R. (1981). "Optimization of field flatness and depth-dose for electron beams," Phys. Med. Biol. **26,** 435.

MARINELLO, G. and SLIWINSKI, C. (1974). "Les émulsions photographiques et leurs applications en dosimétrie," J. Radiol. Electrol. **55,** 507.

MARION, J. B. and ZIMMERMAN, B. A. (1967). "Multiple scattering of charged particles," Nucl. Instrum. Methods **51,** 93.

MARKUS, B. (1956). "Über den Begriff der Gevebeäquivalenz und einige 'wasserähnliche' Phantomsubstanzen für Quanten von 10 keV bis 100 MeV sowie schnelle Elektronen," Strahlentherapie **101,** 111.

MARKUS, B. (1961). "Energiebestimmung schneller Elektronen aus Tiefendosiskurven," Strahlentherapie **116,** 280.

MARKUS, B. (1964). "Beiträge zur Entwicklung der Dosimetrie schneller Elektronen," Strahlentherapie **123,** 350, and **123,** 508, and **124,** 33.

MARKUS, B. (1969). "Problems of high energy electron dosimetry in radiological experiments," Ann. N.Y. Acad. Sci. **161,** 282.

MARKUS, B. (1975). "Eine polarisierungseffekt-freie Graphit-Doppelextrapolationskammer zur Absolutdosimetrie schneller Elektronen," Strahlentherapie **150,** 307.

MARKUS, B. (1976). "Eine Parallelplatten-Kleinkammer zur Dosimetrie schneller Elektronen und ihre Anwendung," Strahlentherapie **152,** 517.

MARKUS, B. (1978). "Eine einfache Formel zur Bestimmung der mittleren Elektronenergie in einem mit schnellen Elektronen bestrahlten Körper," Strahlentherapie **154,** 388.

MARKUS, B. and PAUL, W. (1953). "Photographische Dosimetrie in elektronenbestrahlten Körpern," Strahlentherapie **92,** 612.

MARQUARDT, K. and MARKUS, B. (1965). "Die Wirkung von 14 MeV-Elektronen und 22 kV Röntgenstrahlen auf die Proliferations-fähigkeit von Karzinomzellen von Stamme HeLa," p. 344 in *Deutscher Röntgenkongress*, Band 61 (Urban and Schwarzenberg-München, Berlin).

MARTENSSON, B. K. A. (1969). "Thermoluminescence of LiF: A statistical analysis of the influence of preannealing on the precision of measurement," Phys. Med. Biol. **14,** 119.

MASON, E. W. (1971). "Thermoluminescence response of ^{7}LiF to ultra-violet light," Phys. Med. Biol. **16,** 303.

MATHIEU, J., BLANC, D., CASANOVAS, J., DUTREIX, A., WAMBERSIE, A. and PRIGNOT, M. (1969). "Mesure de la répartition de la dose déposée en profondeur dans un fantôme de Plexiglas irradié par un faisceau d'électrons monicinétiques de 10, 15, 20 ou 30 MeV," p. 437 in *Proceedings of the Second Symposium on Microdosimetry*, Report No. 5442, Ebert, H. G., Ed. (Commission of the European Communities, Luxembourg).

MATHIEU, J., BLANC, D., CASANOVAS, J., DUTREIX, A., WAMBERSIE, A. and PRIGNOT, M. (1970). "Mesure de la répartition de la dose déposée en profondeur dans un fantôme de Plexiglas irradié par un faisceau d'électrons monocinétiques de 10, 15, 20 ou 30 MeV," p. 437 in *Proceedings of the Second Symposium on Microdosimetry*, Report No. EUR 5452, Ebert, H. G., Ed. (Commission of the European Communities, Luxembourg).

MATSUZAWA, H., KAWASHIMA, K. and HIRAOKA, T. (1974). "Dose conversion factors for electrons," Phys. Med. Biol. **19,** 744.

MATTAUCH, J. H. E., THIELE, W. and WAPSTRA, A. H. (1965). "1964 Atomic mass tables," Nucl. Phys. **67,** 1.

MATTHEWS, J. L. and OWENS, R. O. (1973). "Accurate formulae for calculation of high energy electron Brehmsstrahlung spectra," Nucl. Instrum. Methods **111,** 157.

MATTSSON, O. and SVENSSON, H. (1984). "Charge build-up effects in insulating phantom materials," In press Acta Radiol. Onc. 1984.

MATTSSON, O., JOHANSSON, K.-A., and SVENSSON, H. (1981). *Detectors and Methods for the Determination of Absorbed Dose in Electron Beams of Energies between 1 and 50 MeV*, Rad. Phys. Dept., University of Umeå, Sweden.

MCCONNELL, W. J., BIRKHOFF, R. D., HAMM, R. N. and RITCHIE, R. N. (1968). "Electron flux spectra in aluminium: Analysis for LET spectra and excitation and ionization yields," Radiat. Res. **33,** 216.

MCDONALD, J. C., LAUGHLIN, J. S. and FREEMAN, R. E. (1976). "Portable tissue equivalent calorimeter," Med. Phys. **3,** 80.

MCGINNIES, R. T. (1959). *Energy Spectrum Resulting from Electron Slowing Down*, NBS Circular 597 (National Bureau of Standards, Washington, D.C.).

MEYLER, T. S., BLUMBERG, A. L. and PURSER, P. (1978). "Total skin electron beam therapy in mycosis fungoides," Cancer **42,** 1171.

MIE, G. (1904). "Der elektrische Strom in ionisierter Luft in einem ebenen Kondensator," Ann. Physik (4) **13,** 857.

MIKADO, T., TOMIMASU, T. and YAMZAKI, T. (1976). "Emission-angle dependence of energy spectra of 24.8-MeV electrons passing through thick materials," J. Appl. Phys. **47,** 3948.

MILL, A. J. (1979). "Recovery of cultured mammalian cells from sublethal damage when irradiated at ultra high dose rates," Nucl. Instrum. Methods **163,** 577.

MILLAN, P. E., MILLAN, S., HERNANDEZ, A. and ANDREO, P. (1979). "Parameterization of linear accelerator electron beam for computerized dosimetry calculations," Phys. Med. Biol. **24,** 825.

MILLER, A., and MCLAUGHLIN, W. L. (1975). "Imaging and measuring electron beam dose distributions using holographic interferometry," Nucl. Instrum. Methods **128,** 337.

MILLER, A. and MCLAUGHLIN, W. L. (1976). "Holographic measurements of electron-beam dose distributions around inhomogeneities in water," Phys. Med. Biol. **21,** 285.

MILLER, G. H., LOCKWOOD, G. J. and HALBLEIB, J. A. (1974). "Improved calorimetric method for energy deposition measurement," IEEE Trans. Nucl. Sci. **21,** 359.

MOLIÈRE, G. (1947). "Theorie der Streuung schneller geladener Teilchen. I. Einzelstreuung am abgeschirmten Coulomb-Feld," Z. Naturforsch. **2a,** 133.

MOLIÈRE, G. (1948). "Theorie der Streuung schneller geladener Teilchen. II. Mehrfach- und Vielfachstreuung," Z. Naturforsch. **3a,** 78.

MOOKERJEE, A., VAN DYKE, J. G. and LAUGHLIN, J. S. (1964). "The relative biological efficiency of 20-MeV electrons and 250-Kvp x-rays in saccharomyces cerevisiae inactivation," Radiat. Res. **22,** 431.

MØLLER, C. (1932). "Zur Theorie des Durchgangs schneller Elektronen durch Materie," Ann. Phys. **14,** 531.

MÖLLER, T. R., NORDBERG, U. B., GUSTAFSSON, F., JOHNSSON, J. E., LANDBERG, T. G. and SVAHN-TAPPER, G. (1976). "Planning, control, and documentation of external beam therapy," Acta Radiol. Suppl. No. 353.

MOORE, D. (1961). "Neutron, electron and x-ray beams used radiation research from a Van de Graff generator," Nucl. Instrum. Methods **11,** 238.

MOREL, J. E. and HALBLIEB, J. A. (1979). *A Versatile Numerical Method for Electron Slowing-down Spectral Calculations*, SAND 78-1780 (Sandia Laboratories, Albuquerque, New Mexico).

MORRIS, W. T. and OWEN, B. (1975). "An ionization chamber for therapy-level dosimetry of electron beams," Phys. Med. Biol. **20,** 718.

NACP (1972). Recommendations of the Nordic Association of Clinical Physics (1971). "Procedures in radiation therapy dosimetry with 5 to 50 MeV electrons and roentgen and gamma rays with maximum photon energies between 1 MeV and 50 MeV," Acta Radiol. Ther. Phys. Biol. **11,** 603.

NACP (1980). Recommendations by the Nordic Association of Clinical Physics. "Procedures in external radiation therapy between 1 and 50 MeV," Acta Radiol. Onc. **19,** 55

NACP (1981). Supplement to the recommendations by the Nordic Association of Clinical Physics (1980). "Electron beams with mean energies at the phantom surface below 15 MeV," Acta Radiol. Onc. **20,** 402.

NAGEL, J. and SANIELEVICI, A. (1967). "Dosisvergleich-messungen für hochenergetische Elektronen mit Eisensulfat-Dosimeter," Strahlentherapie **133,**

561.

NAHUM, A. E. (1976). *Calculations of Electron Flux Spectra in Water Irradiated with Megavoltage Electron and Photon Beams with Applications to Dosimetry.* Thesis, University of Edinburgh, United Kingdom (Available from University Microfilms International, 30–32 Mortimer Street, London W1N 7RA, order number 77-70,006).

NAHUM, A. E. (1978). "Water/air mass stopping power ratios for megavoltage photon and electron beams," Phys. Med. Biol. **23,** 24.

NAHUM, A. E. (1980). Calculations commissioned by the ICRU electron dosimetry committee.

NAHUM, A.E. and GREENING, J. R. (1976). "Inconsistency in derivation of C_λ and C_E," Phys. Med. Biol. **21,** 862.

NAHUM, A. E. and GREENING, J. R. (1978). "A detailed re-evaluation of C_λ and C_E with application to ferrous sulphate G-values," Phys. Med. Biol. **23,** 894.

NAHUM, A. E. and SVENSSON, H. (1980). "Electron beam dosimetry: The state of the art," Paper presented at the Tenth Nordic Meeting on Clinical Physics, Nilsiä, Finland (available from Rad. Phys. Dept., Univ. Umeå, Sweden).

NAHUM, A. E. and SVENSSON, H. (1981). "The new Nordic dosimetry recommendations for external beam therapy," p. 135 in *Abstracts, Section 2 of XVth International Congress of Radiology.*

NAHUM, A. E., SVENSSON, H. and BRAHME, A. (1981). "The ferrous sulphate G-value for electron and photon beams: A semi-empirical analysis and its experimental support," p. 841 in *Proceedings of the Seventh Symposium on Microdosimetry,* Vol. II (Harwood Academic Publishers GmbH Chur, Switzerland).

NATH, R. and SCHULZ, R. J. (1979). "Calculated response and wall correction factors of practical ionization chambers for Co-60 gamma rays," Annual AAPM meeting, Atlanta, Georgia.

NBS (1964). National Bureau of Standards, *Handbook of Mathematical Functions,* NBS Applied Mathematics Series 55, Abramowitz, M. and Stegun, I.A., Eds. (U.S. Government Printing Office, Washington, D.C.).

NBS (1973). National Bureau of Standards, *Photonuclear Reaction Data, 1973,* NBS Special Publication 380 (National Bureau of Standards, Washington, D.C.).

NBS (1979). National Bureau of Standards, *Proceedings of a Conference on Neutrons from Electron Medical Accelerators,* NBS Special Publication 554 (U.S. Government Printing Office, Washington, D.C.).

NBS (1982). National Bureau of Standards, *Photonuclear Data Index, 1973–1981,* NBSIR 82-2543 (National Bureau of Standards, Washington, D.C.).

NCRP (1961). National Council on Radiation Protection and Measurements, *Stopping Powers for Use with Cavity Chambers,* NCRP Report No. 27, published as National Bureau of Standards Handbook 79 (National Council on Radiation Protection and Measurements, Bethesda, Maryland).

NCRP (1964). National Council on Radiation Protection and Measurements, *Shielding for High Energy Electron Accelerator Installations,* NCRP Report No. 31 (National Council on Radiation Protection and Measurements, Bethesda, Maryland).

NCRP (1971). National Council on Radiation Protection and Measurement, *Protection against Neutron Radiation,* NCRP Report No. 38 (National Council on Radiation Protection and Measurements, Bethesda, Maryland).

NCRP (1977). National Council on Radiation Protection and Measurement, *Radiation Protection Design Guidelines for 0.1–100 MeV Particle Accelerator Facilities,* NCRP Report No. 51 (National Council on Radiation Protection and Measurements, Bethesda, Maryland).

NCRP (1980). National Council on Radiation Protection and Measurements, *Influence of Dose and Its Distribution in Time on Dose-Response Relationships for Low-LET Radiations,* NCRP Report No. 64 (National Council on Radiation Protection and Measurements, Bethesda, Maryland).

NETTELAND, O. (1965). "Isodose measurements in inhomogeneous matter," p. 116 of *Symposium on High-Energy Electrons,* Zuppinger, A. and Poretti, G., Eds. (Springer-Verlag, Berlin).

NIAS, A. H. W., SWALLOW, A. J., KEENE, J. P. and HODGSON, B. W. (1973). "Absence of fractionation effect in irradiated HeLa cells," Int. J. Radiat. Biol. **23,** 559.

NIATEL, M. T. (1967). "An experimental study of ion recombination in parallel-plate free-air ionization chambers," Phys. Med. Biol. **12,** 555.

NIATEL, M. T. (1975). "Influence de la vapeur d'eau sur l'ionisation de l'air dans le cas d'une chambre à cavité," C. R. Acad. Sci. Ser. B. **281,** 361 (Also published in Recueil de Travaux du Bureau International des Poids et Mesures (BIPM) 5).

NÜSSE, M. (1969). "Factors affecting the energy-range relation of fast electrons in aluminium," Phys. Med. Biol. **14,** 315.

NÜSSLIN, F. (1975). "The influence of air cavities on the dose distribution of high-energy electron beams," Phys. Med. Biol. **20,** 728.

NÜSSLIN, F. (1978). "Electron treatment planning based on the solution of the Fermi-Eyges equation," p. 685 in *Computers in Radiation Therapy,* Rosenow, U., Ed. (Universitätus-Fravenblinik, Göttingen).

O'CONNELL, J., DYAL, P. and GODEMBERG, J. (1959). "$(\gamma, 2n)$-reactions in light elements," Phys. Rev. **116,**

173.

OKUMURA, Y. (1972). "Correction of dose distribution for air space in high-energy electron beam therapy," Radiology **103,** 183.

OKUMURA, Y., KITAGAWA, T. and KITABATAKE, T. (1969). "Scattering foil device for high energy electron beam therapy," Radiology **93,** 667.

OLIEN, T. C. and HOLLOWAY, A. F. (1969). "Energy-loss spectra for high-energy electrons as a function of depth in an absorber," Radiat. Res. **38,** 1.

OLLER, W. L., MENKER, D. F. and DAUER, M. (1969). "Evaluation of the Fricke dosimeter with other dosimetry systems," Health Phys. **17,** 653.

ORTON, C. G. (1966). "Clear perspex dosimetry," Phys. Med. Biol. **11,** 377.

OSMAN, G. (1976). "Dose distribution of therapeutic electron beams and automation of treatment planning," J. Med. **7,** 143.

OVADIA, J. and UHLMANN, E. M. (1960). "Isodose distribution and treatment planning with electrons of 20–35 MeV for deep seated tumors," Am. J. Roentgenol. **84,** 754.

OVADIA, J., DANZKER, M., BEATTIE, J. W. and LAUGHLIN, J. S. (1955). "Ionization of 9 to 17.5 Mev electrons in air," Radiat. Res. **3,** 430.

PAGES, L., BERTEL, E., JOFFRE, H. and SKLAVENITIS, L. (1972). "Energy loss, range and bremsstrahlung yield for 10 keV–100 MeV electrons in various elements and chemical compounds," At. Data **4,** 1.

PATAU, J. P. (1972). *Simulation du Transport des Électrons et des Photons entre 1 keV et 100 MeV par le Methode de Monte-Carlo.* Thesis, University of Toulouse, France.

PATAU, J. P., BLANC, D., MATHIEU, J. and MASON, G. (1969). "Transport simulé d'electrons de 2 MeV dans divers materiaux," p. 401 in *Proceedings of the Second Symposium on Microdosimetry*, Report No. EUR 4452, Ebert, H. G., Ed. (Commission of the European Communities, Brussels).

PETTERSSON, C. (1967). "Calorimetric determination of the G-value of the ferrous sulphate dosimeter with high energy electrons and ^{60}Co gamma-rays," Ark. Fys. **34,** 385.

PETTERSSON, C. and HETTINGER, G. (1967). "Dosimetry of high energy electron radiation based on the ferrous sulfate dosimeter," Acta Radiol. Ther. **6,** 160.

PINKERTON, A. P. (1969). "Comparison of calorimetric and other methods for the determination of absorbed dose," Ann. N.Y. Acad. Sci. **161,** 63.

POHLIT, W. (1960). "Dosisverteilung in inhomogenen Medien bei Bestrahlungen mit schnellen Elektronen," Fortschr. Geb. Röntgenstr. Nuklearmed. **93,** 631.

POHLIT, W. (1965). *Dosimetrie zur Betatrontherapie* (Georg Thieme Verlag, Stuttgart).

POHLIT, W. and TEICH, M. (1962). "Zur Dosimetrie schneller Elektronen mit Kondensator-Ionisationskammern," Strahlentherapie **118,** 288.

PRILLINGER, G. (1977). *Berechnung von Elektronen und Bremsstrahlungsfeldern in heterogenen Gewebschichten*, IKE 6-96, Institut für Kernenergetik, Stuttgart.

PURDY, J. (1977). "Patient specific data acquisition in electron beam treatment planning," p. 22 in *Practical aspects of electron beam treatment planning*, Orton, C. G. and Bagne, F., Eds. (American Association of Physicists in Medicine, New York).

RAO, P. S. (1975). "Attenuation of monoenergetic gamma rays in tissues," Am. J. Roentgenol. **123,** 631.

RASE, S. and POHLIT, W. (1962). "Eine Extrapolationskammer als Standardmessgerät für energiereiche Photonen- und Elektronenstrahlung," Strahlentherapie **119,** 266.

RASSOW, J. (1969). "Beitrag zur Elektronentiefentherapie mittels Pendelbestrahlung, I. Grundlegende Vorversuche an Stehfeldern mit 43 MeV-Elektronen," Strahlentherapie **138,** 267.

RASSOW, J. (1970). "Beitrag zur Elektronentiefentherapie mittels Pendelbestrahlung, IV. Über eine neuartige, für primär unaufgestreute Elektronen spezifische telezentrische Klein-winkelnpendeltechnik," Strahlentherapie **140,** 156.

RAUSCHE, A. (1963). *Berechnung der Energieverteilung bei der Abbremsung von Elektronen in einem dicken Absorber.* Thesis, University of Würzburg, Germany.

REGOURD, D. (1962). "Contribution à la dosimetrie par films dans des faisceaux d'electrons de haute énergie. Application à l'étude des surface irrégulières," Mémoires (CES Electroradiologie, Paris).

RESTER, D. H. and DERRICKSON, J. H. (1971). "Electron transmission measurements for Al, Sn, and Au targets at electron bombarding energies of 1.0 and 2.5 MeV," J. Appl. Phys. **42,** 714.

ROBINSON, J. E. and MCDOUGALL, R. S. (1966). "A variable electron beam collimator for a medical betatron," Acta Radiol. Ther. Phys. Biol. **5,** 155.

ROBINSON, J. E. and ERWIN, T. L. (1969). "A study of the relative biological effectiveness for 35 MeV electrons with mammalian cells (100%)—10% depth-dose levels," Ann. N.Y. Acad. Sci. **161,** 301.

ROHRLICH, F. and CARLSON, B. C. (1954). "Positron-electron differences in energy loss and multiple scattering," Phys. Rev. **93,** 38.

ROOS, H., DREPPER, P. and HARDER, D. (1973). "The transition from multiple scattering to complete diffusion of high energy electrons," p. 779 in *Proceedings of the Fourth Symposium on Microdosimetry*, EUR 5122 (Commission of the European Communities, Luxembourg).

ROSSI, B. B. (1952). *High Energy Particles*, (Prentice

Hall, New York).

ROSSI, H. H. and FAILLA, G. (1956). "Tissue equivalent ionization chambers," Nucleonics **14,** No. 2, 32.

ROSSI, H. H. and ROESCH, W. C. (1962). "Field equations in dosimetry," Radiat. Res. **16,** 783.

ROTBLAT, J. and SUTTON, H. C. (1960). "The effects of high dose rates of ionizing radiations on solutions of iron and ceric salts," Proc. R. Soc. London Ser. A. **255,** 490.

RUDÉN, B. I. (1971). "Two years experience of clinical thermoluminescence dosimetry of Radiumhemmet," p. 781 in *Proceedings of the 3rd International Conference on Luminescence Dosimetry*, Risø (Danish AEC, Risø).

RUDÉN, B. I. (1975). *Some Applications of Thermoluminescence Dosimetry in Medical and Health Physics.* Thesis, Institute of Radiation Physics, Stockholm, Sweden.

RUDÉN, B. I. and BENGTSSON, L. B. (1977). "Accuracy of megavoltage radiation dosimetry using thermoluminescent lithium fluoride," Acta Radiol. Ther. Phys. Biol. **16,** 157.

RUDÉN, B. I. and NILSSON, B. (1975). "Clinical dosimetry by means of thermoluminescent dosemeters," Proc. XIII Int. Congress of Radiology. Excerpta Med. Int. Congr. Ser. No. 339, **2,** 495. Also published as Risø Report No. 249 (Danish AEC, Risø).

SÄBEL, M., SCHMIDT, T. and PAULY, H. (1972). "Heat defect of low energy x-ray absorbed in tissue-equivalent plastic," Health Phys. **23,** 744.

SANDBERG, G. (1973). "Electron beam flattening with an annular scattering foil," IEEE Trans. Nucl. Sci. **20,** 1025.

SCHIFF, L. I. (1946). "Energy angle distribution of betatron target radiation," Phys. Rev. **70,** 87.

SCHIFF, L. I. (1951). "Energy-angle distribution of thin target bremsstrahlung," Phys. Rev. **83,** 252.

SCHMID, E., RIMPL, G. and BAUCHINGER, M. (1974). "Dose-response relation of chromosome aberrations in human lymphocytes after *in vitro* irradiation with 3-MeV electrons," Radiat. Res. **57,** 228.

SCHMIDT, K. H. and BUCK, W. L. (1969). "Conductimetric dosimetry: A calorimetric method for measuring high-intensity pulsed radiation," Radiat. Res. **40,** 473.

SCHNEIDER, D. O. and CORMACK, D. V. (1959). "Monte Carlo calculation of electron energy loss," Radiat. Res. **11,** 418.

SCHOPKA, H. J. (1977). *Messung der Energieverluste der Transmission und der Reichweite schneller Elektronen in dicken Materieschichten.* Thesis, University of Frankfurt, Germany.

SCHRÖDER-BABO, P. and HARDER, D. (1981). "Die charakteristischen Funktionen der Dosisverteilung energiereicher Elektronen," p. 637 in *Medizinische Physik*, Bunde, E., Ed. (A. Hüthig Verlag, Heidelberg).

SCHULER, R. H. and ALLEN, A. O. (1956). "Yield of the ferrous sulfate radiation dosimeter: An improved cathode-ray determination," J. Chem. Phys. **24,** 56.

SCHULZ, H. J. (1970). *Aufbau des Sekundärelektronen-Spektrums Energiereicher Elektronen. Ein spezielles Problem des Durchgangs von Elektronen durch Materie.* Thesis, University of Würzburg, Germany.

SCHULZ, H. J. and HARDER, D. (1969). "Aufbau des Sekundärelektronenspektrums bei energiereicher Elektronenstrahlung," p. 595 in *Proceedings of the Second Symposium on Microdosimetry*, Report No. 4452, Ebert, H. G., Ed. (Commission of the European Communities, Brussels).

SCHULZ, R. J., SCHULTZ, S. and BOTSTEIN, C. (1963). "Clinical and physical aspects of electron beam therapy," Radiology **80,** 301.

SCOTT, W. T. (1963). "The theory of small-angle multiple scattering of fast charged particles," Rev. Mod. Phys. **35,** 231.

SCOTT, P. B. and GREENING, J. R. (1961). "Recombination in parallel plate free-air ionization chambers," Br. J. Radiol. **34,** 791.

SCOTT, M. B., HANSON, A. O. and KERST, D. W. (1955). "Electro- and photo-disintegration cross sections of ^{63}Cu," Phys. Rev. **100,** 209.

SCRAD (1966). The Sub-Committee on Radiation Dosimetry of the American Association of Physicists in Medicine, "Protocol for the dosimetry of high energy electrons," Phys. Med. Biol. **11,** 505.

SELIGER, H. H. (1955). "Transmission of positrons and electrons," Phys. Rev. **100,** 1029.

SELTZER, S. M. and BERGER, M. J. (1973). "Photoneutron Production in Thick Targets," Phys. Rev. **C7,** 858.

SELTZER, S. M. and BERGER, M. J. (1982a). "Evaluation of the collision stopping power of elements and compounds for electrons and positrons," Int. J. Appl. Radiat. Isot. **33,** 1189.

SELTZER, S. M. and BERGER, M. J. (1982b). "Procedure for calculating the radiation stopping power for electrons," Int. J. Appl. Radiat. Isot. **33,** 1219.

SELTZER, S. M., HUBBELL, J. H. and BERGER, M. J. (1978). "Some theoretical aspects of electron and photon dosimetry," p. 3 in *National and International Standardization of Radiation Dosimetry, Vol. II,* IAEA Publication STI/PUB/471 (IAEA, Vienna).

SEMPERT, M. (1960). "New developments in high energy electron beam therapy with the 35 MeV Brown Boveri Betatron," Radiology **74,** 105.

SEWCHAND, W., KHAN, F. M. and WILLIAMSON, J. (1979). "Total-body superficial electron-beam therapy using a multiple-field pendulum-arc technique," Radiology **130,** 493.

SHALEK, R. J. and SMITH, G. E. (1969). "Chemical dosimetry for the measurement of high energy photons and electrons," Ann. N.Y. Acad. Sci. **161,** 44.

SHALEK, R. J., SINCLAIR, W. K. and CALKINS, J. C. (1962). "The relative biological effectiveness of 22 Mevp x-rays, Cobalt-60 gamma rays, and 200 Kvcp x-rays II. The use of the ferrous sulphate dosimeter for x-ray and gamma-ray beams," Radiat. Res. **16,** 344.

SHIGEMATSU, Y. and HAYAMI, A. (1969). "Electron therapy with a 6 MeV linear accelerator," Strahlentherapie **138,** 645.

SHIRAGAI, A. (1977). "An approach to an analysis of the energy response of LiF-TLD to high energy electrons," Phys. Med. Biol. **22,** 490.

SIEGBAHN, K. (1965). *Alpha-, Beta- and Gamma-Ray Spectroscopy*, Vol. I (North Holland Publishing Company, Amsterdam).

SINCLAIR, W. K. and KOHN, H. I. (1964). "The relative biological effectiveness of high energy photons and electrons," Radiology **82,** 800

SIRLIN, A. (1956). "Angular distribution of betatron target radiation," Phys. Rev. **101,** 1219.

SKAGGS, L. S. (1949). "Depth dose of electrons from the betatron," Radiology **53,** 868.

SKAGGS, L. S., LANZL, L. H. and AVERY, R. T. (1958). *"A new approach to electron therapy,"* page 312 in *Proceedings 2nd International Conference on Peaceful Uses of Atomic Energy*, Vol 26 (United Nations, New York).

SKOROPAD, D. (1975). "The effect on an air cavity on the dose distribution of accelerated electrons," Med. Radiol. **7,** 55.

SPENCER, L. V. (1955). "Theory of electron penetration," Phys. Rev. **98,** 1597.

SPENCER, L. V. (1959). *Energy Dissipation by Fast Electrons*, NBS Monograph 1 (National Bureau of Standards, Washington D.C.).

SPENCER, L. V. and ATTIX, F. H. (1955). "A theory of cavity ionization," Radiat. Res. **3,** 239.

SPENCER, L. V. and FANO, U. (1954). "Energy spectrum resulting from electron slowing down," Phys. Rev. **93,** 1172.

SPIRA, J., BOTSTEIN, C., EISENBERG, B. and BERDON, W. (1962). "Betatron: Electron Beam 10–35 MeV," Am. J. Roentgenol. **88,** 262.

STEBEN, J. D., AYYANGAR, K. and SUNTHARALINGAM, N. (1976). "Characterization of betatron electron beams for dosimetry calculations," Digest of the 4th ICMP, Phys. in Canada **32,** 28.10.

STEBEN, J. D., AYYANGAR, K. and SUNTHARALINGAM, N. (1979). "Betatron electron beam characterization for dosimetry calculations," Phys. Med. Biol. **24,** 299.

STEFFEN, K. G. (1965). *High Energy Beam Optics*, (J. Wiley, New York).

STERNHEIMER, R. M. (1952). "The density effect for the ionization loss in various materials," Phys. Rev. **88,** 851.

STERNHEIMER, R. M. (1953). "The energy loss of a fast charged particle by Cerenkov radiation," Phys. Rev. **91,** 256.

STERNHEIMER, R. M. (1954). "Multiple scattering correction for counter experiments," Rev. Sci. Instrum. **25,** 1070.

STERNHEIMER, R. M. (1956). "Density effect for the ionization loss in various materials," Phys. Rev. **103,** 511.

STERNHEIMER, R. M. and PEIERLS, R. F. (1971). "General expression for the density effect for the ionization loss of charged particles," Phys. Rev. **B3,** 3681.

SUGIYAMA, H. (1970). "Monte Carlo calculation of electron slowing-down spectra at high energies," Danki Shikensho Iho **34,** 572.

SUNTHARALINGAM, N. and MANSFIELD, C. M. (1971). "Lithium fluoride dosimeters in clinical radiation dose measurements," p. 816 in *Proceedings 3rd International Conference on Luminescence Dosimetry* (Danish AEC, Risø).

SUNTHARALINGAM, N. (1980). "Current status of clinical applications of thermoluminescent dosimetry in the United States," presented at the 6th International Conference on Solid State Dosimetry, Toulouse, France.

SVENSSON, H. (1970). *Dosimetric Measurements at the Nordic Medical Accelerators. Part II. Absorbed Dose Measurements* (Rad. Phys. Dept., Univ. of Umeå, Umeå, Sweden).

SVENSSON, H. (1971). "Influence of scattering foils, transmission monitors and collimating system on the absorbed dose distribution from 10 to 35 MeV electron radiation," Acta Radiol. Ther. Phys. Biol. **10,** 443.

SVENSSON, H. (1978). "Quality aspects of the electron and photon beams from a 22 MeV microtron," page 7 in *Proceedings of the Swedish Society of Radiation Physics, 19 May.*

SVENSSON, H. (1981). Private communication.

SVENSSON, H. and BRAHME, A. (1976). "Electron Beam Parameters," p. 65 in *Radiation Dosimetry*, American Association of Physicists in Medicine 1976 Summer School (University of Vermont, Burlington).

SVENSSON, H. and BRAHME, A. (1979). "Ferrous sulphate dosimetry for electrons, a re-evaluation," Acta Radiol. Oncol. **18,** 326.

SVENSSON, H. and BRAHME, A. (1981). "Fundamentals of electron beam dosimetry," p. 17 in *Proceedings of the Symposium on Electron Beam Therapy*, Chu, F. C. H. and Laughlin, J. S., Eds. (Memorial Sloan-Kettering Cancer Center, New York).

SVENSSON, H. and HETTINGER, G. (1967). "Measurement of doses from high energy electron beams at small phantom depth," Acta Radiol. **6,** 289.

SVENSSON, H. and HETTINGER, G. (1971). "Dosimetric measurements at the nordic medical accelerators. Part I. Characteristics of the radiation beam," Acta Radiol. Ther. Phys. Biol. **10,** 369.

SVENSSON, H. and NAHUM, A. E. (1981). "A plane-parallel ionization chamber for the dosimetry of electron beams," p. 5 in *Radiophysique*, Recueil des Communications du XXème Congrès des Physiciens d'Hôpitaux d'Expression Française (Clinique Ste-Catherine, Avignon, France).

SVENSSON, H. and PETTERSSON, C. (1967). "Absorbed dose calibration of thimble chambers with high energy electrons at different phantom depths," Ark. Fys. **34,** 377.

SVENSSON, G. K., MCCALL, R. C., JENKINS, T. M. and NELSON, W. R. (1968). "Use of thermoluminescent dosimeters in high energy health physics," *2nd Int. Conf. on Luminescence Dosimetry*, Gatlinburg, Tennessee, CONF-680920 (National Technical Information Service, Springfield, Virginia).

SWANSON, W. P. (1979). "Improved calculation of photoneutron yields released by incident electrons," Health Phys. **37,** 347.

TABATA, T. and ITO, R. (1974). "An algorithm for energy deposition by fast electrons," Nucl. Sci. Eng. **53,** 226.

TABATA, R. and ITO, R. (1975). "A generalized empirical equation for the transmission coefficient of electrons," Nucl. Instrum. Methods **127,** 429.

TABATA, T., ITO, R. and OKABE, S. (1967). "Angular distribution of transmitted electrons with incident energies 3.2–14.1 MeV," Annu. Rep. Radiat. Cent. Osaka Prefect. **8,** 60.

TABATA, T., ITO, R., OKABE, S. and FUJITA, Y. (1971a). "Charge distribution produced by 4 to 24 MeV electrons in elemental materials," Phys. Rev. **B3,** 572.

TABATA, T., ITO, R., OKABE, S. and FUJITA, Y. (1971b). "Extrapolated and projected ranges of 4–24 MeV electrons in elemental materials," J. Appl. Phys. **42,** 3361.

TAIMUTY, S. I. and DEAVER, B. S. (1961). "Transmision current monitor for high energy electron beams," Rev. Sci. Instrum. **32,** 1098.

TAPLEY, N. DUV. (1976). "General Considerations," p. 81 in *Clinical Applications of the Electron Beam*, Tapley, N. duV., Ed. (John Wiley and Sons, New York).

TAUTFEST, G. W. and FECHTER, H. R. (1955). "A nonsaturable high-energy beam monitor," Rev. Sci. Instrum. **26,** 229.

TAYURSKII, V. A. (1976). "Efficiency for conversion of electron into positrons at 20–70 MeV," At. Energ. **40,** 70.

TELFORD, W. M., CRAWFORD, J. E., ZWICK, H. H. and STEPHENS-NEWSHAM, L. G. (1967). "Linear electron accelerator for medical purposes," J. Can. Assoc. Radiol. **28,** 278

TETENES, P. J. and GOODWIN, P. N. (1977). "Comparative study of superficial whole-body radiotherapeutic techniques using a 4-MeV nonangulated electron beam," Radiology **122,** 219.

THEISSEN, H. and GUDDEN, F. (1966). "Energieverlust von 53 MeV-Elektronen in Graphit," Z. Phys. **191,** 395.

THOMAS, J. K. and HART, E. J. (1962). "The radiolysis of aqueous solutions at high intensities," Radiat. Res. **17,** 408.

TOCHILIN, E., GOLDSTEIN, N. and LYMAN, J. T. (1968). "The quality and LET-dependence of three thermoluminescent dosimeters and their potential use as secondary standards," p. 424 of *Proc. of Second Int. Cont. on Luminescence Dosimetry*, USAEC and ORNL Conf. 680920 (National Technical Information Service, Springfield, Virginia).

TSAI, Y. S. (1974). "Pair production and bremsstrahlung of charged leptons," Rev. Mod. Phys. **46,** 815.

TURANO, L., BIAGINI, C., BOMPIANI, C. and PALEANI-VETTORI, P. G. (1959). "Radiobiologische, dosimetrische und klinische Grundlagen der Therapie mit schnellen Elektronen eines 15-MeV-Betatrons," Strahlentherapie **109,** 489.

UPTON, A. C., RANDOLPH, M. L. and CONKLIN, J. W. (1970). "Late effects of fast neutrons and gamma-rays in mice as influenced by the dose rate of irradiation: induction of neoplasia," Radiat. Res. **41,** 467.

VAN CAMP, V. and VANHUYSE, V. J. (1965). "Energy loss of electrons in thick foils," Phys. Lett. **19,** 504.

VAN DER LAARSE, R., BRUINVIS, I. A. D. and FARID NOOMAN, M. (1978). "Wall scattering effects in electron beam collimation," Acta. Radiol. Oncol. **17,** 113.

VAN DYK, J. and MACDONALD, J. C. F. (1972). "Penetration of high energy electrons in water," Phys. Med. Biol. **17,** 52.

VANHUYSE, V. J., WATTECAMPS, E. D., VAN DE VIJVER, R. E., and VANPRAET, G. J. (1962). "Secondary emission beam monitors for 0.5 to 3.5 MeV electrons," Nucl. Instrum. Methods **15,** 59.

VAVILOV, (1957). "Ionization losses of high energy heavy particles," Sov. Phys. JETP **5,** 749.

VERAGUTH, P. (1961). "Clinical experiments with electron therapy up to 30 MeV," Br. J. Radiol. **34,** 152.

VON ARX, A., KUPHAL, K. and SEMPERT, M. (1970). "Energieeichung der Elektronenstrahlung eines 45 MeV-Betatrons mit Hilfe des Cerenkov-Effektes," Stud. Biophys. **23,** 51.

WAMBERSIE, A. (1967). *Contribution à l'Étude de l'Efficacité Biologique Relative des Faisceaux de*

Photons et d'Électrons de 20 MeV du Bétatron. Thesis, Université Catholique de Louvain, Journal Belge de Radiologie, Monographie No. 1.

WAMBERSIE, A. (1971). "Problèmes radiobiologiques posés par l'utilisation thérapeutique des électrons de haute énergie," J. Radiol. et Electrol. **52,** 574.

WAMBERSIE, A. and DUTREIX, A. (1971). "Problèmes dosimétriques posés par la détermination de l'EBR dans un large domaine d'énergie (électrons de 15 à 34 MeV, photons de 55 kV à 20 MV), p. 261 in *Biophysical Aspects of Radiation Quality*, IAEA Publication STI/PUB/286 (International Atomic Energy Agency, Vienna).

WAMBERSIE, A., DUTREIX, A., DUTREIX, J. and TUBIANA, M. (1965). "Depth dose curves determined by ionization, film density, ferrous sulphate and survival rate of coli bacteria and diploid yeasts using a 20 MeV electron beam," p. 140 in *Symp. on High-Energy Electrons*, Zuppinger, A. and Poretti, G., Eds. (Springer-Verlag, Berlin).

WAMBERSIE, A., PRIGNOT, M., VAN DAM, J., DARDENNE, J. C. and GUEULETTE, J. (1971). "EBR des électrons de 34 MeV par rapport au ^{60}Co, évaluée par la mort intestinale chez les souris aprés irradiation unique et fractionnée. Etude dosimétrique par le $FeSO_4$," Strahlentherapie **142,** 182.

WAMBERSIE, A., BOUHARMONT, J., LELLOUCH, J., PRIGNOT, M. and LAMOTTE, M. (1972). "EBR d'un faisceau d'électrons de 15 MeV en fonction des modifications de son spectre d'énergie en profondeur déterminée par l'étude des aberrations chromosomiques radio-induites chez 'Allium cepa'," p. 345 in *Proceeding of the Third Symposium on Microdosimetry*, Report No. 4810, Ebert, H. G., Ed. (Commission of the European Communities, Luxembourg).

WAMBERSIE, A., BOUHARMONT, J. and PRIGNOT, M. (1973). "RBE of a 15 MeV electron beam as a function of depth in the first millimeters of the irradiated medium, determined by radio-induced chromosomal aberration in onion roots (Allium cepa)," Atomkernenergie **21,** 254.

WAMBERSIE, A., ZREIK, H., PRIGNOT, M. and VAN DORPE, J. C. (1974). "Variation of RBE as a function of depth in a high energy electron beam in the first millimeters of the irradiated tissues determined by the observation of skin reactions on patients (a clinical trial)," Strahlentherapie **148,** 279.

WAMBERSIE, A., DUTREIX, A. and PRIGNOT, M. (1975). "Experience in the use of $FeSO_4$ in some practical aspects of high-energy electron dosimetry," p. 563 in *Biomedical Dosimetry*, IAEA Publication STI/PUB/401 (International Atomic Energy Agency, Vienna).

WAPSTRA, A. H. and GOVE, N. B. (1971). "1971 Atomic mass evaluation. Part II. Nuclear-reaction and separation energies," Nucl. Data (Sect. A) **9,** 303.

WARD, H. W. C. (1964). "Electron therapy at 15 MeV," Br. J. Radiol. **37,** 225.

WARD, H. W. C. (1965). "Clinical evaluation of RBE," p. 213 in *Symposium on High-Energy Electrons, Montreaux 1964*, Zuppinger, A., and Poretti, G., Eds. (Springer-Verlag, Berlin-Heidelberg-New York).

WESSELS, B. W., PALIWAL, B. R., PARROTT, M. J. and CHOI, M. C. (1979). "Characterization of Glinac-18 electron-beam energy using a magnetic analysis method," Med. Phys. **6,** 45.

WHITE, D. R. (1974). *The formulation of Substitute Materials with Predetermined Characteristics of radiation Absorption and Scattering.* Thesis, University of London.

WHITE, D. R., MARTIN, R. J. and DARLINSON, R. (1977). "Epoxyresin based tissue substitutes," Br. J. Radiol. **50,** 814.

WHYTE, G. N. (1959). *Principles of Radiation Dosimetry* (John Wiley, New York).

WICKMAN, G. (1974a). "A liquid ionization chamber with high spatial resolution," Phys. Med. Biol. **19,** 66.

WICKMAN, G. (1974b). "Radiation quality independent liquid ionization chamber for dosimetry of electron radiation from medical accelerators," Acta Radiol. Ther. Phys. Biol. **13,** 37.

WIDEROE, R. (1959). "Measurement problems arising in high-energy electron and X-ray therapy with a 31 MeV betatron," p. 251 in *Quantities Units and Measuring Methods of Ionizing Radiation*, Fossati, F., Ed. (U. Hoepti, Milan).

WILLIAMS, P. C. and HENDRY, H. (1978). "The RBE of megavoltage photon and electron beams," Br. J. Radiol. **51,** 220.

WILLIS, C., BOYD, A. W. and MILLER O. A. (1971). "The absolute dosimetry of 600 kV high intensity pulsed electron accelerator used for radiation chemistry studies of gaseous samples," Radiat. Res. **46,** 428.

WOODARD, H. Q. (1962). "The elementary composition of human cortical bone," Health Phys. **8,** 513.

YAMAZAKI, T., TOMIMASU, T., MIKADO, T., CHIWAKI, M. and SUGIYAMA, S. (1977). "Spatial absorbed dose distribution in water, C and Al for 25 MeV electrons," Nucl. Instrum. Methods **144,** 515.

YANG, C. N. (1951). "Actual path length of electrons in foils," Phys. Rev. **84,** 599.

ZATZ, L. M., VON ESSEN, C. F. and KAPLAN, H. S. (1961). "Radiation therapy with high energy electrons. Part D. Clinical experience 10 to 40 MeV," Radiology **77,** 928.

ZERBY, C. D. and KELLER, F. L. (1967). "Electron transport theory, calculations and experiments." Nucl. Sci. Eng. **27,** 190.

ICRU Reports

ICRU Reports are distributed by the ICRU Publications' office. Information on prices and how to order may be obtained from:

ICRU Publications
7910 Woodmont Avenue, Suite 1016
Bethesda, Maryland 20814
U.S.A.

The currently available ICRU Reports are listed below.

ICRU Report No.	*Title*
10b	*Physical Aspects of Irradiation* (1964)
10c	*Radioactivity* (1963)
10f	*Methods of Evaluating Radiological Equipment and Materials* (1963)
12	*Certification of Standardized Radioactive Sources* (1968)
13	*Neutron Fluence, Neutron Spectra and Kerma* (1969)
14	*Radiation Dosimetry: X Rays and Gamma Rays with Maximum Photon Energies Between 0.6 and 50 MeV* (1969)
15	*Cameras for Image Intensifier Fluorography* (1969)
16	*Linear Energy Transfer* (1970)
17	*Radiation Dosimetry: X Rays Generated at Potentials of 5 to 150 kV* (1970)
18	*Specification of High Activity Gamma-Ray Sources* (1970)
20	*Radiation Protection Instrumentation and Its Application* (1971)
22	*Measurement of Low-Level Radioactivity* (1972)
23	*Measurement of Absorbed Dose in a Phantom Irradiated by a Single Beam of X or Gamma Rays* (1973)
24	*Determination of Absorbed Dose in a Patient Irradiated by Beams of X or Gamma Rays in Radiotherapy Procedures* (1976)
25	*Conceptual Basis for the Determination of Dose Equivalent* (1976)
26	*Neutron Dosimetry for Biology and Medicine* (1977)
27	*An International Neutron Dosimetry Intercomparison* (1978)
28	*Basic Aspects of High Energy Particle Interactions and Radiation Dosimetry* (1978)
29	*Dose Specification for Reporting External Beam Therapy with Photons and Electrons* (1978)
30	*Quantitative Concepts and Dosimetry in Radiobiology* (1979)
31	*Average Energy Required to Produce an Ion Pair* (1979)
32	*Methods of Assessment of Absorbed Dose in Clinical Use of Radionuclides* (1979)
33	*Radiation Quantities and Units* (1980)
34	*The Dosimetry of Pulsed Radiation* (1982)
35	*Radiation Dosimetry: Electron Beams with Energies Between 1 and 50 MeV* (1984)

Binders for ICRU Reports are available. Each binder will accommodate from six to eight reports. The binders carry the identification, "ICRU Reports," and come with label holders which permit the user to attach labels showing the Reports contained in each binder.

The following bound sets of ICRU Reports are also available:

Volume I. ICRU Reports 10b, 10c, 10f
Volume II. ICRU Reports 12, 13, 14, 15, 16, 17, 18, 20
Volume III. ICRU Reports 22, 23, 24, 25, 26
Volume IV. ICRU Reports 27, 28, 29, 30, 31, 32

(Titles of the individual Reports contained in each volume are given in the list of Reports set out above.)

The following ICRU Reports were superseded by subsequent Reports and are now out of print:

ICRU Report No.	*Title and Reference**
1	*Discussion on International Units and Standards for X-ray Work.* Brit. J. Radiol. **23,** 64 (1927).
2	*International X-Ray Unit of Intensity*, Brit. J. Radiol. (new series) **1,** 363 (1928).
3	*Report of Committee on Standardization of X-ray Measurements*, Radiology **22,** 289 (1934).
4	*Recommendations of the International Committee for Radiological Units*, Radiology **23,** 580 (1934).
5	*Recommendations of the International Committee for Radiological Units*, Radiology **29,** 634 (1937).
6	*Recommendations of the International Commission on Radiological Protection and of the International Commission on Radiological Units*, National Bureau of Standards Handbook 47 (U.S. Government Printing Office, Washington, D.C., 1951).
7	*Recommendations of the International Commission for Radiological Units*, Radiology **62,** 106 (1954).
8	*Report of the International Commission on Radiological Units and Measurements (ICRU)* 1956, National Bureau of Standards Handbook 62 (U.S. Government Printing Office, Washington, D.C., 1957).
9	*Report of the International Commission on Radiological Units and Measurements (ICRU)* 1959, National Bureau of Standards Handbook 78 (U.S. Government Printing Office, Washington, D.C., 1961).
10a	*Radiation Quantities and Units*, National Bureau of Standards Handbook 84 (U.S. Government Printing Office, Washington, D.C., 1962).
10d	*Clinical Dosimetry*, National Bureau of Standards Handbook 87 (U.S. Government Printing Office, Washington, D.C., 1963).
10e	*Radiobiological Dosimetry*, National Bureau of Standards Handbook 88 (U.S. Government Printing Office, Washington, D.C., 1963).
11	*Radiation Quantities and Units* (International Commission on Radiation Units and Measurements, Washington, D.C., 1968).

19 *Radiation Quantities and Units* (International Commission on Radiation Units and Measurements, Washington, D.C., 1971).

19S *Dose Equivalent* [Supplement to ICRU Report 19] (International Commission on Radiation Units and Measurements, Washington, D.C., 1973).

21 *Radiation Dosimetry: Electrons with Initial Energies Between 1 and 50 MeV* (International Commission on Radiation Units and Measurements, Washington, D.C., 1972).

* References given are in English. Some of the Reports were also published in other languages.

Index

Absorbance, *see:* Ferrous Sulphate Dosimeter
Absorbed Dose, 22, 65–121
  Determination of, 65–76, 89, 99–103
  Distribution in a patient, 112–121
  In Phantom, 96–111
  Measurement techniques, 77–95
Absorbed Dose in Air Conversion Factor, 87–89
Absorbed Dose Distribution, 31, 32, 34–38, 99–110 *see also:* Depth-Dose Curve
  At the Reference Point, 99, 100
  Broad beam, 36, 37
  in planes parallel to the beam, 109, 110
  in planes perpendicular to the beam axis, 109, 110
  Measurement of, 109
  On the Reference Axis, 101–109
  Plane isotropic source, 38
  Plane parallel beam, 36
  Point isotropic source, 37
  Point monodirectional beam, 35
Accelerator, 44, 55, 56, 63
  Beam current, 63
  Betatron, 44, 55, 63
  Linear accelerator, 55, 63
  Microtron, 44, 55, 63
Adjacent Beams, *see:* Treatment Planning
Air Kerma Calibration Factor, 89
Alignment, 125
Angular Distribution, 28–31, 49–55, 105 *see also:* Scatt
  Angular spread, 51, 52, 55, 105
  Central mean square angular spread, 49
  Deflection angle, 29
  Effective mean square angular spread, 49
  Fermi-Eyges distribution, 28, 29
  Full diffusion, 28, 55
  Gaussian distribution, 28–31
  Large angle single scattering, 28, 29
  Lateral distribution, 28, 29
  Mean square angular spread, 29, 50
  Molière distribution, 29
  Small-angle approximation, 29
Angular Spread, *see:* Angular Distribution
Avogadro Constant, 3

Backscattering, 33
Beam, 30, 31, 35–37, 43–45, 49, 97
  Beam axis, 97
  Beam optical system, 45
  Broad, 36, 37
  Circular, 31
  Clinical electron, 43
  Elementary narrow (or pencil beam), 31
  Gaussian, 30
  Intrinsic accelerator, 44
  Initial electron, 44
  Radial spread of, 49
  Rectangular, 31
  Plane-parallel, 36
  Point monodirection, 35
Beam Monitor, 122–124
  Monitor check, 125
  Transmission monitor, *see:* ion chamber
Beam Optics, 43
Bending Magnet, *see:* Magnet
Bolus, 116
Bragg-Gray Relationship, 65, 70
Bremsstrahlung, 39, 46, 106
  Contamination, 39, 46, 106
  Target, 39
Build-up, 32
Build-up Cap, 88

Calorimetry, 77, 78
  Aqueous calorimeter, 78
  Carbon calorimeter, 77
  Holographic interferometry, 78
  Tissue-equivalent calorimeter, 77
Cavity-wall Interface, 71
Cerenkov Radiation, 3, 59–61
  Emission treshold, 59–61
  Measurement of, 59
Charge Collecting Volume, 85
Charge Deposition, 34, 85, 86
Charge Measurement, 85
Charge Transport, 32
Check, 125, 126
  Absorbed dose, 125
  Energy, 125
  Monitor, 125
  Uniformity, 126
Chemical Defect, 77, 78
Chemical Determination of Absorbed Dose, 80
"Cold Spot," 113
Collimation, 43, 44, 46–48
  Diaphragm, 46
  Tube (cone), 46, 47
Collision Loss, 3, 6–8
Contamination and Leakage Measurements, 126, 127
Continuous-Slowing-Down, 14
Coordinate System, 28
Covariance of Radial and Angular Distribution, 30, 49, 50
Cut-off Energy, 9

Decelerator, 115
Delta ray(s), 23, 32
Density, 4, 5, 74, 82, 114
  Compounds and mixtures, 5
  Elements, 4
  Graphite density, 4, 74, 82
  Tissues, 114
Density Effect, 3, 4, 71, 72
Depth Distribution, *see:* Absorbed-Dose Distribution
Depth-Dose Curve, 51, 57, 101–109 *see also:* Absorbed-Dose Distribution
  Characteristics of, 103–105
  Dependence on field size, 107, 108
  Dependence on source-surface distance, 109
  Dose gradient, 102–106
  Influence of angular distribution, 51
  Influence of energy distribution, 57
  Measurement of, 101
Detector, 65, 66, 68, 72, 90–95
  Gas-filled, 66 (*see also:* ion chamber)

Large, 65
Liquid, 68
PMMA, 92
Silicon diode, 92
Small, 65
Solid, 68, 90–95
TLD, 90–92
Wall-less, 72
Distance Indicator, 125
Dose Gradient, 103–107
Dosimetric Measurement on the Patient, 127

Effective Point of Measurement, 65, 67–69
Determination of, 67
Electron 3, 30, 32, 70, 71, 114
Electron densities, 114
Electron radius, 3
Primary, 30, 70
Rest energy of, 3
Secondary, 32, 71
Electron Interaction, 3
Electronuclear Reaction, 41, 58
Elemental Composition, 5
Emittance, 43
Energy, 23–27, 55–63, 105
Determination of, 57–63
Energy at the phantom surface, 56
Energy-loss spectra, 26, 27
Energy-range relations, 62
Energy spectra, 23, 56
Energy spread, 23, 24, 25, 55, 105
Energy straggling, 25
Maximum energy, 23, 55
Mean energy, 23, 24, 55
Most probable energy, 23, 24, 55
Slowing-down spectra, 27
Statement of, 57
Entrance (or Surface-) Absorbed Dose, 103–107
Equivalent Thickness, 113
Excitation Energy, 3, 4

Faraday Collector, 33
Ferrous Sulphate Dosimeter, 80–82
Absorbance, 80
Molar linear absorption coefficient, 80, 81
Radiation chemical yield, 80–82
Field Size, 107–109
Field Instruments, 86–90
Film Dosimeter, 92–95
Optical density, 92, 93
Sensitometric curve, 92, 93
Fine Structure Constant, 11
Flattening, 43, 45, 46
Fluence, 22–24, 29, 31, 32
Differential particle fluence, 22
Fluence differential in angle, 22, 24, 29
Fluence differential in energy, 22, 24
Planar fluence, 22, 23, 31
Primary fluence, 32
Uni-directional planar fluence, 23
Vectorial energy fluence, 22
Vectorial particle fluence, 22
Focal Spot, 44

Gas Ionization Chambers, 83–90

"Hot Spot," 47, 110, 113

Humidity Correction, 84, 85

Inhomogeneity, 113–115
Interface, 71
Ion (or ionization) chamber, 44, 65, 66, 83–90, 101, 122–123
Absolute, 84
Air-equivalent wall, 87
Calibrated, 84
Cylindrical (thimble), 67
Calibration of, 87–90
Extrapolation, 84, 85
Field instrument, 86
Calibration of field instrument, 87
Flat (or coin-shaped), 66
Guard ring, 66, 86
Ionization chamber measurements, 101
Transmission monitor, 44, 122, 123
Water equivalent wall, 87
Irradiation Geometry, 43 (*also see:* Phantom)
Isocenter, 44

Kerma, 89

Lateral distribution 29, 30
Leakage Radiation, 111, 126–127
Leakage measurements, 126
Linear Energy, 132
Liouville Theorem, 43
Liquid Ionization Chamber, 90

Magnet, 44–45
Bending, 44, 45
Scanning, 45
Mass Scattering Power, 18–21
Molar Linear Absorption Coefficient, *see:* Ferrous Sulphate Dosimeter
Monte Carlo Calculation, 31, 73
Moving Beams, *see:* Treatment Planning
Multiple Scattering (*see also:* Angular Distribution), 28

Neutron, 40, 58, 126
Nuclear Reaction Threshold, 58, 59

Oblique Incidence, 112

Path Length, 15
Parallel Opposed Beams, *see:* Treatment Planning
Pencil Beam, *see:* Beam
Penumbra, 111
Physical penumbra, 111
Performance checks, 125, 126
Perturbation Correction Factor, 65–67, 69, 84–86, 103
Measurement of, 67
Phantom, 96–99, 111, 112
Absorbed Dose in, 96–111
Material equivalence, 96–99
Conversion of phantom data to tissue data, 112
Standard phantom, 96, 97
Phase-Space Ellipse, 49, 50
Photon Background, 103–107
Photon Contamination, 106
Photonuclear Reaction, 40, 58, 59
Pinhole Camera, 55
PMMA Detector, 92
Polarization Effect, *see:* Density Effect
Positron, 40
Primary Electron(s), 33, 70

Quadrupole Lens, 44

Radiation Length, 11
Radiobiology, 128
Radiotherapy, 128
Range, 14–17, 55, 61–63, 97, 103
  Continuous-slowing-down (csda), 14–17, 97
  Energy-range relations, 62
  Half-value depth, 63, 103
  Maximum, 61
  Measurement(s) of, 61–63
  Practical, 55, 61, 103
  Therapeutic, 103
RBE, 128
Reciprocity, 39
Recombination, 85, 86, 87, 122
Reference Axis, 101
Reference Material, 78
Reference Plane, 97
Reference Point, 99, 100
  Depth of, 99, 100
  Mean energy of electrons at the, 100
Reference Volume, 68

Scaling Law, 37
Scattering (*see also:* Angular Distribution), 18, 31, 46, 47
  Scattering by air, 31, 47
  Scattering by collimator wall, 46
Scattering Foil, 44–46
  Choice of, 46
  Primary foil, 44, 45
  Secondary foil, 44, 45
Scintillation Counter, 33
Screening Effect, 11, 18
Secondary Electrons, 32, 39, 71
Silicon Diode Detector, 92
Skin Absorbed Dose, *see:* Entrance Absorbed Dose
Solid State Dosimetry, 90–92
Source, 37, 38, 48–54, 109
  Effective electron source, 48–51
  Plane isotropic source, 38
  Point isotropic source, 37
  Source-surface-distance, 53, 54, 109
  Virtual point source, 48–52
Specific-Energy Distribution, 131
Spectra, *see:* Energy
Stopping Power, 3, 6–13, 39, 70,73–76, 97–99, 103
  Bragg-Gray, 70, 74–76
  Collision, 3, 6–8
  Harder, 72, 74–76
  Radiative, 11–13, 39
  Ratios of linear collision stopping powers, 97–99
  Ratios of linear total stopping powers, 97–99
  Ratios of linear radiative stopping powers, 97–99
  Recommended, 76
  Restricted (mass) collision, 9, 10
  Spencer-Attix, 73, 74–76, 102, 103
  Stopping power ratio, 70, 76
  Total mass, 3
Surface Dose, *see:* Entrance Absorbed Dose

Target, 28, 39
Thermoluminescent Dosimeters (see TLD)
Threshold, 58–61
  Cerenkov emission, 59–61
  Nuclear reaction, 58, 59
Time Structure, 63, 64
  Macropulse, 64
  Micropulse, 64
  Pulse repetion frequencies, 63
Tissue, 5, 114
  Density and composition, 5, 114
TLD, 90–92
  Fading, 92
Track-end(s), 22, 73
Track Length, 27
Transmission, 33
Transmission Monitor, *see:* Ion Chamber, 44
Treatment Planning, 116–121
  Adjacent beams, 117, 118
  Computerized treatment planning, 119–121
  Moving beams, 117, 119
  Multiple beams, 117

Uncertainty, 3, 4, 79–81, 85
  In the determination of absorbed dose
    at a point in carbon, 79
    at a point in material (m), 85
    at a point in water, 80, 81
  Of mass collision stopping power values, 3, 4
Uniformity, 110
  Uniformity index, 110

Vacuum Window, 44

W-value, 4, 84
Wedge, 116

X-ray(s), *see:* Bremsstrahlung